

DPhil Thesis

Load Measurement and Analysis of Kick Scooters

Sebastian Pearson

Supervised by Prof. Felix Hofmann and Prof. Edmund Tarleton

12 October, 2024

Abstract

Kick scooters are rapidly growing in popularity as a form of transport and are used recreationally. They are also seen as an effective way to combat inner-city pollution. This project is (to the author's knowledge) the first published work that aims to investigate the loads applied to scooters in real-world use. A data logging system has been built that is able to handle the vibrations associated with stunt scooter riding. The system can measure up to eight channels of strain data and log data up to a frequency of 62.5 kHz. A static force reconstruction model has been made for the scooter to gauge the magnitude of the applied loading to the scooter. Strain data is measured in the deck and the down tube of the scooter. Experimental results match well with finite element simulations. In addition, another force reconstruction model is made that considers dynamic effects. Results for measured strain and reconstructed forces for more than 25 of the following 12 different scooter stunts are given: bunnyhops, j-hops, tailwhips, heelwhips, barspins, opposite barspins, backside 180s, backside half-cabs, frontside 180s, frontside half-cabs, backside 360s and frontside 360s. Results show a significant variation in measured strains both within and between different scooter stunts. Regular barspins gave rise to the highest mean peak strains in the deck and down tube. Some of the peak strains do not appear to follow a normal distribution, as they fail the Shapiro-Wilk test for normality. Finally, a brief sketch is given of how the information could be used to optimise scooter components using topology optimisation. Results from a preliminary topology optimisation study are not successful in reducing the peak stresses in the neck of the scooter deck, highlighting the care needed in optimal scooter design.

Acknowledgements

First, I would like to express tremendous gratitude to my supervisors, Professors Felix Hofmann and Edmund Tarleton, for taking me on to do this research. I was unaware that one could do a DPhil on one's hobby, and it is not something I take for granted. I appreciate the many hours you both have put in to help this project. I thank Felix, especially for his advice on the experimental side of the project. Without your numerous insightful ideas, this project would never have gotten off the ground. Thank you both also for reading through the thesis and giving feedback.

I have also received much help from workshop staff in the department, particularly Duncan Constable and Christopher Hatcher. Duncan you were very helpful with making suspension bracket for the data logging system. You also gave general advice, and helped measure various parts of the scooter with your numerous tools. Chris, you helped in sanding down the wood profiles for the static calibration. Thank you Cleveland Williams and Phillip Lacey for facilitating the use of the staff-student workshop and giving a hand when needed. Major parts of the thesis done in the workshop include applying the strain gauges to the scooter, drilling the necessary holes to mount the data logger, and the machining for the aluminium beam (used for the static calibration). Thank you, Stuart Higgs and Patrick, for answering many of my electronics-related questions, especially in the earlier stages of the project. Dr. Feibiao Zhou and Professor Dan Rogers, thank you for your advice regarding the design of the signal conditioning board. I am grateful to Igor for training me on the Instron, which helped significantly with the static calibration. Thank you also, Professors Clive Siviour and Manolis Chatzis, for letting me use equipment and lab space for the dynamic calibration experiments. I would also like to thank Paul Warren for his help running the computers used for most of the finite element simulations.

Thank you also, Matthew King, for proofreading some of this thesis. I thank Professor Chris Grovenor for helping initiate discussions between me and Felix, without which the project would probably never have happened. I am also, of course, extremely thankful for the funding received from the EPSRC to carry out this research. I did not expect to get funding to do research on stunt scooters!

Thank you mum and dad for your general support, hospitality and love over the course of the DPhil. Thank you Nigel for your ongoing support and care, and offering to help in any way you could. Thank you for giving me a place to stay for the first year of the DPhil. Similarly, thank you Anna for offering to proofread my thesis, and for other offers of support throughout the last four years.

Finally, I would like to thank Jesus Christ through whom this universe was made. This is a fascinating universe in which it is possible to do science, ride scooters, and even do both at the same time!

Contents

1 Introduction **2**

1.1 What is a scooter? . . . 2

1.2 A history of stunt scooters . . . 5

1.3 Engineering context . . . 6

2 Literature Review **8**

2.1 Measuring loads on bicycles . . . 9

2.2 Other force reconstruction approaches . . . 19

2.3 Load analysis on bicycles . . . 24

2.4 Topology and shape optimisation . . . 28

2.5 Conclusion . . . 29

3 Background Theory **31**

3.1 Introduction . . . 31

3.2 FEA background . . . 31

3.3 Optimisation . . . 33

3.3.1 Topology optimisation . . . 34

3.3.2 Shape optimisation . . . 37

4 Building the Data Acquisition System **39**

4.1 Introduction . . . 39

4.2 The data acquisition system (DAQ) . . . 39

4.2.1 Overall structure of the DAQ and the data logger . . . 39
4.2.2 The signal conditioning board . . . 42
4.2.3 Suspension and other considerations . . . 47
4.3 Conclusion . . . 55

5 Static force reconstruction 56
5.1 Introduction . . . 56
5.2 Finite element model (static simulations) . . . 57
5.3 Strain measurement . . . 61
5.3.1 Strain gauge location . . . 61
5.3.2 A sample of strain measured in real-time . . . 67
5.4 Force reconstruction . . . 69
5.4.1 Static force reconstruction theory . . . 69
5.5 Early computational work . . . 73
5.5.1 FE model details . . . 73
5.5.2 Dealing with experimental noise and model imperfections. . . . 75
5.6 Static calibration . . . 79
5.6.1 Static calibration of the handle bar load . . . 79
5.6.2 Static calibration of deck loads . . . 91
5.6.3 Constraints and other conditions . . . 99
5.6.4 Mismatch load cases and reduced reconstructions . . . 100
5.7 Conclusion . . . 107

6 Dynamic Force Reconstruction 108
6.1 Introduction . . . 108
6.2 Dynamic force reconstruction theory . . . 108
6.2.1 Justification of the dynamic force reconstruction method . . . 114
6.3 Dynamic calibration . . . 116
6.3.1 General approach . . . 116

6.3.2 Accounting for the decay of the hammer signal . . . 124
6.3.3 Comparison with static model and drift correction . . . 125
6.4 Adjusting the shape of the basis impulses . . . 132
6.5 Conclusion . . . 133

7 Force Reconstructions **135**
7.1 Introduction . . . 135
7.2 Tikhonov regularisation . . . 136
7.3 General information . . . 142
7.3.1 A note on rider stances . . . 142
7.4 Bunnyhops and j-hops . . . 143
7.4.1 A note on terminology . . . 143
7.4.2 Bunnyhops . . . 143
7.4.3 J-hops . . . 146
7.5 Tailwhips and heelwhips . . . 155
7.5.1 Tailwhips . . . 155
7.5.2 Heelwhips . . . 157
7.6 Barspins and opposite barspins . . . 159
7.6.1 Barspins . . . 159
7.6.2 Opposite barspins . . . 162
7.7 Backside 180s (and backside half-caballerial) . . . 164
7.8 Frontside 180s (and frontside half-caballerial) . . . 167
7.9 Backside 360s . . . 170
7.10 Frontside 360s . . . 172
7.11 Discussion . . . 174
7.11.1 Testing for the normality of the data . . . 174
7.11.2 Other considerations . . . 179
7.12 Conclusion . . . 181

8 Simulations and Optimisation **182**

8.1 Introduction . . . 182

8.2 Finite element model (dynamic simulations) . . . 183

8.2.1 Single vs double output precision . . . 184

8.2.2 Element type and mesh convergence . . . 186

8.2.3 Using symmetry . . . 190

8.2.4 Timestep convergence and mass-scaling . . . 190

8.2.5 Small area load vs large area load comparison . . . 192

8.2.6 Axle boundary condition . . . 196

8.2.7 Natural frequency tests . . . 197

8.2.8 Filtering . . . 199

8.2.9 Linearity tests . . . 199

8.3 Axle boundary conditions, Material damping, and headset bearing stiffness . . . 202

8.3.1 Material damping . . . 202

8.3.2 Axle boundary conditions . . . 208

8.3.3 Headset bearings . . . 209

8.3.4 Testing the impact of the various conditions . . . 211

8.4 Comparison between static and dynamic model . . . 214

8.5 Topology optimisation . . . 215

9 Conclusion **222**

10 Future Work **225**

A Additonal Calibration Data and Errors **229**

Chapter 1

Introduction

1.1 What is a scooter?

The kind of scooters this thesis is concerned with are kick scooters. They all have a design similar to figure 1.1 a). Scooters generally have two wheels, although they can have more. Unless specified, the word 'scooter' will henceforth refer to kick scooters (as opposed to motorised moped-like scooters or mobility scooters). The basic design of the scooters discussed have handlebars, a clamp, forks, a deck and wheels, as well as an array of axles, bolts and bearings. An example can be seen in figure 1.1 a), with a deck shown in 1.1 b), and handlebars in 1.3. Scooters are usually made (primarily) from aluminium, steel, and polymeric materials such as urethane. Scooter decks tend to be made from aluminium, handlebars from steel or aluminium, and forks from steel or aluminium. Grips and wheels are made from polymeric materials.

Commuting scooters are made to be portable, light, and fast. They are often used on inner-city journeys that include parts of the journey on public transport. This is because they are far less cumbersome on public transport than bicycles, and much faster than walking. To increase portability, most modern commuting scooters have a folding mechanism in the deck (see figure 1.2 b)), height-adjustable and narrow handlebars (see figure 1.2 a), and a lightweight design. The adjustable handlebars help the rider adapt the height of the handlebars to fit the rider, leading to a more comfortable ride.

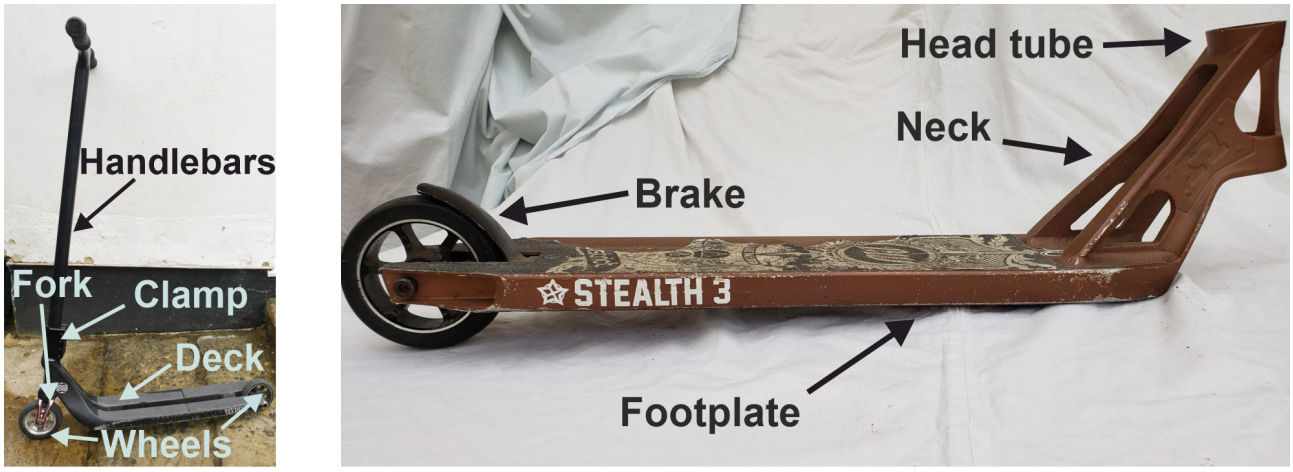


Figure 1.1: a) An image showing the main components of a scooter. b) A one-piece scooter deck. The neck and head-tube is forged for increased strength.

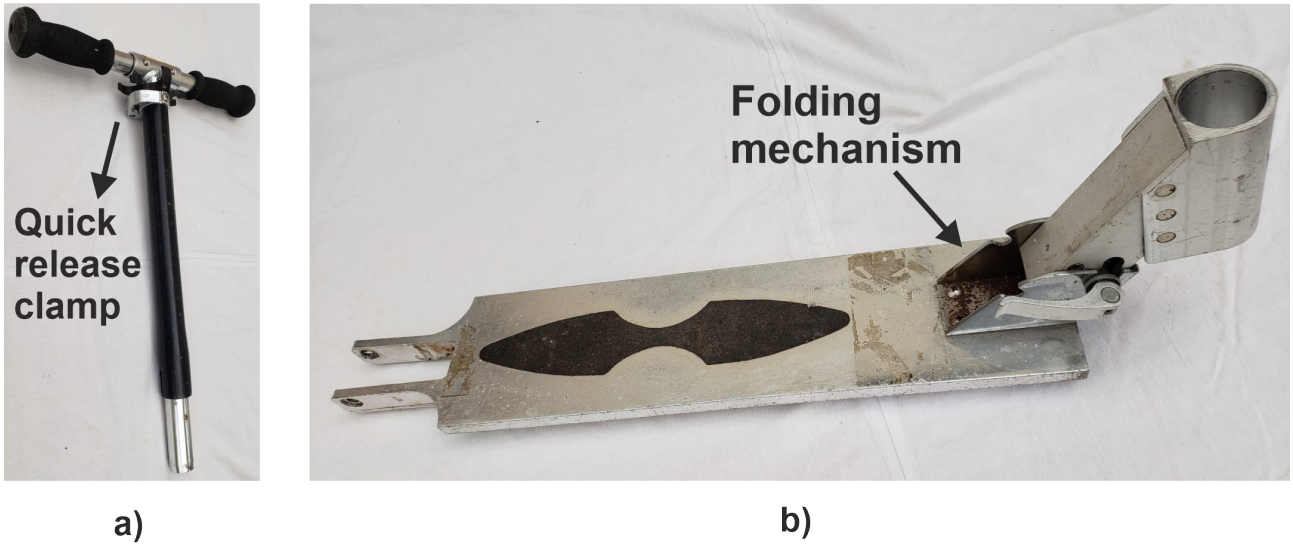


Figure 1.2: a) Adjustable handlebars are used for commuting as they can be made much smaller for travel, and the height can easily be adjusted to fit the rider. b) A scooter deck with a folding mechanism, common for commuting scooters.

Children's scooters are sometimes similar to commuting scooters, but with smaller wheels. Often, they are made almost entirely of polymeric materials, and sometimes have three or four wheels to make them easier to ride.

Electric scooters are a type of scooter that has rapidly grown in popularity over recent years. Often used for longer journeys, they require very little effort to ride because of their electric motor. Due to the large batteries inside and their generally bulkier design, they are much heavier than other types of kick scooter. They also have tyres, instead of the urethane wheel tread most other scooters have.

Stunt scooters are mostly used by children and teenagers in skateparks and elsewhere around cities. As riders often perform stunts whilst meters above the ground (e.g. when jumping down stairs, or doing stunts out of a ramp), the loading these scooters face is much higher than for other types of scooter. Generally, the scooter is designed to be lightweight to make stunts easier whilst still being resilient to repeated heavy loads. Handlebars are one-piece (see figure 1.3 a)) and of a fixed size. This allows them to be strong and stiff (they do not rattle like most adjustable handlebars). Gussets (figure 1.3 b)) are often added to increase strength. Decks have no folding mechanism (see figure 1.1 b)) – this is to avoid the play that can result from having a folding mechanism, avoid additional weight, and to increase the strength of the scooter. Wheel cores are made of aluminium (see figure 1.4), and forks are threadless, again to increase the strength of the scooter. Common alloys used for stunt scooter components include 6061 aluminium [1, 2] for welded components and either 6061 or 7075 aluminum [3] for machined parts. Both components tend to be heat-treated to the T6 condition (after welding, if applicable) to maximise strength. Steel handlebars are often made from AISI 4130 steel [4, 5]. The footplate of scooter decks tend to be extruded. The neck and headtube are either made from extruded components, which are then machined and welded, or from a single forged part which is machined (as in figure 1.1 b)). Forks tend to be welded (cheaper steel forks), or CNC machined from a single block of aluminium. Handlebars are made from welded tubes and sometimes have gussets welded on, as in figure 1.3. Decks tend to fail where the neck meets the headtube, where the neck meets the deck, at cut-out in the extrusion profile for the rear wheel, or the part of the extrusion profile that holds the rear axle fails. In these cases, the deck fails due to crack growth along the cross-section of the extrusion profile (or sometimes forging in the case of



Figure 1.3: a) One-piece handlebars are used on stunt scooters because of their increased strength. b) A closeup shot of the gussets, these are added to increase the strength of the crossbar.

the neck). The footplate can also bend (colloquially 'banana') by plastically deforming it such that it is no longer useable. Forks will break either by the fork legs bending or, more commonly, by the forktube snapping. Handlebars will either fail at the point where the gussets or down tube meet the crossbar or where the down tube meets the clamp.

The focus of this research is on stunt scooters. Stunt scooters face the highest loading, and the goal of maximising the strength to weight ratio of the scooter is a clear priority and end-goal. The same principles can then be applied to commuting and electric scooters to enhance their strength to weight ratio.

1.2 A history of stunt scooters

Modern stunt scooter riding has its roots in the arrival of the razor a-model in 2000 [6]. These scooters were used by children and teenagers to perform stunts (e.g. [7]). They were not designed for stunts and therefore failed prematurely. Because of this, scooter riders started modifying components to increase their longevity. Examples including replacing the folding mechanism with bolts [8] to



Figure 1.4: a) An aluminium metal core wheel. b) and c) Plastic core wheels did not respond well to the stresses of stunt scooter riding. b) was filled with hotglue to increase it's strength, but to little avail.

remove play from the scooter and adding hot glue to the cores of scooter wheels to increase their resilience [9]. Stunt scooter companies started to emerge from 2005, producing one-piece handlebars, as opposed to adjustable ones, and more heavy-duty forks. Threadless forks were invented, and associated compression systems were developed to keep the headset bearings tight [10]. The first 'aftermarket' scooter parts were much more durable than their predecessors, however, they were often considerably heavier. The stunt scooter scene exploded in growth around 2009-11 [11] and with it a host of new companies emerged. Since this, there has been further progress in the design of lightweight stunt scooters, but no rigorous analysis on the loading of stunt scooters has been performed.

1.3 Engineering context

The details of the stunt scooter market are hard to come by. The conducted investigation did not reveal the public accounts (of the revenue) of any of the major stunt scooter companies, and some did not even list the limited company name on their websites (e.g. [12]). There are, however, over 25 active stunt scooter brands at the time of writing. Research on stunt scooters also pave the way for research of other types of scooter. Stunt scooters have a simpler construction (e.g. no batteries, no folding mechanisms and no adjustable handlebars). Because of this it simpler to make and analyse

computer models of stunt scooters, such that they are more suitable for a first analysis. In addition, any force measurement system suitable for stunt use should work for other types of scooter (as they face the most extreme type of loading). The author also has a greater interest in stunt scooters.

The kick scooter market is rapidly growing. With a compound annual growth rate (CAGR) of 9.4 %, the global electric kick scooter market is forecast to reach a size of $ 9.94 B by 2026 [13]. Scooters are a key solution to problems of inner-city congestion. E-scooters can travel up to 83 miles while consuming the amount of energy that it takes for a car to travel one [14]. Short distance (1-3 mile) journeys account for $\sim$70% of UK and $\sim$50% of US vehicle journeys in cities [14]. Scooters could be key in the aims of many countries to reduce carbon emissions, such as the UK governments aim to be carbon neutral by 2050 [15]. In addition to this, scooters can often outpace other transport methods - being faster than walking, avoiding congestion problems faced by cars, and being much easier to take on public transport than bicycles. Scooters are a natural mode of transport for those in cities that commute on public transport for some of their journey, but also have to travel without a motorized vehicle for significant portions on it.

The motivation of this project is to help understand the loading that scooters experience in real-world use. Thus far, there has not been a rigorous investigation into the loading scooters face. Once the loading is understood, optimisation of their geometry will be possible using engineering principles and tools such as finite element (FE) software. This paves the way for lighter, more durable scooters. The large and growing market for scooters of all kinds, and the lack of research currently undertaken, gives this project potential for helping improve their design. This should further help scooters reduce pollution and green house gas emissions, as well as improving user enjoyment and optimising scooter performance. Techniques such as topology optimisation may be key in achieving this. The approach used in this project can be adapted to optimise other sports equipment such as skateboards and skis.

Chapter 2

Literature Review

There is currently no published research on measuring the forces in kick scooters. Because of this, this literature review begins by surveying published literature on strain and force measurement on bicycles in section 2.1. First, it reviews how loads on bicycles have been measured, looking to see which approach could best measure loads on kick scooters. It also reviews the various strain measurement systems used on bicycles, looking at their specifications and potential suitability for use on scooters. Key factors in analysing their suitability include the portability of a data logging system, the system's mass, the number of data channels and the sampling rate. Section 2.2 reviews other force reconstruction methods in the literature that were not used on bicycles. A key difference with these force reconstruction methods is that they try to account for the dynamic effects of loading. Section 2.3 reviews the use of the finite element method (FEM) to analyse stresses in bicycles and how it has been used to try and optimise them. This section aims to understand how finite element analysis (FEA) could be used to improve the design of scooter components. Section 2.4 reviews work done with topology and shape optimisation techniques (not exclusively on bicycles). These techniques have not received extensive attention for optimising bicycle geometries (at least in published literature) but look like promising tools for optimising scooter design.

2.1 Measuring loads on bicycles

A rigorous investigation into the loads applied to kick scooters has not been reported in the literature. An assessment of the loading in the nearest parallel to kick scooters, bicycles, will first be given.

In many ways, bicycles are similar to scooters. Both have two wheels, can be battery-powered, and have similar materials in their design. Bicycles, like scooters, come in many varieties. Bicycles are subject to three different types of load [16, 17]. There are rider induced loads that stem from the static weight of the rider and muscular interactions associated with pedaling. Stunts will be included in this category when discussing scooters. Loads can also result from surface irregularities over which a bicycle may travel, termed surface induced loads. Rider control actions such as steering or braking cause the third type of load. It is primarily rider induced loads that have been measured. Loads have been evaluated on the various points at which humans subject the bicycle to loads: cranks/pedals [16–29], saddle/seatpost [17, 18, 25] and the handlebars/stem [16–18, 25]. The earliest of the above research is from 1968 [27]. Loads have also been evaluated on the hubs to measure the reaction forces of the wheels on the ground [19, 30, 31].

Most of the literature published on the loading and/or strain of bicycles is on road/track bicycles or ergometers (which generally simulate road cycling) [16, 17, 19–25, 27–29]. Mountain bicycles [18,30–32] have also been extensively studied, and limited work has been done on folding bicycles [33] and racing BMX bicycles [34, 35].

As the loads a bicycle is subject to cannot be measured directly, various methods have been used to derive the loading. Most studies have used strain gauges to indirectly measure load [16–19, 21–23, 25, 27–31], however, video analysis [25], an ergometer mounted on a force platform [26] and Hall effect force transducers [20] have been used.

Pedal/crank loads are the most extensively studied. These are the largest loads exerted by the rider on the bicycle and are important in the analysis of cycling technique. The first published study using strain gauges to measure crank/pedal loads is from Hoes et al. in 1968 [36]. Presumably due to technological limitations, only two channels of data were measured. Measurements were performed on an ergometer. Strain was measured at the right crank and pedal, as can be seen in figure 2.1. The strain (and therefore force) was only measured in one direction on the pedal and one direction

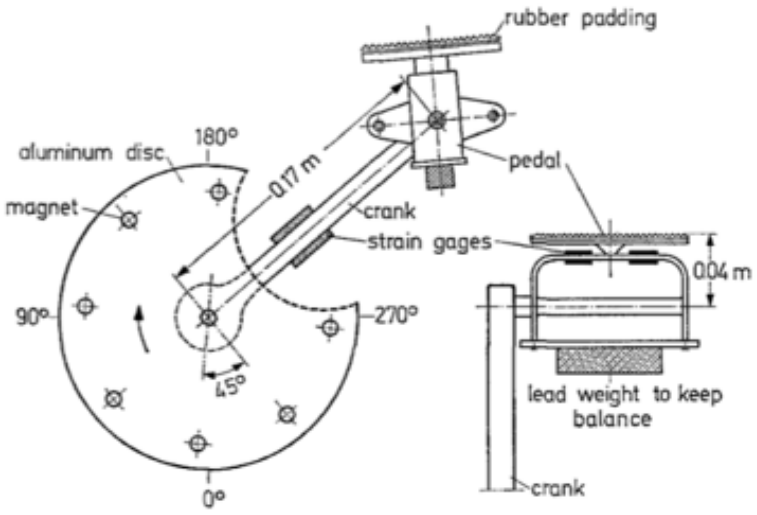


Figure 2.1: The strain gauge setup used by Hoes et al. [27]. The diagram shows the strain gauges applied to the crank for loading. The crank angle is measured using a rotating induction coil along with the magnets on the aluminium disk.

on the crank. To measure the load, calibration was performed by disconnecting the crank from the bicycle and hanging weights of up to 1000 N from the the pedal. During calibration, a cross sensitivity of up to 10 % was found for loading perpendicular to the plane of motion of the crank, and torsion along the axis of the crank had a negligible effect. Forces not measured were assumed to be negligible in magnitude. The crank angle was measured simultaneously with the strain using an aluminium disk mounted with magnets and an induction coil that rotated with the cranks. Force outputs as a function of crank angle and time can be seen in figure 2.2. The variation in force and pedalling rate was also used to calculate the power generation. Only the crank load measurements could be used for this as the angle between the pedal and the crank was not measured. Plots of power generation as a function of time are in figure 2.2. Tests also showed that in the steady cycling situations, even with toe-clips, no rider provided an upward pulling force on the crank when the right crank was travelling upwards. A professional cyclist participant did, however, show some upwards force generated when intending to do so.

In the following years, work was done on real bicycles as opposed to ergometers. In 1979, Soden and Adeyefa [25] analysed the cycling of proficient male cyclists using a mixture of video analysis (referred to as cinefilm analysis in the paper), in-field strain measurements and a dynamometer set-up. Video analysis was used to estimate pedal loads, and results were compared to a pedal force

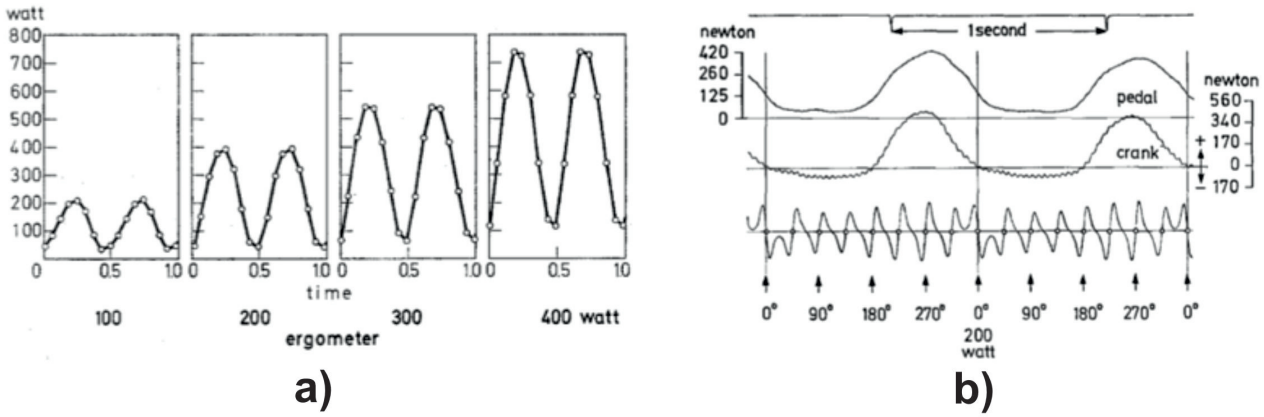


Figure 2.2: a) Force as a function of crank angle and time as recorded by Hoes et al. [27]. b) Power generation as a function of time for different ergometer settings.

transducer (platforms that measure the force applied to them) and dynamometer readings. The video analysis involved taking snapshots of bicycle riders and inferring accelerations and forces from images combined with a simplified model of the bicycle (Figure 2.3). When compared to results from the dynamometer, the estimated forces from the video analysis gave a maximum of 526 N as opposed to $430 - 500$ N. The video analysis was also used to estimate the forces in the arms of the cyclist when tilting the bicycle as opposed to keeping the bicycle level and found that tilting the frame when hill climbing reduced the forces applied by the arms by an estimated 36 N. Loads measured during hill starts (with a gradient of 0.1) reached peak values of approximately 3 times bodyweight, with highs of $\sim$ 2100 N. Starts on level ground reached maximum loads of $\sim$ 1500 N. For in-field measurements such as these "The wires from the transducer were secured to the rider's leg about 300 mm above the ankle, and at the recorder end, the trailing wires were held about knee-high by a helper. The travel of the bicycle was limited by the 12 m length of the cable, but the motion appeared to be otherwise unrestricted." The quote shows the technological limitations of early studies such as this. Using camera equipment for load analysis appears to be less suitable for scooters than for bicycles. Decelerations are very fast upon the landing of a stunt, and much of the compression is probably not practically analysable with the resolution of a camera. Note that due to the dynamic nature of scooter riding (especially if the rider is spinning/rotating), necessary alignment of the rider's orientation to the camera needed for techniques like digital image correlation is likely not practicable.

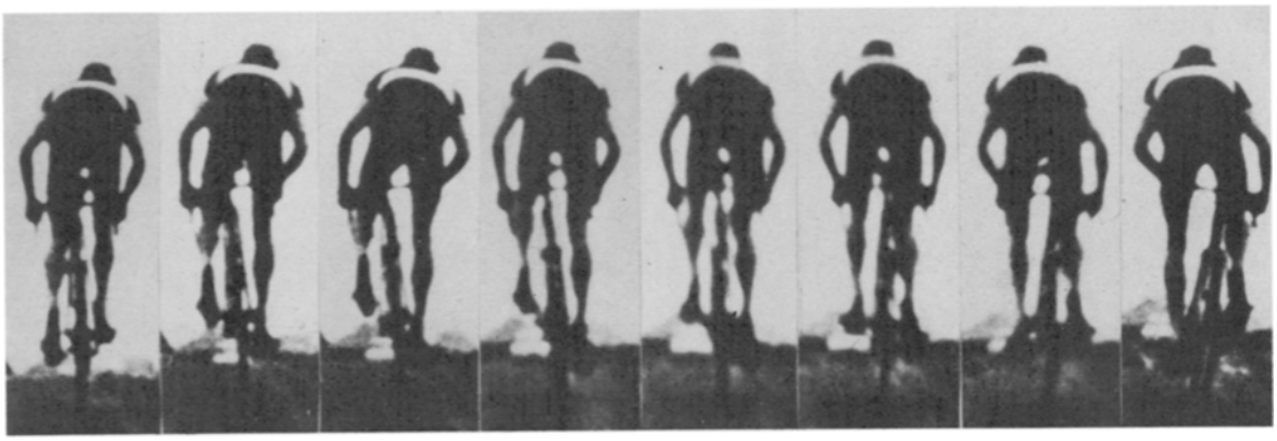


Figure 2.3: Snapshots of a cyclist used for the video analysis during a hill climb (from [25]).

$$\begin{Bmatrix} v_{Fx} \\ v_{Fy} \\ v_{Fz} \\ v_{Mx} \\ v_{My} \\ v_{Mz} \end{Bmatrix} = \begin{bmatrix} 7.17 & 0.01 & -0.10 & 3.09 & 0.90 & 10.95 \\ -1.82 & 7.81 & 0.01 & 3.82 & -41.61 & 6.93 \\ 0.15 & 0.20 & 11.89 & -5.51 & -0.19 & 4.11 \\ -0.52 & -21.81 & -0.16 & 465.02 & -7.31 & -5.40 \\ 22.33 & 0.19 & -0.19 & -0.20 & 481.97 & 0.61 \\ 0.00 & 0.51 & 0.67 & 3.04 & -3.27 & 243.55 \end{bmatrix} \begin{Bmatrix} Fx \\ Fy \\ Fz \\ Mx \\ My \\ Mz \end{Bmatrix}$$

Figure 2.4: A matrix relating the measured voltages and the various force/moment components on the pedal (from [21]).

Hull and Davis [21, 22, 37] made a pedal load measuring device that made use of octagonal strain rings (rings mounted with strain gauges). The device could measure all six of the force and moment components on a pedal. The device also served as a dynamometer as it could measure the cycling power output. Calibration was performed by measuring the strain for test scenarios with known input loads, making it possible to relate the applied force to the measured voltage (from the strain gauges) as in figure 2.4. The crank angle and the relative angle of the crank and pedal were calculated using linear continuous rotation potentiometers, allowing power to be measured. Key features of the system include allowing for the dynamometer to be installed on a variety of bicycles without modifying them, a full scale accuracy of $+/- \, 0.5 \, \%$, 12-bit analogue to digital signal conversion, and a sampling rate of 500 Hz. The data logging system was not portable and therefore the measurements were done by cycling on unconstrained rollers to simulate in-field loading. Instantaneous pedalling efficiency was measured by analysing the contribution of forces in the relevant directions. Results implied that using cleated bicycling shoes slows fatigue in the quadriceps. Measurements also showed that out-of-plane loads were significant, as can be seen in figure 2.5 a).

The first published load analysis taking a wholistic approach to load measurements induced by the

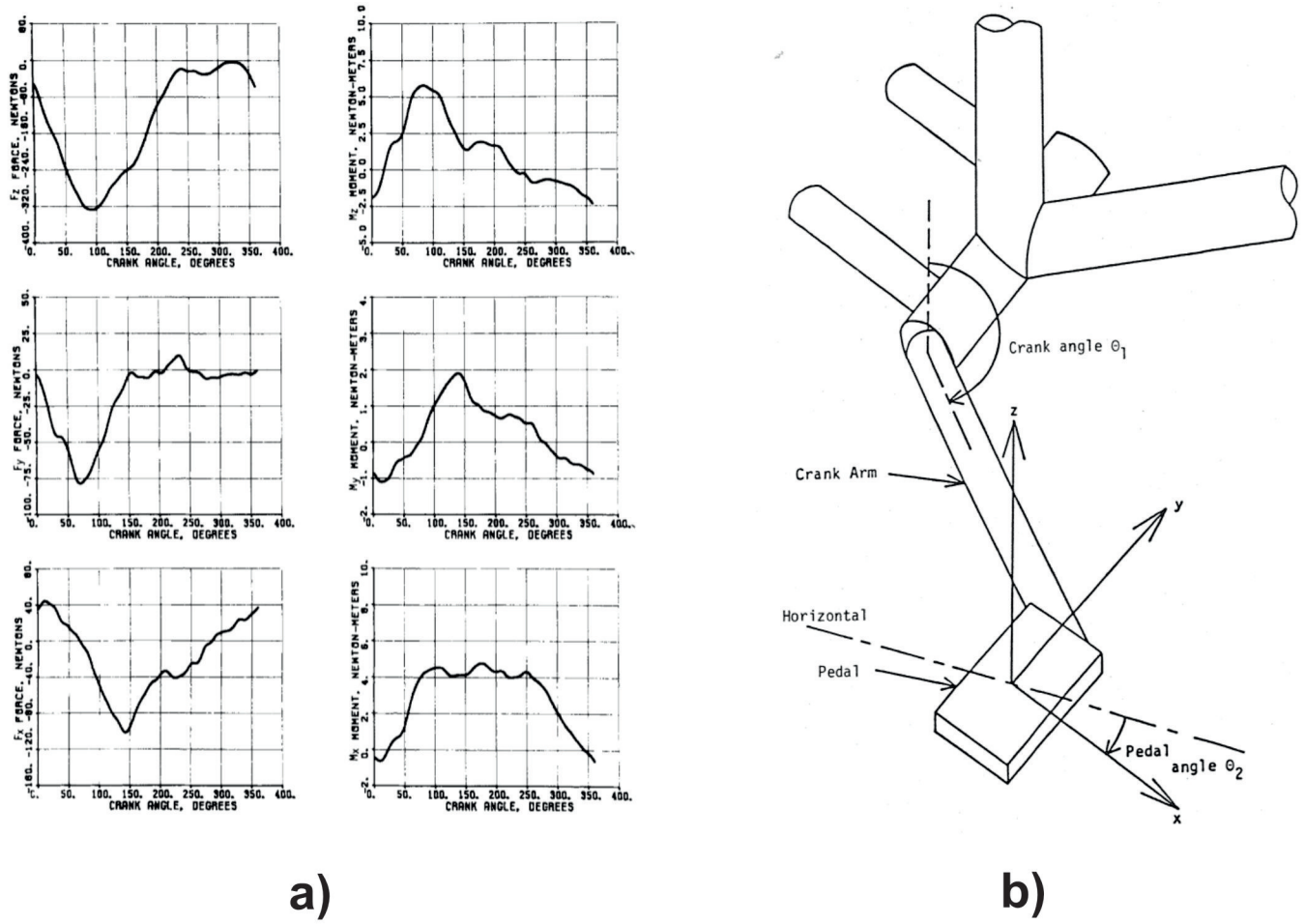


Figure 2.5: a) Results showing the different force and moment contributions in [21]. Note that out of plane load components are significant. b) The local coordinate system of the pedal for measurements done by Hull et al. Similar local coordinates systems exist for the seatpost and handlebar force measurements in [38].

rider was produced by Bolourchi and Hull in 1985 [38]. All of the load components in the pedal were measured (as in [21]), as were horizontal and vertical bar forces, loading along the axis of the seatpost and moments about the seatpost. A loading component perpendicular to the axis of the seatpost was calculated. The measurement of the relative magnitudes of the forces allowed for new exploration into the biomechanics of cycling. Unsurprisingly, handlebar and seat loads reacted to pedal loads. All measured handlebar and seatpost load/moment components exhibited two cycles in one crank cycle, except saddle moment x (SMx), which had a single cycle per crank cycle. As loading was only measured on one side of the bicycle, force symmetry was assumed in pedalling. Obtaining the ratios and timing of the different forces acting on the scooter will likely be crucial in optimising their design, as they affect the location of peak stresses in the scooter.

A comprehensive analysis of standing cycling soon followed by C Stone and M Hull (1993) [16]. Cycling was done with a road bicycle on a treadmill as opposed to rollers or an ergometer to allow for more natural movement. Ergometers do not allow the frame to tilt freely in the same way a bicycle does, and difficulties in balancing on rollers were thought to possibly affect loading inputs. The treadmill made it simple to set the incline and cycling speed. Six pedal and five handlebar load/moment components were measured. Non-driving loads were significant in pedalling, and there were significant pure moments in the handlebars. There were several differences between seated and standing cycling. The peak magnitude of pedal loads were significantly greater for standing cycling, about 20% above the body weight of the rider. On the other hand, seated cycling usually has peak loads below the rider's weight, and the maximum loading occurs at a later stage in the crank cycle ($\sim 140^\circ$ as opposed to $90^\circ - 110^\circ$). Handlebar loads did significant work when standing (pulling up and back during the upstroke and pushing down and forward during the downstroke) as opposed to serving as a hand rest. Instantaneous power output reached highs of 1000 W and an average of 221 W in the right leg alone.

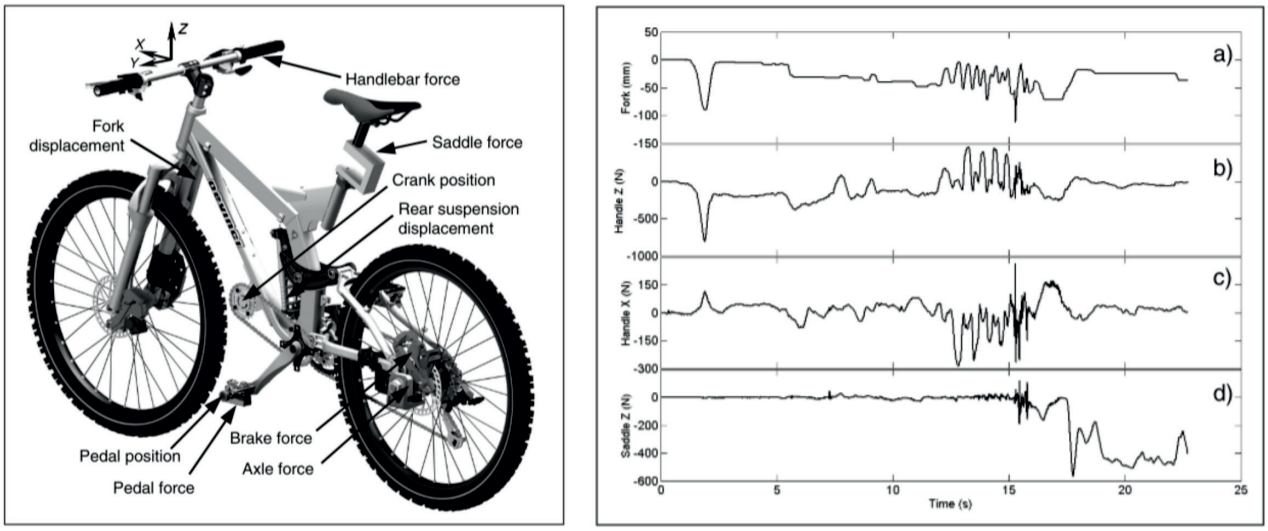
Stone and Hull [17] also investigated the relationship between rider weight and induced loads for set cycling speeds. With 3 cycling scenarios, and data from 5 riders they found that there was a linear relationship between the normal pedal force component and rider weight.

Gianetti et al. [29] produced a data acquisition system for measuring the stresses in bicycle frames

near the bottom bracket. This system was portable, storing data on a laptop. The total mass of the system is not given, although the analogue to digital conversions were on a 900 g board. The laptop used probably had a significant weight given the date of the paper (1998). Stacked half-bridge strain gauges (strain gauges mounted on top of each other so as to measure strain at the same location) were also preferred. Half-bridges (see [39] for details on different Wheatstone bridge configurations) were used where possible to stop thermal drift effects in the system. Where the radius of curvature is low (e.g. On the chain stays), non-stacked quarter-bridges were used. This is because thermal growth increases significantly for surfaces with a radius of curvature less than 13 mm [40]. Thermal growth is the change in resistance of the strain gauge caused by temperature changes to both the strain gauge and specimen (e.g. any strains caused by mismatches in thermal expansion coefficients between the gauge and the material it is bonded to). Half-bridges can also not be used when there is no symmetrical strain profile in a given region of a scooter or bicycle. A DC voltage supply was favoured over AC because the slightly lower power dissipation from the AC supply did not compensate for the increased implementation complexity. This portable eight-channel system reached sampling rates of approximately 160 Hz per channel.

Measurements of the forces at the axles of a mountain bicycle were performed by Lorenzo and Hull in 1999 [30, 31]. The system was sensitive to radial and tangential forces whilst the rider is coasting or braking. Modified, strain gauge mounted, axles were used with commercial hubs to keep riding as similar to real-world use as possible. Ground contact forces were measured for a subject that coasted on downhill terrain. Maximum load magnitudes of ~ 1300 N were experienced in the axles. Due to the small axle size of scooters, axle loads will not be measured in stunt scooters.

Champoux et al. [18] constructed a comprehensive in-situ measurement system suitable for off-road cycling. The system (figure 2.6 a)) measured suspension displacement, wheel speed, pedal and crank position, both pedal and handlebar forces and saddle forces (vertical and horizontal load components in each case). Full-Wheatstone bridge configurations were used to measure forces on the saddle and handlebars. Forces on the pedals and axles were measured using force transducers. Axle and break forces were also measured using commercially available force transducers. Measurements were sampled at 2500 Hz. The data acquisition system was stored in a backpack, which had a



a) b)

Figure 2.6: a) A model of the bicycle that Champoux used to record data with labels signalling the different parameters measured at the various locations on the bicycle. b) Data for various forces on the handlebars and saddle of the bicycle, sychronised in time with the fork travel. [18]

total weight of $\sim$ 35 lbs. Data was collected of a professional mountain bicycle rider who achieved speeds of up to 75 kmh^{-1} whilst riding in rough, downhill terrain. Sample data can be seen in figure 2.6 b). The measurement system presented was extremely comprehensive, although very heavy for a portable measurement system. Such a weight would impact performance drastically and could cause injury when landing stunts. Force transducers (plates that measure forces of objects on them) are not especially suitable for use on scooters as they are more invasive than strain gauges, and the loading location can vary on the scooter deck.

In 2006 Mornieux et al. [26] published a method of measuring pedal forces using an ergometer mounted on a force platform. The advantage of this method is that the bicycle pedals do not need to be modified. This is, however unlikely to be useful for scooter measurements, as this project aims to measure forces in real-world use.

Stapelfeldt et al. (2007) [20] produced a force measurement device that made use of the Hall effect. The system recorded two pedal force components at a rate of 500 Hz. When a load was applied in a measurable direction, a sensor would move with respect to a magnet. Because of the Hall effect, there would be a measurable change in voltage, which could be used to calculate the measured force.

As this device was mounted between the pedals and the cranks, the advantage of this compared to instrumented pedals was that the pedals themselves could be changed. The mass of the system was 230 g and the dimensions were 10.3 cm $\times$ 7 cm $\times$ 2.2 cm. Strain gauges are preferable on scooters due to their smaller size and mass.

Bibbo et al. (2008) [41] devised a wireless system that could measure the forces perpendicular to the load plane and tangential to motion direction. The sampling rate was not given, but the specification for the bluetooth module had a maximum sampling rate of 4000 Hz for 1 channel (presumably thus 500 Hz for eight channels) [42].

"Because on-track situations such as full-power starts from a dead stop, drafting during a team event and riding on a banked track are difficult or impossible to replicate in a laboratory", Drouet et al. [28] measured in-field data for track cycling with dedicated force pedals. The pedal could use two different pedal platforms. Results from a world class sprinter during a 125 m all-out-effort showed that the force component perpendicular to the plane of the pedal reached highs > 2200 N and on the upstroke had upwards forces of almost 400 N. Forces along the direction of the crank had values in the range of -500 N and $+600$ N. Effective work calculations were done by resolving the force perpendicular and along the crank directions and it was found that even in the upstroke the effective force could be above 500 N. Unfortunately, detail on the force asymmetry for each leg was not given.

The first research on the real-world loading of folding bicycles was performed by Pirnat and Boltezar in 2011 [33]. Crank angle was measured and loads were measured at the pedals, seat, handlebars and wheels. Real-world data on public roads was recorded. To aid the interpretation of data, a GPS tracker and camera attached to the frame were used to help with the physical interpretation of various cycling situations. The authors suggested that the rear end of the bicycle, handlebars, and stem were critical regions for stress in folding bicycles because their geometry was significantly different.

Koellner et al. [34, 35] Published work on a strain and acceleration measurement system and subsequent data of a racing BMX bicycle. The data acquisition system measured 24 channels of strain and 4 channels of acceleration, and weighed 1.7 kg. This is the most advanced strain measurement

system published in the literature, and was the lightest, at least in cases where the weight of the system was given. Data was sampled at 10 kHz and down sampled to 100, 200, 500, 1000 and 2000 Hz. Comparisons of the frequency spectra and acceleration spectra (using accelerometer data) were used to determine the optimal sampling rate of 1 kHz. Strain was measured for a variety of common cycling situations and a race simulation. The maximum strain measured on the frame occurred during a 'crashing into a kerb' scenario. The maximum strain was 2750 μ leading to an estimated maximum stress of 190 MPa within the 6061 T6 aluminium frame (with a yield stress of ~ 275 MPa [1, 2]).

Of the methods used above, strain gauges (directly applied to a scooter) are deemed the most appropriate. Video analysis likely lacks the resolution to be useful for high-rate deceleration-induced loads. In addition, it would be extremely challenging to implement in cases where the rider is rotating or where the scooter is rotating relative to the rider. Bicycle ergometers are not useful for scooters, and no scooter equivalent could be found. Besides, ergometers are not suitable for stunt use (they are stationary). Force platforms (acting as a surface for the scooter to land on) are not ideal for real-world use, as they measure force over a small area. They also do not give any resolution of the force location on the scooter deck and do not measure forces on the scooter handlebars. Methods that do not directly measure strain on the scooter (such as octagonal strain rings, regular force transducers, etc.) are inferior to applying strain gauges directly to a scooter. The alternative methods add weight and change the rider experience. The same reasons make Hall effect force transducers unsuitable. Dynamometers are unsuitable because they are irrelevant for measuring forces when landing stunts.

One method not used on bicycles was further considered. TekScan pressure sensors [43] work by having a series of points spread out across a 2D surface that measure the locally applied load. The surface changes conductivity as the applied pressure changes, such that the pressure at each point (and thus the overall load distribution) can be measured. Whilst this approach appeared to have some advantages in being able to give an accurate map of the loading distribution, it was not deemed a suitable substitute for strain gauges. The associated data logging equipment was significantly larger than that used for the strain measurement system and could well be liable to be

damaged in use if not modified for protection. It was also much more expensive.

Of the various data logging systems used to measure strain on bicycles, not one of them was deemed suitable for use on kick scooters. As the aim of this project is to measure the real-world forces applied to stunt scooters, measuring systems confined to a laboratory are undesirable. Systems that can measure strains in the outside world yet which would require the rider to carry the system are not suitable, as the cable connecting the scooter rider would be hazardous under normal circumstances, and especially during stunts where the scooter rotates relative to the rider. Of the systems in the literature mounted to the bicycle, all of them were too large and too heavy. In addition to this, none of the systems had shock absorbing capabilities which may be necessary for stunt use. As stunt scooters tend to have polyurethane wheels as opposed to inflated tires, they have less impact absorption and are liable to face higher shock loads than bicycles in a similar scenario.

2.2 Other force reconstruction approaches

Force reconstruction was performed on bicycles in the previous section. We did not manage to find force reconstruction methods that took into account dynamic effects of loading. Whilst this may be appropriate for bicycles in some scenarios, further research should investigate this. Dynamic effects must play at least some role in some forms of bicycling. For example, mountain bicycles have suspension that exhibits time-dependent behaviour. Dynamic effects are likely significant for scooters. Scooters do not have inflatable tyres, and the forces associated with landing stunts are expected to involve rapid deceleration as the scooter comes into contact with the ground. Because of this, inertial terms may be significant.

There is another difference when calculating the loads applied to a scooter. On a bicycle, the locations of the applied loads are fixed. The rider's hands are on the grip, their backside (sometimes) on the seat, and their feet are on the pedals. Because of this, the loads have a relatively well-known position of application to the bicycle. The seat and hand loads have a fixed location, and the location of the pedal loads can be known by using a potentiometer to measure the cycle through the rotation of the pedal. In addition, the pedal loads are transmitted to a fixed region of the frame through

the bottom bracket. The loads transmitted through a scooter rider's feet can change location, as the feet can be placed anywhere on the footplate. A simple way to update one's approach to this problem is simply to divide the area of the footplate into several regions. If one assumes that the applied loading in these regions is constant, the superimposed load will approximate the applied loading. This approach will be further explained in chapter 5.

Usually, engineering systems will have forcing variables that have a causal effect on response variables. An inverse problem is where one measures the response variable and, from this, tries to understand what the forcing variable is. In the context of the previous section, the forces applied to the bicycles were the forcing variables, and the response variables were (usually) the measured strains. There is a body of work on reconstructing forces that account for dynamic effects.

Early work on solving inverse problems and applying them to the context of heat flux and structural dynamics can be seen in work by D. M Trujillo [44]. The work sets up the general matrix differential equation formulation for the evolution of a response variable in time, given initial conditions and a time-varying vector of forcing variables. The model is discretised in time, and a least squares formulation is presented to solve the inverse problem. This problem includes a term that controls the smoothness of the solution (to stop the solution from overfitting noise). A recursion formula is derived using principles from dynamic programming (applying Bellman's Principle of Optimality). This method is tested on numerically generated data for a heat flux problem (determining the heat flux from a source removed in space from a temperature measurement) and a structural dynamics system with a force applied to a structure with a moving base. The reconstructed forcing functions match the applied forcing functions well. In the case of this paper and those that follow, the goodness of fit to measured data is generally shown simply by comparing plots of the reconstructed outputs with the input and not by including any more rigorous tests. This often makes it difficult to quantify precisely the efficacy of a force reconstruction approach without looking at plots of the data.

Further work by Busby and Trujillo [45] extends the approach above. The order of the problem can be reduced by performing a modal analysis and truncating the modes used in the response. After finding the eigenmodes of the system, it is possible to make a matrix from the modal response vectors and

import them into the governing equations using a substitution. It is then possible to reduce the order of the governing equations by removing the use of specific modes for the analysis, thus reducing the computational cost of the problem. Testing this inverse method on numerically generated data yielded a good match upon the inverse reconstruction in many cases. This research still only used numerically generated data. A follow-up paper used the same approach in an experimental setting [46], in this case, measuring impact loads on a cantilever. Data was collected in 250 or 40 μs time intervals. Four channels of data were recorded. In most cases, one channel was used for the force measurement of an impact hammer (to check how well the reconstruction worked), and three channels were used for accelerometer data. Force reconstruction results were most accurate when using an accelerometer close to the location of the applied force.

Martin and Doyle [47] took a different approach to force reconstruction, instead utilising a frequency domain deconvolution method. The method involves analysing the wave propagation response of an impulse and performing a spectral (frequency domain) analysis to establish a relation between the Fourier transform of the wave propagation response and the impacting force. An inverse Fourier transform was then performed to obtain the force as a function of time. To avoid problems with singularities (when the frequency domain values of the impulse response were very small), a small amount of noise was added in the frequency domain. Reconstructions were performed on simple beam structures, as well as a more complex structure. For the more complex structure, by modelling the joints in different ways, there was a significant difference in the accuracy of the reconstructed force, highlighting the benefit of supplementing theoretical models with experimental data. The paper also highlights the importance of good experimental data more generally, noting how bad data greatly exacerbates ill-conditioning. It also mentions the importance of supplementing models with experimental data to determine an appropriate model for force reconstruction.

Work by Ma et al. [48] used an approach combining a Kalman filter with an input estimation technique on single-degree-of-freedom (SDOF) and multiple-degree-of-freedom (MDOF) spring-mass-damper systems. A Kalman filter is an algorithm that combines a predictive model of a system with experimental data to make a joint prediction of the behaviour of the model (in the next timestep). In this work, the applied impulses are estimated from the measured dynamic response of the system. A

prediction is made on how the system will behave based on the model of the system. This prediction is updated based on measurements, giving a final estimate of the state of the system (in this case, the force applied at a given timestep). One benefit of this approach is that only data from the most recent timestep needs to be kept in the memory of the system, making the approach scale well. Reconstruction results were accurate but only performed on numerical data. Noise was, however, added to the data to test its robustness. Adams and Doyle [49] give an approach similar to that using the Kalman filter. The cost of this force reconstruction approach scales approximately as that of a finite element analysis. The authors state that one disadvantage of the approach used is that because an FEM model is embedded in the force reconstruction approach (i.e. as the solver goes along, it needs results from each step of the FE simulation to perform its reconstruction), it cannot be used in conjunction with commercial FE software.

Sanchez and Benaroya [50] give an overview of force reconstruction techniques and even claim that their list of references is "essentially complete" (although interestingly, they do not cite several of the references above). They divide the approaches for force reconstruction into three broad categories: direct methods, regularised methods and probabilistic/statistical methods. Direct methods make use of a physical or mathematical model to formulate the problem and do not use regularisation methods. The approaches reviewed include an analysis of calculating the force applied on a split Hopkinson pressure bar [51], a modal superposition model used to analyse a moving force applied to a Bernoulli-Euler beam [52] and a modal analysis that reconstructs the forces acting on turbine blades [53]. Regularisation methods either constrain or restrict the problem, or add additional terms to overcome the ill-posedness that often arises in force reconstruction. Various frequency domain truncation methods (e.g. [54]) and Tikhonov regularisation are some of the approaches discussed [55]. Liu and Sheppard [55] used an approach with weighted forcing basis functions, weighted response functions, and Tikhonov regularisation to reconstruct forces. To choose an appropriate regularisation parameter for the Tikhonov regularisation, the L-curve criteria was used (see section 7.2 for a description of Tikhonov regularisation and the L-curve criteria). The results without regularisation show a peak load per unit length of 13 000 Nm^{-1} when reconstructing a load triangular load with a peak force per unit length of 1 Nm^{-1}. With regularisation applied, the

reconstructed peak force was accurate to within 20 %. Several probabilistic/statistical methods are also presented. One method [56] seeks to identify a distributed random excitation force from a modal model of the structure. It includes a spatial orthonormal decomposition of the excitation field. Regularisation is required for this method as it is ill-posed. Another method uses recurrence plots and combinatorial optimisation to reconstruct the forces applied to a 1-D system [57]. This approach had significant limitations, such as insuitability for large-scale recurrence plots, and no standard way to select appropriate values for parameters in the approach. Zhang et al. [58] used a Bayesian approach to force reconstruction to reconstruct a force applied at a single location. A few different approaches based on using a Kalman filter are given that identify applied forces or pressure loads on structures [59–61]. [60] highlights the positive effect that overdetermination by using more data measurement points can have on the accuracy of reconstructed forces. Since the review paper, many new force reconstruction approaches have been implemented. Some of these include:

- an approach using a joint input-state estimation algorithm [62]
- a two-step approach that locates an applied force and reconstructs its time history [63]
- a paper that gives two time-domain approaches, both derived from Newmark's time integration algorithm [64]. One method uses a direct formulation of the time integration algorithm. The other, which is much more successful, uses regularisation and solves the associated inverse problem.
- a method that uses a genetic algorithm to obtain a regularisation parameter, then a recursive Gaussian filter to reduce the noise of the input, before using FEM to reduce the force discretisation error and reconstruct the force [65]
- an iterative regularisation approach only suitable for noisy signals [66]
- a non-negative Bayesian learning method for impact force reconstruction that does not allow the force to be negative [67]

Whilst there are many different force reconstruction approaches listed above, most of them do not seem practical for implementation in kick scooters. As the models usually rely on detailed models of

the structure analysed, they will be much more expensive to implement on a scooter than on simple structures like beams, due to the more complex geometry of scooters. Also, because of potential sources of error in modelling the scooter (e.g. different behaviour at bearings), it is probably safer to rely on experimental calibration rather than modelling. As seen in section 6.2, a different force reconstruction approach is used to those above. After the model has been explained, a more detailed discussion for the justification of using this model model is given in section 6.2.1.

2.3 Load analysis on bicycles

The key tool for modern stress analysis on objects such as scooters and bicycles is finite element analysis (FEA). See chapter 3 for a brief overview of FEA. Again, as literature has not been published on scooters, an overview of results on bicycles will be given. It is worth noting that much FEA analysis on bicycles goes unpublished due to the commercial sensitivity of findings. For example, whilst the setup Champoux designed in [18] only showed preliminary results, Champoux was involved with the design of the Devinci Wilson 2008 MTB frame that used real-world loading in its design [68].
Once accurate loads of bicycles in real-world use have been obtained, finite element analysis can be performed on model bicycles to analyse and compare characteristics. Peak stresses, frame mass and lateral frame compliance are often looking to be minimised. In 1986, Peterson and Londry used FEA as a tool when designing the Trek 2000 frame [69]. Stiffness (the minimisation of strain energy) of the frame and mass were the key characteristics looking to be optimised, all whilst maintaining a structure that would not fail prematurely. As a new frame design (with little prior trial and error) combining high tensile strength aluminium and adhesives was being used, FEA was deemed especially useful. FEA analysis was carried out on two existing frames, a Trek 770 steel frame and a Vitus 979 (manufactured by Bador) welded aluminium frame. Only the frame was modelled, with boundary conditions applied at the headtube and rear axle. About 100 1D elements were used per model. Using eight load cases derived from experiment, testing standards and through analytical deduction, they tried to minimise the strain energy of the whole frame for the various load cases. The authors did note that minimising strain energy with respect to loads in all directions is not the

best principle for frame design, and that for the sake of rider comfort, minimising stiffness in the vertical direction was appropriate. Results showed that the vast majority of strain energy throughout the frame was due to torsion or out of plane bending. Geometries of new potential frame designs were not compared. A plot of the figure of merit for strain energy and mass characteristics of the various frames can be seen for the stand up load case in [69]. Compliance is not always a negative characteristic in stunt scooter riding because it helps minimise peak loads exerted on the rider. The main criteria to be optimised are the lifetime of the component, and the mass.

A comparison of different bicycle frame geometries was performed by Covil et al. [70]. Two load cases were used, and optimisation is formed to maximise vertical compliance and lateral stiffness of the frame. 317 1D beam elements were used for the FEA. Tube thicknesses were assumed to be constant, and only steel tubing was considered in the analysis. The only frame geometry type examined was the 'diamond' shape often used for steel frames. 82 frames were used for the analysis and optimisation was performed according to a Box-Benkhen algorithm. When optimisation was performed according to one criterion only, a 13 $\%$ increase in vertical displacement and a 15 $\%$ increase in lateral stiffness were achieved. In addition to the limitations above, the study did not evaluate handling performance or rideability of the optimised tube designs, only steel was considered as a material, tube butting was not considered (due to the constant tube thickness) and tube joining methods were not compared. A comparison of the effect of scooter dimensions on peak stresses and other characteristics would be insightful. However, this sort of optimisation is likely of limited use for stunt scooters as the dimensions of the scooters are usually based on the riders preference. For example, the increase in the wheelbase from a longer deck helps with performing balancing tricks, but increases the moment of inertia, requiring more effort to perform a given stunt. This preference will primarily be influenced by the riders size and style of riding. Instead, optimisation should be performed on components with predetermined dimensions.

Covil et al. also published findings on the stress distribution within a 810 000 element 3D FE model of a bicycle for various loading conditions derived from the literature [71]. The maximum stresses were found for a load case representing a bump on the rear wheel (2500 N in the vertical direction and 1000 N in the horizontal direction). A maximum von Mises stress of 268 MPa was reached in

the top-tube. Comparable stresses were found in riding out of the saddle and a front wheel bump scenario (227 and 228 MPa respectively), whilst seating cycling provided a maximum stress of only 84 MPa. Given that the model was of a steel bicycle (stresses should be compared to the UTS, yield and fatigue stresses), these are quite low stresses. Given modern computational capabilities, and the geometrical complexity in regions of the scooter that commonly fail (e.g. the neck/headtube) 3D elements should be used to create the optimal FE model of a scooter.

Early work on composite frames was conducted by Lessard et al. (1995) [72]. Monocoque (complete frame designs with no lugs) carbon frames were designed and simulated in 2D FE environments. Lateral stiffness and vertical compliance were compared with simulations and experimental results of an aluminium and steel bicycle frame. Results from experiment used cohered to within 7 % of the FE results. Even the lightest carbon frame design had better stiffness properties than the other frame designs. As the frames were not made and tested, it is difficult to say how such frames would have performed in practice as there are other bicycle properties (e.g. torsional strength) that are of great importance.

FEA has been used to guide Investigations into the impact resistance of carbon fibre reinforce polymer (CFRP) bicycle frames. CFRP has numerous desirable properties for cycling (high stiffness, high strength in pure bending, low density and high formability); however, it has poor impact resistance. The impact energy arising from chain slaps (when the chain moves and hits the frame after sudden changes in vertical movement of the bicycle) on the chainstays was measured using an accelerometer and video camera combined with a multi body simulation to access their impact on the design of carbon frames [73]. Results suggested that chain slaps do not provide significant structural damage on CFRP frames. Similar research using only a high speed camera was used to analyse the impact of stones hitting bicycle frames, extrapolated values of stone energies up to 1.5 J were present in the bicycle frame [74].

In another study [75], Impacts of 1.5 and 6 J were applied to CFRP down tube samples using a hemispherical impactor with a diameter of 16 mm and a mass of 2.05 kgs. The impactor was dropped from 74.5 and 298 mm. The scenario represented pebbles launched by the front wheel into the downtube in a road cycling situation. After impacts, the samples were subjected to bending-

torsion and torsion-only tests until fracture. Experimental results showed that the impacts did not appear to affect the rigidity or the failure load of the materials in either test. Numerical results indicated slight decreases in strength (5.4 - 5.5 %) and rigidity (1.5 - 2.1 %) for the bending-torsion strength. In the torsion-only test, the rigidity was only affected slightly (1.0 - 3.0 %), but the failure torque decreased by 7.8 and 13.4 % for the 1.5 J and 6 J impacts, respectively. Further simulations of a whole bicycle frame subject to the loads from the AFNOR 14781 4.8.4 certification test [76] indicated rigidity losses of 4.1 % and 5.5 % for 1.5 J and 6 J impacts, respectively, indicating the benefit of testing a whole bicycle frame as opposed to a down tube with simplified loading. After this, a parametric analysis of fibre orientation (with the same number of plies and materials to optimise for the stiffness of the frame). The optimised downtube saw rigidity increases of 5.6 % without impact, and 1.5% and 2.1% for the 1.5 J and 6 J impacts respectively.

FEA has also been used to investigate the stacking sequence of composite layup in bicycle frames. Liu and Wu (2010) analysed 33 different 8 ply carbon fibre (with orientation changes every two plies) layups using 2D shell elements under three load cases [77]. Safety factor was the design parameter. The best layup tested was [0/90/90/0] for this purpose. This layup would not, however have the optimal lateral stiffness. Weak points for the geometry used were at the fillets (where tubes joined other parts of the frame) and failure occurred in the inner or outer layer of the composite layup. Other geometries were not considered.

Modal analysis has been done on bicycle frames, both experimentally using experimental modal analysis (EMA) and FEA. Results on an MTB by Sani [78] agreed to within 10% for all modes. FEA has been used to measure Vertical compliance (often related to comfort) in bicycle frames, with results indicating that the seat tube generally has the largest influence on this [79]. Comfort has also been evaluated in other ways on bicycles [19, 80, 81], but it is not a priority for stunt scooter riding at the moment. Of the analyses above, it is possible that parametric anlyses will be useful. As stunt scooter components are not currently made of composites, parametric analyses may, however, be of more limited use than in bicycles. One application of FE modelling is to optimise geometries subject to loads with topology and shape optimisation. This is a promising method of analysis and will be examined in its own right in the section below.

2.4 Topology and shape optimisation

Topology optimisation (TO) and shape optimisation (SO) have found applications in many areas, including aerospace [82–84], civil [85–87], automotive [88] and sports [89–91] engineering. On the larger scale, TO has been used to explore the design space for bridge optimisation. A 2.1 billion element model was used to optimise for the stiffness of a bridge girder under five static load cases [85]. An interpreted design derived from the optimised structure, resulted in weight savings of 28% when compared to the conventional design. The interpreted design had similar manufacturability to the original. Further research would be needed before implementing such a design, to cope with fatigue, buckling and dynamics. For a review of developments of topology optimisation in civil engineering, see [86, 87]. A similar large-scale approach has been used in aerospace to optimise the wing of a Boeing 777 aircraft using a model with 1.1 billion elements [82]. Interpreting the design by implementing curved spars and a new rib layout would lead to an estimated weight saving of 2-5%. [83] gives an overview of TO processes in aerospace, including the optimisation of aircraft pylons (that carry the turbine engine) and stiffeners. For an automotive application, see [88] for the optimisation of a Ferrari F458 chassis.

McEwen et al. described the design process of making a bicycle crank by additive manufacturing, using topology optimisation to improve this process [90]. Loading was taken from the literature and scaled to comply with standard bicycle testing conditions. The crank was optimised for stiffness, modelled with 505 000 tetrahedral elements in the final crank mesh to allow for a large amount of geometrical freedom. It was post-processed and designed for manufacturability. The crank was then 3D printed from Ti-6Al-4V before being heat treated. The crank performed well for the static load case, however failed prematurely during fatigue, because the yield stress was used as a constraint in the optimisation stage, rather than fatigue stress. This paper is insightful in providing the complete process from the choice of design variables through to the manufacture and testing stages of development.

Closely following this work, Ismail et al. did similar work, again on cranks [91]. Various optimisation processes were performed, including stiffness (mass constrained) optimisation and mass minimisation (stress constrained). 7005 aluminium and carbon fibre were both optimised for, with different

resultant designs due to the anisotropy of the carbon fibre. Surface optimisation to reduce peak stresses followed. Parametrically varying hole fillet radii in ANSYS Response Surface optimisation Software was used to achieve this. A polylactic acid (PLA) crank arm model was made to validate the model and was followed by static and dynamic tests.

Maestrelli and Falsini [89] used load cases from the literature in combination with shape optimisation to improve the design of a carbon fibre bicycle frame. Shape optimisation uses iterative algorithms to change the size and shape of the FE mesh to optimise the frame by minimizing a set of objective functions. A perturbation vector approach was used inside Hyperworks on an existing frame design. The lateral displacement of the bottom bracket was optimised and subject to constraints including a minimum increase in vertical compliance of 10% for a load irregularity subcase. The resultant frame design was Union Cycliste Internationale (UCI) compatible with an increase of lateral stiffness of 39%, and an increase of vertical compliance of 11%. The chainstay design was asymmetrical due to the difference in distance of the right and left crank from the bottom bracket (due to the front gear cogs). A survey for the manufacturability of the new designs was not performed.

2.5 Conclusion

From the survery above, we can draw the following conclusions:

- Currently, there is no published literature that seeks to determine the forces applied to kick scooters.
- Various methods have been used to determine the forces on bicycles (which are similar to kick scooters), including: video analysis, ergometer mounted on a force platform, octagonal strain rings (and other paraphernalia that utilise strain gauges in a non-direct way), Hall effect force transducers, force transducers/platforms (presumably using strain gauges), dynamometers, and direct use of strain gauges.
- Direct use of strain gauges are the most suitable way to determine the loads applied to stunt scooters.

- Limitations of using equipment such as ergometers is that they may miss key loading characterstics that real-world cycling faces. This highlights the benefits of collecting data in situ.
- None of the data logging systems used on bicycles were suitable for use on scooters. The systems were all too large, too heavy, and did not have any indication of a suitable level of shock protection. Because of this, a new data logging system must be developed.
- A good initial data-logger sampling rate to collect data is likely a few kHz, given that Koellner et al [34] found that 1 kHz was optimal for bicycles. Scooters have significantly stiffer wheels and therefore are likely to experience a higher frequency response to loading.
- Given that FEA is useful for analysis on bicycles, it is also likely useful for analysis on scooters.
- The most likely techniques used in combination with FEA for the optimisation of scooter components are: topology optimisation, shape optimisation and possibly parametric analyses.
- Specific results from literature on bicycles are not especially relevant to what results may be on scooters.

Chapter 3

Background Theory

3.1 Introduction

This chapter provides some background theory on relevant topics not covered in the literature review or the following chapters. Section 3.2 gives a basic overview of finite element (FEA) analysis. FEA is a tool widely used in engineering disciplines for stress analysis in structures. Section 3.3 outlines the methods used in Topology optimisation (TO) and shape optimisation (SO) techniques. These are specific techniques used on FE models to optimise the geometries of structures given specific loading and boundary conditions.

3.2 FEA background

Note that the outline/structure of the 'FEA background' section of this chapter is similar to that of my master's thesis [92].

Finite element analysis (FEA) is a technique used to investigate the stresses and strains of many structures, from the micron-scale (in the case of crystal plasticity FEM) [93] to bridges [85] and aeroplanes [82]. In practice, it is used as a computational technique to solve real-world problems. It is key to accurately determining stresses in regions of the scooter where the geometry is complex. The method works by approximately solving partial differential equations (PDE) for geometrical objects and can therefore be applied in other contexts such as heat flow. The PDE used for stress

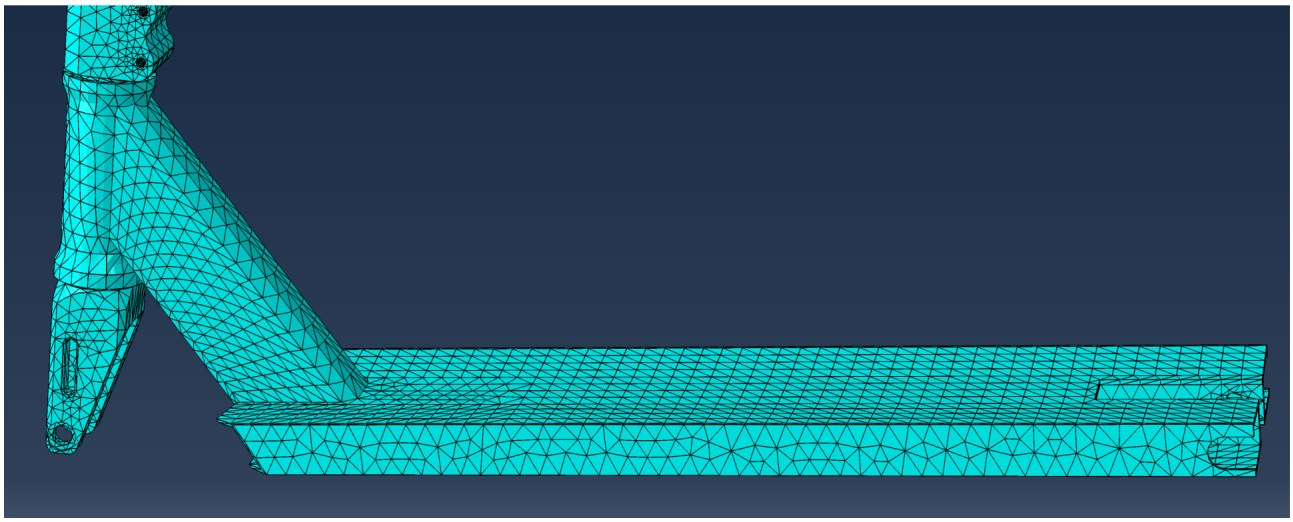


Figure 3.1: An example mesh of a scooter deck. The elements that compose this mesh have an approximate global size of 10 mm.

analysis, that can be derived from the conservation of linear momentum is:

$$\nabla \cdot [\boldsymbol{\sigma}] + \mathbf{f} = \rho \frac{d^2\mathbf{u}}{dt^2} \tag{3.1}$$

$\nabla \cdot [\boldsymbol{\sigma}]$ is the divergence of the stress tensor, $\mathbf{f}$ is the body force per unit volume acting on the body, ρ is the density, and $\frac{d^2\mathbf{u}}{dt^2}$ is the acceleration. For static problems, the right hand side of equation 3.1 is zero.

FEA is a continuum mechanics method and therefore much cheaper computationally than atomistic models such as molecular dynamics. This is why it can model much larger structures for longer times. The PDEs that FEA approximately solves are analytically solvable for very simple geometries and boundary conditions. There are no such solutions for more complex geometries. Instead the object to be modelled is broken down into a finite number of elements. Each element has a simple shape, but the elements together can approximate the shape of complex geometries. The elements have nodes at their edges. An example structure can be seen in figure 3.1. The PDE is solved at the nodes, and the displacement is interpolated between the nodes. Convergence tests should be used (repeating the calculation with progressively smaller elements) until the results converge within a specified limit. When analysing scooters, the body force can be ignored as the weight of the scooter is insignificant in comparison to the magnitude of the loads that the scooter faces. The

modified equation can then be discretised and written in matrix form for each element. Continuity equations constrain the elements to ensure that neighbouring nodes do not tear apart or overlap. In addition, some of the simulations in this thesis ignore inertial effects. Such simulations are much less computationally expensive. This leads to the global matrix equation:

$$\mathbf{F} = [\mathbf{K}]\mathbf{U}$$

Where **F** is the nodal force vector, [**K**] is the stiffness matrix and **U** is the vector of nodal displacements. Note that bold font without square brackets indicates a vector, and bold with square brackets indicates a matrix. Boundary conditions need to be applied to the system (surface tractions, point forces and nodal displacements), fixing values in the matrix equation, making the displacements solvable:

$$\mathbf{F}_{BC} = [\mathbf{K}_{BC}]\mathbf{U}_{BC}$$

(The BC subscript is to highlight that the boundary conditions are applied). Boundary conditions must be realistic to get accurate results. The displacements can be linked to strain via the compatibility equations and strain can, in turn, be used to obtain stress via Hooke's law (for linear isotropic materials, suitable for scooters in this project):

$$[\boldsymbol{\varepsilon}] = [\mathbf{B}]\mathbf{U}$$

$$[\boldsymbol{\sigma}] = \lambda Tr([\boldsymbol{\varepsilon}])[\mathbf{I}] + 2\mu[\boldsymbol{\varepsilon}]$$

[**B**] where is the shape function derivative matrix, and λ and μ are elastic Lamé constants.

3.3 Optimisation

A significant component of the future work will include optimising the design of scooter components once the loading they experience in use is known. Traditionally, intuition, combined with trial and error and FE simulations is used in design processes to improve the performance of components. There are now, however, optimisation techniques that can aid in the design process. Structural

optimisation methods all work to distribute material in a way that optimises a structure according to some specific critera (e.g. minimum total strain energy, lowest maximum stress in the structure etc.). Types of structural optimisation that will likely be used include shape and topology optimisation. A brief overview of the techniques is given below.

3.3.1 Topology optimisation

To understand the framework of topology optimisation (TO), some terms will need to be explained, namely the objective function, design variables, state variables and constraint functions. Optimisation will be explained within a FE framework, as that is how the method is implemented. Optimisation will be performed within some domain (volume) Ω. The objective function, F, represents the function for which the system is trying to optimise. Usually, the problem is set up such that minimising F will give the optimal result. For example, in the common case of optimising for the stiffness of a structure, the compliance is minimised (F is often the sum of the strain energies in all of the elements). The design variables $\boldsymbol{\rho}$ are what can be varied within the system, for example, the density of each element could be a design variable, and its value could determine whether the element is empty (0), or full (1) of material. The state variables **u** represent the structural response of interest in the domain, for example, the stress of each element, or the displacement of each element. There will also be constraints on the system, such as equilibrium constraints, which usually are formatted as equations (C) that cannot be greater than 0. The mathematical formulation of this can be expressed as:

$$\begin{cases} \min_{\boldsymbol{\rho}} & : F(\boldsymbol{u}(\boldsymbol{\rho}), \boldsymbol{\rho}) \\ \text{subject to} & : \sum_{x=1}^{n} C_x(\boldsymbol{u}(\boldsymbol{\rho}), \boldsymbol{\rho}) \leq 0 \end{cases}$$

where there are n constraint equations. Note that the objective function gives a single output, dependent on all of the design variables. If one is trying to maximise the stiffness of a beam, the objective function could be compliance, the state variables could be the deflection (of each element), and the design variables would be the density of each element. This could be subject to

the constraint that the total volume (and therefore mass) of the beam is fixed to some fraction of the design domain. Alternatively, the maximum deflection of the beam could be a constraint, and the objective function could be the volume (or mass) of the system.

It is often the case that there are multiple objectives to be optimised. In such cases, there will be what is known as Pareto optimal solutions; solutions where one cannot further minimise one objective function without increasing others [94]. The set of Pareto solutions form what is called the Pareto front, on which the optimal solution will lie. When optimising for multiple criteria, it is common to minimise the weighted sum of several objective functions:

$$\min_{\boldsymbol{\rho}} \quad : \sum_{i=1}^{p} w_i F_i(\boldsymbol{u}(\boldsymbol{\rho}), \boldsymbol{\rho})$$

where w is the weight and their value sums to 1; although other weighting methods exist [95]. Another method is the ϵ-constraint method, where one simply converts all objective functions except one into a constraint with a desired value, and optimises accordingly. For the ϵ-constraint method, one can perform multiple optimisations with different set constraint values and compare results.

Generally, each element in the design domain should either be full ($\rho = 1$) or empty ($\rho = 0$) by the time the optimisation process is finished. Each possible topology is called an isotropic solid or empty (ISE) topology. If there are n elements in the design domain, there are 2^n ISE topologies. The consequence of this is that simply trying all of the possible topologies is unfeasible for even small designs with thousands of elements. The main way to solve this problem is to use density methods [96] in the case of real-world problems. Other methods such as topological derivative, level-set, phase-field and evolutionary approaches have been developed, but have not seen the success that density methods have had in real-world applications [96, 97].

Density methods relax the optimisation problem by allowing for intermediate densities between 1 and 0. The density of each element can then become a continuous design variable. An intermediate density of an element is not generally something that is physically realistic, although this useful fiction allows for efficient gradient methods to be used in optimisation [98]. If one simply scales the stiffness with the density of each element, the stiffness of an element becomes $\boldsymbol{E} = \rho \boldsymbol{E}^0$. Thus the

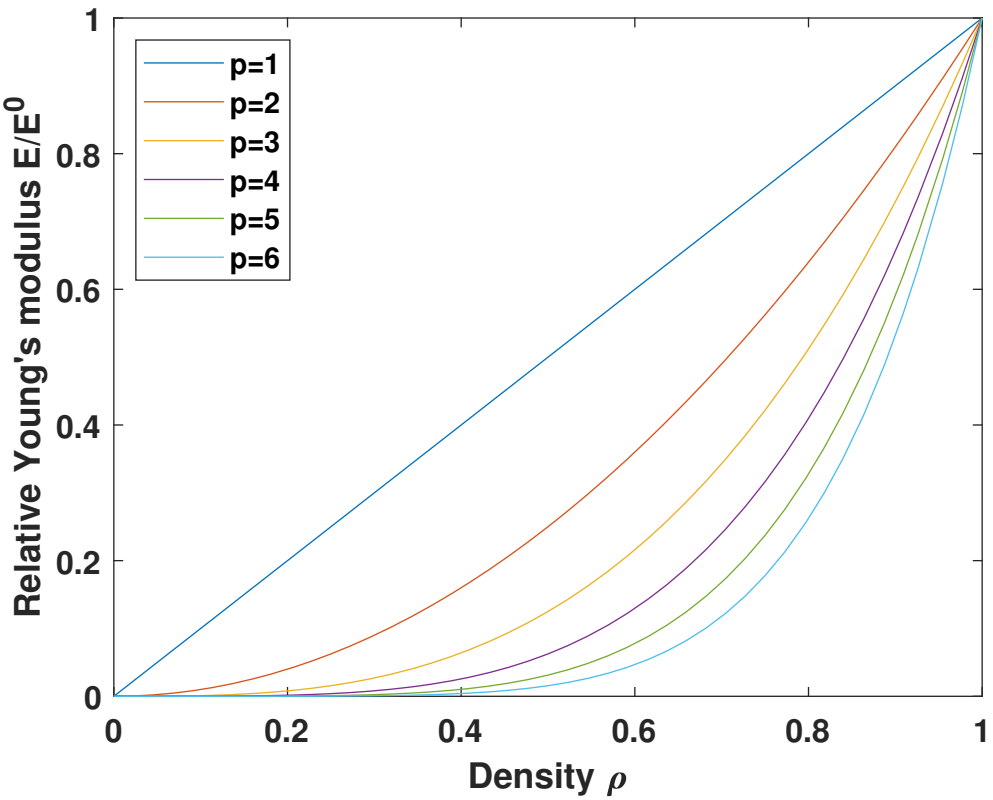


Figure 3.2: A graph showing the relative stiffness of elements with a given density (ρ is a dimensionless quantity noting the relative density of an element) for different penalisation factors. Penalisation ensures that there will be fewer intermediate densities within the optimised model.

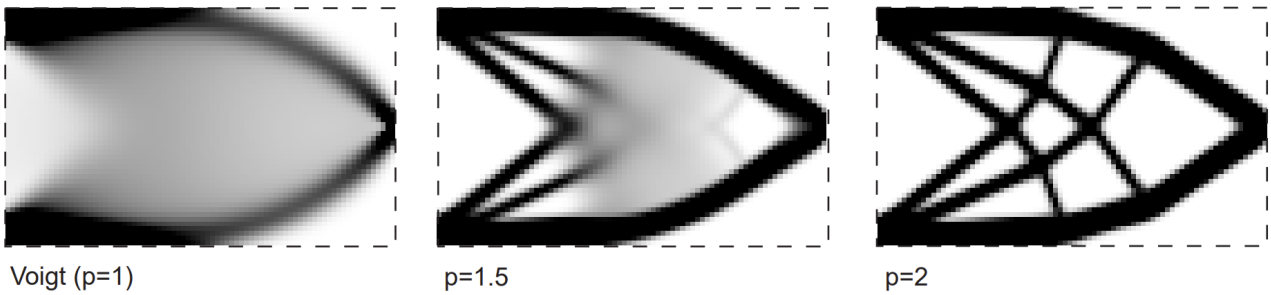


Figure 3.3: Images showing the progressive loss of intermediate densities as the penalisation factor is increased (from [97]). Note that the 'fuzzy' edges are not due to a bad quality image, but due to discrete elements, often of intermediate density.

obvious drawback is that structures will result with intermediate density regions, which cannot be actualised. To get rid of intermediate densities, a penalty is introduced: $\boldsymbol{E} = \rho^p \boldsymbol{E}^0$ where p is a penalisation factor greater than 1. The relative stiffness as a function of density can be seen in figure 3.2 for different penalization factors. Penalisation reduces the number of elements with intermediate densities (see figure 3.3). This density method is known as the solid isotropic microstructures with penalisation (SIMP) method [97]. A problem with this method is that it makes convex optimisation non-convex [99], to try and mitigate this, an iterative process is often used whereby the penalization factor is gradually increased to get a near-optimal solution [96, 99].

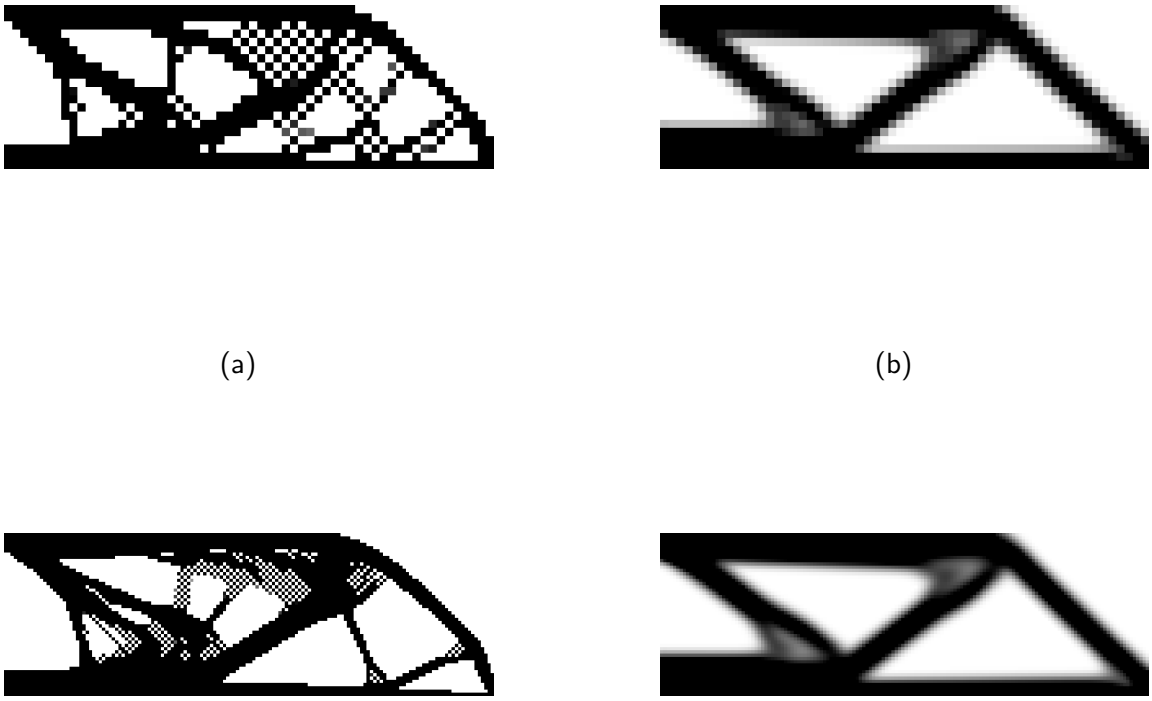
Due to the discretization errors caused by FEA, checkerboard patterns will have an overestimated stiffness [96]. There are several ways to mitigate this problem, for example by using density filters [98], where the density of an element is based on neighbors within a radius, or controlling the gradient of allowed densities [101]. Another method commonly used is sensitivity filters (see figure 3.4 for details). For more methods see [96], [98] and [102]. In the final design, one will usually have a cutoff, saying that densities above a certain value are kept, and those below removed.

3.3.2 Shape optimisation

Shape optimisation (SO) utilises many of the same optimisation principles as topology optimisation (e.g. having objective functions and state variables etc.), however, instead of removing material in a finite element mesh, it optimises the location of the nodes of elements. SO cannot generate new holes in a structure, so a good approximation of the optimised structure should be used as the base design. SO is often applied after TO to remove stress concentrations and fine-tune the surface design [103]. A successful method of shape optimisation is the perturbation vector approach. Here, the original nodes are listed as a vector $\mathbf{r}_0$, and then a linear combination of perturbations ($\mathbf{p}$) is added to the system. The perturbation vectors are the design variables:

$$\mathbf{r} = \mathbf{r}_0 + \sum_{i=1}^{n} w_i \mathbf{p}_i$$

The optimised solution is the one with the correct weightings.



(a) (b)

(c) (d)

Figure 3.4: The calculated optimised solutions for a truss under loading. The load is applied in the bottom right corner of each subfigure and is vertically downwards. Figures a) and c) exhibit checkerboarding, whilst figures b) and d) have a sensitivity filter applied. The sensitivity is the rate of change of the objective function with respect to the design variable (in this case, density) at a point. A sensitivity filter uses a weighted combination of the sensitivity of nearest neighbours in the optimisation algorithm, ensuring that a checkerboard pattern does not emerge. The trusses are generated from the code in [100]. Figures a and b) are 60×20 elements in size, and c) and d) are 150×50 elements. In both cases, the penalisation factor is 3, the final volume fraction constraint is 0.5 (of the total volume), and the sensitivity filters have a radius of 1.5 and 3.75 elements respectively, making them operate over the same absolute distance.

Chapter 4

Building the Data Acquisition System

4.1 Introduction

This chapter outlines the steps taken to make a data acquisition system (DAQ) suitable for obtaining strain data of stunt scooter riding in real-world conditions. In section 2.5, reasons were given as to why strain gauges are suitable to calculate the forces applied to kick scooters. Strain gauges were deemed the most suitable measurement system due to their lack of invasiveness and ease of use. Section 4.2 highlights the main stages of the building of the DAQ, starting with the layout of the various parts of the DAQ and the data logger used (section 4.2.1). Section 4.2.2 describes the main features of the signal conditioning board, and the chapter is finished with other relevant considerations, including the use of suspension for the data logger in section 4.2.3.

4.2 The data acquisition system (DAQ)

4.2.1 Overall structure of the DAQ and the data logger

An overview of how the data acquisition system (DAQ) works to acquire strain data is given in figure 4.1. The power source applies a potential across the Wheatstone bridge as well as powering the data logger and the amplifiers (see [39] for detail on different Wheatstone bridge configurations). Thus, in operation, when using the scooter, the strain gauges will strain, this will create a small

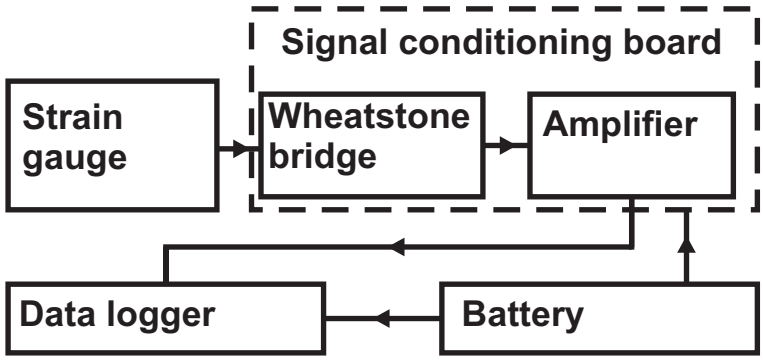


Figure 4.1: An overview of the data acquisition set-up and how the parts relate to each other. The arrows show the connections between each part of the system, and if there is a signal (or power in the case of a battery) being passed on, which direction this is happening in.

change in potential across the Wheatstone bridge, which the amplifier will apply a gain to. This will in turn be recorded by the data logger and the data can then be post-processed to give strain measurements as a function of time. There were no suitable complete DAQs available for the research. Commercially available systems were either too large, did not support enough channels, or did not have a sufficiently high sampling frequency. They were also often too expensive. None of the DAQs in published literature on bicycles had the desired qualities. A suitable DAQ would need to be small and light, to avoid significantly impacting the way the scooter is ridden in use. Given the current systems in use in the literature, it is hard to overstate the importance of having a system small enough to avoid majorly impacting the way the scooter is ridden. The DAQ should also be durable (preferably housed in a shockproof container) to reduce the risk of breaking when stunts are performed. When performing stunts the scooter is sometimes thrown by the rider if the stunt does not go according to plan.

The system must also be mounted on the scooter. Several bicycle DAQs (e.g. [18, 29, 104, 105]) were carried by the rider in backpacks. Because the scooter rotates relative to the rider in many stunts, this would lead to the tangling of wires, likely leading to injury and damage to the data logger. The data logger needed a sufficiently high sampling rate to cope with the rapid strain response of scooters. As Koellner et al. [34] deemed 1 kHz was optimal for recording data on a bicycle, a sampling frequency of at least a few kHz would be ideal to perform tests. In addition to this, the system needed to have quarter bridge setups to measure strain on the scooter. Half or full-bridge configurations need strain gauges to be placed such that they experience a strain of the

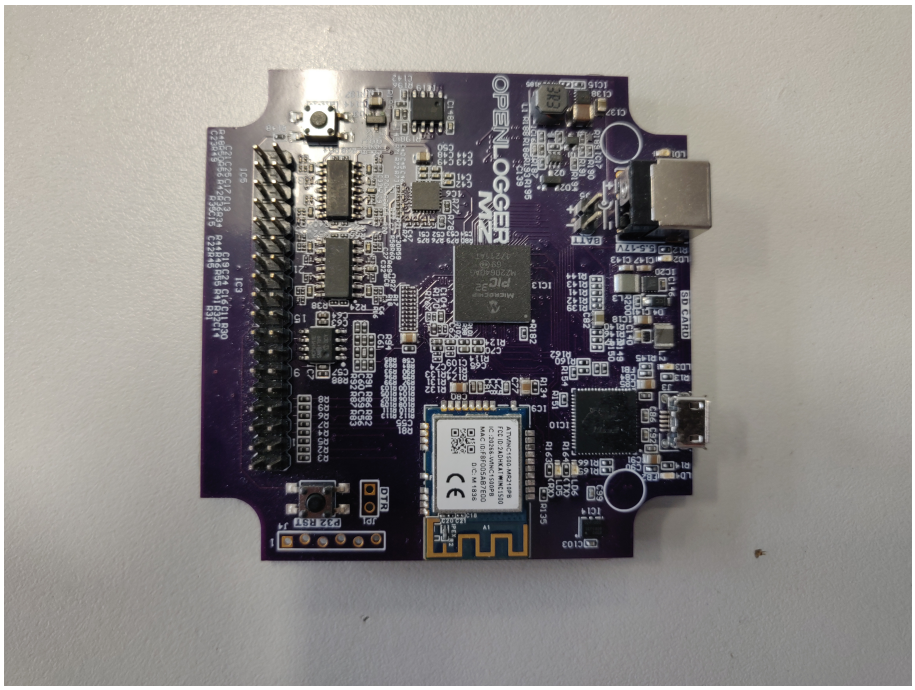


Figure 4.2: The Digilent Openlogger

same magnitude but opposite sign to each other. This would involve implementing strain gauges on the surfaces which the rider's feet is on, as well as require much more wiring for the same number of channels. Such a system would be more prone to breaking, more cumbersome to use (due to having more wires), and would require many more terminals on the signal conditioning board. Due to geometrical features such as concave in the scooter deck, it would be very hard to accurately place strain gauges in locations where they would experience strain of equal magnitude and opposite direction, making half or full-bridge setups much more prone to error. In my master's thesis, I used a Digilent Openlogger [106], which also proved to be suitable for this project. It has eight channels for recording data, can sample all channels up to a frequency of 62.5 kHz simultaneously, has a cross-sectional area of 72 mm $\times$ 72 mm, is significantly cheaper than other data loggers and records data over a 10 V range with 10-bit resolution (analogue to digital conversion, storing data in increments of 1 mV). An image of the datalogger can be seen in figure 4.2.

4.2.2 The signal conditioning board

The role of the signal conditioning board is to send a clean, filtered analogue signal to the data logger. The data logger will then convert the signal to a digital signal and store the data on a micro SD card. The main requirements of the signal conditioning board are that it should:

- connect the strain gauges to the data logger
- process the signal from the strain gauge into a usable form (using a quarter bridge setup). The ideal gain of the amplifier should be around 200. This balances avoiding saturation of the signal, yet keeping the signal to noise ratio reasonable. The gain on the board could be adjusted by changing the gain resistors connected to the instrumentation amplifiers.
- have a suitable output voltage range. i.e. amplify the signal to a range less than the range of the data logger, whilst also having a large enough range to minimize discretisation errors). Ideally this would be around $0 - 10\ V$ as that is the range of the data logger, however even if the range is $5\ V$, discretisation error is only $0.2\ \%$ of the total range, and thus small compared to other error sources.
- provide a clean, consistent signal that can easily and correctly be interpreted (i.e. reduce noise as much as possible). The way instrumentation amplifiers do this is discussed below.
- be small and light. Preferably the whole data acquisition system should weigh less than 500 g (the exact weight is somewhat arbitrary, but the more the system weighs, the more noticeable it will be whilst riding).

To meet the above criteria it was necessary to design a custom printed circuit board (PCB). The 2D cross-sectional shape of the PCB was designed to be the same as the data logger to minimize space (see figure 4.3), and was made so that it could mount precisely on top of it. This involved it having a 72 mm $\times$ 72 mm square profile, with holes drilled in the corners so that it co0uld be bolted in over the data logger. This made the connection between the data logger and the signal conditioning board more secure. A terminal block was used to provide a connection between

the strain gauge wiring and the data logger. Data tests using SMD resistors soldered on to the PCB and through-hole resistors connected through the terminal block were used to confirm that this connection did not cause any additional noise (see figure 4.4 where the through hole resistor is stable). Power was supplied through a screw terminal, and similar tests were performed. It was necessary for a steady, clean voltage signal to be used, so one could be confident on the strain that the measured voltage change corresponded to. To ensure that this was the case a Texas Instruments TLV76760QWDRBRQ1 linear voltage regulator [107] was used. Tests to confirm this included having a through hole resistor connected to the screw terminals, and logging data when the scooter was being ridden to see if signal changed upon impact landing. The steady voltage output during use can be seen in figure 4.4 (this is also after stiffening the signal conditioning board, which is discussed below). Other tests took readings of voltage across the whole signal conditioning circuit (by temporarily soldering wires on various parts of the PCB). Results showed a clean, consistent signal. The voltage regulator actually only supplied a voltage of 6 V across the Wheatstone bridge. Using this allowed for the use of 7.4 V Li-Po batteries which were lighter than larger battery packs. The discretization error between a 6 V and 10 V range also had a relatively small impact on the total error (see appendix A). The small battery pack allowed for the battery to be taped to the data logger housing so that it received the benefits of suspension (before mounting the batteries on the suspension system, they were breaking due to the impact loading).

Strain signals need to be amplified so they are not drowned out by noise. Instrumentation amplifiers use common mode rejection, making them suitable to provide a high fidelity signal. This means that voltages common to both signals it receives (from each side of the Wheatstone bridge) are rejected, so small signals from the strain gauge can be detected and amplified. Common mode rejection is very important as noise common to both terminals can be much larger than the strain signal. TI INA-828 amplifiers [108] were selected as they give low noise (7 nV$/\sqrt{\text{Hz}}$) signals, and have an operating voltage greater than 10 V, so they can be used to maximise the range of the OpenLogger. To maximise the common mode rejection ratio (CMRR) it was necessary to have a low impedance voltage source at the reference voltage on the amplifiers. To achieve this a voltage follower setup was used (see figure 4.5).

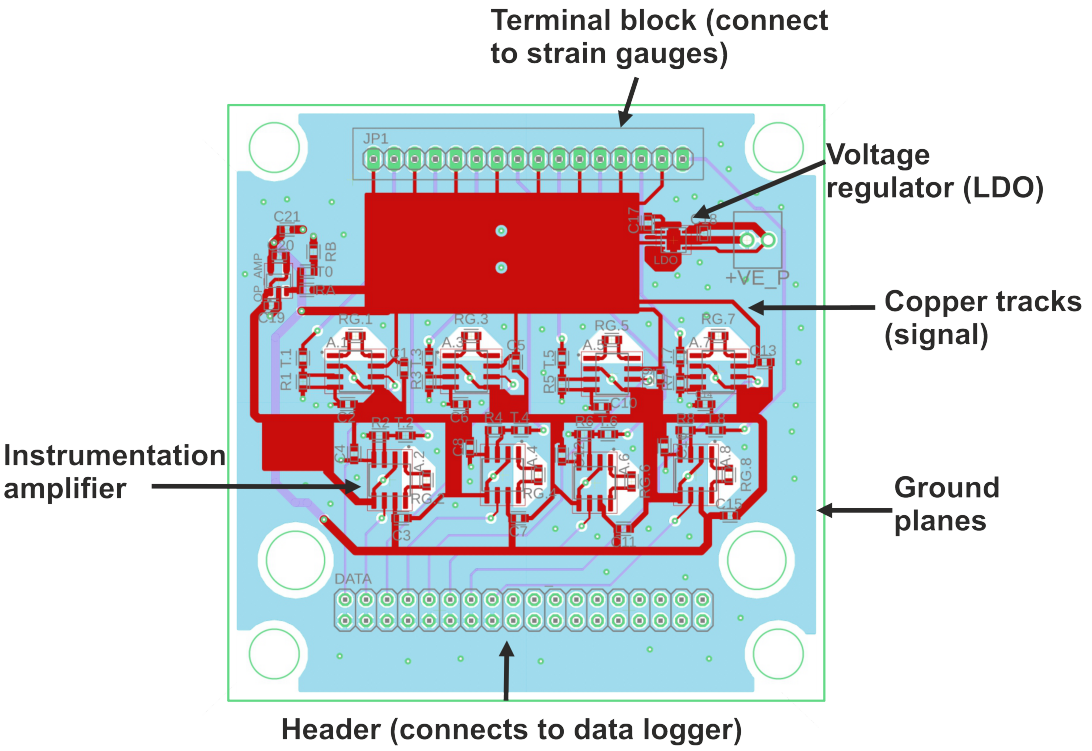


Figure 4.3: A diagram of the 2D layout of the routing and components on the PCB. The green border is the same size as the data logger that the PCB was housed upon. Some of the key features of the board are labelled.

Upon testing, a surprising source of unwanted signal was generated through the flexing of the signal conditioning board due to inertial effects (even though it is mounted with the plane of the PCB perpendicular to the [physical] ground when the scooter is upright). This led to a change in resistance in the tracks, which when amplified was significant. To solve this problem, a piece of plywood was glued to the back of the signal conditioning board with epoxy to stiffen it. Tests were confirmed by having a through hole resistor connected to the signal conditioning board in use (see figure 4.4). Data showed that the resistor did not give significantly different voltage readings during stunts on the scooter (as it did before the plywood was glued on).

Small differences in resistance lead to significant changes in voltage after amplification. A $1\ \Omega$ difference, results in a difference in strain reading of 5×10^{-4}. The concern was that this offset could lead to a saturation of the output signal. Also, the resistance of the strain gauges and their associated resistors were not exactly their nominal value of $1000\ \Omega$. Because of this, tuning resistors were implemented in the circuits. Tuning resistors are resistors of a relatively small resistance (in

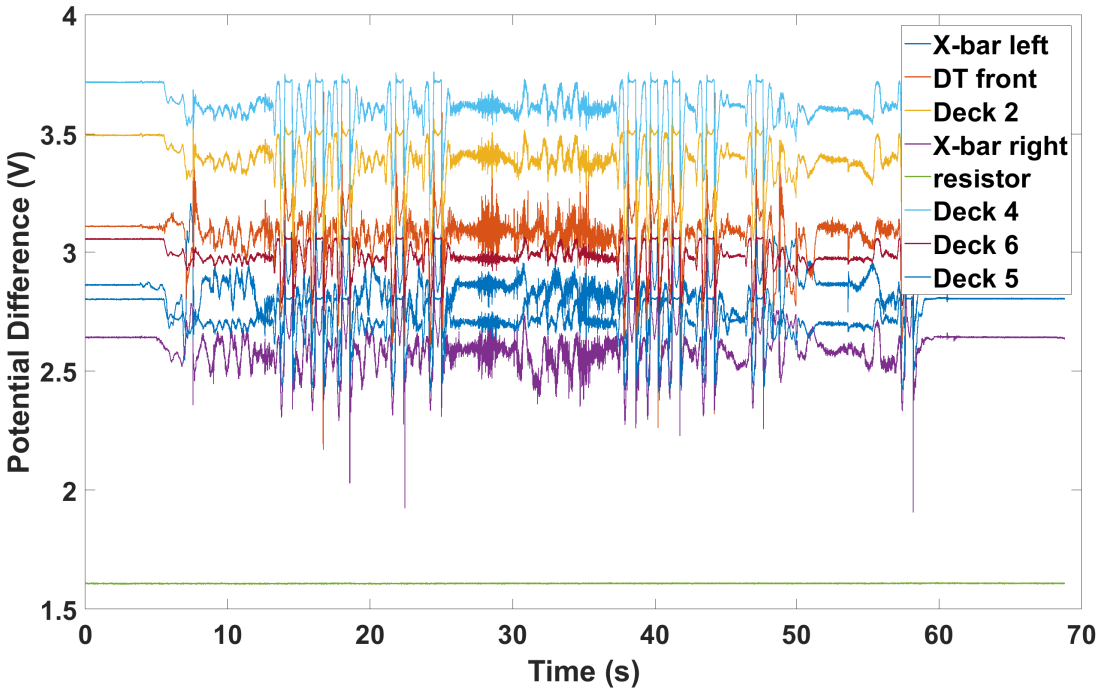


Figure 4.4: The raw voltage readings from the1 data logger. A resistor has been connected to see if the voltage reading given out is stable during stunts. The fact that the line is flat shows that the voltage reading is stable.

this case $0-8\ \Omega$) that are placed in circuits after the $1000\ \Omega$ resistors. This meant that if necessary, the bridges could be balanced with more precision which can be seen in figures 4.3 and 4.5. Variable resistors were not used, as due to the vibrations in use, there was a risk that the resistance value could change.

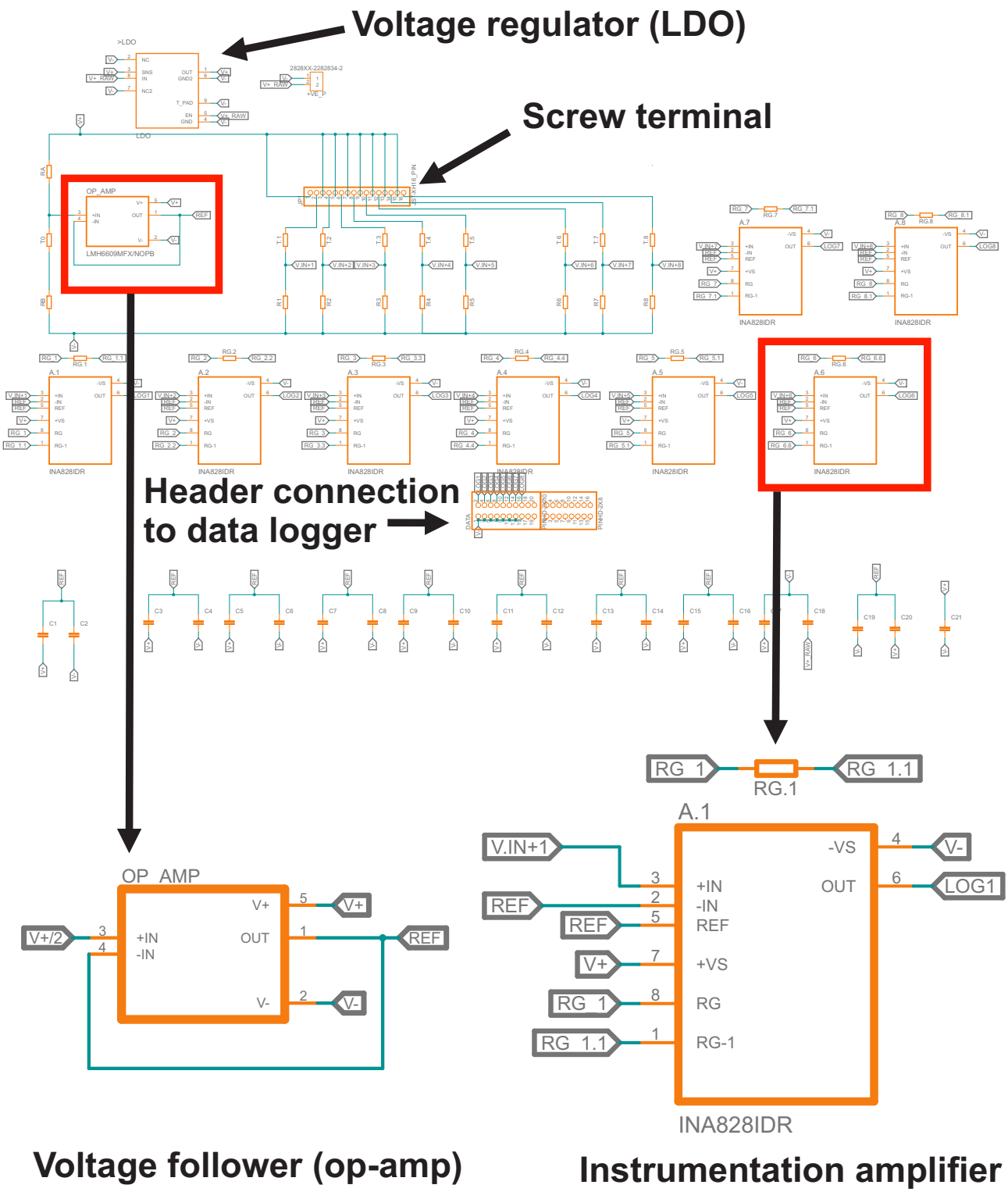


Figure 4.5: A schematic of the PCB, showing how the components are connected. The voltage follower provides a stable unity gain voltage source which is used in the rest of the circuit as a reference voltage. For the instrumentation amplifier, connections one and eight are connected to a resistor that sets the gain of the amplifier. Connections two and three take in the differential signal (one from the reference voltage and one from a strain gauge signal). The difference between these signals is amplified. The output voltage is given relative to the reference voltage (connection five). connections four and seven power the amplifier. Connection six sends the amplified signal to the data logger.

4.2.3 Suspension and other considerations

Due to the extensive vibrations that occur when performing stunts on a scooter, erratic data spikes would occasionally appear in the data. Such peaks almost always appeared when landing a stunt, when the acceleration was highest. An example of such a spike can bee seen in figure 4.6. Because of these erratic spikes, a suspension system was made that suspended the data logger and signal conditioning board between four springs to reduce peak accelerations on them (and can be seen in figure 4.7a). It was mounted to the deck via two bolts, as shown in figure 4.7b. As can be seen, the bolt closer to the front end of the deck penetrates the underside of the footplate entirely. This makes the scooter less likely to get caught on stones or other objects on the ground. The reason for leaving the bolt further back on the deck out was to avoid drilling a larger hole in the deck. Further reducing the second moment of area in this region was deemed to be a risk as decks often break where the neck is welded to the footplate. Lateral damping was further reduced by wedging in a piece of foam and taping it to the neck of the scooter deck as can be seen in figure 4.8.

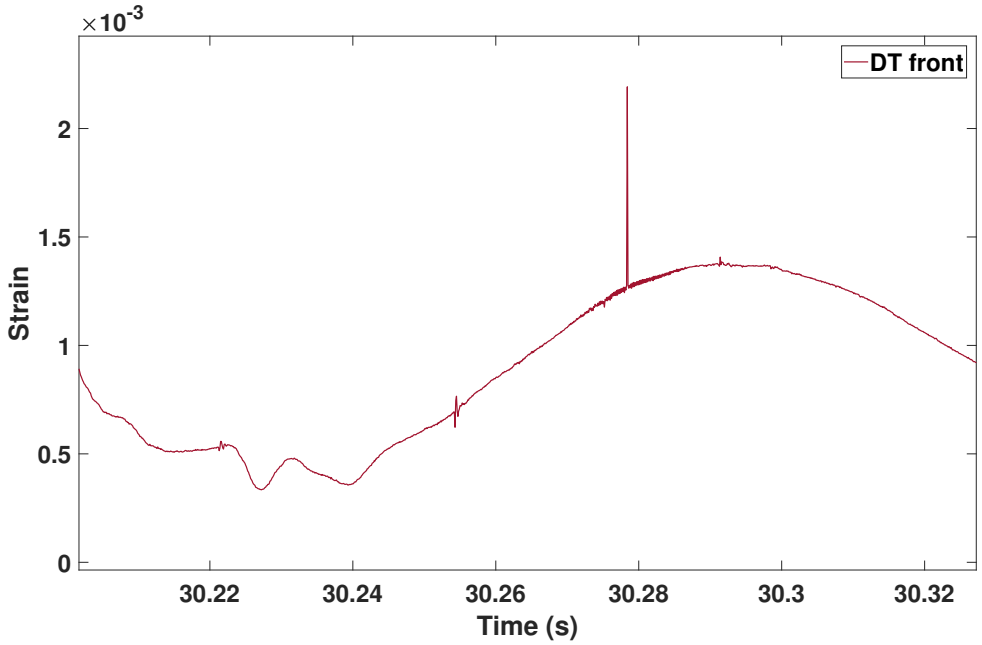
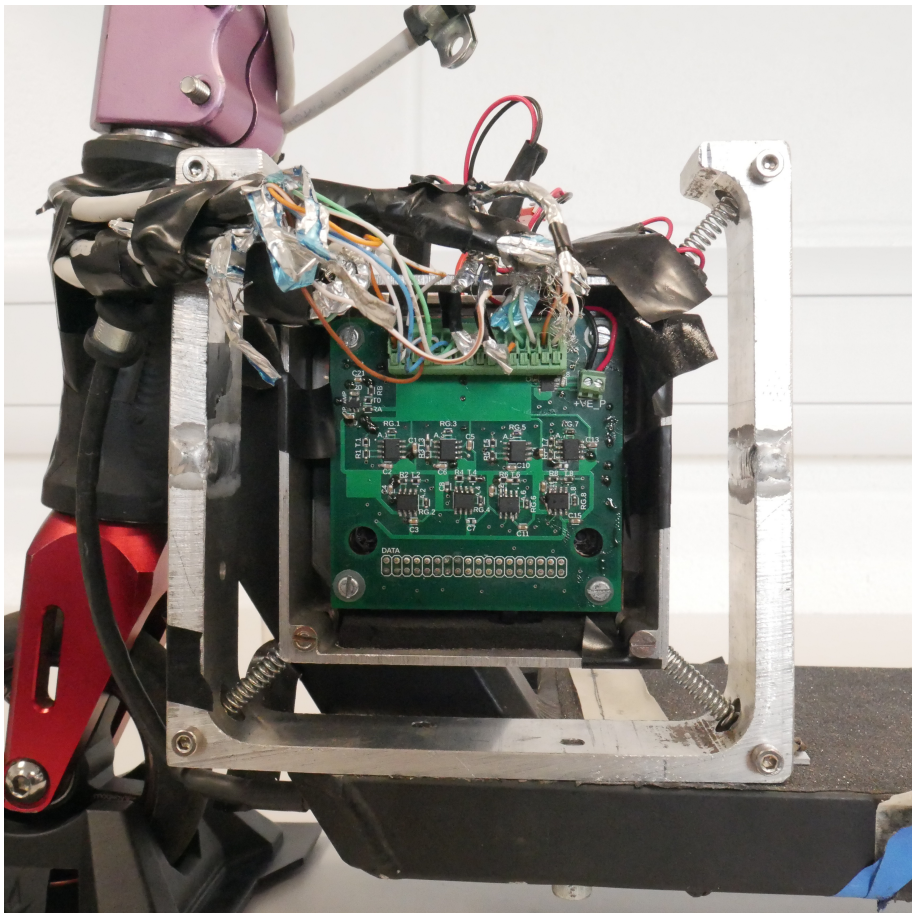
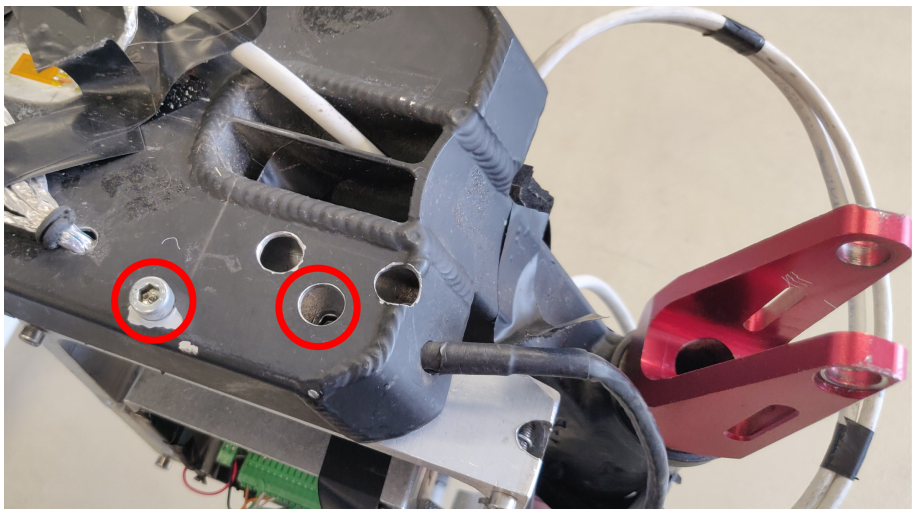


Figure 4.6: Sometimes data would have artefacts such as this erratic spike in the strain reading. Such artefacts generally only last for one sample of data (in this case 10^{-4} s, are at a much higher frequency than the recorded strain data and are therefore easy to remove. Adding suspension to the setup greatly reduced the number of such artefacts.

Without the piece of foam, the data logger would occassionally stop logging just after landing a

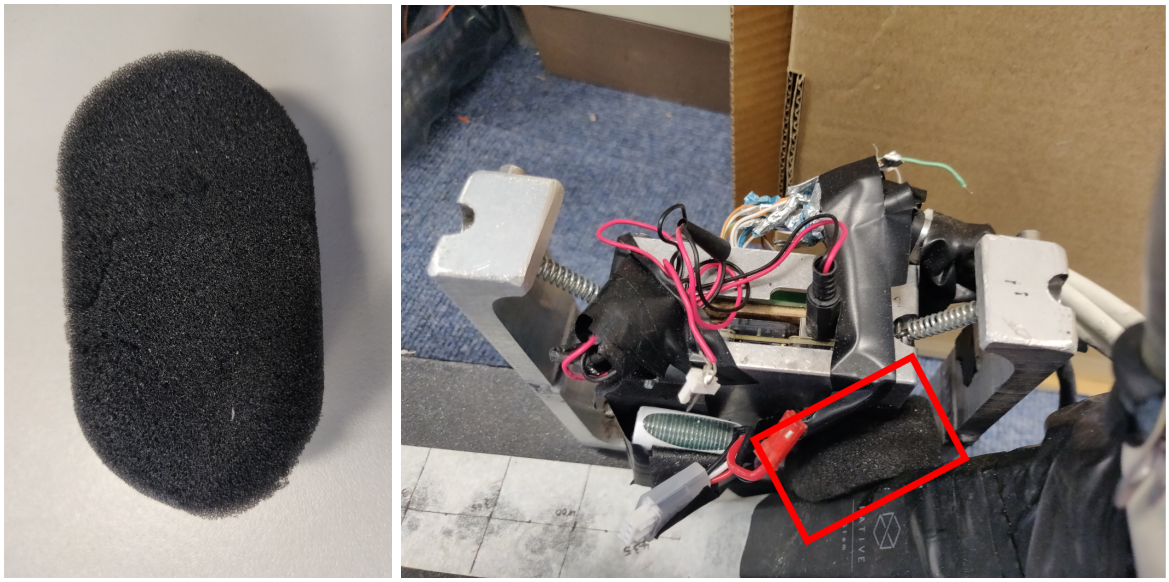


(a) The suspension system for the data logger. A u-bracket of aluminium was necessary rather than boxed section to allow for the powering of the data logger from the top, and for easy insertion and removal of the micro-SD card. The data logger is mounted on springs, decreasing the shock load on the system significantly.



(b) An image showing the underside of the suspension mounting to the deck.

Figure 4.7



(a) (b)

Figure 4.8: a) The piece of foam that was used to dampen lateral movement of the data logger. b) An image showing where the foam was wedged to damp lateral movement of the DAQ. It is also possible to see the battery mounted on the outside of the aluminium housing of the datalogger/signal conditioning board.

stunt. This happened more often if the stunt involved rotation. A possible reason for this is that the data logger hitting the neck of the scooter deck led to stop button (of the data logger) effectively being pressed. The resultant setup collected data which contained significantly fewer erratic data spikes.

The location of the data logger was also important. The front of the deck near the neck of the scooter was the most suitable location. The DAQ could not easily be mounted to the handlebars, especially with a suspension system. Near the neck of the scooter the data logger will have a low moment of inertia about the axis of the handlebars. This minimises the effect the DAQ will have on tailwhips. Tailwhips are a stunt where the deck rotates one revolution about the axis of the down tube (see figure 7.11). Being near the axis of the down tube also means acceleration on the data logger due to rotations of the deck will be smaller. Finally, and perhaps most importantly, this is the location on the deck where the data logger will have the smallest impact on the rider's experience of riding the deck, as it will compromise the foot space of the rider the least.

Omega Engineering $1000\ \Omega$ SGD-10/1000-LY43 strain gauges [109] were chosen to minimize the current drawn from the signal conditioning board. $1000\ \Omega$ strain gauges also have the advantage of

reducing the error from any cable straining or heating (although these are likely negligible).

To reduce the risk of strain gauge wires ripping-off the strain gauges from the scooter, metal P-clip fasteners were attached to the clamp. A picture of the setup with P-clips in use can be seen in figure 4.9. Tape was applied over the strain gauges where the wires joined the scooter to further protect them (see figure 4.10), and a protective polyurethane coating was applied directly to the strain gauges. With the setup described, real-time strain measurement of scooters is possible. The battery used for the data collection was an Urgenex 1000 mAh 7.4 V Li-Po battery [110]. The reason it was used was due to its small size ($52 \times 27 \times 14$ mm) and light weight. The small size and weight of the battery meant it could be taped to the housing of the data logger and signal conditioning board. This meant that the battery received the benefit of suspension which was advantageous, as previous batteries had broken due to vibrations. This battery did not maximise the 10 V range of the data logger, a lighter battery and a voltage regulator with a lower range was used. The cables used were almost all CAT-7 rated; with screened, foiled twisted cable pairs to reduce noise (details on figure 4.11). As stunts where the handlebars rotate relative to the scooter were to be performed on this setup, it was necessary to allow for this by providing some slack in the cabling of the scooter. Figure 4.12 shows that the cable allowed for a maximum of four rotations of the handlebars in one direction. A Picture of the complete scooter can be seen in figure 4.13.

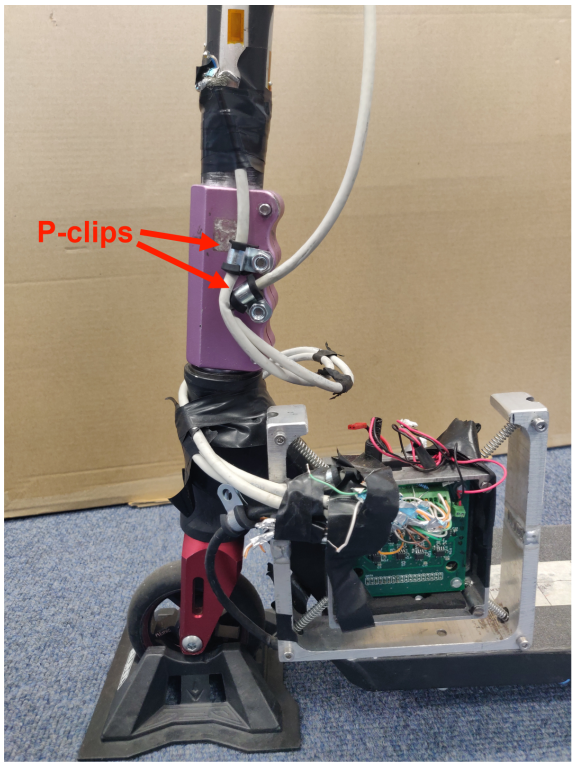


Figure 4.9: P-clips were used to decrease the chance of the strain gauges being ripped-off the scooter. If the cable is pulled on the other side of the P-clip, the force will be exerted on at the P-clip but will not move the cable on the other side of the P-clip substantially. At the top a broken down tube side strain gauge can be seen. This highlights the importance of properly fastening cables so that strain gauges do not break.



Figure 4.10: In the above picture one can see the various ways in which cables have been taped and zip-tied to secure them together and to the scooter. This minimizes the risk of injury to the rider as it is harder for the cables to get entangled. In addition to this, the strain gauges are less likely to get damaged, as the cable is securely held in place.

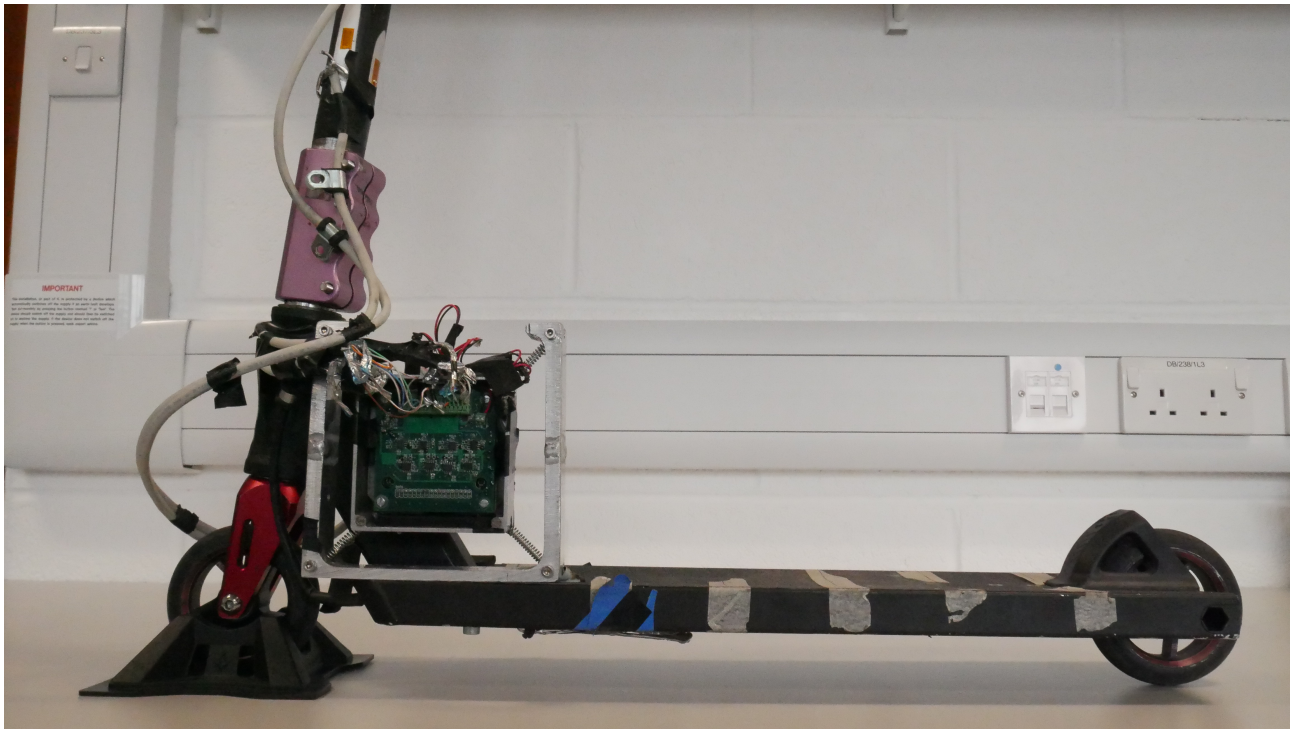


Figure 4.11: An image of the DAQ on the bottom half of the scooter. The grey cables are CAT-7 rated. The black cable, which transmitted the signal from two of the channels on the deck was not CAT-7 rated but were still screened for protection. It is more important for cables to the down tube and crossbar to have protection to external sources of noise, as they are significantly longer than the strain gauge cables to the deck.

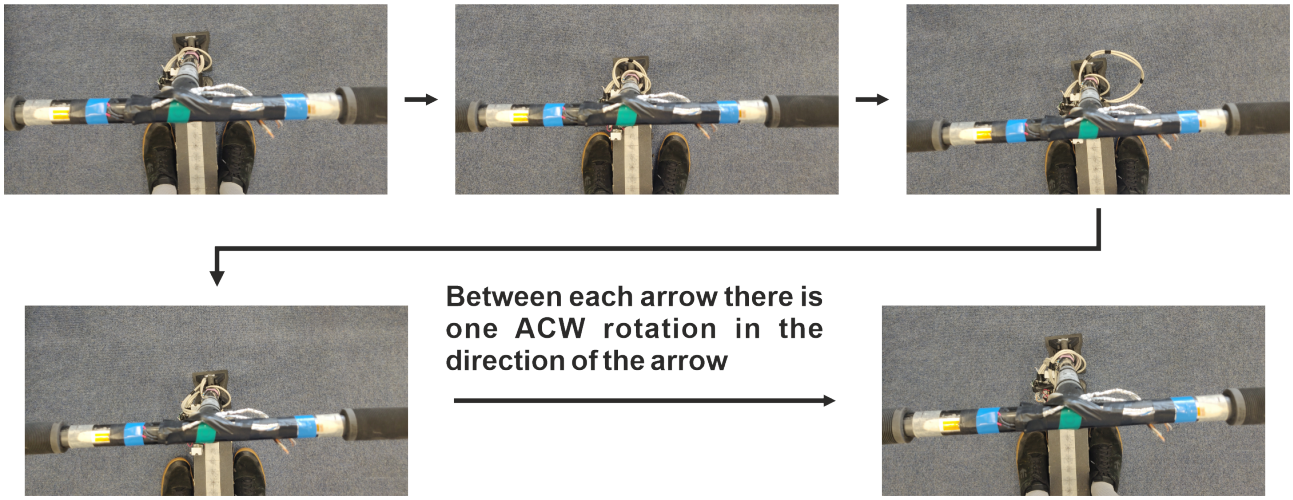


Figure 4.12: The full range of rotation is four full rotations, as can be seen above.



Figure 4.13: An image of the full, instrumented scooter.

4.3 Conclusion

In this chapter, key features of the data acquisition system (DAQ) have been explained, including:

- the overall structure of the DAQ, explaining how the various parts (strain gauges, Wheatstone bridges, amplifiers, the battery and the data logger) relate.
- the need to make a custom DAQ which is different to those in the literature.
- the rationale for using the Digilent Openlogger as the datalogger for this system.
- the requirements of the signal conditioning board, and a subsequent description of its structure.
- the need for modifications to the DAQ to make it suitable in an environment in which it faces shock loading, including the stiffening of the signial conditioning board with plywood sheet and suspension for the DAQ.

Chapter 5

Static force reconstruction

5.1 Introduction

Strain is measured in the scooter to determine the loading applied to it. In the previous chapter, details of the strain measurement system were given. This chapter outlines how to bridge the gap from measured strain to calculated force in cases where static loading assumptions hold. The motivation for calculating the loading on the scooter is to help understand the distribution of stresses within it. An accurate finite element (FE) model can help give a realistic picture of the stresses within the scooter. Section 5.2 describes an FE model that will be compared to experimental results. This section includes the model's boundary conditions and some convergence studies. Section 5.3 details the rationale behind the location of strain gauge placement on the scooter and gives some preliminary strain data. Section 5.4 explains the theory and assumptions undergirding the static force reconstruction model (the approach used to calculate forces from measured strain). Simulation work is presented (section 5.5) to assess the validity of the assumptions made. A section on experimental calibration (section 5.6) follows this, determining the precise relationship between the applied force and the measured strain under static assumptions. In this section, results from experimental test mismatch cases also help gauge the accuracy of the static force reconstruction model.

5.2 Finite element model (static simulations)

The FE model used geometry imported from Autodesk Fusion CAD software [111]. Scooter components were measured with callipers, a ruler and a tape measure. Dimensions of the scooter components up to 150 mm were measured using digital callipers with a precision of 0.02 mm. A ruler was occasionally used to measure distance when callipers were unsuitable, with a precision of 1 mm. Tape measures with a precision of 1 mm were used for larger distances. From this, the dimensions for the axles, fork, SCS clamp (the clamp that connects the forks and handlebars), outline of the extrusion profile, headset bearings, headtube, and handlebar were measured. Scooter components with a simple geometry were purposely selected to help make the CAD model more accurate and to make FE meshes less computationally expensive. The scooter was assembled from: A Native STEM deck [112] (footplate size nominally $20.25'' \times 5.5''$), District S-Series AL115 handlebars [113] (nominally 660 mm tall and 580 mm wide), Micro MX-180 forks [114], a Blazer Pro SCS [115], Ethic Mogway 100 mm diameter wheels [116] and Tilt Metra grips [117].

The CAD model was imported into Dassault Systemes Abaqus CAE [118] (simulations were performed on Abaqus CAE 2016, 2020 and 2022). The simulations used for this chapter were linear, static simulations. The deck and handlebars are made of 6061 aluminium. The forks and clamp are aluminium, but the alloy was not specified. As the Young's modulus of aluminium does not vary significantly (except for 8xxx alloys) [119], this was not considered an issue. The Headset bearings are made of steel. To avoid excessive contact in the model, the steel bearings, which are not solid (and therefore more elastic than an equivalently sized solid steel ring), were modelled as solid aluminium blocks. As the FE simulations did not involve the rotation of the handlebars, the scooter was modelled as one solid aluminium part in contact with the axles. A hard contact was defined between the axles and the fork and back dropout of the deck (the dropouts are the holes that the axle goes through), with a coefficient of friction of 0.001 (used to avoid numerical instabilities). Boundary conditions were applied at the axles. The front axle was fixed at both ends so that it could not move in the x_1, x_2, or x_3 directions (see figure 5.1 for the coordinate system used). The back axle could not move in the x_2 or x_3 directions. An analysis was made to gauge the impact of simplifying the boundary conditions. Fixing a line element on the back dropout, rather than having

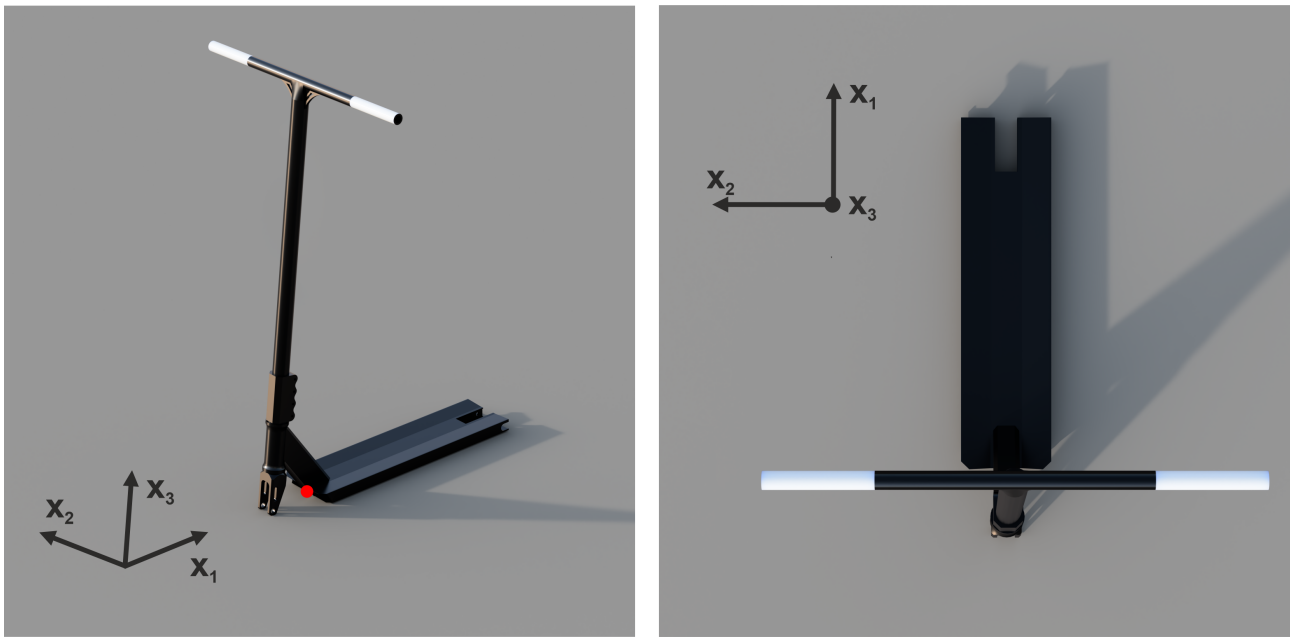


Figure 5.1: The coordinate system used for the scooter. The 1 direction is parallel to the direction of the footplate, the 2 direction is parallel to the crossbar and the 3 direction is mutually perpendicular to the 1 and 2 direction. The red point shows the location of the origin in the model.

a back axle with friction, saved on computational cost. The difference in results for this boundary condition and using an axle is negligible, as shown in figure 5.2. The simulations for the suitability of strain gauge placement in the following sections use the simplified boundary condition.

The material properties given to the scooter were those of 6061 T-6 aluminium, a Young's modulus of 68.9 GPa, and a Poisson's ratio of 0.33 [2,120]. A convergence study with 15 mm, 10 mm, 5 mm and 3 mm C3D10 elements was performed. Results for the strain on the underside of the deck and the front of the down tube can be seen in figures 5.3 and 5.4 respectively. The maximum difference in strain within the region of interest was below 0.5 %. For static simulations, either 5 mm (110 000 elements) or 3 mm (350 000 elements) meshes were used.

Note that when discussing area loads applied in an FE environment, they are defined as surface tractions in Abaqus, where the total load applied over an area has the value of:

$$\mathbf{F} = \int [\boldsymbol{\sigma}] \cdot \mathbf{n} \, dA$$

where **F** is the total force acting on the surface of the body, $[\boldsymbol{\sigma}]$ is the stress tensor and **n** is the

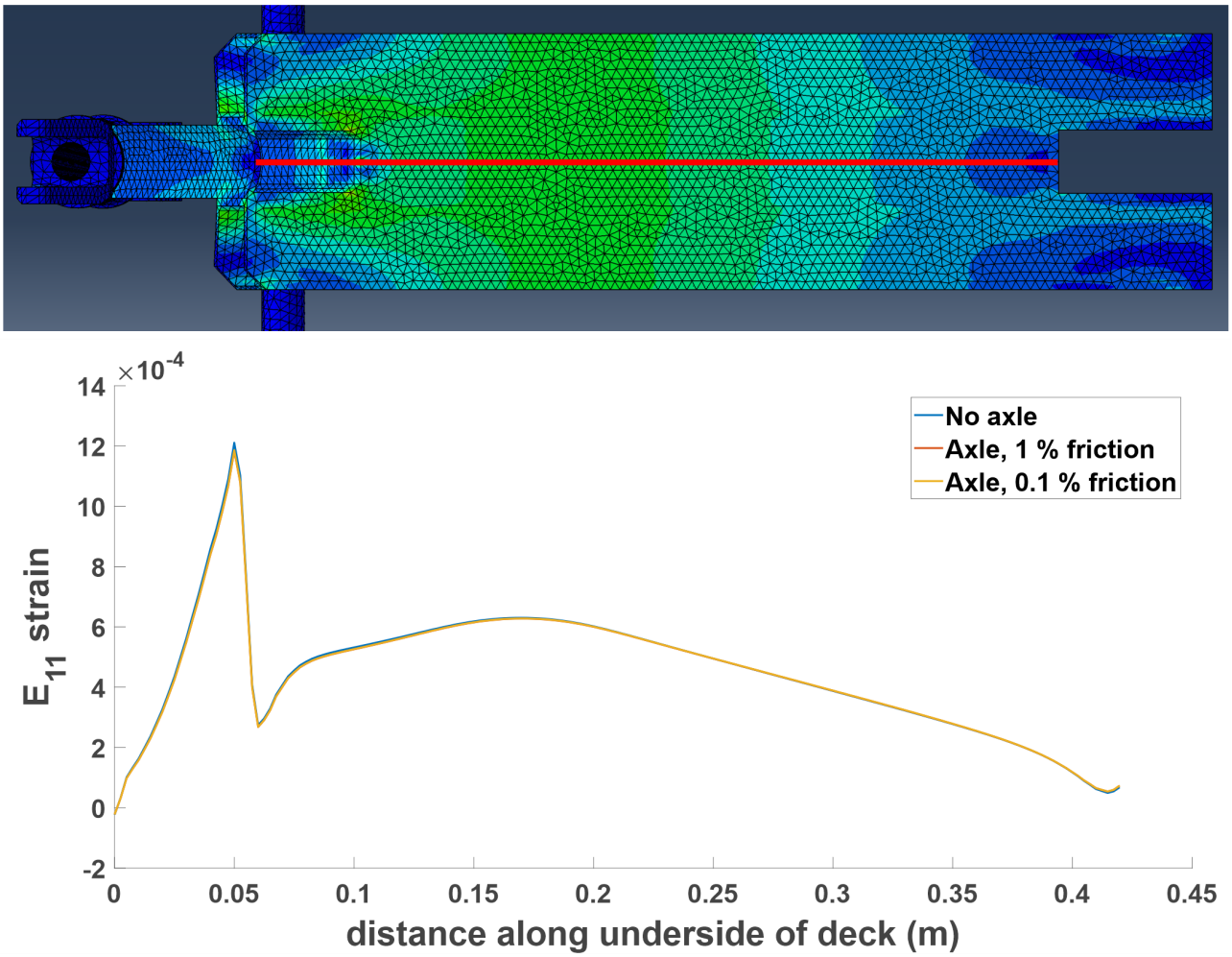


Figure 5.2: A graph showing that the exact boundary condition in the region of the wheel makes very little difference to the strain distribution. A load of 2000 N was applied at the location of $\boldsymbol{f_3}$ (see figure 5.11), and the element mesh size was 5 mm. The red line shows the path on the underside of the deck where the strain is being measured.

unit normal vector to the surface upon which the traction is applied (the surface traction is equal to the product $[\boldsymbol{\sigma}] \cdot \mathbf{n}$).

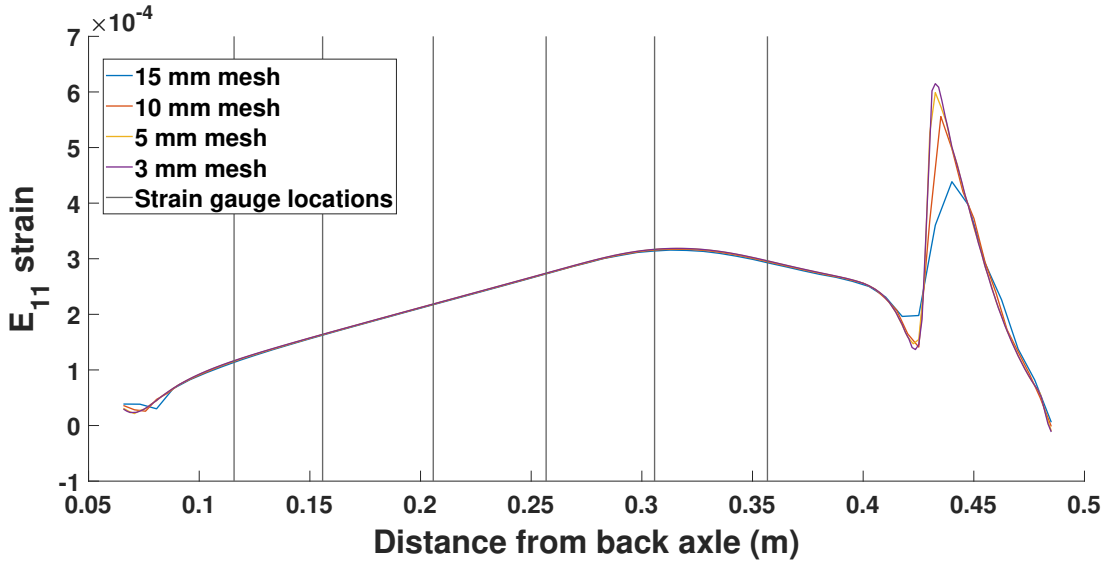


Figure 5.3: A graph showing the convergence of E_{11} strain along the underside of the deck as a function of distance along it. A load of 1000 N is applied at the location of $\boldsymbol{f_3}$ (see figure 5.11).

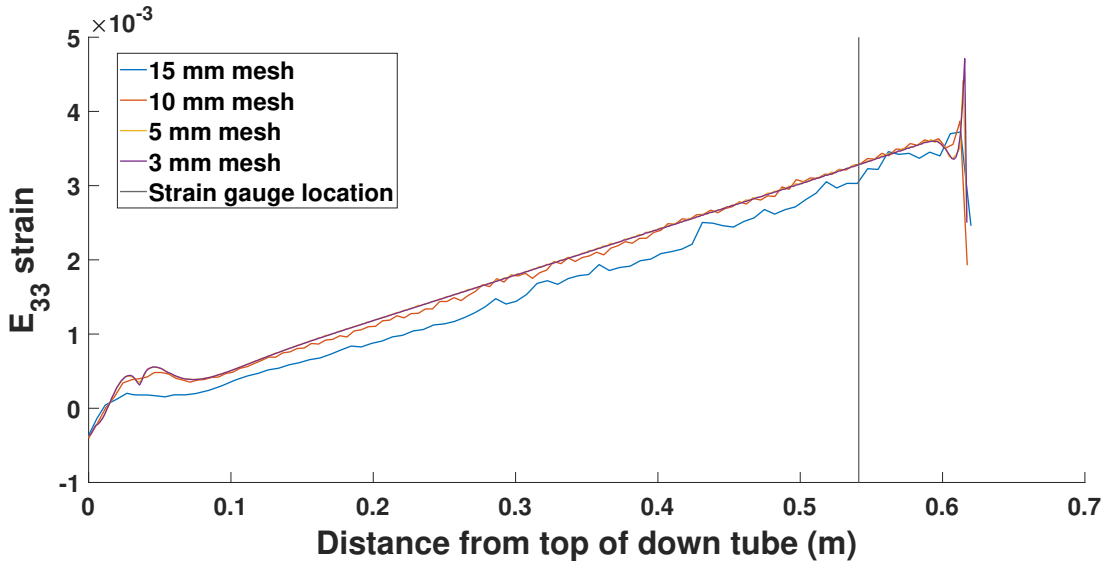


Figure 5.4: A graph showing the convergence of E_{33} strain along the front of the down tube. A load is applied at the location of $\boldsymbol{f_3}$, as well as the area where $\boldsymbol{f_1}$ is applied (see figure 5.11). The load on the deck is 1000 N vertically downwards, whilst the handle bar load has 1000 N components both parallel and perpendicular to the down tube

5.3 Strain measurement

The aim of measuring the strains the scooter faces in real-time is to determine the forces applied to it. With the data logging system described in the previous chapter, there are still questions of how to bridge this gap. The first of these is on the location of the strain gauges.

5.3.1 Strain gauge location

To understand where strain gauges should be placed for force reconstruction, it is helpful to think about where loads will be applied to the scooter. Loads are applied by the rider to the handlebars and the deck. Reaction forces are transmitted through the wheels to the axles. The component of force going through the rider's feet will primarily be normal to the footplate (x_3), whereas loads from the hands will have significant components in the horizontal (x_1) and vertical (x_3) directions. Figure 5.1 shows the coordinate system used for the rest of this thesis.

Strain gauges should be located at points on the scooter that are sensitive to the applied loads, but also in a location where the strain is not too sensitive to position (i.e. where the strain gradient is not steep). This should reduce any errors associated with strain gauge placement when later comparing data to an FE model. It is also better if strain gauges are placed where the variation of strain with position is linear, so the averaging over the length of the strain gauge will accurately represent the strain in the middle of the strain gauge. It is worth noting here that initially, the idea was to do the static calibration with simulations. Because of this, strain gauges were placed in regions where the FE model of the scooter was most likely to be accurate. Regions where the FE model was most likely to be accurate was in places where the loading conditions were simple, and the geometry of the CAD model was most accurate.

Because of these considerations, strain gauges were placed on the crossbar, down tube and the underside of the deck (see figure 5.5). To maximise strain sensitivity, strain gauges should be placed near the centre of the crossbar and near the bottom of the down tube (moment loading is greatest in these locations). On the crossbar, the strain gauges were not placed too close to the gussets (see figure 5.6). Near the gussets, there is welding, which wasn't modelled in CAD model. Also, the

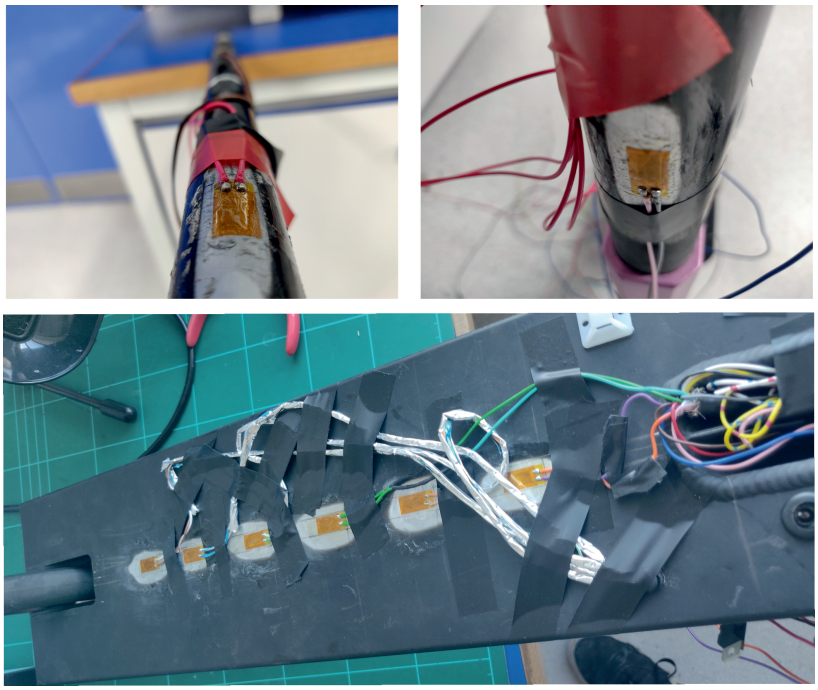


Figure 5.5: Pictures showing the strain gauges on the crossbar (top left), down tube (top right) and on the underside of the deck.

gussets are near a change in cross-section where the reaction forces are more complex. The tube of the crossbar further away from the gussets approximate a cantilever with a load at one end.

The strain gauges on the down tube were placed approximately 70 mm away from the top of the clamp (see figure 5.9). The strain gauges were not placed closer to the clamp due to the strain field becoming less linear (see figure 5.7), and the FE model potentially being less accurate here (e.g. the model does not model the compression applied by the clamp). In the deck, the strain gauges were placed along the line going up the centre of the deck (length ways), and not too close to the headtube and/or back dropout (where the back wheel is). Initial simulations to give a good idea (i.e. to ensure the strain field was varying as expected) for strain gauge location were carried out. Simulation results were compared with an analytic approximation using Euler-Bernoulli beam theory, and early experimental calibration. Results (and details) are given in figure 5.8. The location of the strain gauges on the scooter can be seen in figure 5.5. A more precise drawing giving the locations of the strain gauges can be seen in figure 5.9. As previously mentioned, the DAQ can measure up to eight channels of strain data. More than eight strain gauges were applied to the scooter to allow for investigation of forces on different parts of the scooter.

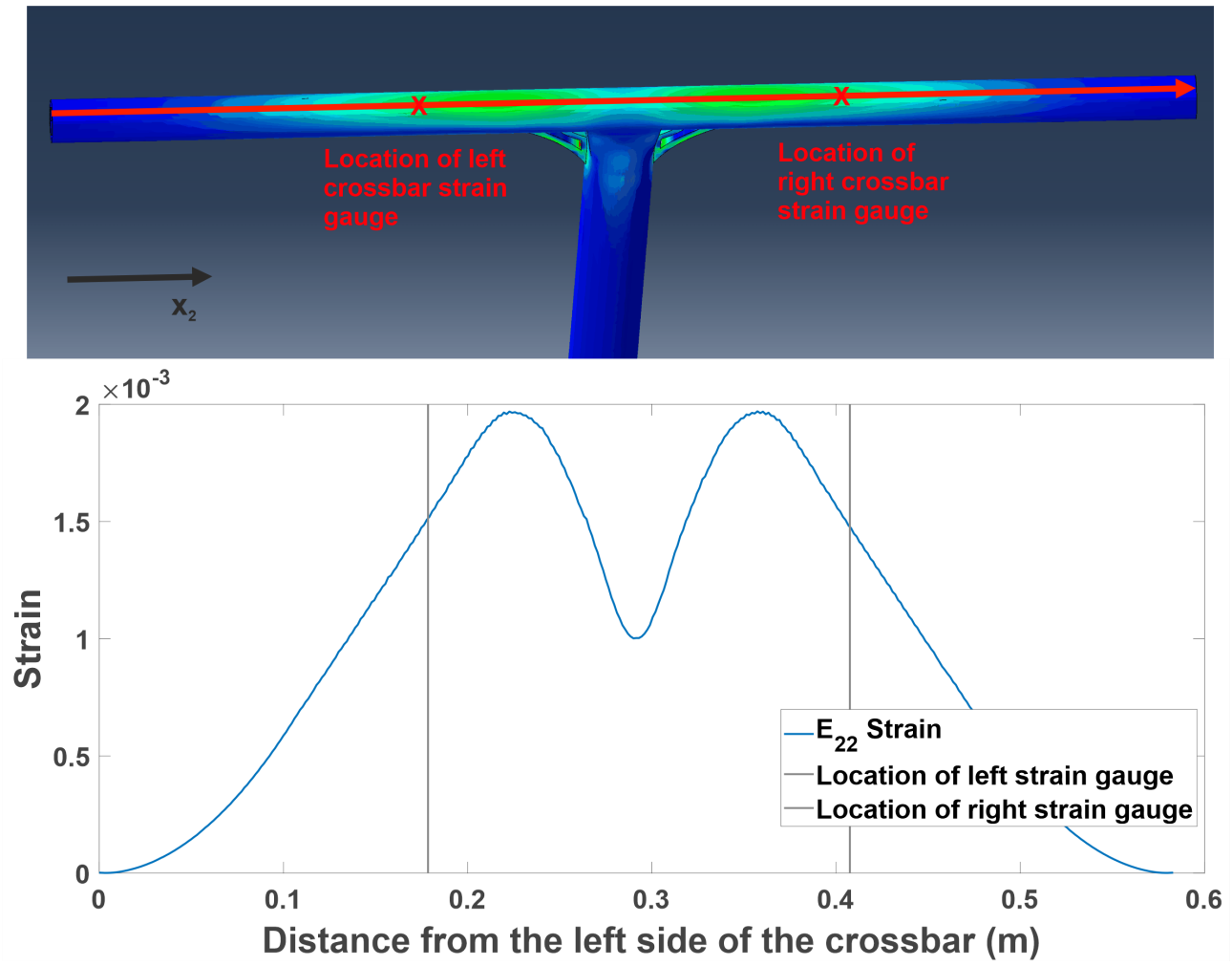


Figure 5.6: A simulation showing the strain on the top side of the crossbar. The direction of strain measurement is represented by the red arrow at the top of the figure. An area load is applied to the area where $\boldsymbol{f_1}$ is applied in figure 5.11. The load has a component of 1396.4 N in the direction parallel to the down tube (towards the clamp), and a component 279.3 N perpendicular to the down tube (towards the footplate). In the direction of the down tube (almost straight downwards). Strain gauges were placed in regions close to the centre of the bar, where the strain was still varying linearly.

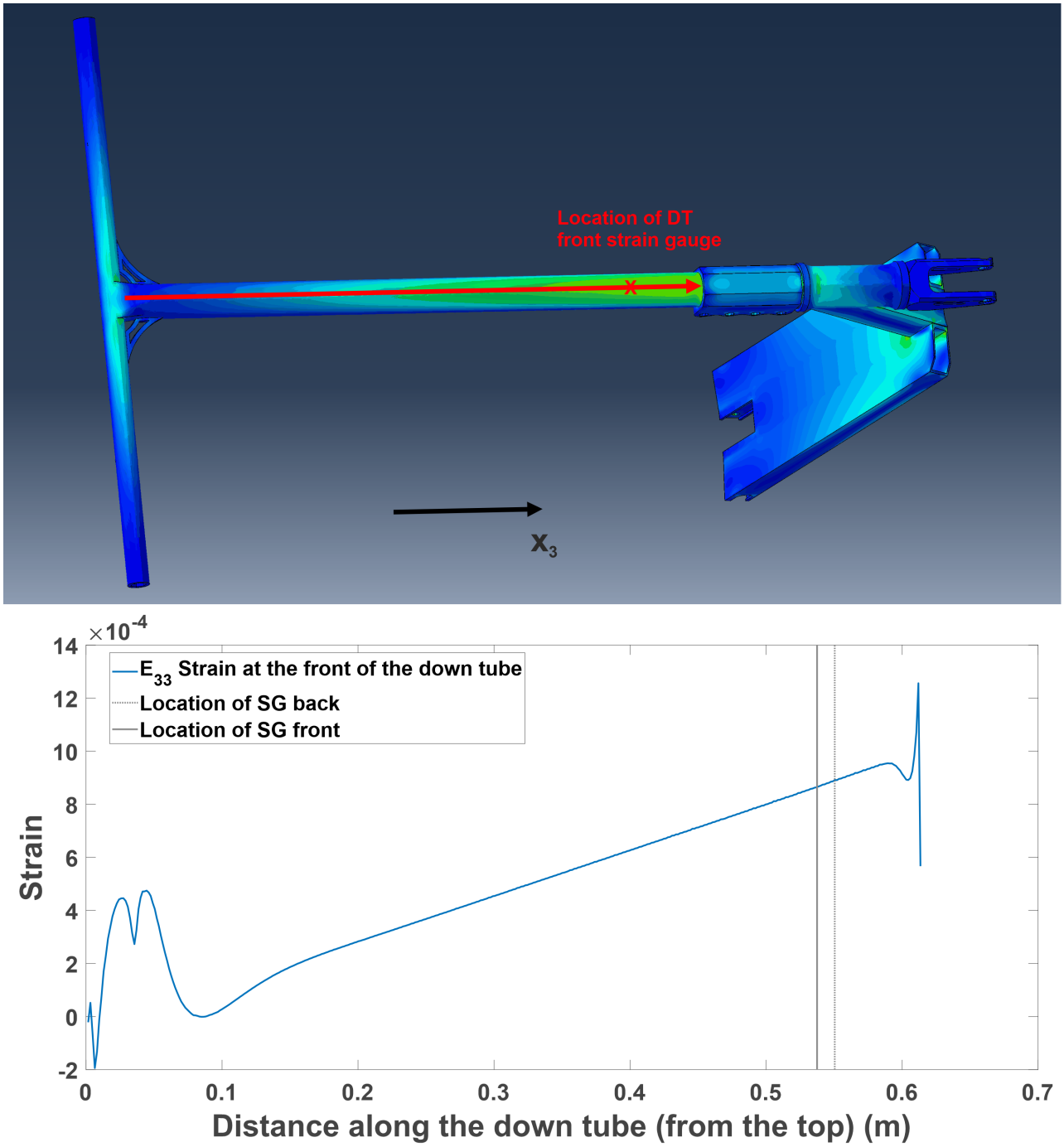


Figure 5.7: A simulation showing the strain as a function of distance down the down tube on the front side. An area load is applied in the area where $\boldsymbol{f_1}$ is applied in figure 5.11. The load has a component of 1396.4 N in the direction parallel to the down tube (towards the clamp), and a component 279.3 N perpendicular to the down tube (towards the footplate). The strain measurements are on the down tube, in the line of the red arrow. Whilst the strain gauge on the back of the scooter is on the other side of the handle bar, the shape of the strain plot on the back is almost identical, except that the strain is compressive.

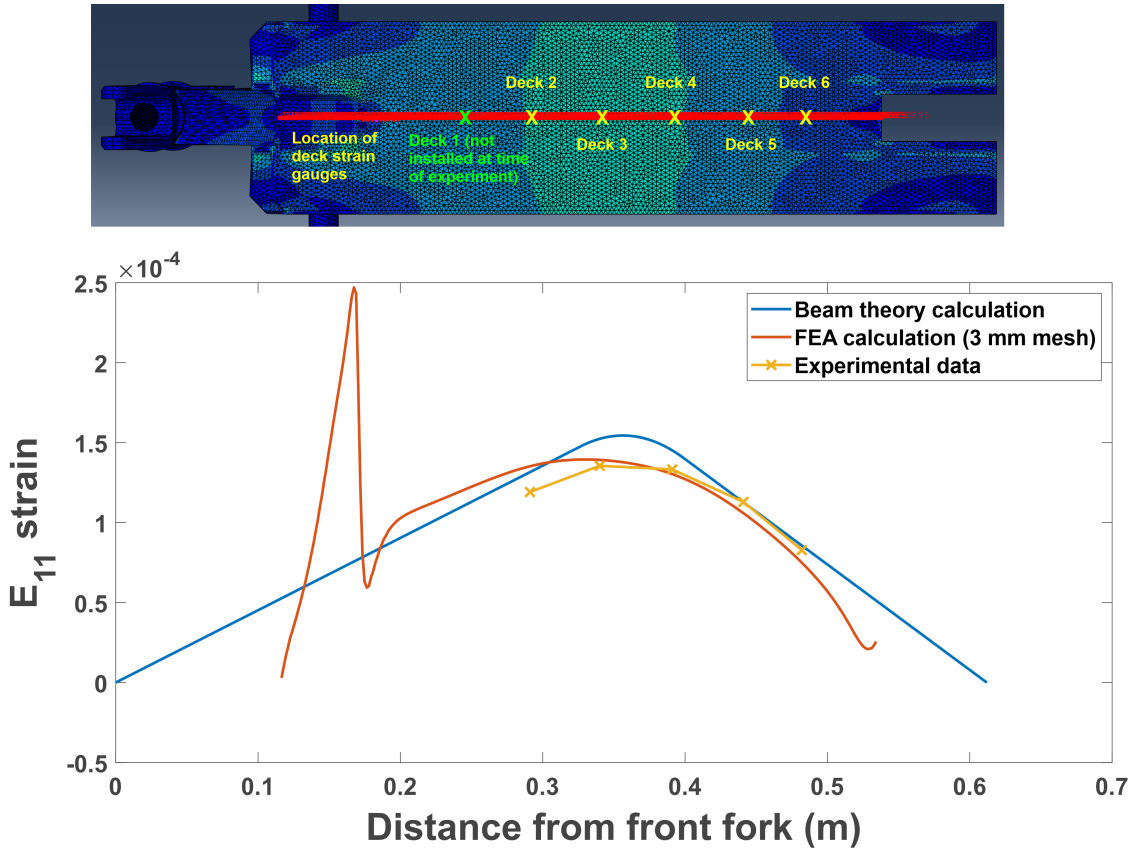


Figure 5.8: The figure shows the strain as a function of distance along the underside of the deck in response to an applied load in the centre of the footplate. The red line shows the line of strain measurement, and is directly above the corresponding location in the plot for the FEA data. The load is vertically downwards (perpendicular to the plane of the footplate) and has a magnitude of 500 N. The location of the area load is where $\boldsymbol{f_4}$ is figure 5.11. Comparisons of beam theory, an FE simulation and some early calibration data show close correspondence in the region of interest.

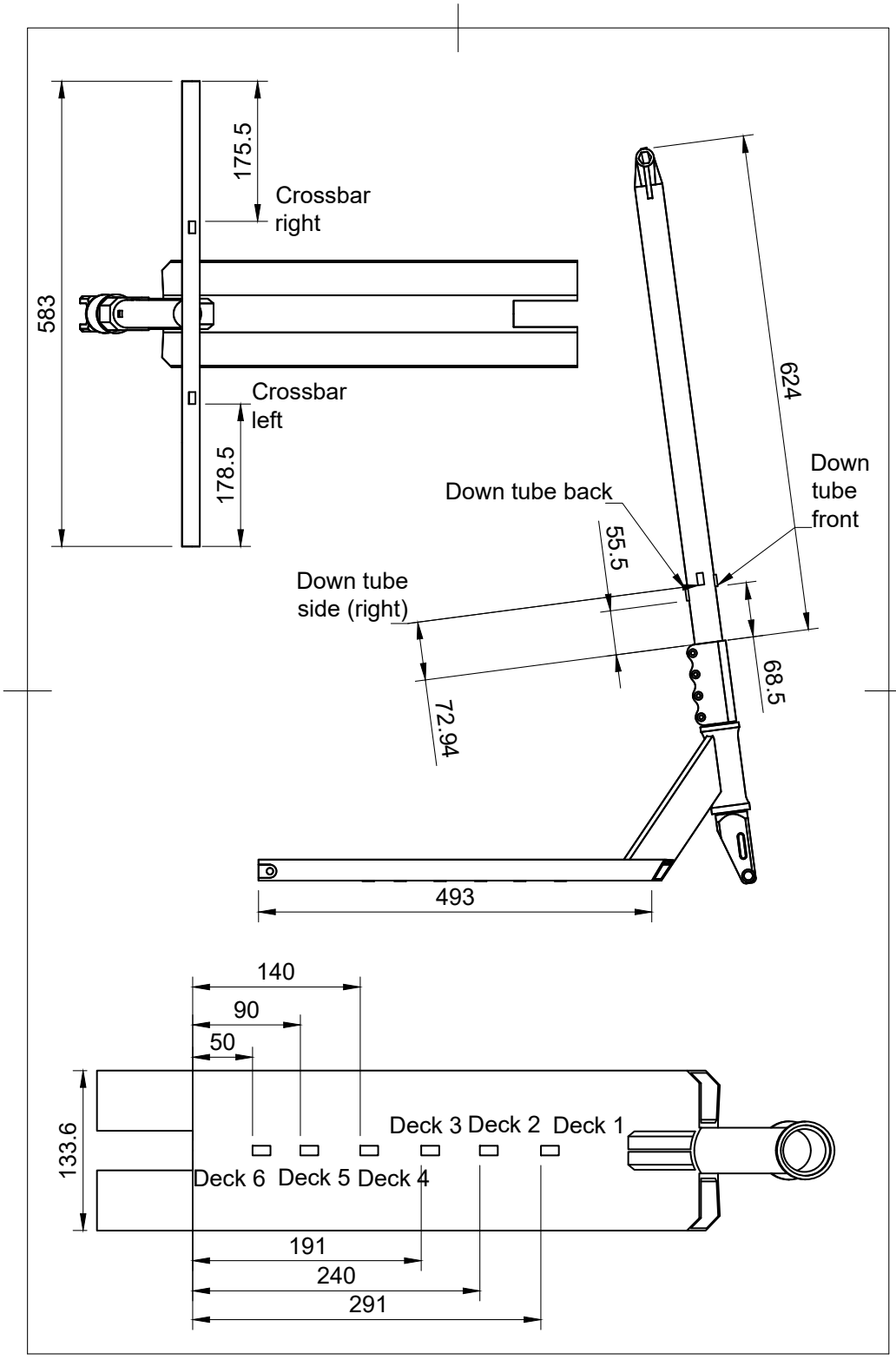


Figure 5.9: The locations of the strain gauges on the scooter. Distances given are to the bottom of the applied strain gauge and are in mm.

5.3.2 A sample of strain measured in real-time

At this point, it is helpful to show some strain data to show what it looks like, before discussing how it can be used to calculate the forces applied to the scooter. To illustrate this, we will look at strain measurements recorded during a bunnyhop. A bunnyhop is the most simple stunt on a scooter. It involves the rider jumping with the scooter before landing again. An illustration of the steps can be seen in figure 5.10.

The figure also shows the strains in the deck, down tube and crossbar associated with a bunnyhop. An overview for the cause of the strain at different points is given in the figure caption. A more detailed description of the strain history, and its relation to the forces applied to the scooter will be given later. Other more advanced stunts have more features in their strain history, but these will be discussed in chapter 7.

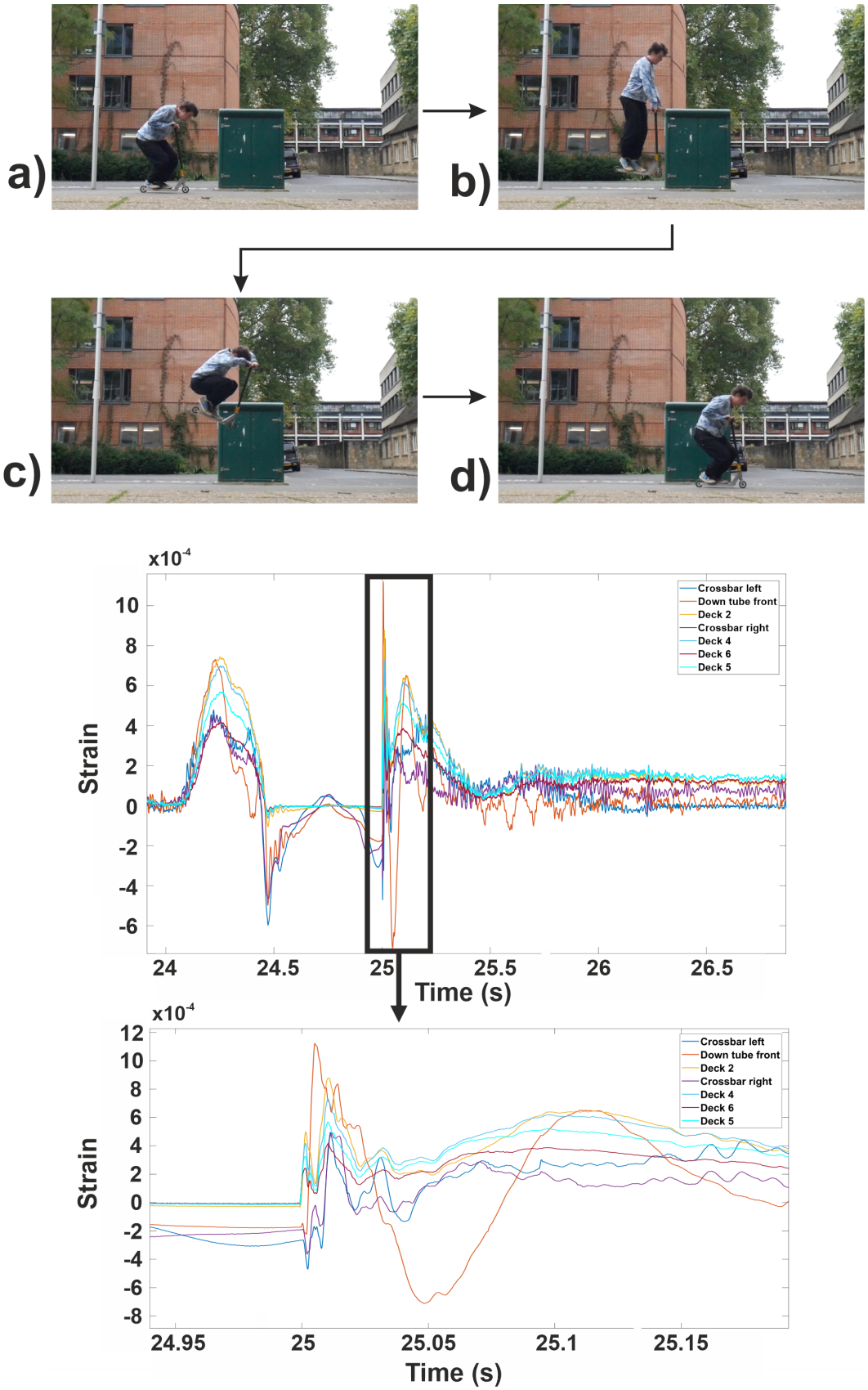


Figure 5.10: During a bunnyhop the rider usually crouches (a), before jumping (b), tucking (c) and then landing (d). In the graphs below, the part in the black box corresponds to the landing.

5.4 Force reconstruction

5.4.1 Static force reconstruction theory

The aim of a force reconstruction approach is to understand the forces applied to a system through measuring some other quantity. In this case strain is being measured to calculate the forces. It is easiest to begin with static assumptions, before describing how dynamic effects change things and comparing the difference in results.

First, because strain is being measured at only a finite number of points, there can only be an (assumed) finite number of loads applied to the scooter for there to be a unique solution. The number of assumed possible applied loads must be less than or equal to the number of strain measurement points. The assumed possible loads must be realistic, and appropriate boundary conditions should also be applied. Details specific to the system in question will be given below.

A convenient way to mathematically describe the inverse problem of reconstructing the applied loads from the measured strains is using basis loads. There are a number of assumed possible loads on the scooter. They all have a fixed magnitude (in this case 1 N), and all give a strain response across the scooter. i.e. each basis load $\boldsymbol{f}_x$ will produce a strain distribution $\boldsymbol{\varepsilon_x}$ which will have elements ε_{mx} where each m value represents a different location on the scooter (which in practice will be at the location of a strain gauge). Note that the length of the basis load vector (based on the total number of basis loads) will in general not be the same as that of the strain vector (based on the number of strain measurement points). If the deformation response is linear elastic, the total strain response of the scooter will then be a linear combination of the applied basis loads. The total approximated loading across the scooter will be:

$$\mathbf{F} = \sum_{x=1}^{n_{basis}} c_x \boldsymbol{f}_x \tag{5.1}$$

where n_{basis} is the number of basis loads and c_x is the coefficient of basis load x. This can be recast into the matrix equation:

$$[\boldsymbol{\varepsilon}_t]\boldsymbol{c} = \boldsymbol{\varepsilon}_{meas.} \tag{5.2}$$

$[\boldsymbol{\varepsilon}_t]$ is the matrix for the strain distribution as a function of location as a result of the basis loads. Element ε_{mx} in the matrix is the strain that arises from basis function $\boldsymbol{f}_x$ at strain measurement location m. $\boldsymbol{c}$ is the vector of the coefficients of the basis loads and $\boldsymbol{\varepsilon}_{meas.}$ is the vector of the (total) measured strain at each strain measurement point. Each row of the vector $\boldsymbol{c}$ corresponds to a different basis load, and each row of the product $[\boldsymbol{\varepsilon}_t]\boldsymbol{c}$ corresponds to the total strain at a strain measurement point caused by the linear combination of basis loads. Initially, experimental calibration is performed. $[\boldsymbol{\varepsilon}_t]$ is determined by measuring $\boldsymbol{\varepsilon}_{meas.}$ when $\boldsymbol{c}$ has one non-zero entry of known magnitude. Then when data is collected $\boldsymbol{c}$ is initially unknown, $\boldsymbol{\varepsilon}_{meas.}$ is measured and $[\boldsymbol{\varepsilon}_t]$ is already known from the experimental calibration. Note that, the number of rows (strain measurement points) of $[\boldsymbol{\varepsilon}_t]$ must be at least equal to the number of columns (basis loads) to have a unique solution. Conversely, over-constraining the equations (by having more rows than columns in $[\boldsymbol{\varepsilon}_t]$) is not an issue. In this case, the force can be calculated by minimising the least-squares error (the MATLAB function used for the actual force reconstruction (lsqlin) implemented an interior-point algorithm to minimise the least-squares error [121]).

On a scooter, the possible loading from the rider can come from either the hands or the feet. Loads from the feet will primarily have a component in the $-x_3$ direction, whereas the loads from the hands may have both an x_3 and an x_1 component. A representation of the basis loads on the scooter used for this project can be seen in figure 5.11. In this model, loads on the handlebars in the x_3 direction are ignored. The reason for this is to simplify the model due to the limited number of strain measurement points, and because forces parallel to the down tube have little impact on strains in the scooter (except the crossbar). A comparison of the strains caused by loads parallel and perpendicular to the down tube can be seen in figures 5.12 and 5.13. For example, when the same magnitude load is applied in each direction, the load parallel to the down tube generates a strain only $1.34\ \%$ the size of the strain generated by the load perpendicular to it at the location of the front down tube strain gauge. In the deck the ratio of the strain magnitudes is $1.8\ :\ 100$. It is

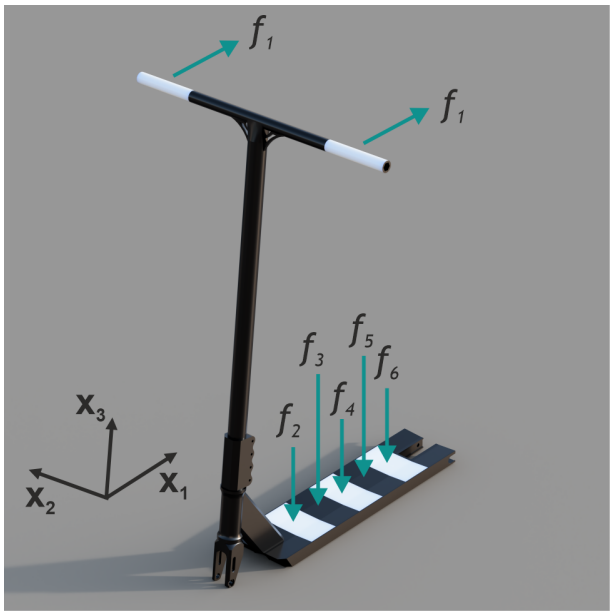


Figure 5.11: The assumed loads on a model scooter. Shaded regions next to arrows show the area over which the basis loads operate. Symmetry is assumed on forces applied from the hands on the handlebars, thus the basis load $\boldsymbol{f_1}$ is equally distributed across each side of the crossbar.

worth noting that the angle between the footplate and the down tube is not $90°$, hence the use of the terms 'perpendicular to the down tube' or 'parallel to the down tube' rather than x_1 or x_3. A corollary of this is that the down tube strain gauges were not used for the final force reconstruction.

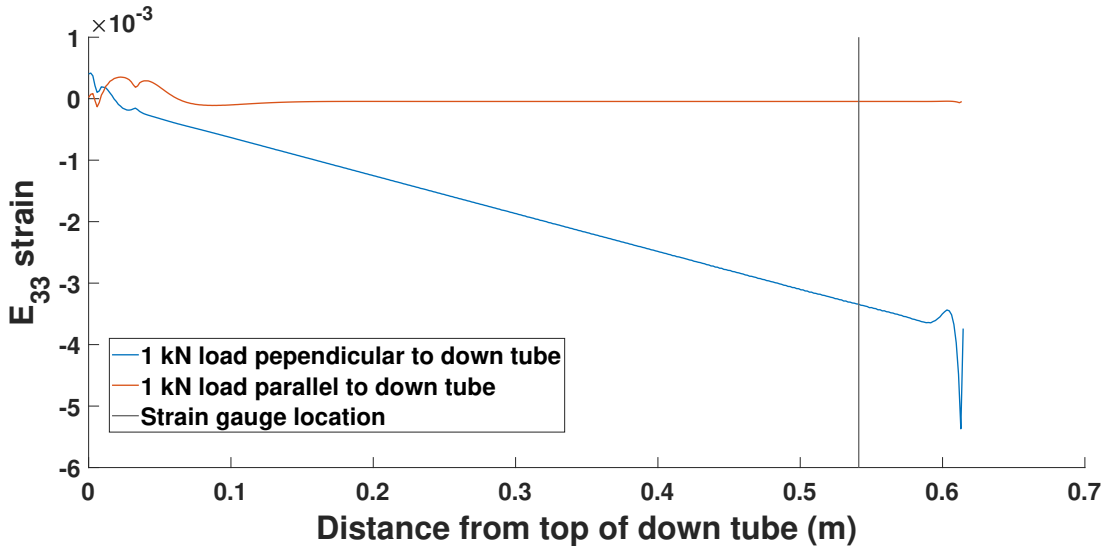


Figure 5.12: The strain in the down tube as a function of distance along it when a 1 kN load is applied either parallel or perpendicular to the down tube. As can be seen, the strain caused by the load perpendicular to the down tube is much greater.

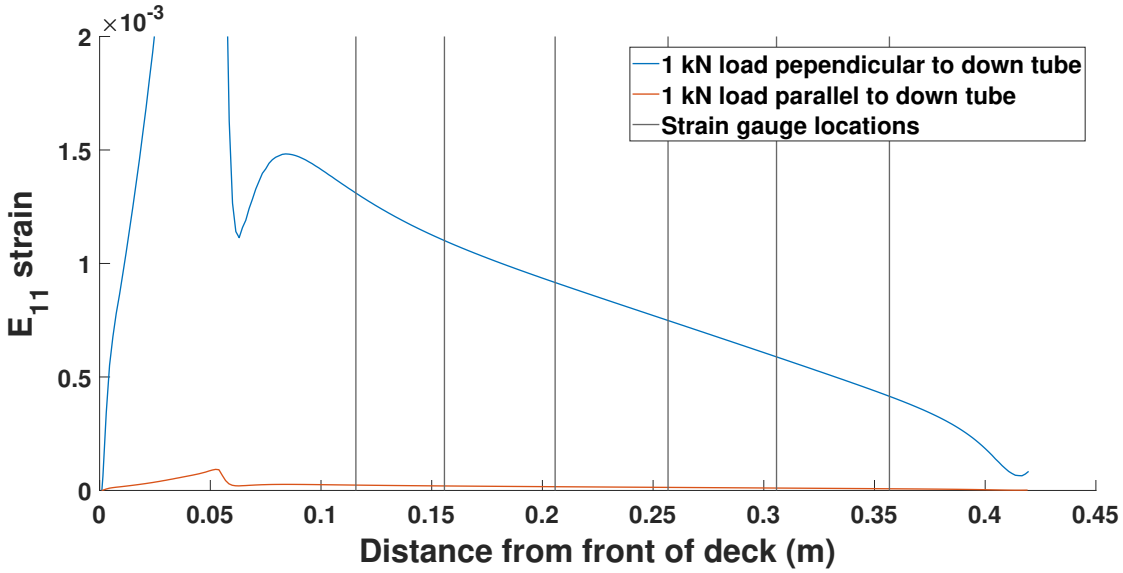


Figure 5.13: The strains along the bottom of the footplate (where the deck strain gauges are) for a 1 kN load applied either parallel or perpendiculat to the down tube. Clearly, the load parallel to the down tube causes much less strain per unit force than the load perpendicular to the down tube.

5.5 Early computational work

5.5.1 FE model details

Early work was performed on a different static model to the one used in the rest of the thesis. The simulations provided here are a proof of concept, showing that with appropriate boundary conditions, force reconstruction is applicable to scooters.

The model was developed during my master's thesis [122]. A picture of the model can be seen in figure 5.14. The deck design was based on the Ethic Pandemonium V1 [123], although the neck and headtube were simplified. This difference should not make a difference in proving whether a force reconstruction approach works in principle nor should it affect the static strain response significantly at the strain measurement points. The headtube designs used for the evenly distributed load and the 'party-hat' loads were slightly different (see the following sections); as expected, this did not affect the efficacy of the force reconstruction approach.

As in the main scooter model, All the major components of the scooter are made of aluminium, mostly 6061-T6. Because of this, the properties of the material used were the same as in the previous section. The performed analysis was linear and static. C3D10 quadratic tetrahedral elements were used. The boundary conditions were applied at the front and rear axles, with no movement at all at the front axle, and movement perpendicular to the cross section of the extrusion profile of the deck was allowed for the rear axle. Strain data was collected from the underside of the deck and on either side of the downtube, furthest away from the neutral axis. The convergence of the model can be seen in figure 5.15. Convergence tests were performed with (approximate global) element sizes ranging from 20 mm to 2.9 mm. The 2.9 mm element model was used for the analysis; it had $310\ 000$ elements.



Figure 5.14: A picture of the scooter model used for the early computational work.

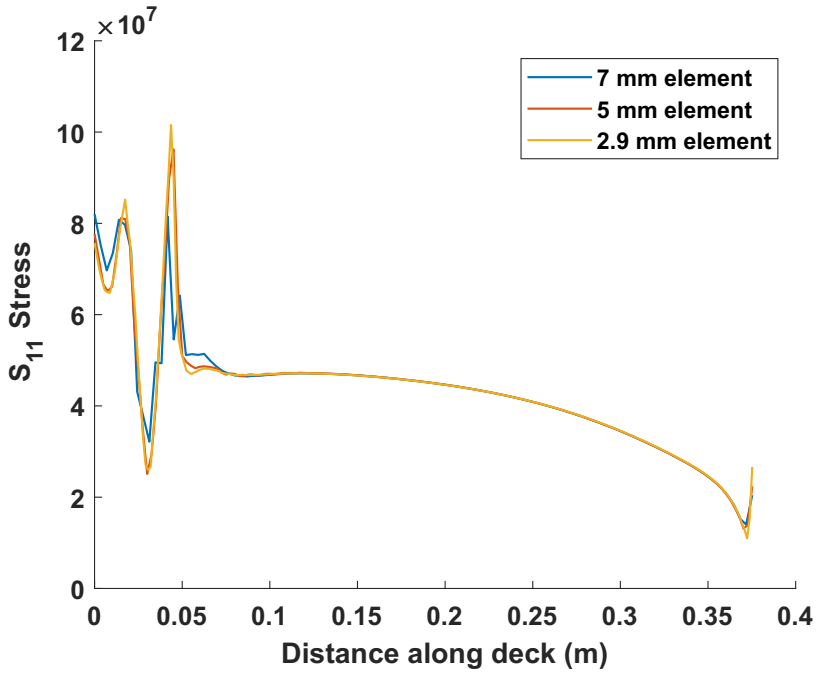


Figure 5.15: A graph showing the convergence of the FE model for the three smallest element sizes.

5.5.2 Dealing with experimental noise and model imperfections.

The first test was to see how loads would be calculated if the location of the applied load had a slight mismatch with the basis loads. The mismatched load was a uniformly distributed load, with a 100 mm length spanning the width of the deck (this load did not align with the basis loads). The load distribution and results are shown in figure 5.16 a) and b). Although the strain map along the deck matched well, the loading distribution was unrealistic if the loads were free to be negative. As the feet are not attached to the deck, they cannot apply an upward (negative) force on it. The solution was to constrain the coefficients of the basis loads on the deck to only positive values on the deck as in figure 5.16 b). As the solution will (generally) no longer be exact, least-squares minimisation is used to determine the best possible match. The strain distribution for this is shown in figure 5.16 c); it matches exceptionally well. The total applied load was 2870 N, with a mean position of 227.8 mm along the footplate of the deck. The constrained solution gives values of the mean load position to be 228.15 mm and a total applied load of 2871.5 N (as opposed to 2853.5 N on the unconstrained model).

The model was also tested against a 'party-hat' load, with a distribution as in figure 5.17. The input load of 200 N had a calculated load of 201.7 N. The mean load position changed from an input of 183.7 mm to an output of 184.4 mm, again matching well. In another test, taking half of the triangular load distribution (as in figure 5.18), with a total force of 100 N, and an average position of 201.4 mm along the deck yielded results of 16.3 N and 88.5 N in basis loads 2 and 3 (total load 104.83 N) at an average position of 202.2 mm along the footplate. The strain distribution matches very well and can be seen in figure 5.18 b).

The constraint of only allowing for positive forces in the deck was more important when experimental noise was introduced. To further test the constrained model, the noise was normally distributed about each strain gauge with a standard deviation of 10^{-5} (the number is based on the error calculated from the master's project and improvements from redesigning the experimental equipment), and the force was calculated. This was repeated 200 times to test the robustness of the system. A comparison between the constrained calculated total load on the deck and the unconstrained load can be seen in figure 5.19a. The strain distribution along the deck is not affected much for the

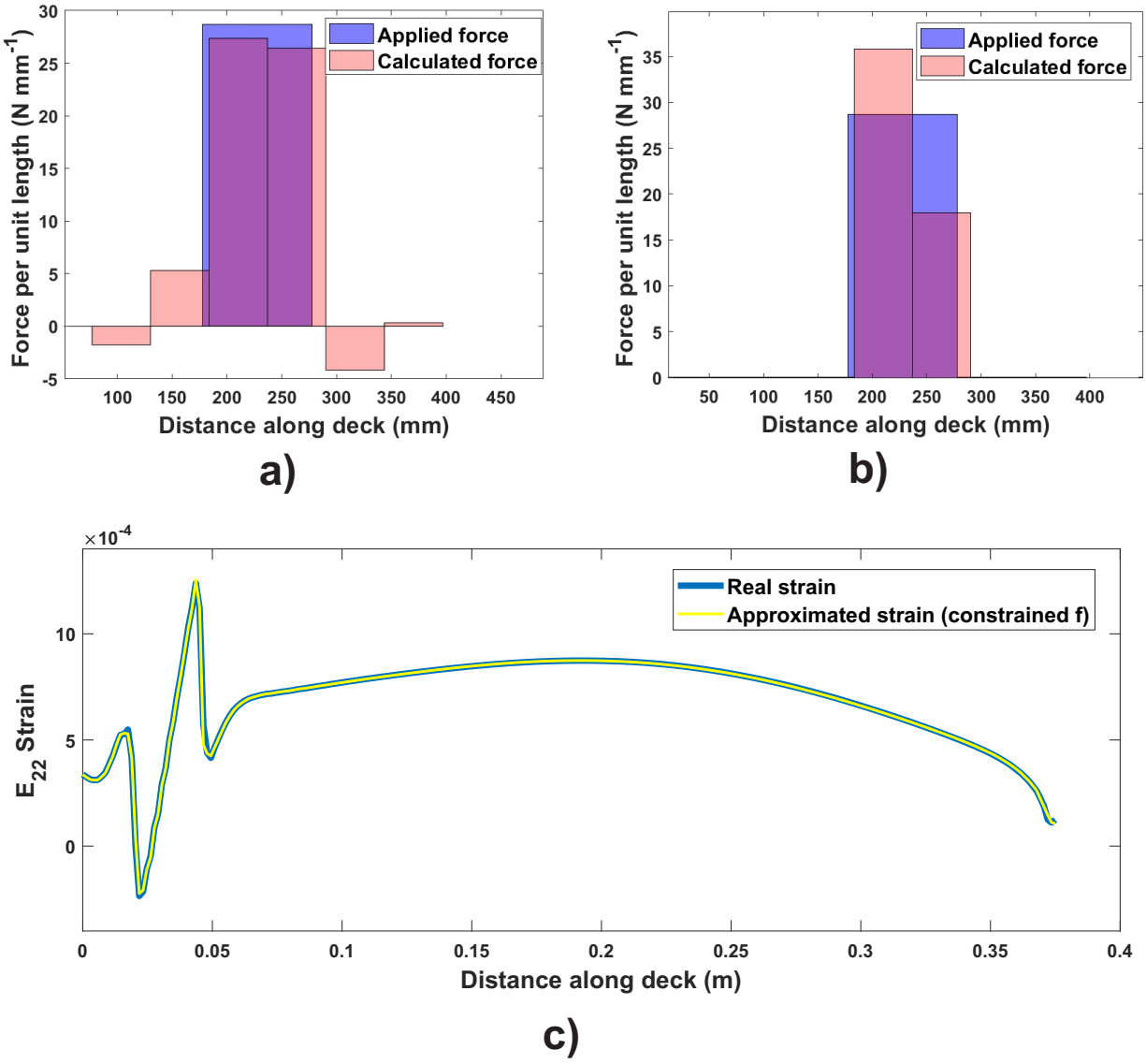


Figure 5.16: The applied load distribution is compared with the calculated load distribution when a) no constraints are put on the allowed basis function coefficients and b) when only positive values are allowed. c) shows the strain distribution from the applied load, and the approximated load from b).

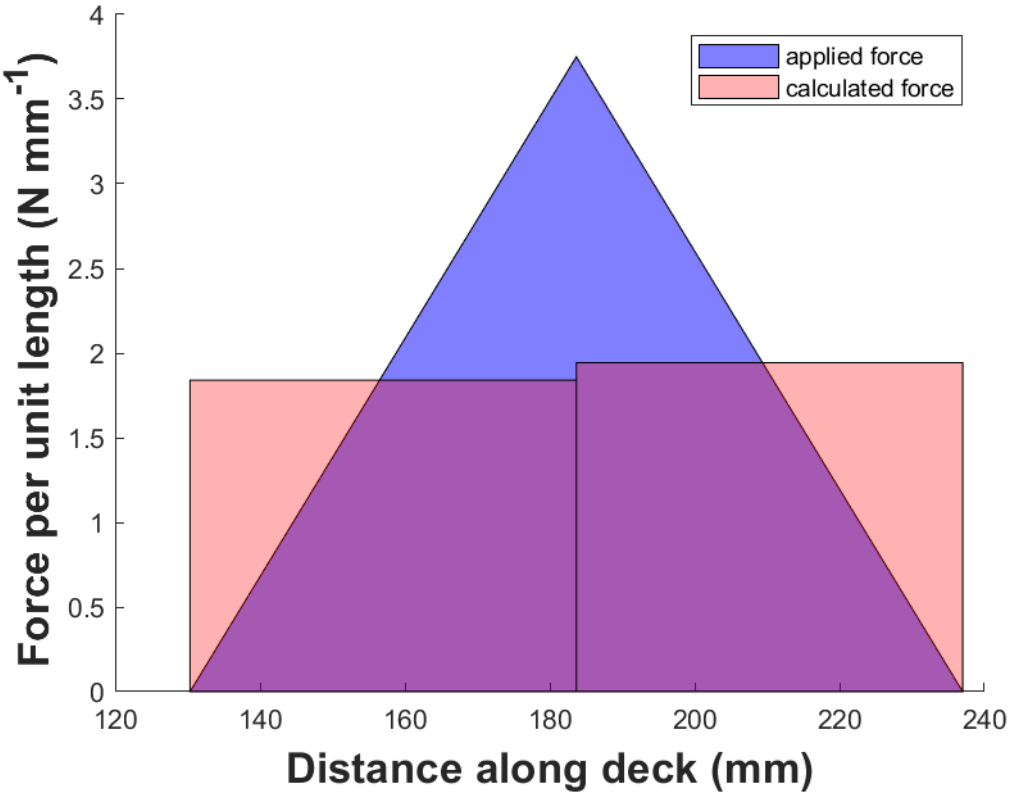


Figure 5.17: The approximated load distribution for a party-hat load.

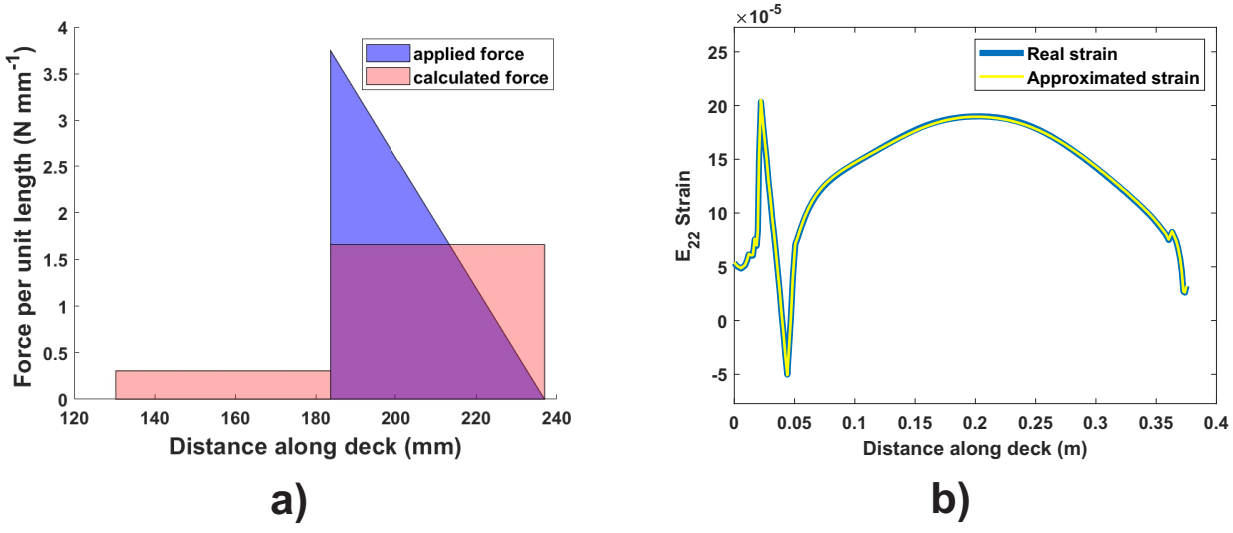


Figure 5.18: a) Showing the approximated load from the force reconstruction model compared with the original load distribution in the case of half a 'party-hat' load. the strain distribution of the applied load matches very well and can be seen in b).

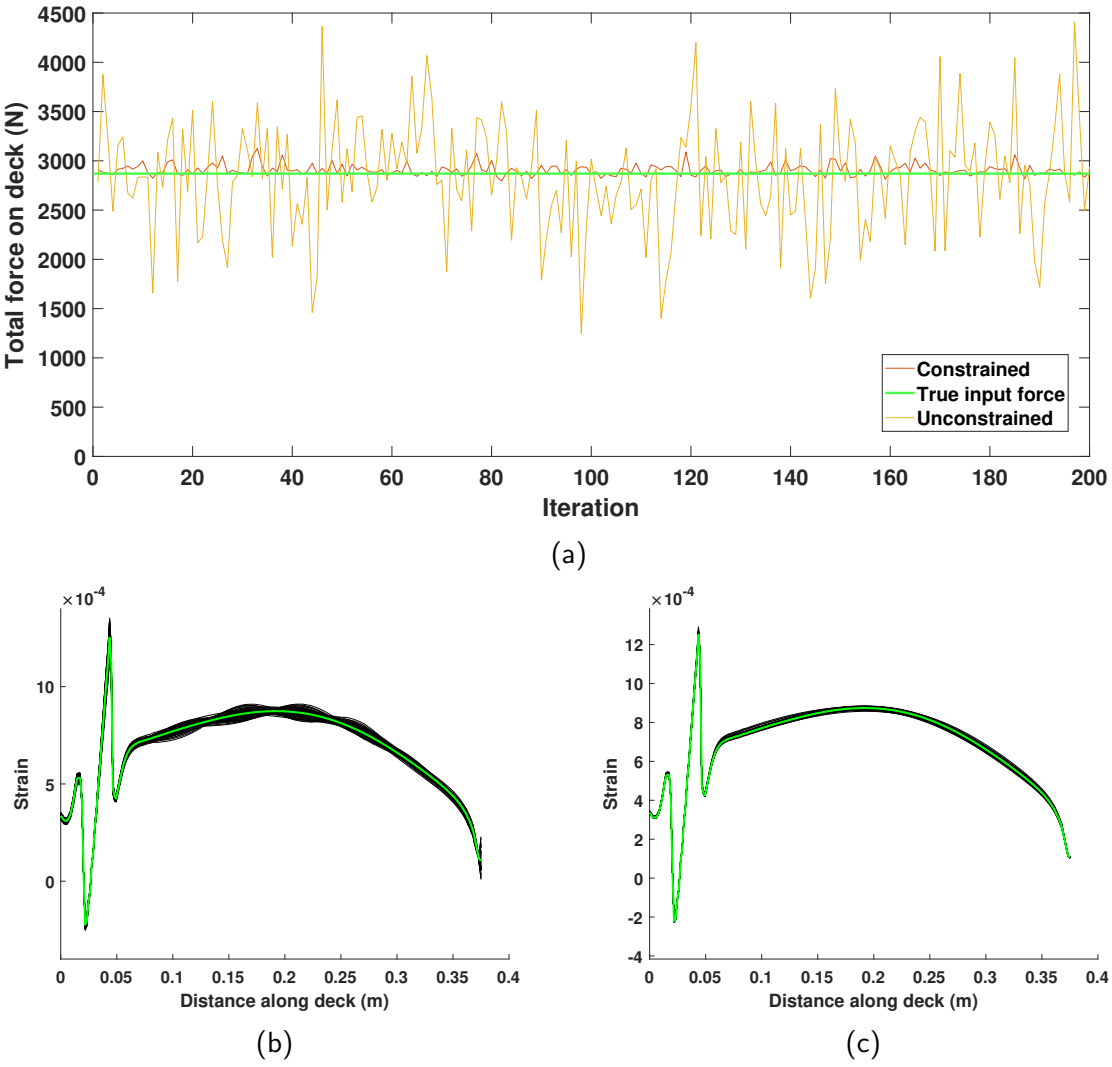


Figure 5.19: a) A comparison of the total load calculated on the deck when noise with a standard deviation of 10^{-5} is applied at each strain gauge. When the calculated load is unconstrained (and allows for negative forces to be applied on the deck), there is significantly larger scatter in the calculated total load. The strain response from the applied force (green) and the reconstructed forces (black) can be seen in b) for the unconstrained force reconstruction, and in c) for the constrained reconstruction. In both cases the black lines are from 100 iterations, and the standard deviation of the strain at the measurement points is 10^{-5} strain.

constrained model, as can be seen in figure 5.19c, whereas the unconstrained model does not fare as well (figure 5.19b).

Another way to improve the system's accuracy is to add strain measurement points, but keeping the number of basis loads the same. This over-constrains the equation and again least-squares minimisation can be used to get the best approximate load distribution. The downside is that it requires more channels of data to measure the strain. This approach of generating basis load responses for a static model could have been used in the final (static) force reconstruction. In the end, we opted however to use an experimental approach. The FE model contains numerous idealisations/sources of error (e.g. material property definitions may vary slightly, there could be small errors in the measurement/geometry of the scooter parts, the scooter is not one solid part etc.) which the experimental calibration should take into account.

5.6 Static calibration

5.6.1 Static calibration of the handle bar load

General approach

Static loads on the deck do not cause strains in the handlebars, so only $\boldsymbol{f}_1$ needed to be considered. Static calibration of the handlebars was performed by applying weights of known mass to the scooter whilst it was mounted on a post. A figure of the static calibration setup of the handlebars can be seen in in figure 5.20. Strain was measured as weights were applied, giving a plot of strain against force on the scooter. Because there were stability issues with hanging weights off the edge of the crossbar (there was significant risk the weights could slide off the setup if the crossbar was not straight), weights were for the most part applied to the down tube.

A plot of strain against time for known applied loads was first obtained (see figure 5.23a). Some data processing was needed in order to accurately obtain the data. The strain levels would first need to be calibrated (by taking the average of the first second or so of data, and setting that average

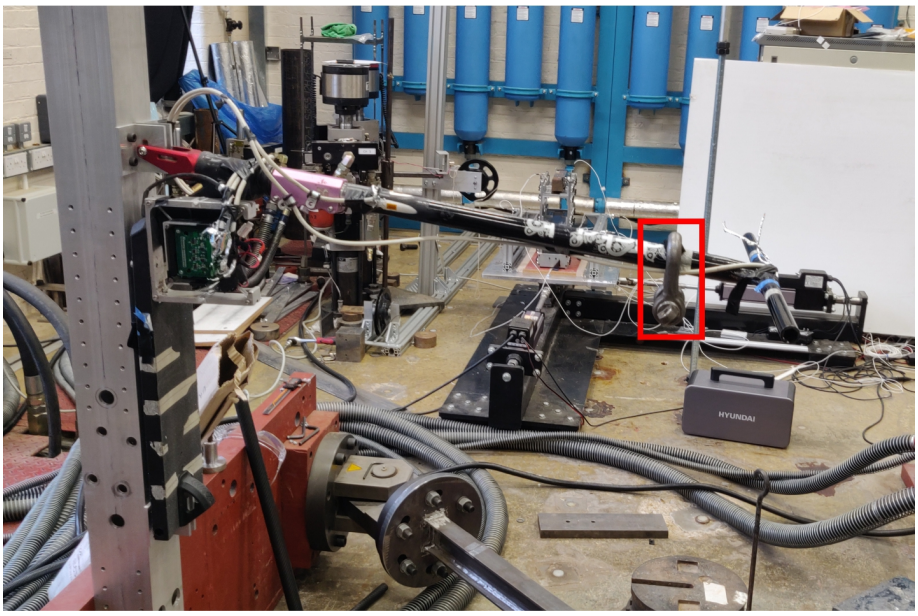


Figure 5.20: The static calibration setup for the handlebars. Weights were hung from the shackle (boxed in red).

to a new zero value), and also by minimizing the effects of any drift. Minimizing drift was done by taking the difference in the strain reading from the first and last part of the data, and assuming that the drift was linear in time. Figure 5.21 shows the difference in drift over the course of approximately 12 minutes when the scooter is idle. Without the drift correction, the maximum variation is just over 3×10^{-5}, however with the linear correction it peaked at approximately $10 - 15$ % of that value. An overview in the steps of processing voltage data into strain data can be seen in figure 5.22.

Once the data was suitably processed, it was possible to obtain calibration results. By averaging the values of the strain against time when a known loading was applied (the flat portions in figure 5.23a), a plot of strain against force can be produced (see figure 5.23b). The gradients of strain against force could then be used to calculate the strain per Newton, giving values of a normalised (1 N) basis load.

As the loads from the rider are applied at the crossbar, a measurement comparing the ratio of the strain/force gradient at the down tube and the crossbar was calculated (figure 5.24). This could be done for the case when the crossbar was horizontal and results could be extrapolated from this for cases when the angle of the crossbar was non-zero. The ratio of strain when the loads were applied

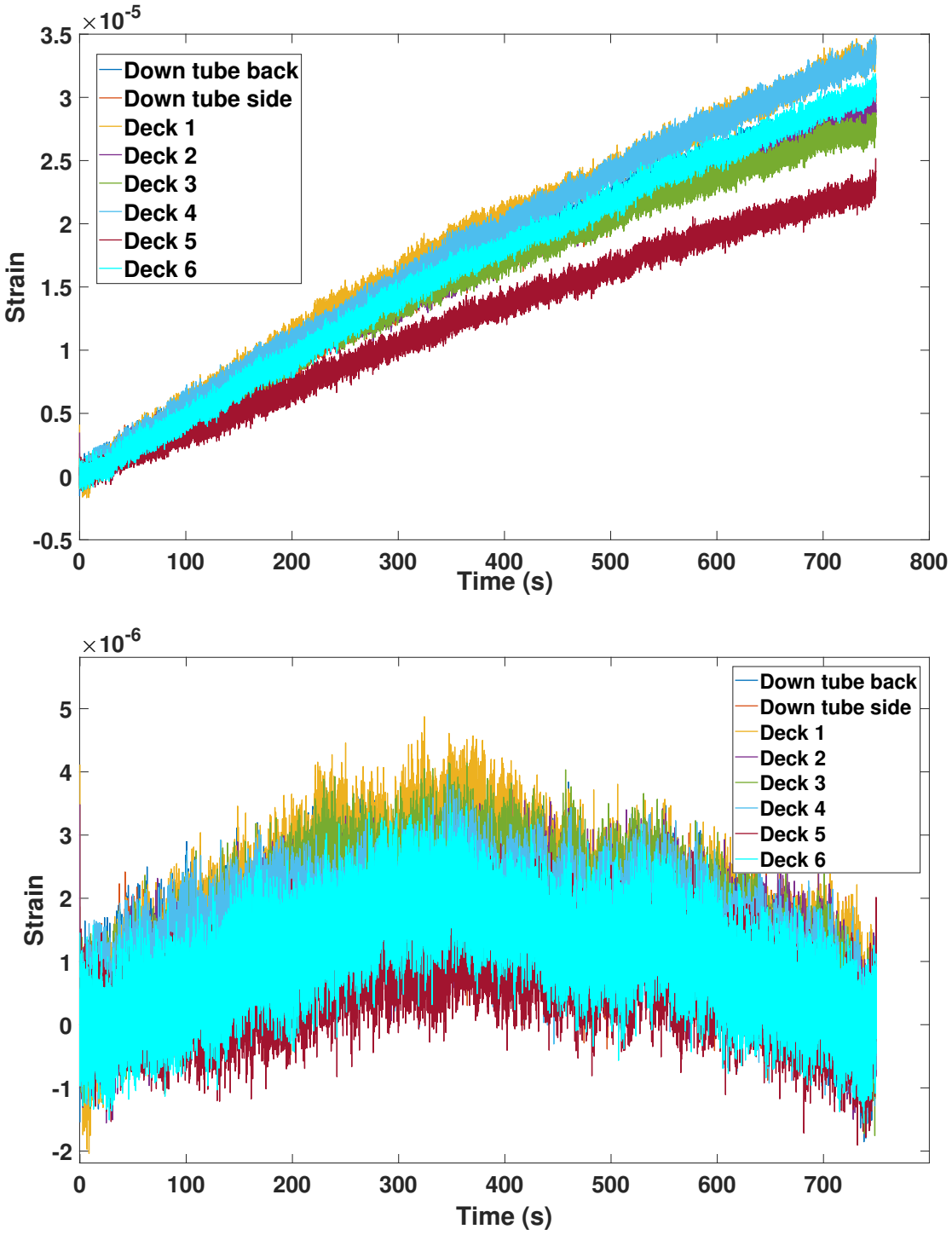


Figure 5.21: A comparison of the drift in strain gauges mounted to the scooter whilst it is idle with/without a gradient correction. The gradient correction lowers the drift by approximately a factor of 10. It appears that the effect of drift is worse when the scooter is idle (possibly due to less ventilation). Also no data collection is anywhere near as long as this test, so the effect of drift should be significantly less.

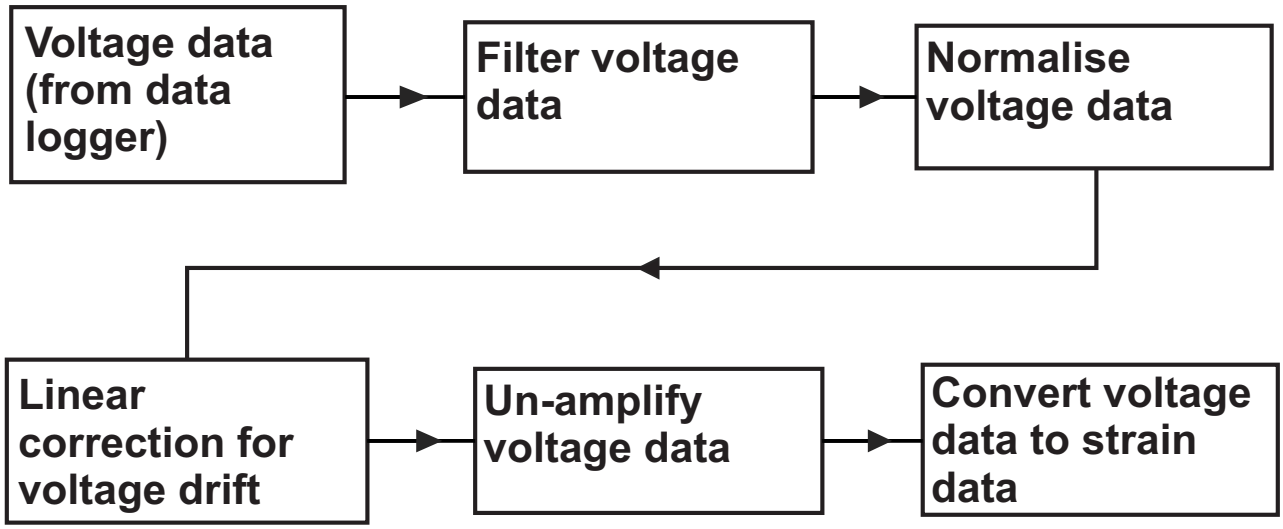
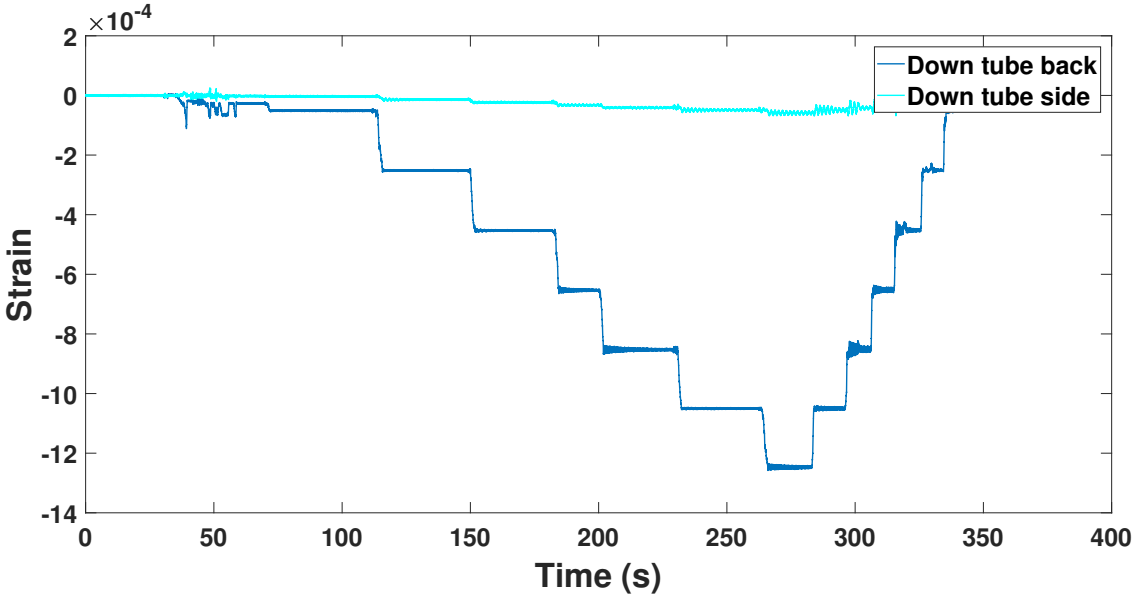
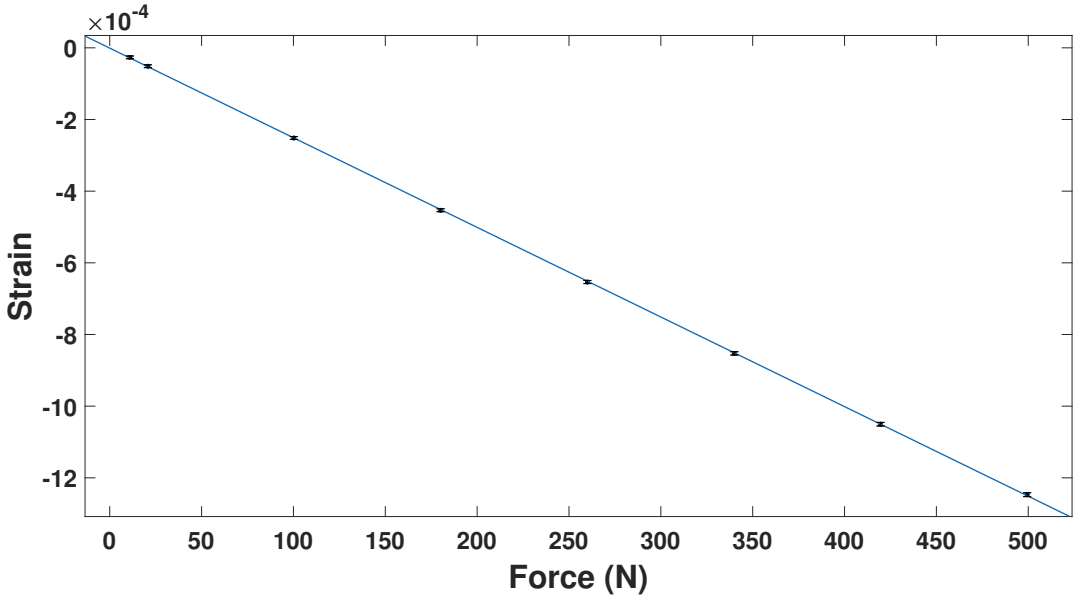


Figure 5.22: An overview of the stages used to process raw voltage data into strain data.

on the down tube compared to the cross bar was measured to be 1.31:1, which was within 1 % of the result predicted by Euler-Bernoulli beam theory.



(a) A plot of strain against time for the strain measurement points in the down tube. When a known weight is applied, the strain value is taken from the average after the value has settled down (the horizontal lines). This goes to form the plot below of strain against force.



(b) A plot of strain against force for the strain gauge in the down tube when the crossbar is perpendicular to the direction of the footplate (along the x_2 direction). The gradient of this plot allows one to calculate the strain per unit force at the applied angle. Similar plots were obtained for every entry in the $[\varepsilon_t]$ matrix from $\boldsymbol{f_1}$.

Figure 5.23

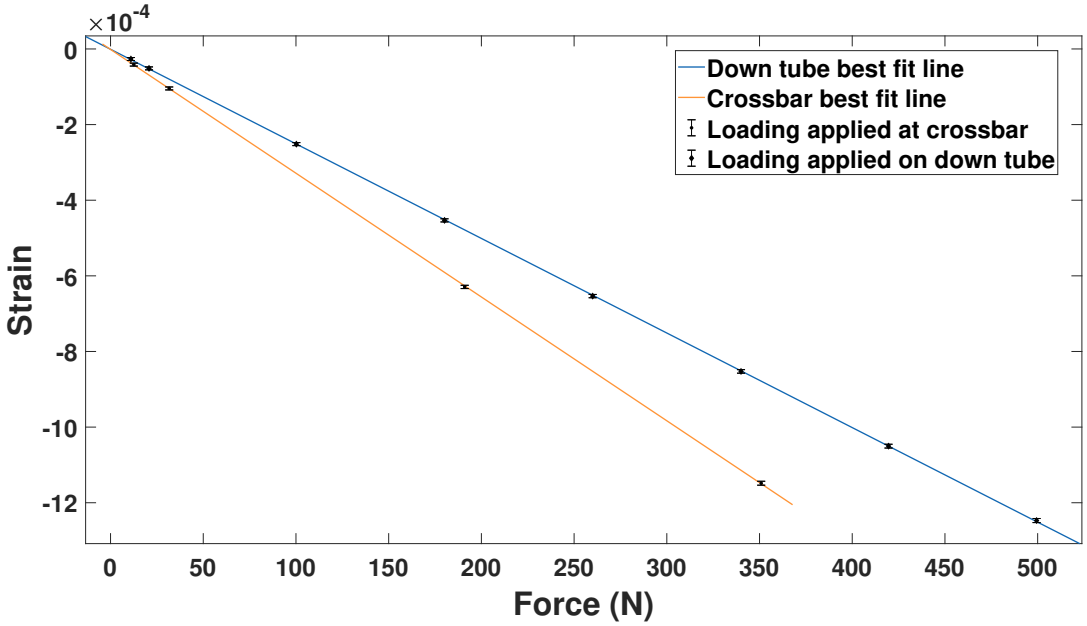


Figure 5.24: The figure shows the relationship between strain in the down tube when a load is applied at the boxed location in figure 5.20 and if the loading is applied at the crossbar. In practice, loading will be applied by the rider at the crossbar. It was, however, not safe to apply loads on the crossbar when the handlebars were rotated (see below), as the masses could slide off the handlebars. As expected, the strains are larger at the crossbar for a given load as it is further from the down tube strain gauges.

Accounting for angular discrepancies

Because riders do not always land with their handlebars completely perpendicular to the direction of motion when landing stunts, a model was made to try and accomodate this. This effect is most poigniant for stunts that involve rotation of the rider (e.g. 360s), or spinning the handlebars (barspins). The direction of the force of interest can be seen in figure 5.25. Note that this load in question is the load that is transmitted through the down tube to the rest of the scooter. The handlebars are free to turn and provide only a negligible resistance to turning forces. If the forces from the left and right hand in the direction of $\boldsymbol{F_{in}}$ ($\boldsymbol{f_1}$ in the force reconstruction model used) are different, the handlebars will simply rotate. The only component of the load supplied by the hands that causes bending in the down tube (the load in the direction of $\boldsymbol{F_{in}}$) are the symmetrical loads in this direction, i.e. the load $\boldsymbol{f_1}$. Note in the model that the magnitude of $\boldsymbol{f_1}$ is the the total load applied by the hands, so each hand applies half of this.

If $\boldsymbol{F_{in}}$ is the load of interest, and the angle of the crossbar can change, it is necessary to have a way of calculating the angle between the crossbar and the footplate. To do this, strain measurements were taken from one strain gauge on the front of the handlebars, and one strain gauge on the right side of the handle bars (directly below the crossbar). Calibration measurements were then taken with weights hanging from the down tube for various angles of crossbar rotation. Fitting the strain/force as a function of crossbar angle yielded an equation relating the strain on the down tube as a function of loading and angle as $\varepsilon_n = A_n\ F_{in}\ sin(\theta\ +\ \phi_n)$. From the calibration A_n and ϕ_n are determined (dependent variables), whilst F_{in} and θ are measured (i.e. independent variable). As there are two unknowns, at least two strain gauge measurements on the down tube are needed to determine this. Results can be seen in figures 5.26a and 5.26b. As expected, a sinusoidal function is suitable for the measurements made. If we implemented this variation with angle, the first two elements of the $[\varepsilon_t]$ matrix would be:

$$\begin{pmatrix} 3.27 \times \sin(\theta - 91.2^\circ) \\ 3.21 \times \sin(\theta - 0.2^\circ) \end{pmatrix} \times\ 10^{-6}$$

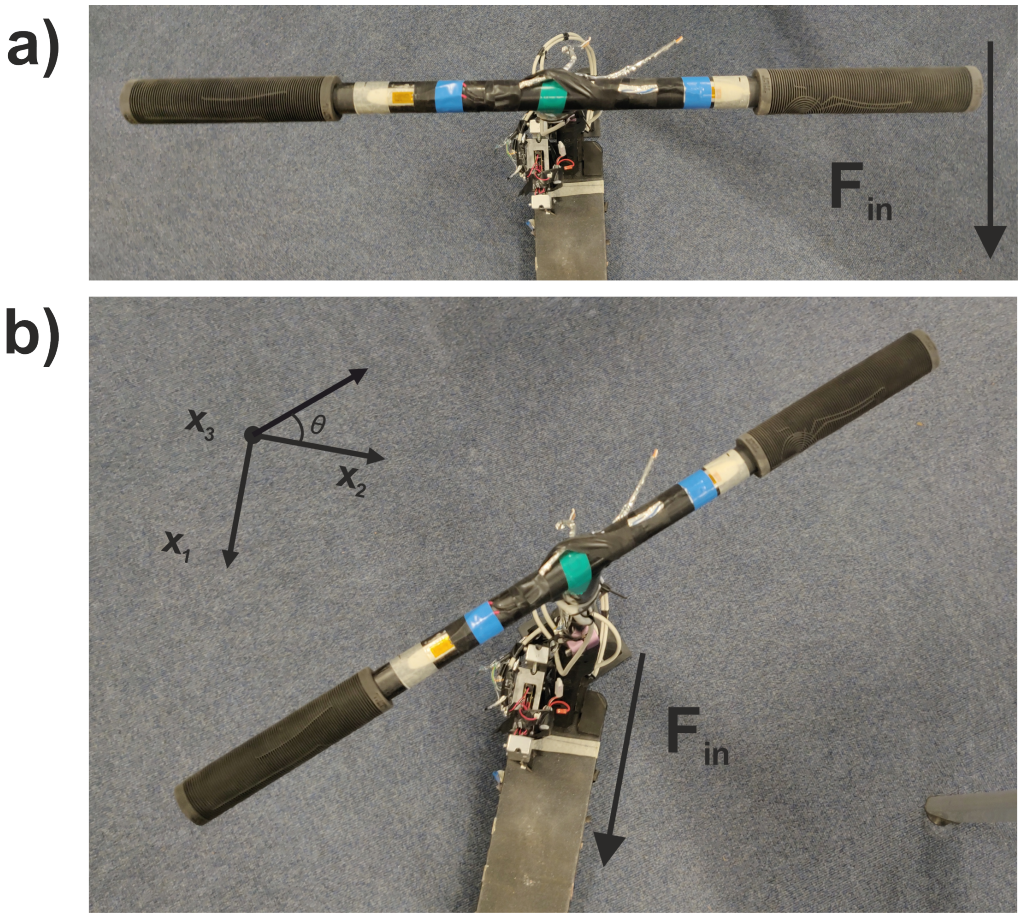
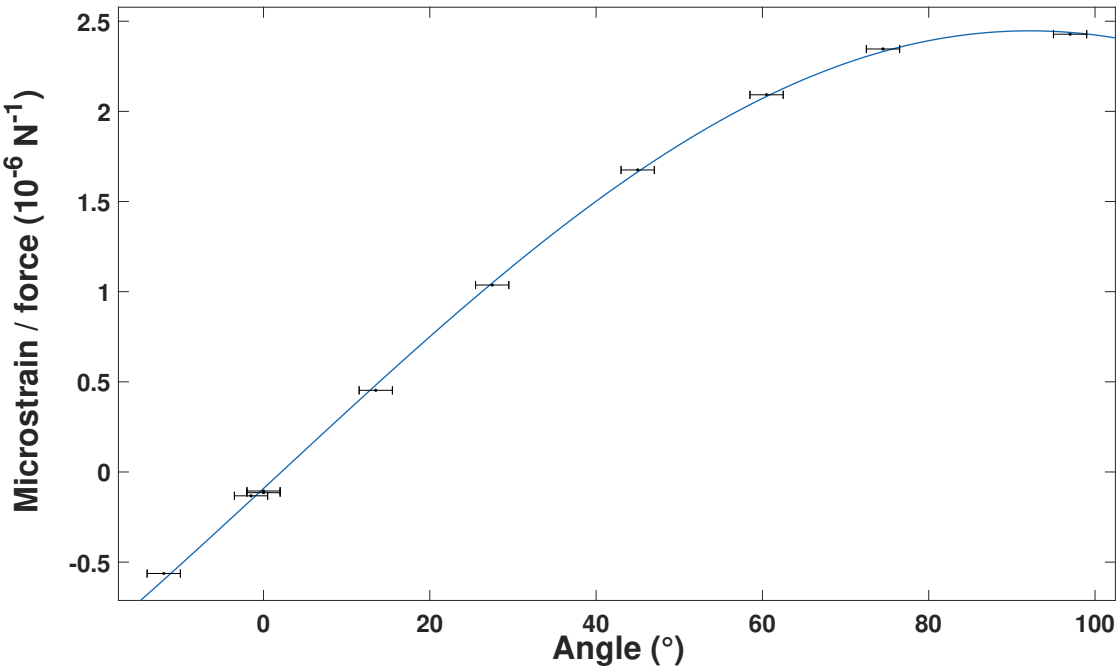


Figure 5.25: A diagram highlighting the fact that the loading on the handlebars that significantly impacts the maximum stress in the down tube, and that contributes to the stresses in the deck is the loading that is in the direction along the length of the footplate (labelled $\boldsymbol{F_{in}}$). Because the angle of the crossbar can change, it is not adequate to use strain data from the front or the back of the down tube. Strain gauges at some other angle must also be used. Then one can determine the angle of the crossbar by looking at the relative values of strain at different points on the down tube.

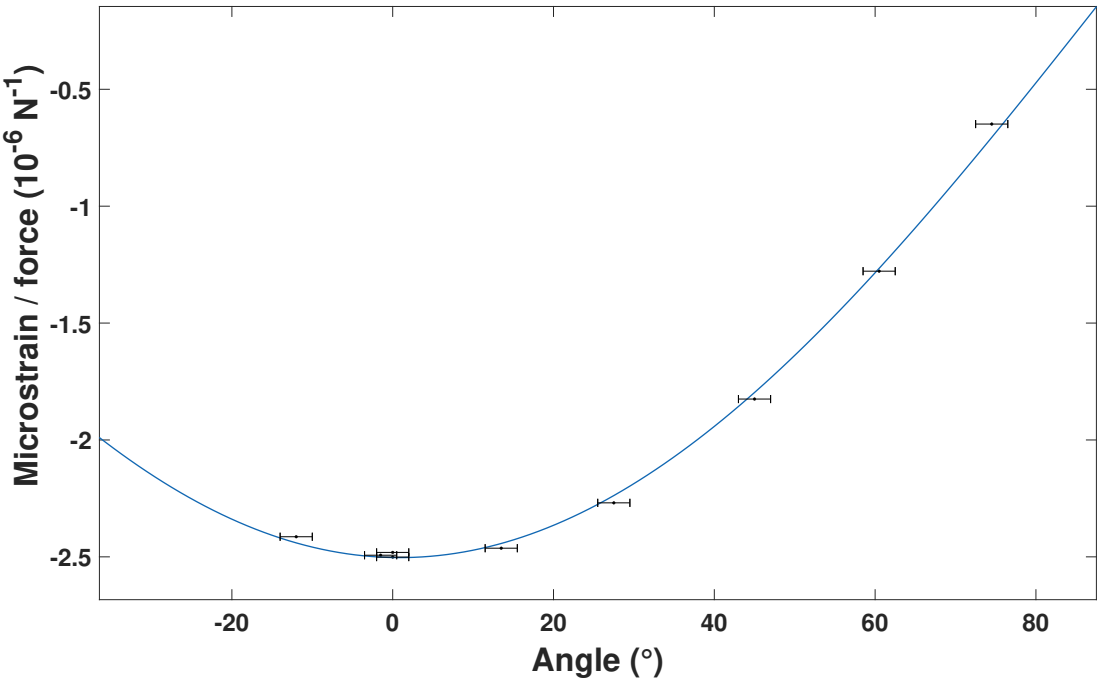
(i.e. the strain from $\boldsymbol{f_1}$ and the first two strain measurement locations at the back and side of the down tube).

This model was not implemented in the final to the force reconstruction approach. The strain gauges on the side of the down tube (but not on the front/back) are sensitive to loading in the x_3 direction from the hands, which makes this calculation impossible without knowing the contribution of strain from the loading in the x_3 direction. Instead, the crossbar was assumed to always be perpendicular to the deck, which is a reasonable approximation in most cases. $\cos(8^\circ)$ gives an error of less than 1 %, $\cos(18^\circ)$ gives an error of less than 5 %, and $\cos(25^\circ)$ gives an error of less than 10 %. (stunts performed were recorded on video for additional analysis) Thus far, the first element of the $[\boldsymbol{\varepsilon}_t]$ matrix has been calculated, the strain from $\boldsymbol{f_1}$ and the first strain measurement location (at the back of the down tube):

$$\Big(-3.27\Big) \times 10^{-6}$$



(a)



(b)

Figure 5.26: Plots of how the force/strain gradient varies (on the down tube) with angle for a strain gauge on the side (5.26a) and back (5.26b) of the down tube. This allows for the calculation of the angle of the crossbar with respect to the footplate.

The strains in the deck (from f_1)

The strains in the deck were straightforward to calculate. Data from the strain for the loading when applied to the crossbar was used to calculate the gradient of strain against force, which was then fed into the $[\varepsilon_t]$ matrix. A plot of the various gradients can be seen in figure 5.27. Combined with the strain response from the down tube, this results in the first column of this matrix (i.e. the strains that result from 1 N applied at $\boldsymbol{f_1}$):

$$\begin{pmatrix} -3.27 \\ 1.23 \\ 1.02 \\ 0.84 \\ 0.70 \\ 0.52 \\ 0.38 \end{pmatrix} \times 10^{-6}$$

A comparison of the simulated and experimental strain per unit force for $\boldsymbol{f_1}$ can be seen in figures 5.28 and 5.29. The results match very well.

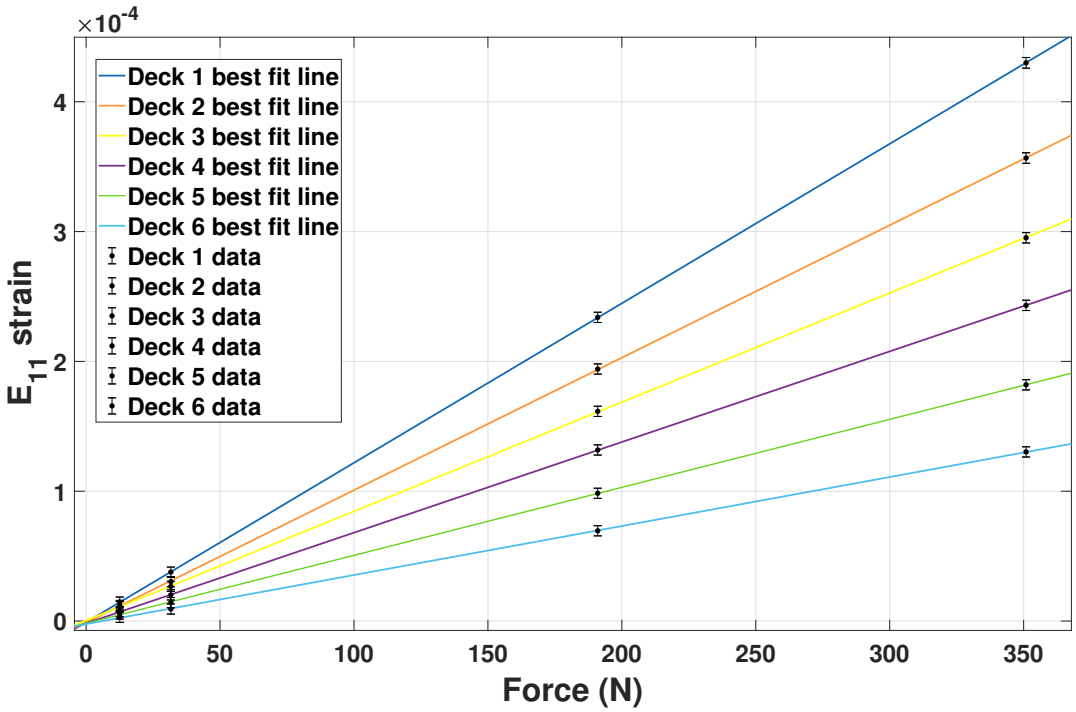


Figure 5.27: A graph showing the strain gradient for the strain gauges in the deck as a function of the force applied to them. Unsurprisingly, the strain gauges further away from the handlebars have a lower internal moment, and therefore less strain.

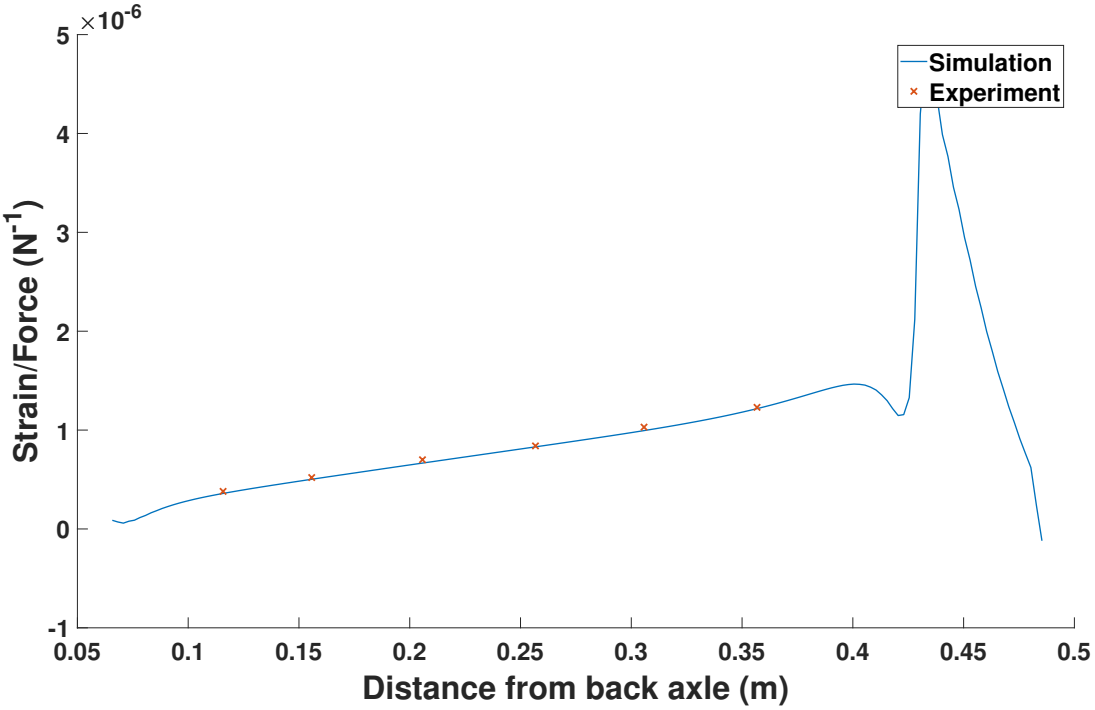


Figure 5.28: A comparison of the simulated and measured E_{11} strain response on the underside of the scooter deck when the load $\boldsymbol{f_1}$ is applied. The simulation used a 1 kN load then normalised it (to get the strain per unit force), and had a 5 mm mesh.

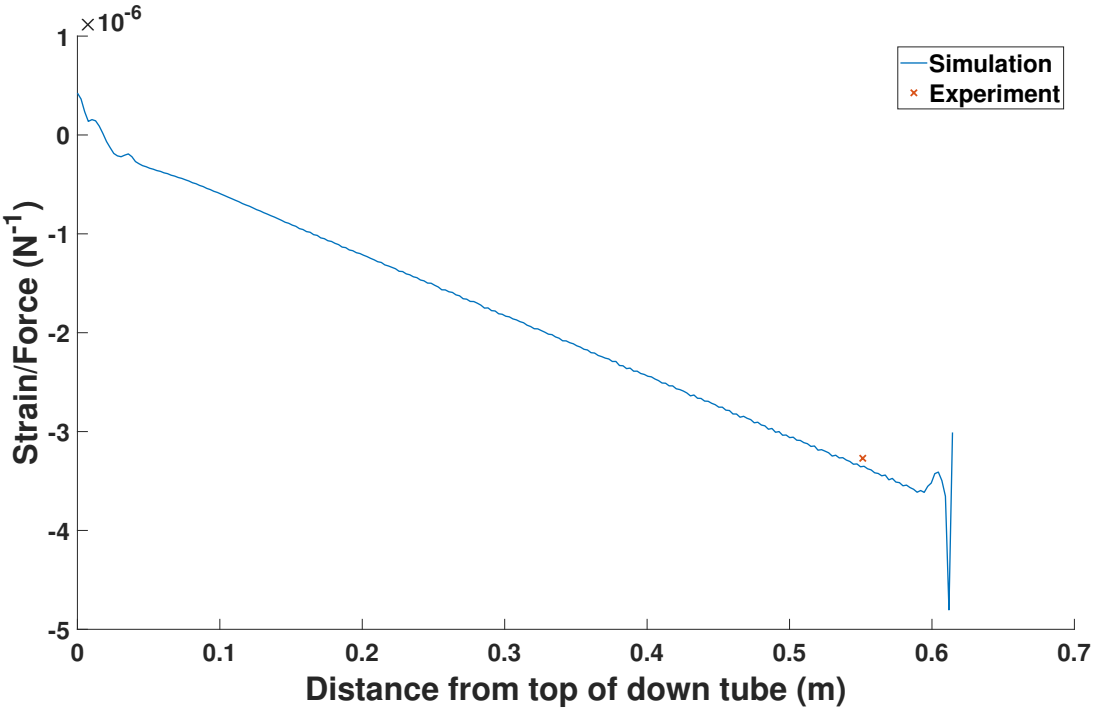


Figure 5.29: A comparison of the measured strain and simulated E_{33} strain response on the back side of the down tube when the load $\boldsymbol{f_1}$ is applied. The simulation used a 1 kN load then normalised it (to get the strain per unit force), and uses a $\boldsymbol{f_1}$, 5 mm mesh.

5.6.2 Static calibration of deck loads

The static calibration of the deck was performed by applying loading of known magnitude to the scooter on an Instron 5582 Universal Testing Machine. A figure of the whole setup can be seen in figure 5.30. As can be seen, the scooter was mounted on an aluminium beam. A diagram showing the dimensions of the beam is given in figure 5.31. Threaded holes in the beam with 35 mm intervals Each pair of M8 threaded holes allows for the central location of the loading to be applied to the scooter at 35 mm intervals. The load cell used had a range of $-5\ kN - +5$ kN. A ball and socket joint was used to help obtain a more even pressure distribution on the area of the applied. Pieces of wood were used to transfer loading from the Instron to the scooter deck. The pieces of wood had a shape moulded to match the concave of the deck, (see figure 5.32). Layers of rubber were also underneath the wooden mould them to help make the pressure distribution more even. Fujifilm Prescale [124] was used to gauge the stress distribution within the material. Figure 5.33 shows how having rubber on the underside of the moulds led to a more even stress distribution.



Figure 5.30: The Instron applying a load to the scooter.

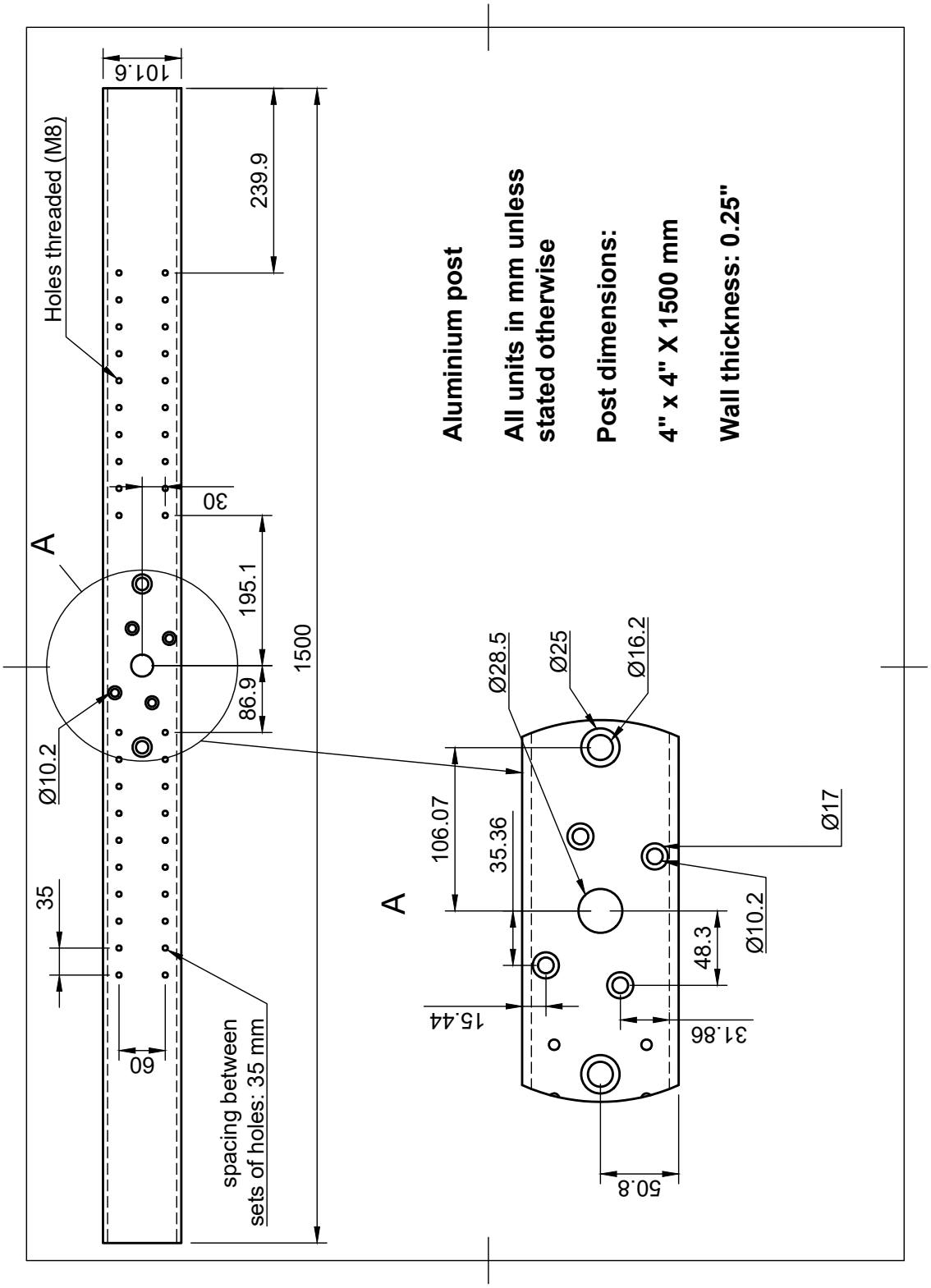


Figure 5.31: The beam on which the scooter rests has threaded holes at specific locations so the location of the applied load known is known precisely.

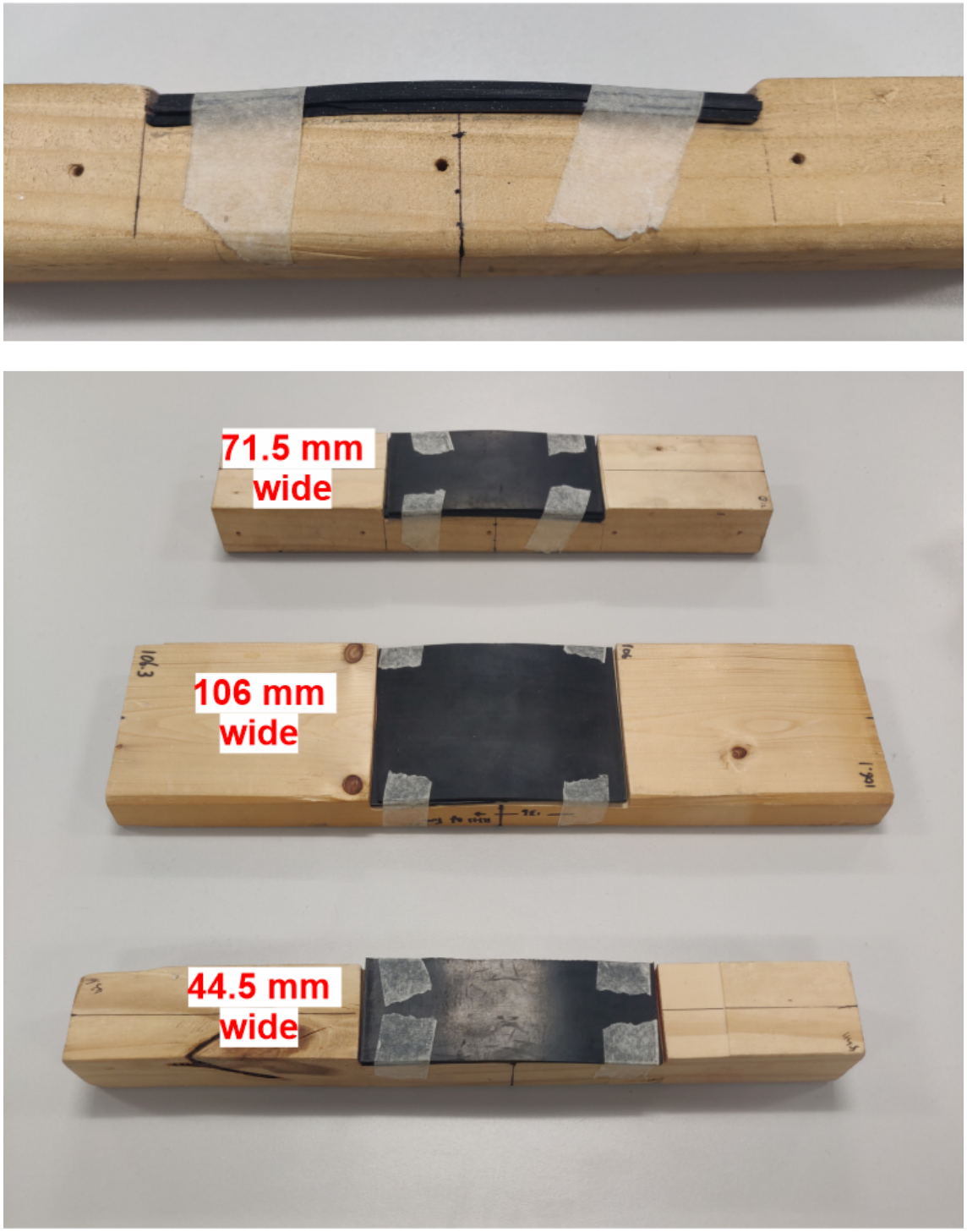


Figure 5.32: Pieces of wood that were used to calibrate the loads on the scooter and for mismatch cases (see sections 5.5 and 5.6.4). Rubber is taped to the bottom to ensure a more even pressure distribution is obtained when the load is applied. When riding a scooter, the rider's feet mould to the concave of the footplate.

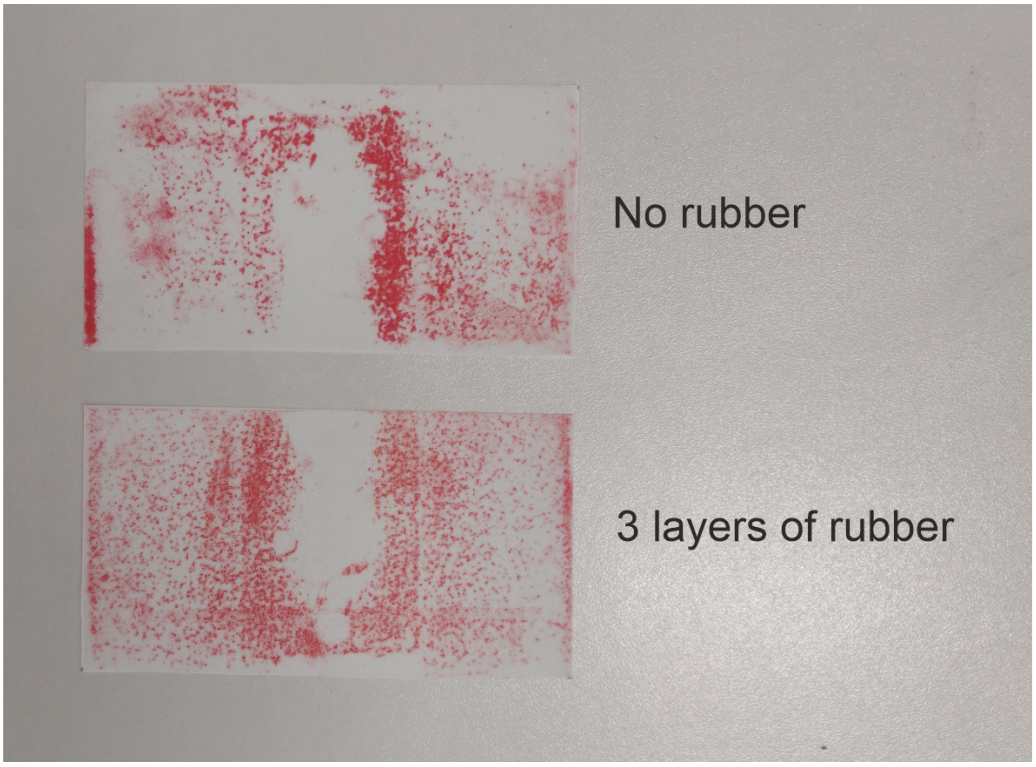


Figure 5.33: A comparison of the pressure distribution with and without some rubber sheet between the wood and surface of the scooter deck. Prescale is a flim that changes colour based on the amount of pressure it is subject to. The more pressure it is subject to, the darker the colour gets. In this case, Prescale LLLW was used which shows colour in the pressure range $0.2 - 0.6$ MPa. The darker the colour, the higher the pressure. If the sheet is still white, not enough pressure has been applied to change its colour. The above picture clearly shows how the pressure distribution with the rubber sheet in between is significantly more even than without.

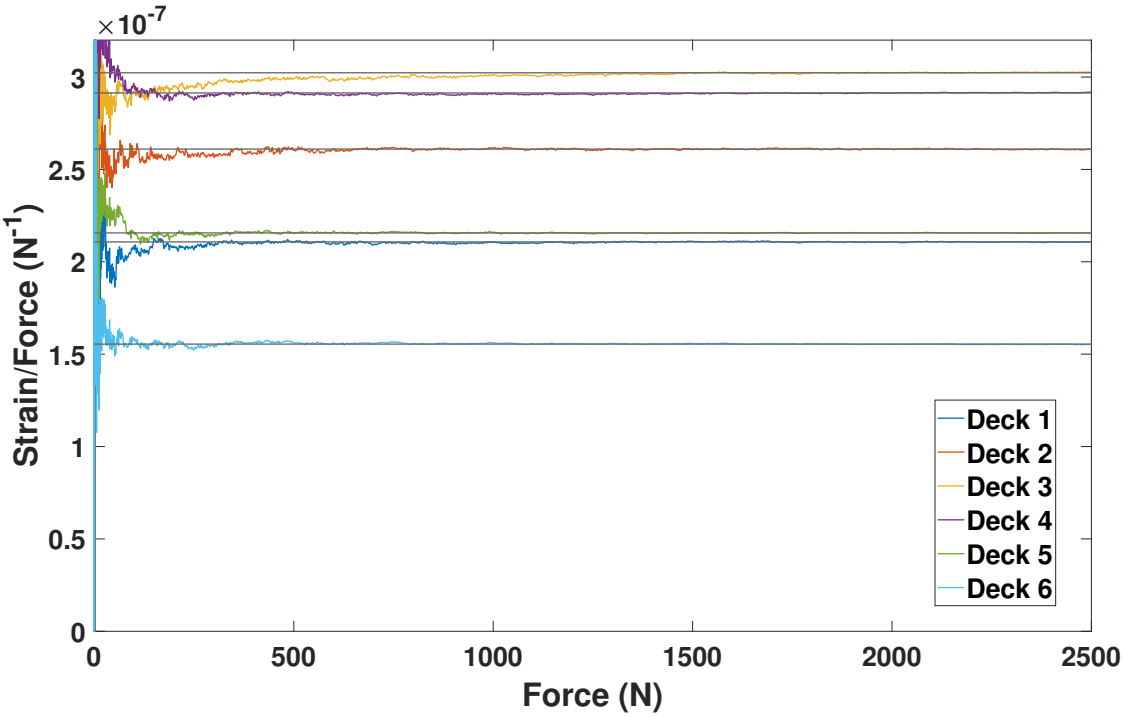


Figure 5.34: A plot of the strain/force gradient against force on the instron for the basis load $\boldsymbol{f_4}$. Deck strain gauge 3, which lies directly beneath $\boldsymbol{f_4}$ takes the longest to flatten out.

An example strain divided by force against force plot for a basis load can be seen in figure 5.34. Initially, the plots are non-linear. This is thought to arise because the contact between the wood and the deck is not perfect and changes as the load increases. As the applied load becomes more uniform and steady, the plot flattens. This effect is most noticeable for the strain gauges closest to the applied load (they will generally be more sensitive to slight changes in load distribution). Because of this initial non-linearity, the average value of the strain/force gradient in the range 1500 N $-$ 2500 N was used. For each basis load, five repeats were performed (meaning five plots were generated per basis load, each with 6 average strain per unit force gradients). The repeats were then averaged, to reduce any errors associated with proper alignment in the calibration experiments. The difference across repeats was generally very small (all standard deviations were under 1 %, and were largest for $\boldsymbol{f_6}$, see figure 5.35). This is expected as $\boldsymbol{f_6}$ is closest to the edge of the deck and therefore the strain distribution it gives is more sensitive to position (according to Euler-Bernoulli beam theory the rate of change of maximum moment with load position is greatest at the ends of the beam).

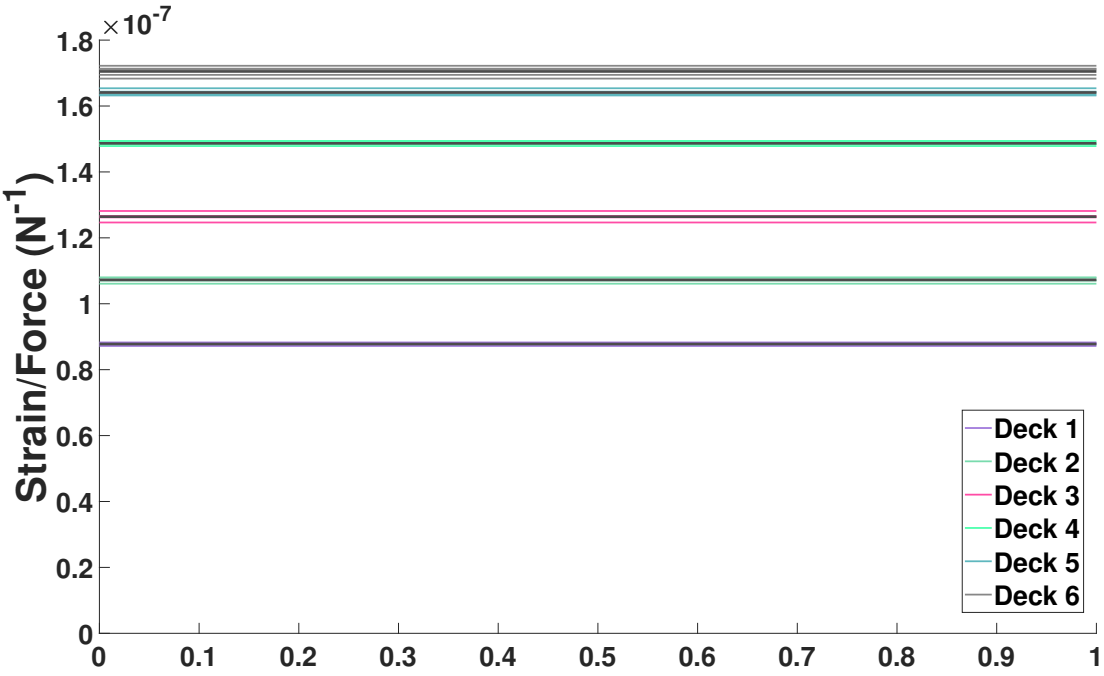


Figure 5.35: A representation of the variation of mean gradients for the various strain gauges when $\boldsymbol{f_6}$ is applied. $\boldsymbol{f_6}$ has the greatest variation of the deck basis loads, but the standard deviations are still all less than $1\ \%$.

The values of the strains from the deck are given, to complete the static $[\boldsymbol{\varepsilon}_t]$ matrix below:

$$[\boldsymbol{\varepsilon}_t] = \begin{pmatrix} -32.73 & 0.00 & 0.00 & 0.00 & 0.00 & 0.00 \\ 12.28 & 2.80 & 2.75 & 2.11 & 1.50 & 0.88 \\ 10.21 & 2.48 & 3.15 & 2.62 & 1.85 & 1.07 \\ 8.41 & 2.07 & 2.80 & 3.02 & 2.16 & 1.26 \\ 6.98 & 1.71 & 2.30 & 2.92 & 2.57 & 1.49 \\ 5.24 & 1.27 & 1.71 & 2.15 & 2.54 & 1.64 \\ 3.77 & 0.91 & 1.23 & 1.55 & 1.89 & 1.70 \end{pmatrix} \times 10^{-7}$$

In the matrix above, the column number corresponds to the basis load number (column 1 is $\boldsymbol{f_1}$), and the row number corresponds to the strain gauge location (row 1 is the location of the down tube (DT) back strain gauge, row 2 is deck strain gauge 1, row 3 is deck strain gauge 2 etc.).

Below is the matrix of the standard deviations (averaged over five repeats) for the strain in the deck strain gauges resulting from the deck loads (i.e the columns represent $\boldsymbol{f_2} - \boldsymbol{f_6}$, and the rows deck strain gauges 1 - 6):

$$\begin{pmatrix} 0.31\% & 0.39\% & 0.30\% & 0.42\% & 0.45\% \\ 0.31\% & 0.16\% & 0.40\% & 0.27\% & 0.72\% \\ 0.37\% & 0.59\% & 0.27\% & 0.83\% & 0.98\% \\ 0.26\% & 0.33\% & 0.23\% & 0.34\% & 0.43\% \\ 0.34\% & 0.32\% & 0.13\% & 0.45\% & 0.52\% \\ 0.39\% & 0.37\% & 0.29\% & 0.10\% & 0.92\% \end{pmatrix}$$

Even the largest standard deviation was less than 1 %. A comparison of the strain distribution given by the experimental data, and an FE simulation of the scooter are shown in figure 5.36. It is interesting to note the closeness of fit between the measured strain from calibration and FE results. It shows that in principle, the static FE model could have been used for the force reconstruction.

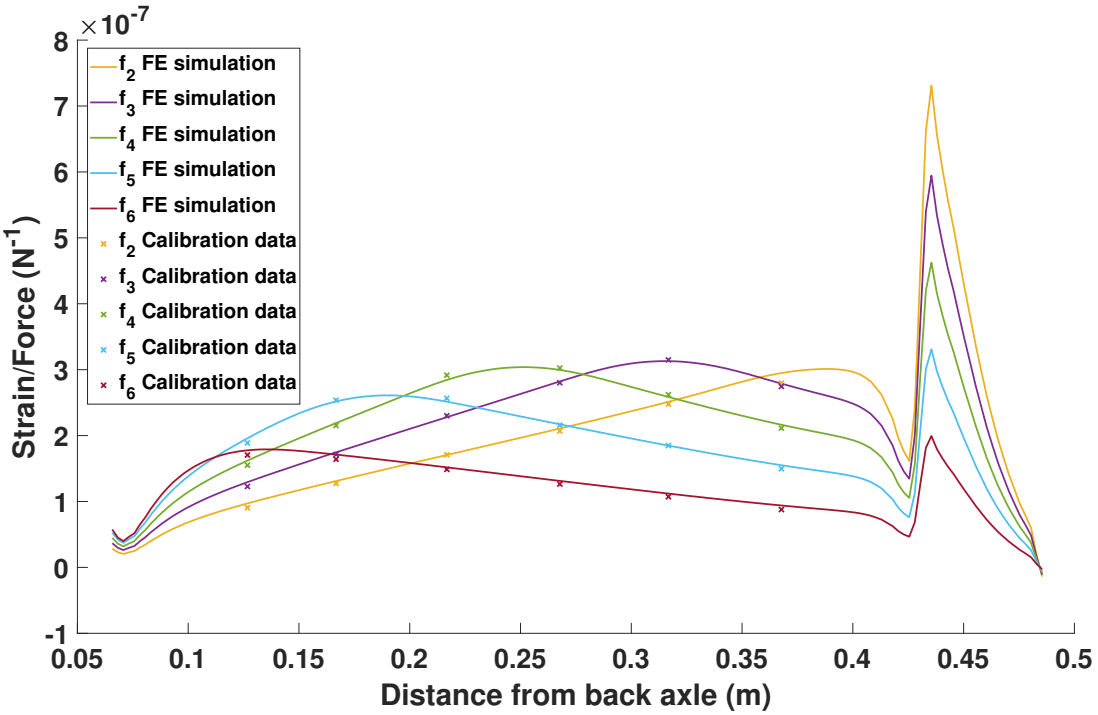


Figure 5.36: A comparison of the E_{11} strain per newton given by experiment, and by FE simulation. For the FE simulation a load of 2000 N was used, for the experimental data averages were taken from the $[\varepsilon_t]$ matrix.

5.6.3 Constraints and other conditions

The above strain ($[\varepsilon_t]$) matrix has now been created, so forces can be calculated from measured strain values. If the basis loads were a perfect representation of the loads the scooter is subject to, and if there was no experimental noise, one could simply solve equation 5.2. Also, if there are only as many strain measurement points as there are basis loads and the problem is not further constrained, an exact solution for any value of strains can be given. In the presence of any noise, the values of the basis loads will be unrealistic in such cases (generally by having loads of huge magnitude and opposing sign for $\boldsymbol{f_2}$ - $\boldsymbol{f_6}$). Constraints were applied to system to avoid this problem.

The constraints in the model included a range of $-2\ kN - +2$ kN for the possible values of $\boldsymbol{f_1}$ (the bar basis load), and possible values for the load in any of the deck basis functions in the range $0\ kN - 5$ kN. The handlebar value was chosen because such a load would give rise to strains far beyond the strains in the down tube recorded in any data (remember that deck loads do not cause strains in the down tube strain gauge in this model). The constraints on the deck were given because

the feet can only press down on the scooter deck. If an upwards load was resultant on ones feet, they would simply come off the scooter deck. the value of 5 kN was chosen because it was again above the expected strain values in the scooter and would exceed the recorded strain magnitude if applied to the scooter. Analysis of results showed that the maximum loads did not come near to this value, indicating that the value is suitable as an upper bound. Before filtering (for the static calibration of the deck), the 10 kHz data was downsampled to 100 Hz to decrease the amount of noise and make the data easier to handle. The filter settings used were a 12^{th} order zero-phase Butterworth filter with a cut-off frequency of 5 Hz. Note that for the dynamic calibration and all of the data collection, the filtering was at a much higher frequency, but in the static case the loading conditions were known, and the filtering helped achieve a cleaner signal.

5.6.4 Mismatch load cases and reduced reconstructions

To test the robustness of the static force reconstruction model, known loads were applied to the system that did not match the assumed possible basis loads (called mismatch cases), and the reconstruction of the data was compared to the load input to see how well the model accounted for mismatch. The calculated total force, the load distribution and the reconstructed strain output were all examined. The load distributions for various load cases can be seen in figures 5.37 - 5.39. A total of seven mismatch cases were examined. The strain per unit force was calculated in the same way it was for the basis loads. Each mismatch case was repeated at least twice (some were repeated three times), and in every case the standard deviation of the force per unit strain was less than 1 %. The types of mismatch case are described in more detail below.

location: f_4, load length: 106 mm and 44.5 mm

This mismatch case was expected to be the easiest to replicate, as the loading is almost in the same location as the applied loading. The only change was the length of the applied load. As can be seen in table 5.1 the error in the calculated force magnitude was 0.5 % or less. The error in the strain magnitude can be seen in table 5.2.

location: $f_{2.5}$, load length: 71.5 mm 106 mm and 44.5 mm

This mismatch case was expected to be more difficult for the force reconstruction system to replicate accurately. In this case, the applied load was halfway between the basis loads $\boldsymbol{f_2}$ and $\boldsymbol{f_3}$. Force reconstruction was expected to be the least accurate when the applied load was approximately halfway between applied basis loads. The reason for this was that the reconstructed area load, primarily consisting of the two basis loads surrounding the area of the applied load are much wider than the applied load. Because of this, in the region directly underneath the reconstructed load, the strain would be less for a similarly reconstructed load with the same magnitude. As expected, the reconstructed loads had a slightly higher magnitude than the applied load (4.6 % - 8.3 %). The error in measured strain response from these loads was less than 2 % in all cases.

location: $f_{5.5}$, load length: 71.5 mm and 106 mm

When a single load is applied to the deck, the scooter deck approximates a simply supported beam under assumptions dervied from Euler-Bernoulli beam theory. In this case, the rate of change of strain distribution in the deck with respect to the position of the applied load is greatest near the edges of the deck. Because of this, the mismatch case applied at $\boldsymbol{f_{5.5}}$ was expected to have the largest discrepancy. In this case, the largest error in calculated total load output was 15.8%. The maximum error in strain measurement was, however, only 3.27%. The reason for the larger error in calculated load output is because most of the reconstructed load is in $\boldsymbol{f_6}$, which has a substantially lower average strain per unit load (along the underside of the deck) than other basis loads. If one performs the reconstruction case applying the constraint where $\boldsymbol{f_6}$ and $\boldsymbol{f_5}$ have the same value, the error in force reconstruction magnitude is less than 4.5 $\%$.

Table 5.1: A table showing the magnitudes and components of the reconstructed force for various mismatch cases. The force is calculated from the force per unit strain, so the error in force magnitude is the value of the sum -1.

	Force reconstruction case						
Reconstructed load value	f_4 106 mm	f_4 45 mm	$f_{2.5}$ 72 mm	$f_{2.5}$ 106 mm	$f_{2.5}$ 45 mm	$f_{5.5}$ 70 mm	$f_{5.5}$ 100 mm
f_1	0	0	0	0	0	0	0
f_2	0.001	0	0.738	0.662	0.809	0	0
f_3	0	0	0.325	0.384	0.274	0	0
f_4	0.998	1.005	0	0	0	0	0
f_5	0.001	0	0	0	0	0.310	0.307
f_6	0	0	0	0	0	0.848	0.849
Sum	1.000	1.005	1.063	1.046	1.083	1.158	1.156

Table 5.2: percentage strain error for various mismatch cases

	Percentage difference between reconstructed value and actual value Force reconstruction case						
Deck strain gauge number	f_4 106 mm	f_4 45 mm	$f_{2.5}$ 71.5 mm	$f_{2.5}$ 106 mm	$f_{2.5}$ 45 mm	$f_{5.5}$ 71.5 mm	$f_{5.5}$ 100 mm
1	0.05%	-0.31%	-0.37%	-0.33%	-0.38%	-1.43%	-1.29%
2	-0.08%	-0.47%	1.66%	1.59%	1.42%	-0.20%	-0.64%
3	0.06%	1.51%	-0.58%	-0.72%	-0.60%	-0.99%	-1.29%
4	-0.04%	-0.75%	-0.89%	-1.04%	-0.93%	-1.33%	-1.19%
5	0.16%	-0.33%	-0.64%	-0.73%	-0.58%	2.99%	3.27%
6	-0.16%	-0.57%	-1.38%	-1.89%	-1.49%	-0.90%	-1.01%
Largest error (magnitude)	0.16%	1.51%	1.66%	1.89%	1.49%	2.99%	3.27%

Table 5.3: A table showing the magnitudes and components of the reconstructed force for various mismatch cases, with the additional constraint that two of the basis loads must have the same value. The force is calculated from the force per unit strain, so the error in force magnitude is the value of the sum -1.

	Force reconstruction case						
Reconstructed load value	f_4 106 mm	f_4 45 mm	$f_{2.5}$ 72 mm	$f_{2.5}$ 106 mm	$f_{2.5}$ 45 mm	$f_{5.5}$ 70 mm	$f_{5.5}$ 100 mm
f_1	0	0	0.0003	0.0002	0.0004	-0.0011	-0.0011
f_2	0.0001	0	0.5104	0.5088	0.5143	0	0
f_3	0.0003	0	0.5104	0.5088	0.5143	0	0
f_4	0.9987	1.0049	0	0	0	0	0
f_5	0.0003	0	0	0	0	0.5227	0.5214
f_6	0.0004	0	0	0	0	0.5227	0.5214
Sum	1.0001	1.0049	1.0211	1.0178	1.029	1.0443	1.0417

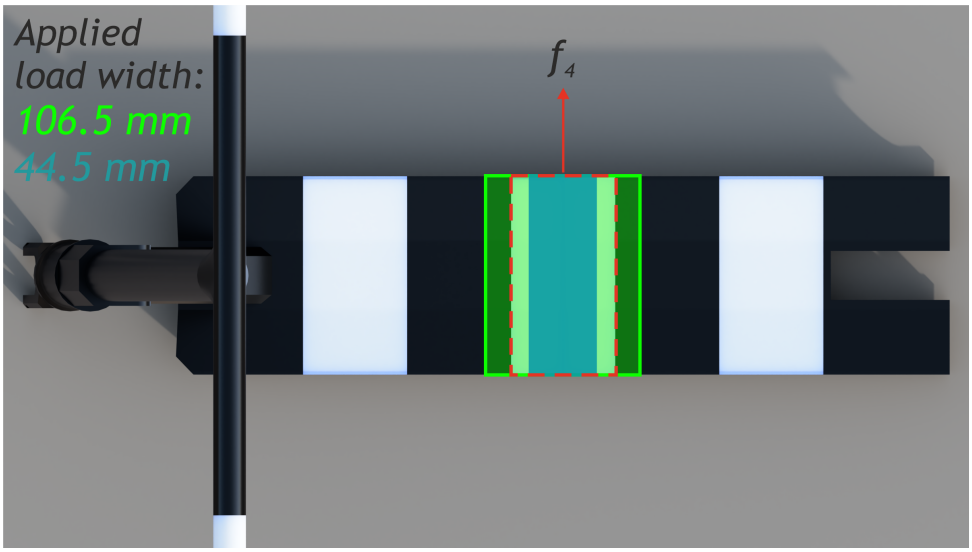


Figure 5.37: The load distribution for the first load mismatch case. The applied loading is centered on f_4, however the width of the applied basis loads is either wider (106.5 mm) or narrower (44.5 mm).

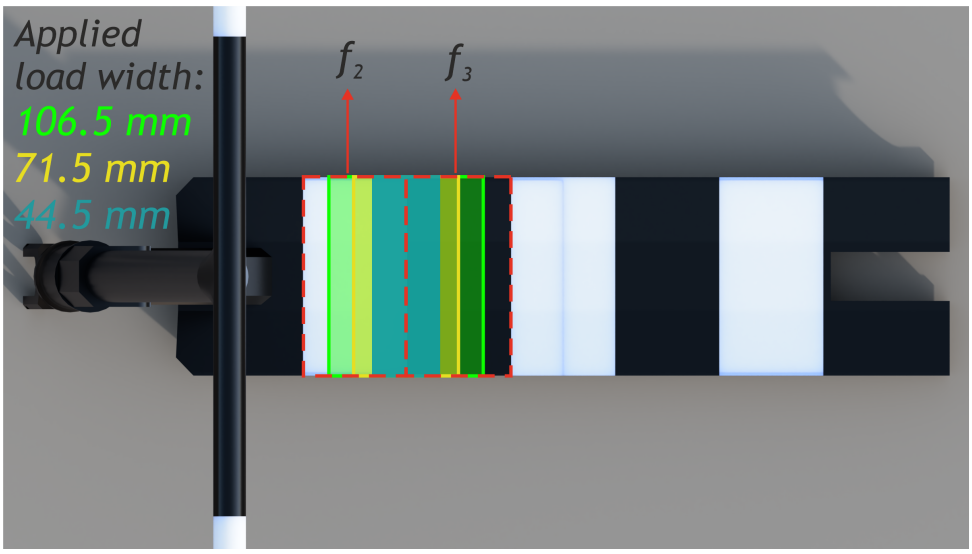


Figure 5.38: The load distribution for the second load mismatch case. The applied loading is centered halfway between $\boldsymbol{f_2}$ and $\boldsymbol{f_3}$. The width of the applied basis loads is 106.5 mm, 71.5 mm or 44.5 mm.

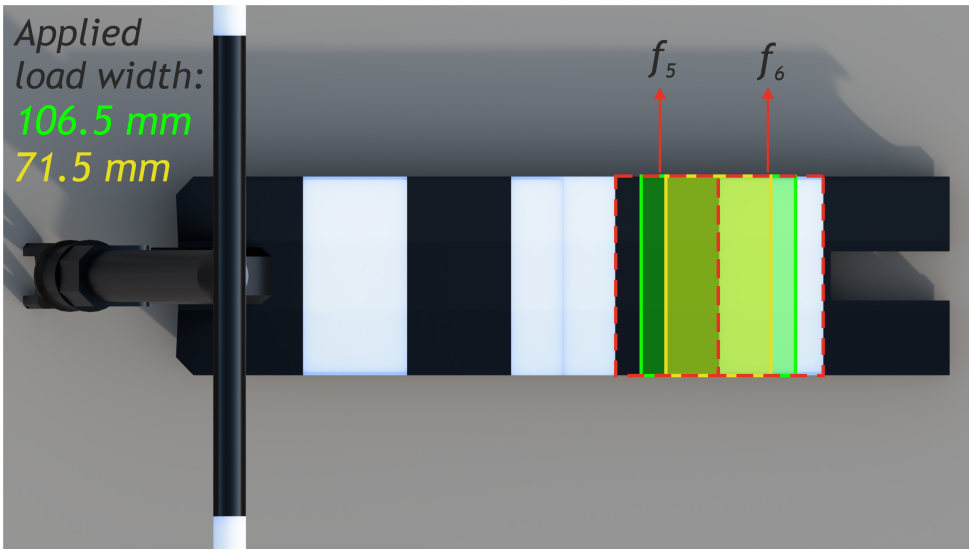


Figure 5.39: The load distribution for the second load mismatch case. The applied loading is centered halfway between $\boldsymbol{f_5}$ and $\boldsymbol{f_6}$. The width of the applied basis loads is either 106.5 mm or 71.5 mm.

Reduced reconstructions

The force reconstruction model used had six basis loads and seven strain measurement points. Because of this, it was possible to do reconstruction cases on a reduced model, where one of the strain measurement points was not used. Results from the reduced reconstruction could then be compared to the full model, to get an idea of how sensitive the force reconstruction approach is to the number of strain gauges applied. The tables below show the errors in the calculated force and strain outputs. when deck strain gauge 3 was removed, the maximum error in measured strain increased. An exception for this was for the loads applied at $\boldsymbol{f_{5.5}}$, as the maximum error in deck strain gauges 5 and 6 decreased. The error in maximum force changed by an insignificant amount. When deck strain gauge 6 was removed, the results were similar, except that the error in the calculated load and strain values in $\boldsymbol{f_6}$ and deck strain gauge 6 were significantly higher. The error in $\boldsymbol{f_6}$ reached highs of $37\ \%$. The reason for this huge increase in calcualted load was that almost all of the load was transferred to $\boldsymbol{f_6}$ (which gives a much lower average force per unit strain in the deck strain gauges). If the calculation was performed with the constraint that $\boldsymbol{f_5}$ and $\boldsymbol{f_6}$ were the same magnitude, the error in $\boldsymbol{f_6}$ was only 2 %!

Table 5.4: Showing the error in the force reconstruction when deck strain gauge 3 is removed.

Reconstructed load value	$\boldsymbol{f_4}$ 106 mm	$\boldsymbol{f_4}$ 45 mm	$\boldsymbol{f_{2.5}}$ 72 mm	$\boldsymbol{f_{2.5}}$ 106 mm	$\boldsymbol{f_{2.5}}$ 45 mm	$\boldsymbol{f_{5.5}}$ 72 mm	$\boldsymbol{f_{5.5}}$ 100 mm
$\boldsymbol{f_1}$	0	0	0	0	0	-0.0003	-0.0003
f_2	0.0016	0.0011	0.7219	0.6519	0.7949	0	0
f_3	0	0.0095	0.3397	0.3933	0.2862	0	0
f_4	0.9953	0.9808	0	0	0	0	0
f_5	0.0034	0.0096	0	0	0	0.3173	0.3161
f_6	0	0	0	0	0	0.8391	0.8383
Sum	1.0003	1.001	1.0616	1.0452	1.0811	1.1561	1.1541

Table 5.5: Showing the error in the strain reconstruction when deck strain gauge 3 is removed.

Deck strain gauge number	f_4 106 mm	f_4 45 mm	$f_{2.5}$ 72 mm	$f_{2.5}$ 106 mm	$f_{2.5}$ 45 mm	$f_{5.5}$ 72 mm	$f_{5.5}$ 100 mm
1	0.00%	0.02%	-0.27%	-0.26%	-0.22%	-1.68%	-1.62%
2	-0.04%	-0.01%	1.42%	1.45%	1.28%	-0.47%	-1.05%
3	0.13%	2.26%	-0.95%	-0.96%	-0.85%	-1.22%	-1.65%
4	-0.01%	0.01%	-1.24%	-1.24%	-1.18%	-1.62%	-1.53%
5	0.16%	0.09%	-1.05%	-0.93%	-0.78%	2.81%	3.05%
6	-0.23%	-0.19%	-1.76%	-2.08%	-1.68%	-0.85%	-0.96%
Largest error (magnitude)	0.23%	2.26%	1.76%	2.08%	1.68%	2.81%	3.05%

Table 5.6: Showing the error in the force reconstruction when deck strain gauge 6 is removed.

Reconstructed load value	f_4 106 mm	f_4 45 mm	$f_{2.5}$ 72 mm	$f_{2.5}$ 106 mm	$f_{2.5}$ 45 mm	$f_{5.5}$ 72 mm	$f_{5.5}$ 100 mm
f_1	0	-0.0001	0	0	0	0	-0.0001
f_2	0.0006	0	0.7296	0.6589	0.8018	0	0
f_3	0	0	0.3322	0.3865	0.2795	0	0
f_4	0.9966	1.0053	0	0	0	0	0
f_5	0	0	0	0	0	0	0
f_6	0.0055	0	0	0	0	1.3664	1.363
Sum	1.0027	1.0052	1.0618	1.0454	1.0813	1.3664	1.3629

Table 5.7: Showing the error in the strain reconstruction when deck strain gauge 6 is removed.

Deck strain gauge number	f_4 106 mm	f_4 45 mm	$f_{2.5}$ 72 mm	$f_{2.5}$ 106 mm	$f_{2.5}$ 45 mm	$f_{5.5}$ 72 mm	$f_{5.5}$ 100 mm
1	0.05%	-0.36%	-0.30%	-0.30%	-0.25%	-0.92%	-0.78%
2	-0.08%	-0.50%	1.56%	1.59%	1.42%	0.88%	0.38%
3	0.06%	1.45%	-0.75%	-0.76%	-0.65%	-0.12%	-0.47%
4	-0.04%	-0.78%	-1.04%	-1.09%	-0.98%	-0.25%	-0.10%
5	0.02%	-0.38%	-0.84%	-0.79%	-0.58%	0.13%	0.42%
6	-0.49%	-0.64%	-1.57%	-1.89%	-1.49%	-15.69%	-15.69%
Largest error (magnitude)	0.49%	1.45%	1.57%	1.89%	1.49%	15.69%	15.69%

5.7 Conclusion

In this chapter, the static force reconstruction model has been laid out. The theory behind the model has been explained. The theory has been applied through experimental calibration and subsequently tested against experimental mismatch cases. In mismatch cases, loads different from those assumed in the model are applied to the scooter. Results show how closely the reconstructed force resembles applied loading. The errors in measured force magnitude are all less than 16%, and errors in strain measurement are less than $3.5\ \%$ for the full static force reconstruction model.

An FE model is described and compared to experimental results. Results from the model match very closely with experiment. The static model in this chapter does not take into account dynamic effects. The next chapter will describe a model that takes dynamic effects into account, and will be followed by a chapter comparing the calculated forces according to both models for various scooter stunts.

Chapter 6

Dynamic Force Reconstruction

6.1 Introduction

The previous chapter described the static force reconstruction model and validated it through experiment and simulation. This chapter presents the theory underlying the dynamic force reconstruction model in section 6.2. This is followed by a section (6.3) describing how the (dynamic) experimental calibration of the model was done in practice. This section details results and solutions to various issues encountered when performing the dynamic calibration. The issues include drift in the superimposed basis functions in section 6.3.3 and the widening of the basis impulses to make them suitable for reconstructing forces applied to scooters in section 6.4.

6.2 Dynamic force reconstruction theory

A key assumption of the static force reconstruction theory was that the strain at any instant was only affected by the force applied at that specific time. This assumption is inaccurate when the magnitude of the applied force varies rapidly (when dynamic effects are significant). In many respects, the dynamic force reconstruction approach resembles that of the static model (see figure 6.12 for the resultant load distribution). Instead of basis forces, basis impulses are used. Each basis impulse gives a strain response that varies as a function of time at each strain measurement location. A plot of a basis impulse and the strain response at one strain measurement point are in figure 6.1.

To make the mathematics more straightforward to follow, simpler models involving only one basis impulse location are introduced first.

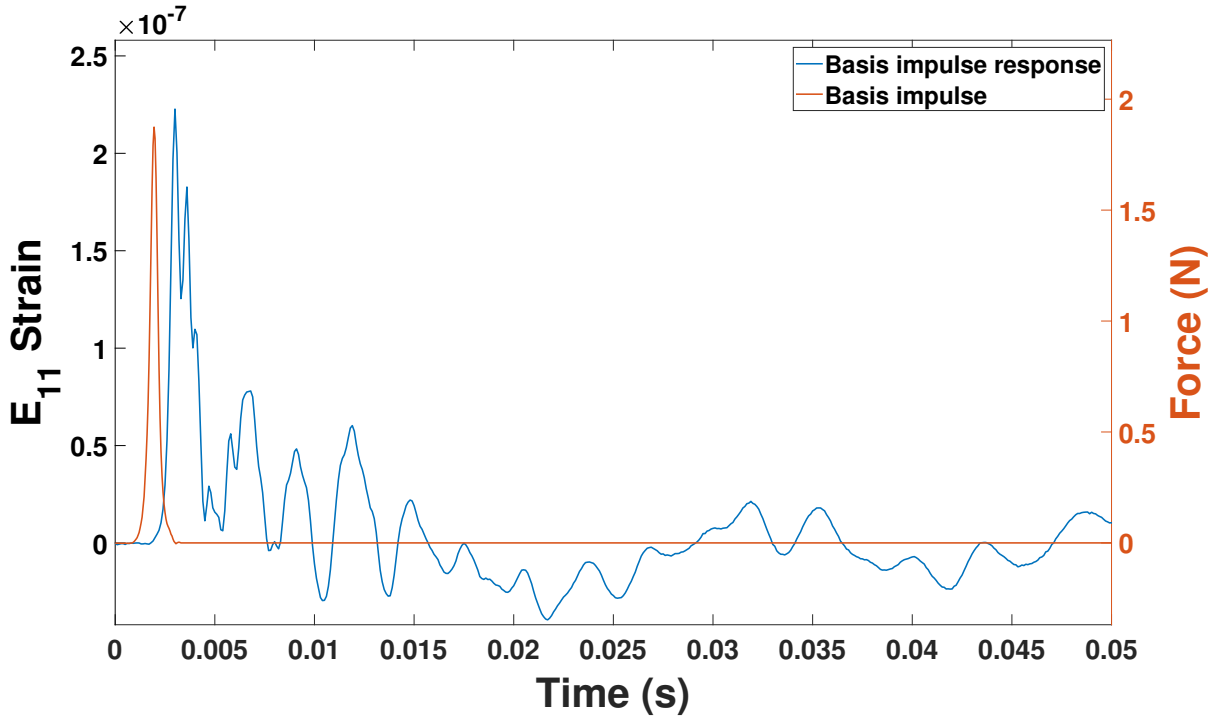


Figure 6.1: A basis impulse and the strain response at one strain measurement point. This strain response is at the location of deck strain gauge 2, and the impulse is applied at the location of $\boldsymbol{f_3}$.

One impulse location one strain measurement point

Because loads can be applied at various times, time-shifted basis impulses are used in the model to give the dynamic loading history. Mathematically, the strain response (impulse response) measured at each timestep is given by a value in a vector:

$$\begin{pmatrix} \varepsilon_{t1} \\ \varepsilon_{t2} \\ \varepsilon_{t3} \\ \vdots \\ \varepsilon_{tn-1} \\ \varepsilon_{tn} \end{pmatrix}$$

The total loading in this model will be a superposition of time-shifted basis impulses. Therefore, the total strain in this model will be a superposition of time-shifted impulse responses. In matrix form (for the case where there are n timesteps), it will be like this:

$$\begin{bmatrix} \varepsilon_{t1} & 0 & 0 & \dots & 0 & 0 \\ \varepsilon_{t2} & \varepsilon_{t1} & 0 & \dots & 0 & 0 \\ \varepsilon_{t3} & \varepsilon_{t2} & \varepsilon_{t1} & \dots & 0 & 0 \\ \vdots & \vdots & \vdots & \ddots & \vdots & \vdots \\ \varepsilon_{tn-1} & \varepsilon_{tn-2} & \varepsilon_{tn-3} & \dots & \varepsilon_{t1} & 0 \\ \varepsilon_{tn} & \varepsilon_{tn-1} & \varepsilon_{tn-2} & \dots & \varepsilon_{t2} & \varepsilon_{t1} \end{bmatrix} \begin{pmatrix} c_{t1} \\ c_{t2} \\ c_{t3} \\ \vdots \\ c_{tn-1} \\ c_{tn} \end{pmatrix} = \begin{pmatrix} \varepsilon_{m,t1} \\ \varepsilon_{m,t2} \\ \varepsilon_{m,t3} \\ \vdots \\ \varepsilon_{m,tn-1} \\ \varepsilon_{m,tn} \end{pmatrix} \tag{6.1}$$

where ε_{tx} is the impulse response at timestep x, c_{tx} is the basis impulse coefficient at that timestep, and $\varepsilon_{m,tx}$ is the total measured strain at that timestep. This is the dynamic equivalent of the equation from the static force reconstruction 5.2:

$$[\boldsymbol{\varepsilon}_t]\boldsymbol{c} = \boldsymbol{\varepsilon}_{meas.}$$

Note that whilst the basis impulse coefficient for a timestep is a single number, the force/time of a basis impulse extends in time (in the figure 6.1, the basis impulse lasts about 1 ms). It is also worth noting that it may not be necessary to have basis impulses at every timestep, in which case the system of equations will be over-determined (there will be more rows than columns) and solved by minimising the least-squares error. If, for example, basis impulses were used every other timestep, the matrix equation would look like this:

$$\begin{bmatrix} \varepsilon_{t1} & 0 & 0 & \dots & 0 & 0 \\ \varepsilon_{t2} & 0 & 0 & \dots & 0 & 0 \\ \varepsilon_{t3} & \varepsilon_{t1} & 0 & \dots & 0 & 0 \\ \varepsilon_{t4} & \varepsilon_{t2} & 0 & \dots & 0 & 0 \\ \varepsilon_{t5} & \varepsilon_{t3} & \varepsilon_{t1} & \dots & 0 & 0 \\ \vdots & \vdots & \vdots & \ddots & \vdots & \vdots \\ \varepsilon_{tn-1} & \varepsilon_{tn-3} & \varepsilon_{tn-5} & \dots & \varepsilon_{t1} & 0 \\ \varepsilon_{tn} & \varepsilon_{tn-2} & \varepsilon_{tn-4} & \dots & \varepsilon_{t2} & \varepsilon_{t1} \end{bmatrix} \begin{pmatrix} c_{t1} \\ c_{t3} \\ c_{t5} \\ \vdots \\ c_{tn-2} \\ c_{tn} \end{pmatrix} = \begin{pmatrix} \varepsilon_{m,t1} \\ \varepsilon_{m,t2} \\ \varepsilon_{m,t3} \\ \varepsilon_{m,t4} \\ \varepsilon_{m,t5} \\ \vdots \\ \varepsilon_{m,tn-1} \\ \varepsilon_{m,tn} \end{pmatrix} \tag{6.2}$$

One impulse location, multiple measurement points

Another way to make the system of equations over-determined is to add more strain measurement points while retaining only one location for the applied impulse. In this case, the number of coefficients for the $\boldsymbol{c}$ vector would not change. However, more strain measurement locations need to be added for each timestep. The rows representing the strains at other strain measurement locations are simply concatenated below the first strain measurement point. If there are p strain measurement locations, the equation would look like this:

$$
\begin{bmatrix}
\varepsilon_{l1,t1} & 0 & 0 & \dots & 0 & 0 \\
\varepsilon_{l1,t2} & \varepsilon_{l1,t1} & 0 & \dots & 0 & 0 \\
\varepsilon_{l1,t3} & \varepsilon_{l1,t2} & \varepsilon_{l1,t1} & \dots & 0 & 0 \\
\vdots & \vdots & \vdots & \ddots & \vdots & \vdots \\
\varepsilon_{l1,tn-1} & \varepsilon_{l1,tn-2} & \varepsilon_{l1,tn-3} & \dots & \varepsilon_{l1,t1} & 0 \\
\varepsilon_{l1,tn} & \varepsilon_{l1,tn-1} & \varepsilon_{l1,tn-2} & \dots & \varepsilon_{l1,t2} & \varepsilon_{l1,t1} \\
\varepsilon_{l2,t1} & 0 & 0 & \dots & 0 & 0 \\
\varepsilon_{l2,t2} & \varepsilon_{l2,t1} & 0 & \dots & 0 & 0 \\
\varepsilon_{l2,t3} & \varepsilon_{l2,t2} & \varepsilon_{l2,t1} & \dots & 0 & 0 \\
\vdots & \vdots & \vdots & \ddots & \vdots & \vdots \\
\varepsilon_{l2,tn-1} & \varepsilon_{l2,tn-2} & \varepsilon_{l2,tn-3} & \dots & \varepsilon_{l2,t1} & 0 \\
\varepsilon_{l2,tn} & \varepsilon_{l2,tn-1} & \varepsilon_{l2,tn-2} & \dots & \varepsilon_{l2,t2} & \varepsilon_{l2,t1} \\
\vdots & \vdots & \vdots & \ddots & \vdots & \vdots \\
\vdots & \vdots & \vdots & \ddots & \vdots & \vdots \\
\vdots & \vdots & \vdots & \ddots & \vdots & \vdots \\
\varepsilon_{lp,t1} & 0 & 0 & \dots & 0 & 0 \\
\varepsilon_{lp,t2} & \varepsilon_{lp,t1} & 0 & \dots & 0 & 0 \\
\varepsilon_{lp,t3} & \varepsilon_{lp,t2} & \varepsilon_{lp,t1} & \dots & 0 & 0 \\
\vdots & \vdots & \vdots & \ddots & \vdots & \vdots \\
\varepsilon_{lp,tn-1} & \varepsilon_{lp,tn-2} & \varepsilon_{lp,tn-3} & \dots & \varepsilon_{lp,t1} & 0 \\
\varepsilon_{lp,tn} & \varepsilon_{lp,tn-1} & \varepsilon_{lp,tn-2} & \dots & \varepsilon_{lp,t2} & \varepsilon_{lp,t1}
\end{bmatrix}
\begin{pmatrix}
c_{t1} \\ c_{t2} \\ c_{t3} \\ \vdots \\ c_{tn-1} \\ c_{tn}
\end{pmatrix}
=
\begin{pmatrix}
\varepsilon_{m,l1,t1} \\ \varepsilon_{m,l1,t2} \\ \varepsilon_{m,l1,t3} \\ \vdots \\ \varepsilon_{m,l1,tn-1} \\ \varepsilon_{m,l1,tn} \\ \varepsilon_{m,l2,t1} \\ \varepsilon_{m,l2,t2} \\ \varepsilon_{m,l2,t3} \\ \vdots \\ \varepsilon_{m,l2,tn-1} \\ \varepsilon_{m,l2,tn} \\ \vdots \\ \vdots \\ \vdots \\ \varepsilon_{m,lp,t1} \\ \varepsilon_{m,lp,t2} \\ \varepsilon_{m,lp,t3} \\ \vdots \\ \varepsilon_{m,lp,tn-1} \\ \varepsilon_{m,lp,tn}
\end{pmatrix}
\tag{6.3}
$$

Another way of expressing this is to say it is a concatenation of $[\boldsymbol{\varepsilon_{lp}}]$ matrices and $\boldsymbol{\varepsilon_{m,lp}}$ vectors:

$$\begin{bmatrix} [\boldsymbol{\varepsilon_{l1}}] \\ [\boldsymbol{\varepsilon_{l2}}] \\ \vdots \\ [\boldsymbol{\varepsilon_{lp}}] \end{bmatrix} \boldsymbol{c} = \begin{pmatrix} \boldsymbol{\varepsilon_{m,l1}} \\ \boldsymbol{\varepsilon_{m,l2}} \\ \vdots \\ \boldsymbol{\varepsilon_{m,lp}} \end{pmatrix}$$

where:

$$[\boldsymbol{\varepsilon_{lp}}] = \begin{bmatrix} \varepsilon_{lp,t1} & 0 & 0 & \dots & 0 & 0 \\ \varepsilon_{lp,t2} & \varepsilon_{lp,t1} & 0 & \dots & 0 & 0 \\ \varepsilon_{lp,t3} & \varepsilon_{lp,t2} & \varepsilon_{lp,t1} & \dots & 0 & 0 \\ \vdots & \vdots & \vdots & \ddots & \vdots & \vdots \\ \varepsilon_{lp,tn-1} & \varepsilon_{lp,tn-2} & \varepsilon_{lp,tn-3} & \dots & \varepsilon_{lp,t1} & 0 \\ \varepsilon_{lp,tn} & \varepsilon_{lp,tn-1} & \varepsilon_{lp,tn-2} & \dots & \varepsilon_{lp,t2} & \varepsilon_{lp,t1} \end{bmatrix}, \boldsymbol{\varepsilon_{m,lp}} = \begin{pmatrix} \varepsilon_{m,lp,t1} \\ \varepsilon_{m,lp,t2} \\ \varepsilon_{m,lp,t3} \\ \vdots \\ \varepsilon_{m,lp,tn-1} \\ \varepsilon_{m,lp,tn} \end{pmatrix}$$

Multiple impulse locations, multiple measurement points

For many systems, multiple impulse locations (locations where impulses are applied) will be required to obtain a reasonable force reconstruction of a system. In this case, additional columns will be needed to account for the additional loads. We can introduce a subscript to denote which force a given strain response is from in the following way:

$$[\boldsymbol{\varepsilon_{lp,fq}}] = \begin{bmatrix} \varepsilon_{lp,fq,t1} & 0 & 0 & \dots & 0 & 0 \\ \varepsilon_{lp,fq,t2} & \varepsilon_{lp,fq,t1} & 0 & \dots & 0 & 0 \\ \varepsilon_{lp,fq,t3} & \varepsilon_{lp,fq,t2} & \varepsilon_{lp,fq,t1} & \dots & 0 & 0 \\ \vdots & \vdots & \vdots & \ddots & \vdots & \vdots \\ \varepsilon_{lp,fq,tn-1} & \varepsilon_{lp,fq,tn-2} & \varepsilon_{lp,fq,tn-3} & \dots & \varepsilon_{lp,fq,t1} & 0 \\ \varepsilon_{lp,fq,tn} & \varepsilon_{lp,fq,tn-1} & \varepsilon_{lp,fq,tn-2} & \dots & \varepsilon_{lp,fq,t2} & \varepsilon_{lp,fq,t1} \end{bmatrix}, \boldsymbol{c_{fq}} = \begin{pmatrix} c_{t1,fq} \\ c_{t2,fq} \\ c_{t3,fq} \\ \vdots \\ c_{tn-1,fq} \\ c_{tn,fq} \end{pmatrix}$$

$\boldsymbol{\varepsilon_{m,lp}}$ remains the same as in the previous section, as it is just the total measured strain at each location. There are an equal number of strain measurement points, it is just now the case that the strain can be contributed from multiple locations for an impulse to be applied.

Using this notation, the total matrix equation $[\boldsymbol{\varepsilon}_t]\boldsymbol{c} = \boldsymbol{\varepsilon}_{meas.}$ becomes:

$$\begin{bmatrix} [\boldsymbol{\varepsilon_{l1,f1}}] & [\boldsymbol{\varepsilon_{l1,f2}}] & \dots & [\boldsymbol{\varepsilon_{l1,fq}}] \\ [\boldsymbol{\varepsilon_{l2,f1}}] & [\boldsymbol{\varepsilon_{l2,f2}}] & \dots & [\boldsymbol{\varepsilon_{l2,fq}}] \\ \vdots & \vdots & \ddots & \vdots \\ [\boldsymbol{\varepsilon_{lp,f1}}] & [\boldsymbol{\varepsilon_{lp,f2}}] & \dots & [\boldsymbol{\varepsilon_{lp,fq}}] \end{bmatrix} \begin{pmatrix} \boldsymbol{c_{f1}} \\ \boldsymbol{c_{f2}} \\ \vdots \\ \boldsymbol{c_{fq}} \end{pmatrix} = \begin{pmatrix} \boldsymbol{\varepsilon_{m,l1}} \\ \boldsymbol{\varepsilon_{m,l2}} \\ \vdots \\ \boldsymbol{\varepsilon_{m,lp}} \end{pmatrix}$$

The resulting $[\boldsymbol{\varepsilon}_t]$ matrix is $(n \times p) \times (n^* \times q)$ in size where n is the number of timesteps, p is the number of strain measurement locations, n^* is the number of timesteps divided by the size of the gap between basis impulses, and q is the number of basis impulses (the number of locations at which basis impulses are applied). $\boldsymbol{\varepsilon}_{meas.}$ is $(n \times\ p)\ \times\ 1$.

6.2.1 Justification of the dynamic force reconstruction method

Given the many different methods of force reconstruction, it is worth giving an explanation on why the dynamic force reconstruction described above was used instead of alternative methods in the literature (see section 2.2).

One advantage of this model is that, unlike most of the approaches described in the literature review, this model is entirely experimentally based (rather than based on a theoretical/computational model of the scooter). Given the complex geometry of the scooter and potential sources of error, it seems wiser to use experimental data. An experimental approach should account for these effects insofar as they are linear. Results could then be checked with a dynamic FE model, to gauge this mismatch between the force reconstruction results and simulation, rather than basing force reconstructions on a theoretical model of the scooter. If the experimental force reconstruction approach is used, it can be checked with simulations more easily than simulations can be checked with experimental results. The experimental approach allows one to collect strain data in the field, reconstruct the forces, apply

these to a dynamic FE model, and compare the simulated results with measured strain. Whilst one could measure strain and then reconstruct the forces with a theoretical/computer-based model, it would be difficult to compare this to experimental results for verification. The experimental loads (of real-world data) cannot be measured directly with the equipment available for this project.

In addition, having a solver based on the physics of the model would likely be significantly more computationally costly. The geometries used for force reconstruction in the literature review were significantly simpler than a scooter. A theoretical or computational model based on the whole scooter would take much longer to solve. Only data from six possible force locations and seven strain measurement points were used for the experimental approach in this thesis.

Another positive of this model is that when solving, it minimises the error across all of the timesteps at once. One worry with iterative approaches (that only solve for one timestep at a time) is that if there is some error in the force reconstruction at a point early in the reconstruction, this could compound over subsequent timesteps, making the total error worse. The model above computes the least-squares error for the whole of the stunt. This method of solving is not very efficient and, therefore, is likely significantly slower than a recursive model. This inefficiency was not significant for this project, as the computers used could still solve for a set of data in 60 – 90 seconds (the computers had at least 64 GB of RAM each). Each set of data was one second of strain data, which was easily enough to capture the landing of a stunt.

The computational inefficiency of the approach used is one reason an equivalent model was not found in the literature. It is possible that a similar approach is in the literature somewhere. As the approach is a natural extension of the static calibration model, which bears many similarities to the static force reconstruction approaches on bicycles (e.g. [22, 37]), it would not be surprising if others have taken a similar approach. This may be particularly likely in cases where the aim of the research is to reconstruct the forces in a particular setting (rather than focusing on force reconstruction methods). This sort of force reconstruction could be performed in many different fields (without necessarily using the name 'force reconstruction'). Therefore, whilst effort has been taken to find an equivalent model in the literature, there is no guarantee that a similar model has not been used.

Another reason is the ease of implementation of the model. Given that the dynamic force reconstruc-

tion approach is just an extension of the principles used in the static force reconstruction approach, writing suitable code and testing the model was relatively straightforward. Given the many different areas of investigation in this thesis, using an approach that could be implemented quickly was a benefit. As long as the force reconstruction approach is reasonable, the primary source of error is more likely to come from errors in either the experimental calibration or the modelling of the scooter, rather than from the force reconstruction approach used. [47] highlights the importance of experimental data for the success of a force reconstruction model.

A deconvolution approach to force reconstruction was briefly explored to have as a comparison. The aim was to use built-in MATLAB functions to do this. This approach failed because the force reconstruction model would require point spread functions (PSFs) that varied for each timestep. Whilst it is possible to do deconvolution with varying PSFs (e.g. [125, 126]), implementation of this is not straightforward. Due to time constraints, this approach was not further developed.

6.3 Dynamic calibration

6.3.1 General approach

The dynamic calibration approach has a few noticeable differences from the static approach of the previous chapter. The first difference is that the loads/impulses are applied over a relatively small area. A DJB IH-05 instrumented impact hammer [127] (figure 6.2) was used to measure the applied impulse as a function of time.

One reason for choosing an instrumented hammer that applied loads over a small area was because, in practice, any load applied over a larger area would likely hit the scooter with one edge first. Consequently, the applied impulse could be at a significantly different location than intended. Moreover, this error would be very difficult to measure. Also, none of the other methods of applying impulses to the scooter could apply impulses at the desired rate whilst measuring the applied impulse accurately. The hammer could be fitted with steel, aluminium, Nylon or rubber tips. Steel and aluminium tips were not used, as they would likely plastically deform the footplate, and the impulse would be extremely short. The rider will generally wear shoes with rubber soles, so tests were performed with

rubber tips.

The instrumented hammer is used to apply a known impulse to the scooter (representative of one of the basis impulses), and the strain response is measured by the data logger. The data for the hammer was captured on Labview 2017 [128] and recorded through a National Instruments PXIe-4492 dynamic signal acquisition (DSA) analog input device [129], connected to a PXIe-1082 Chassis [130] which supplied the data to a computer. An example impulse strain response can be seen in figure 6.5. In the case of applying impulses to the handlebars, it was necessary to have some way of stopping the deck from moving backwards when a load was applied. To do this, I used my foot to stop the back wheel from moving, as can be seen in figure 6.3.



Figure 6.2: The impact hammer used for dynamic calibration. A rubber tip is on the hammer, and the nylon (white) tip can be seen adjacent to it.

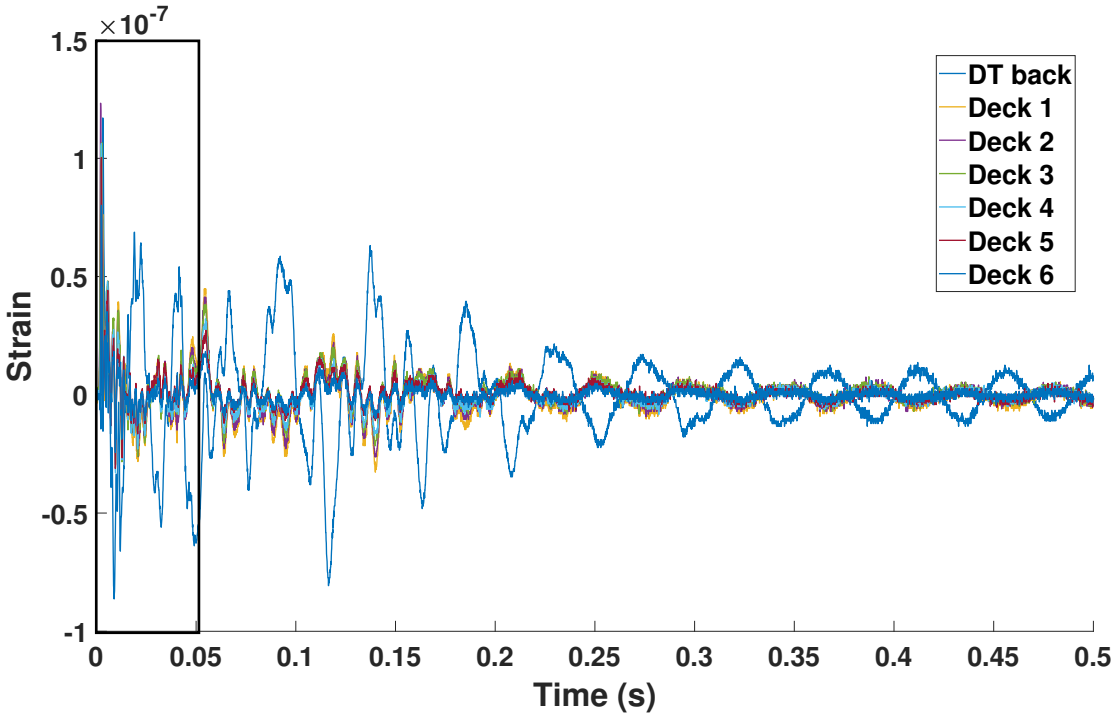


Figure 6.3: The way my foot was planted to stop the motion of the scooter in the x_1 direction when applying an impusle at $\boldsymbol{f_1}$.

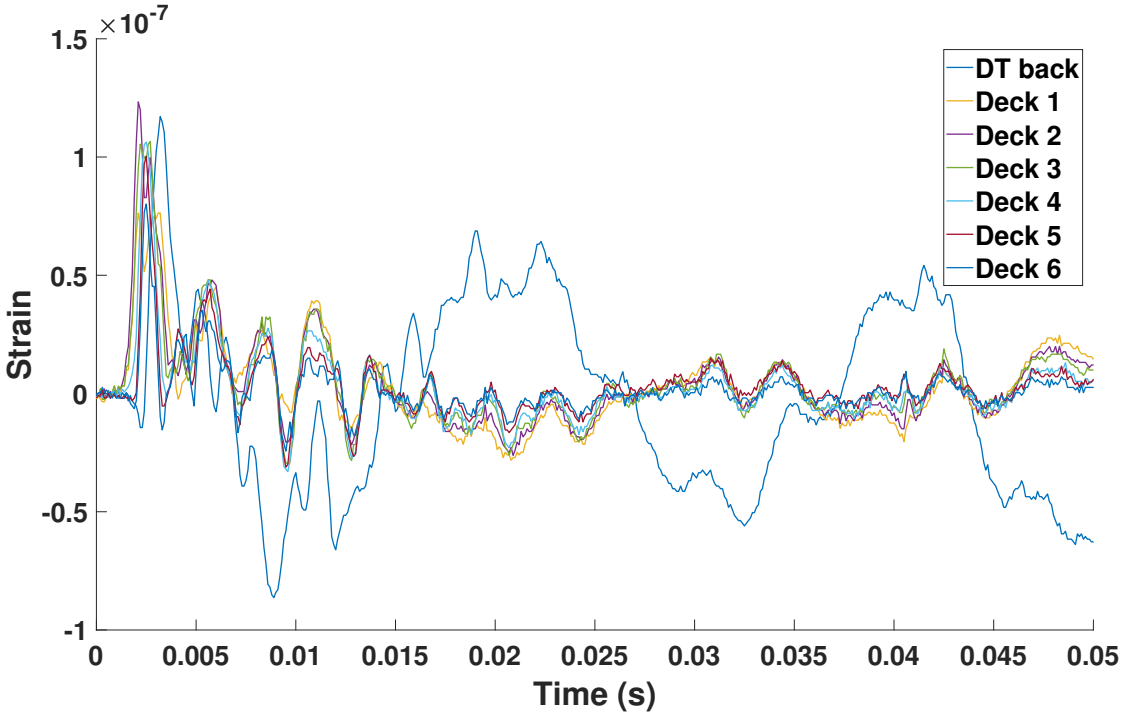
Figure 6.4

The scooter was subject to impacts from the hammer in the set-up shown in figure 6.6a. Masking tape was applied to the top surface of the scooter, and the locations where the loading was to be applied were marked along the centre line on the top of the deck (figure 6.6b). A characteristic impulse from a single hammer hit can be seen in figure 6.7.

As can be seen in the figure, the level of noise after one impulse is significant. Because the duration of an impulse is short, the energy imparted to the scooter is small, and the maximum strain is low. Another source of error stemmed from the fact that the impulses were being applied by hand. Applied impulses did not land exactly upon the nominally specified location. Fujifilm Prescale LLLW was

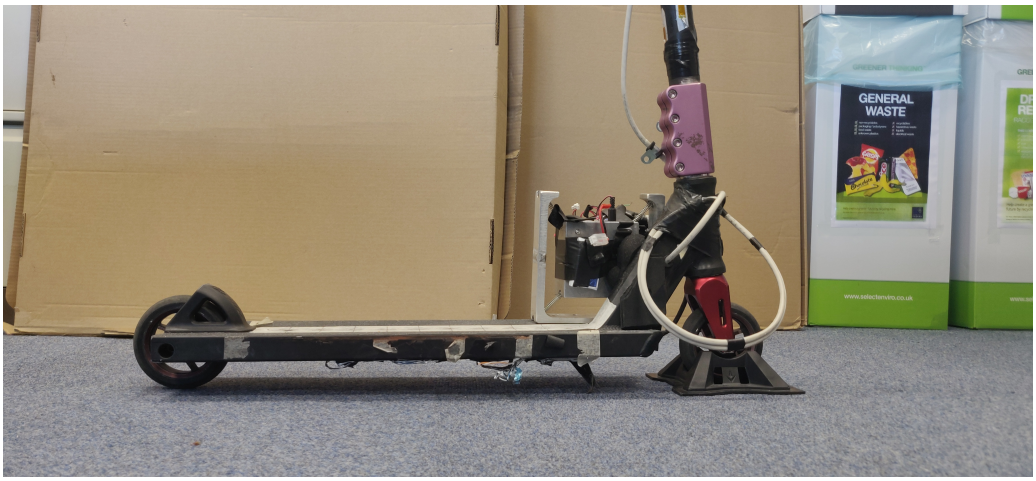


(a)

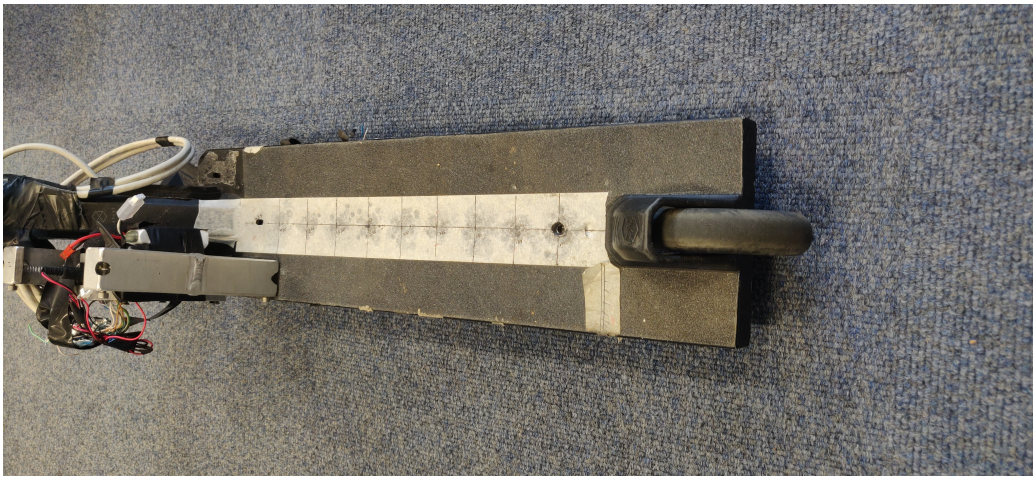


(b)

Figure 6.5: Strain responses at various points in the scooter from an impulse applied at f_3. b) is a mganified plot from the black window in a).



(a) The setup of the scooter in the stand for dynamic calibration.

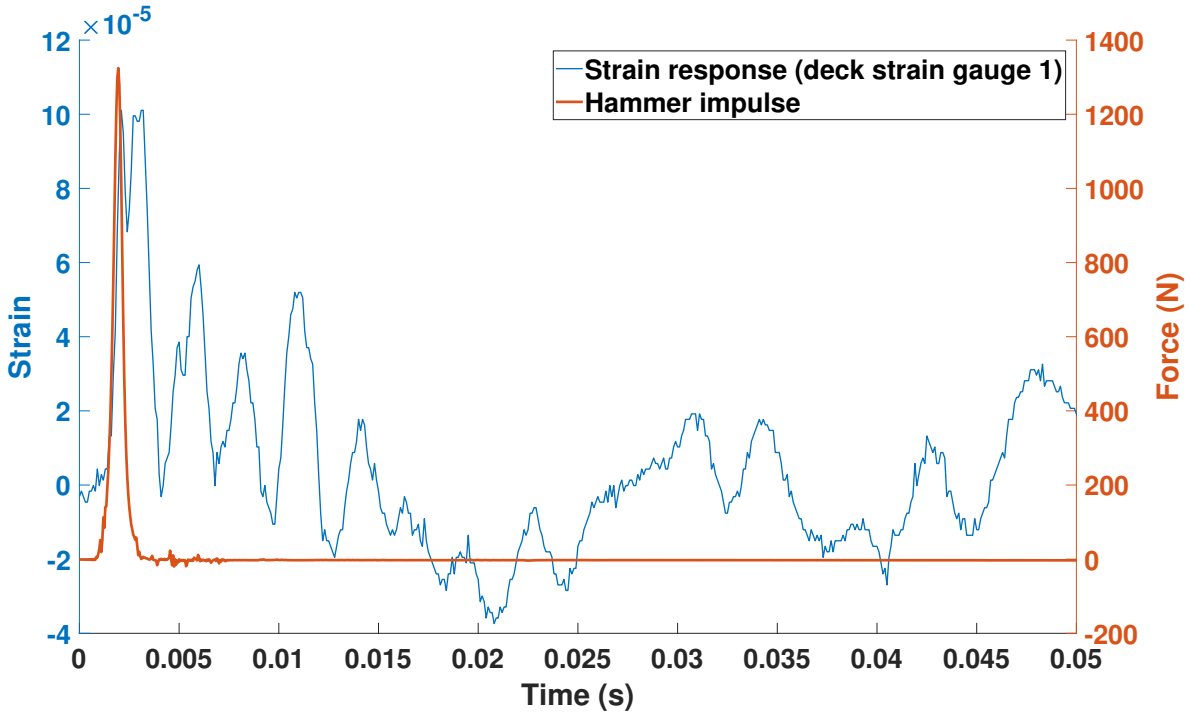


(b) The masking tape with vertical and horizontal lines was used to mark the location for applied impulses.

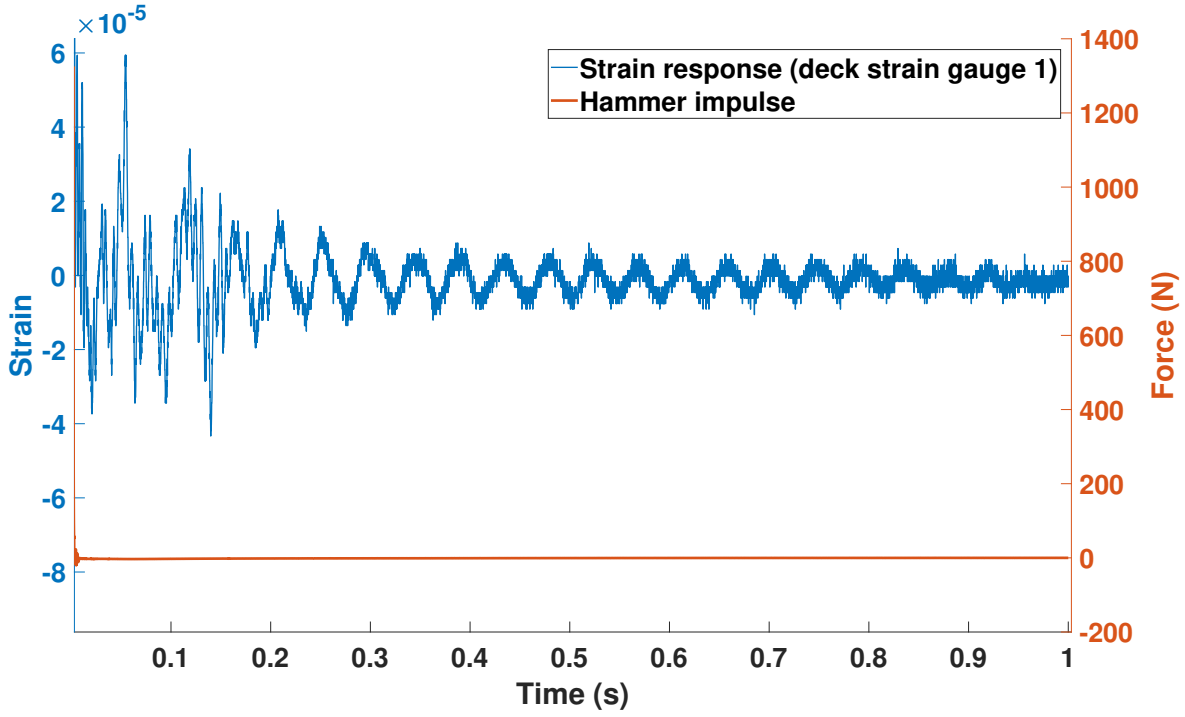
Figure 6.6: Showing some of the ways the scooter was set up for the dynamic calibration.

applied to the deck to help gauge the accuracy of the hammer hits. 78 impulses were subsequently applied to the deck. The resulting distribution of the applied load can be seen in figure 6.8.

To mitigate the effect of noise and applied impulse location errors, at least 50 impulses were applied to each nominal location. Every individual impulse was normalised by dividing it and its associated strain response by 1000 times the total magnitude of the impulse. This made it such that each normalised impulse had a magnitude of 1 mNs. The basis impulses were then superimposed with each other, and the resulting impulse was normalised again, this time by dividing it by the number of applied basis impulses at that location. The effect averaged out the location of the applied impulses and reduced the noise. Figure 6.9 shows an example averaged basis impulse and its average response



(a)



(b)

Figure 6.7: The strain response in deck strain gauge 1 from an applied impulse at f_3. a) and b) are of same graph, but a) only covers the first 0.05 s of the stunt.

to deformation.

The strain response appears to become sensitive to exact loading conditions about 55 ms after applying the impulse. This is clear in figure 6.10 where various hammer hits start to go out of sync. Real-world loading will, however, not be in precisely the same location each time (nor is it over the same area as the hammer impulses). One possible reason for the variation in strain response is sensitivity in the boundary conditions, maybe from acoustic reflections from the ends of the scooter. The axles (especially the back axle) can move relatively easily as they are not fixed.

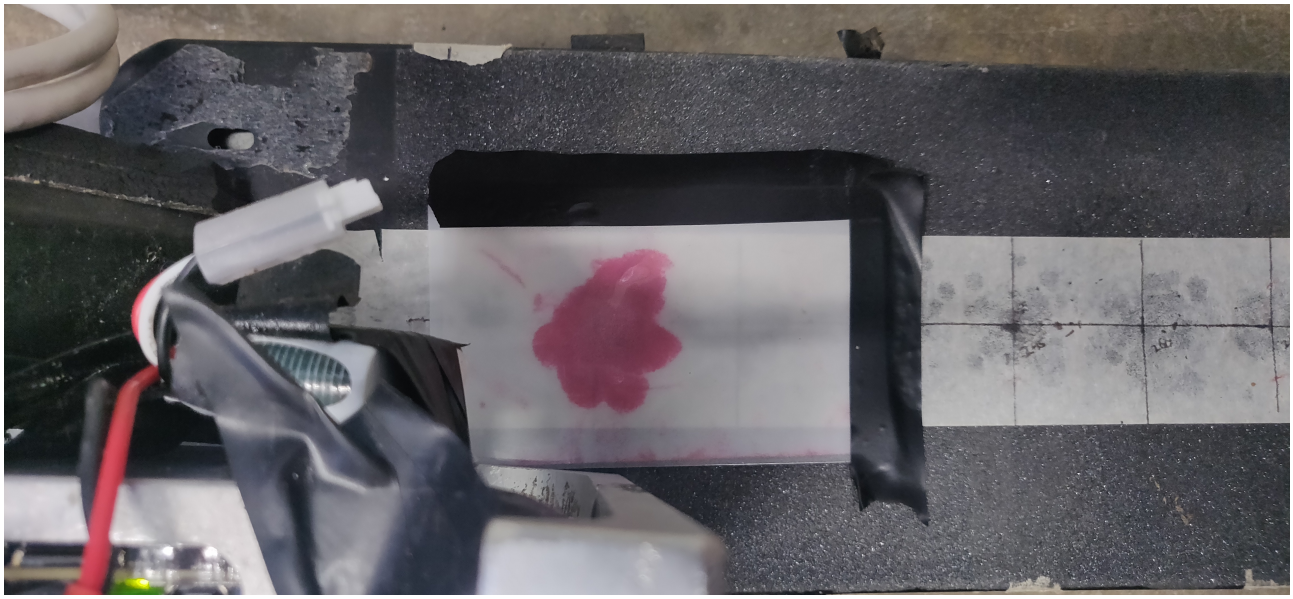
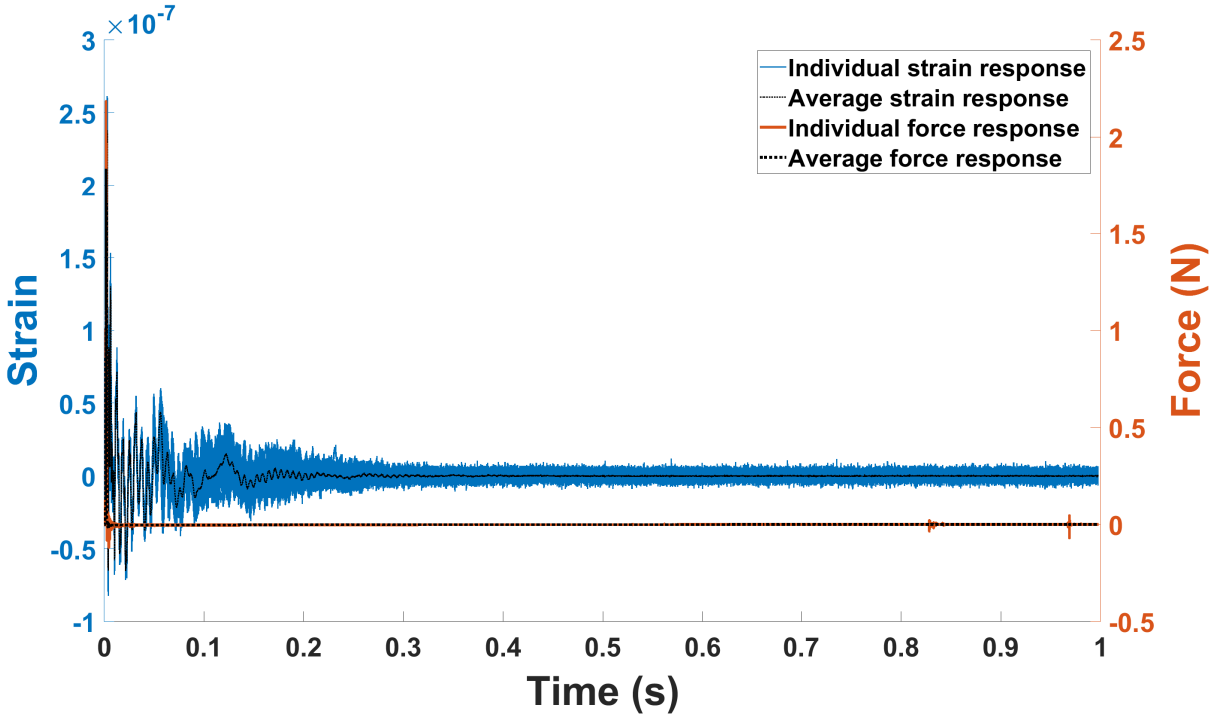
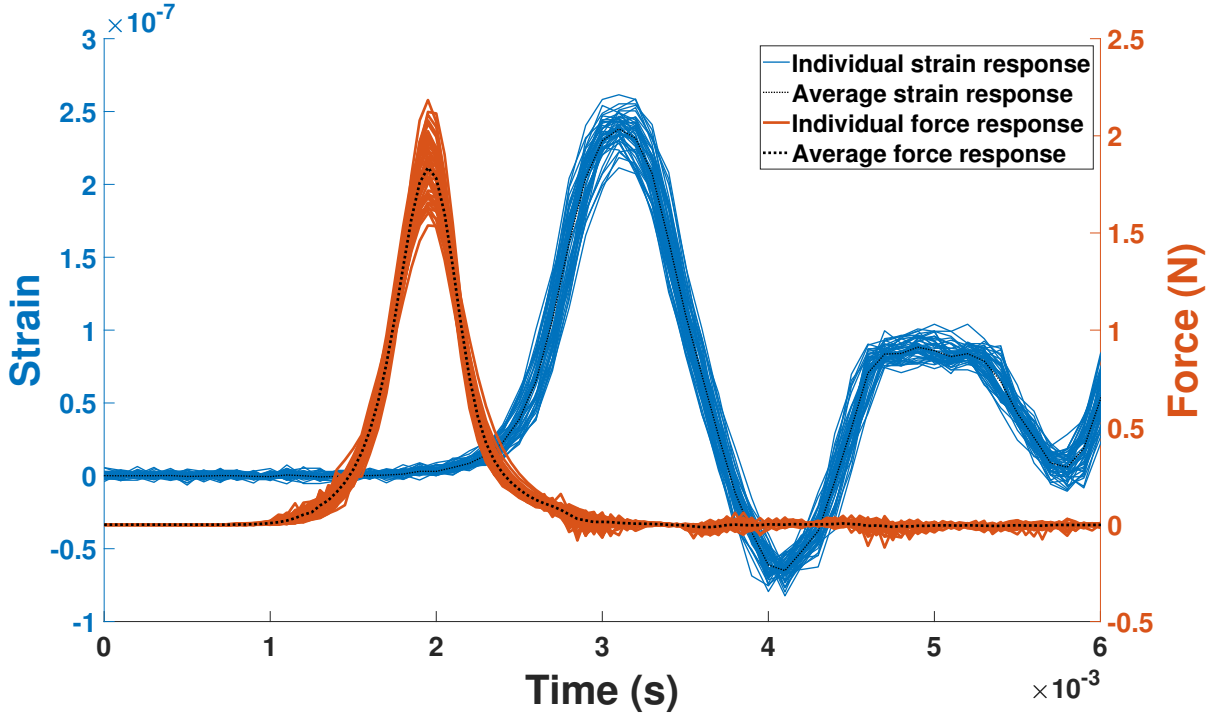


Figure 6.8: Fujifilm prescale has been taped to the top of the scooter deck, at the location of $\boldsymbol{f_1}$. The deck has subsequently been hit 78 times to gauge the spread in the location of applied basis loads.



(a)



(b)

Figure 6.9: The normalised impulse response and strain response at f_5.

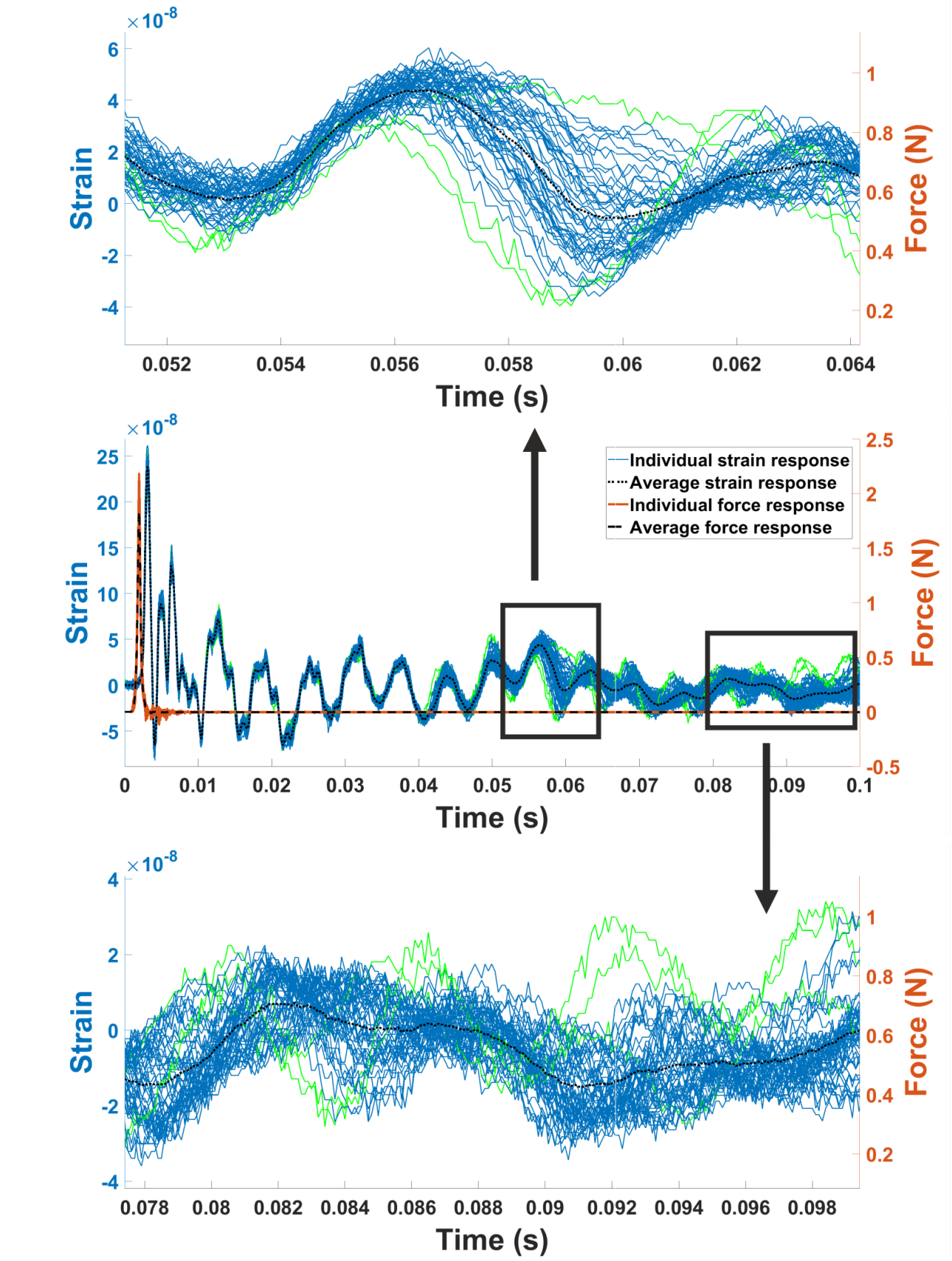


Figure 6.10: The impulse response of some hammer hits starting to go out of sync after approximately 55 ms. Green traces are only green to highlight which ones are going out of sync. This effect was similar on all strain gauges.

6.3.2 Accounting for the decay of the hammer signal

The instrumented impact hammer operates through an Integrated Electronics Piezo-Electric (IEPE) sensor. IEPE sensors only allow AC signals through. Because of this, the instrumented hammer can only measure dynamic loads. The measured response of a constant load will decay over time if applied to the hammer. To gauge the rate of decay, an approximately constant force was applied to the hammer by holding it against a rigid surface, before removing it as quickly as possible. A curve showing the resultant reading given by the hammer is in figure 6.11. As can be seen, the effects do not significantly affect results. However, the effect often led to a slight negative value of the reported impulse of the hammer hits long after the impulse was applied (i.e. for large times the recorded force value was often still slightly negative). This effect was negligible on a single hammer hit; however, the effect could be significant if superimposed thousands of times (as is the case in the dynamic force reconstruction approach). To mitigate this effect, the force values of each basis impulse were truncated to only persist for 5 ms (i.e. values after this were all modified to be zero).

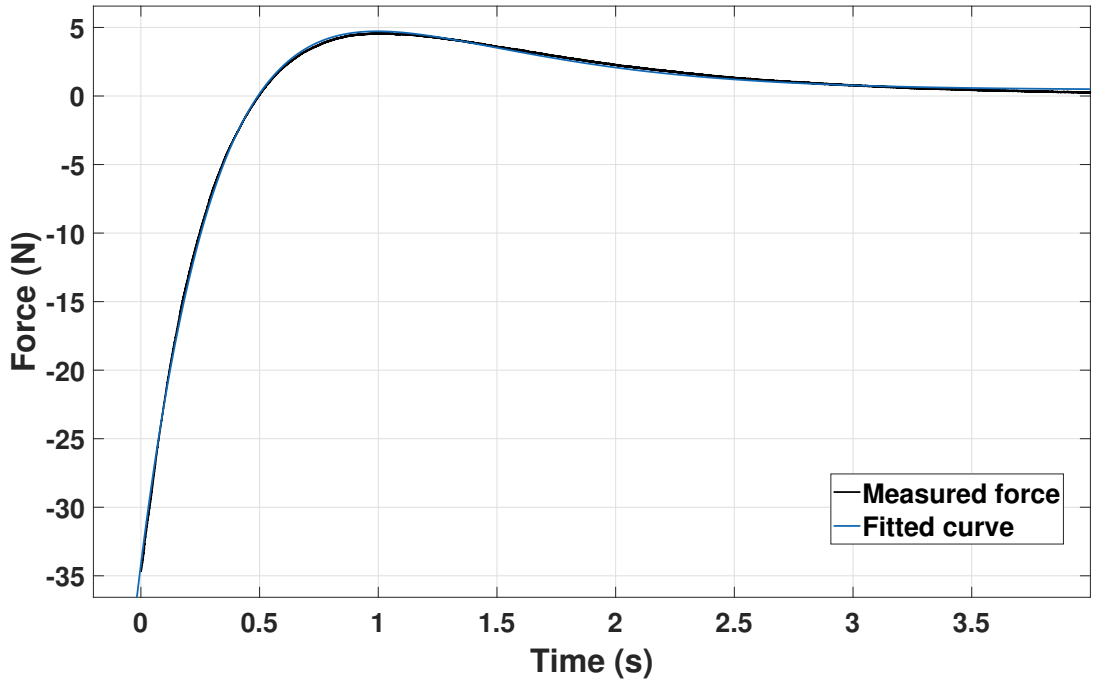


Figure 6.11: The equation fitted for the decay was: a exp$(-bx)$ $\sin(dx + e) + c$, where a = 234, b = 2.048 (confidence interval: 2.047, 2.049) ,c = 0.4457 , d = 0.2906 and e = -0.1485. Looking at different curves and fitting parameters, the value of b was between 2.05 and 1.93. even in the worst case where b = 2.05, the rate of decay after 2 ms is such that the function will still be at 99.6 % of its original value (and by this time the hammer impulse would be almost zero anyway).

6.3.3 Comparison with static model and drift correction

To further help gauge the accuracy of the dynamic model, it was compared to the static model. To do this, a series of time-shifted basis impulses (each basis impulse offset by 10^{-4} s from the previous one) were superimposed. The reason for doing this was to mimic a constant load, which could then be compared to the static model. The force output of this quickly became flat (as can be seen in figure 6.12. The strain output of this constant load was compared with the output predicted by the static model. One reason for doing this is that if basis impulses are superimposed every timestep, small errors in individual basis impulses can become extremely large. For example, if there were a constant error term in a basis impulse such that every value of the strain response was off by 0.1% of the magnitude of the peak strain. If a constant load were applied for $1\ s$, the error term at the end would be 10 times the magnitude of the peak strain of the individual impulse response!

In figure 6.13, one can see that without any correction, the results are significantly different. There

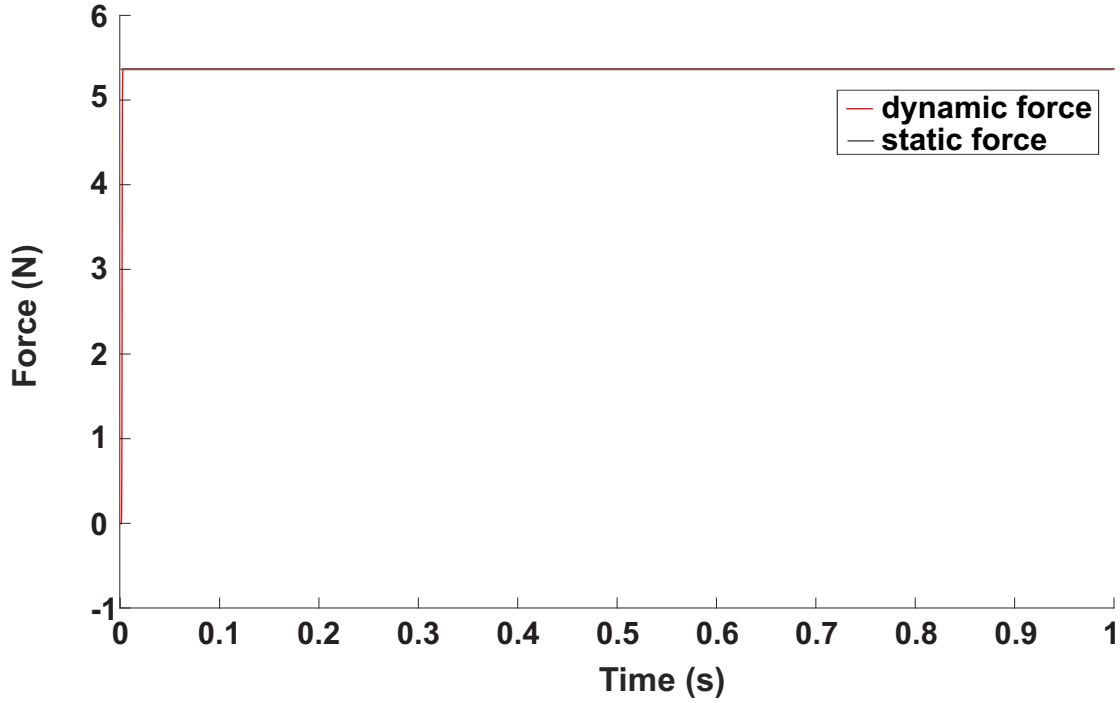


Figure 6.12: The resultant load distribution from 10 000 superimposed basis impulses. The loading distribution is very flat, so would under static assumpoints yield the flat strain distibutions in figure 6.13 below. The strain response in this graph is from loads applied at the location of $\boldsymbol{f_6}$.

are two main sources for this error. The first of these is noise. Assuming the noise for an individual basis impulse will have the same value (standard deviation) at any timestep, we can denote the magnitude of this noise e_n. As we are superimposing time-shifted basis impulses, at timestep x, the error (standard deviation) due to noise at that timestep will be $\sqrt{x}e_n$ (it is a 1D random walk of length x and step size e_n). In addition to this, there can be noise due to thermal drift. If we assume the thermal drift can be fitted to a cubic function, we can write the form of the thermal drift as:

$$e_d = Ax^3 + Bx^2 + Cx + D$$

for an individual basis impulse (where A, B, C and D are constants to be fitted to the data). Thus, in total, the measured strain of an individual basis impulse at a time t will be:

$$\varepsilon_{m,t} = \varepsilon_{tr,t} + e_{n,t} + At^3 + Bt^2 + Ct + D$$

Where $\varepsilon_{m,t}$ is the measured strain at time t, and $\varepsilon_{tr,t}$ is the true strain at time t. In the case of a

series of superimposed time-shifted basis impulses, this can be discretised into vector form (where the units of time are the size of a timestep):

$$\begin{pmatrix} \varepsilon_{m,0} \\ \varepsilon_{m,1} + \varepsilon_{m,0} \\ \varepsilon_{m,2} + \varepsilon_{m,1} + \varepsilon_{m,0} \\ \vdots \end{pmatrix} = \begin{pmatrix} \varepsilon_{tr,0} \\ \varepsilon_{tr,1} + \varepsilon_{tr,0} \\ \varepsilon_{tr,2} + \varepsilon_{tr,1} + \varepsilon_{tr,0} \\ \vdots \end{pmatrix} + \begin{pmatrix} e_{n,0} \\ e_{n,1} + e_{n,0} \\ e_{n,2} + e_{n,1} + e_{n,0} \\ \vdots \end{pmatrix} + A \begin{pmatrix} 0 \\ 1+0 \\ 8+1+0 \\ \vdots \end{pmatrix} + B \begin{pmatrix} 0 \\ 1+0 \\ 4+1+0 \\ \vdots \end{pmatrix} + C \begin{pmatrix} 0 \\ 1+0 \\ 2+1+0 \\ \vdots \end{pmatrix} + D \begin{pmatrix} 1 \\ 1 \\ 1 \\ \vdots \end{pmatrix}$$

which we can denote:

$$\boldsymbol{\varepsilon_m = \varepsilon_{tr} + e_n + e_d} \tag{6.4}$$

(note that this is for the superimposed case)

Two things were done to try and recover ε_{tr} from ε_m. The first of these was to repeat hammer hits at least 50 times per basis function. This should reduce the magnitude of the noise by $\sqrt{50}$, and therefore, the contribution to the total error from the noise by the same amount. In addition to this, it was assumed that the long-term behaviour of the static basis function and dynamic basis functions should be the same, i.e.:

$$\boldsymbol{\varepsilon_{tr} \approx \varepsilon_{static}}$$

for large times. If we subsitute this into equation 6.4, and ignore the effects of noise we get the following equation:

$$\boldsymbol{\varepsilon_m - \varepsilon_{static} = e_d}$$

which can be solved to give appropriate values for A, B and C. See figure 6.14 for a visualisation

of this. The resultant strain matches the static values at high times very well, as shown in figure 6.15. Note that to slightly increase the accuracy of the fit, only data from $0.2 - 1\ s$ was used for the calculation. This meant large variations from dynamic effects in the first 0.2 s were ignored.

In the attempted solution, there were two assumptions. First, that drift from noise could be ignored, and second, that the temperature correction could be fitted with a cubic function. To test how well these assumptions held, the corrected basis functions were superimposed in a linearly increasing manner (i.e. such that at timestep one, there is one basis impulse, at timestep two, two time-shifted basis impulses added, another three added at timestep three etc.). This load distribution is equivalent to a linearly increasing load over time (increasing at 52520 Ns^{-1}). This result was compared with the strain calculated under static assumptions to see how well they agree over a longer time frame. If noise was the dominant source of error, they would not be similar. Results for this can be seen in figure 6.16. The correction matches very well. Thus, it appears that the drift of the averaged basis impulses was largely due to temperature effects and that these effects could be well-modelled by a cubic function.

As the correction was for the impulse response of 10,000 superimposed basis impulses, the change in an individual basis impulse is small, as can be seen in figure 6.17. Deck strain gauge three and deck strain gauge five consistently had the most non-linear measured strain at high times and generally the largest drift. Plots for the corrections of other basis impulses looked similar in their general form, although whether the drift was linearly upwards or downwards and exactly how steep they were did vary.

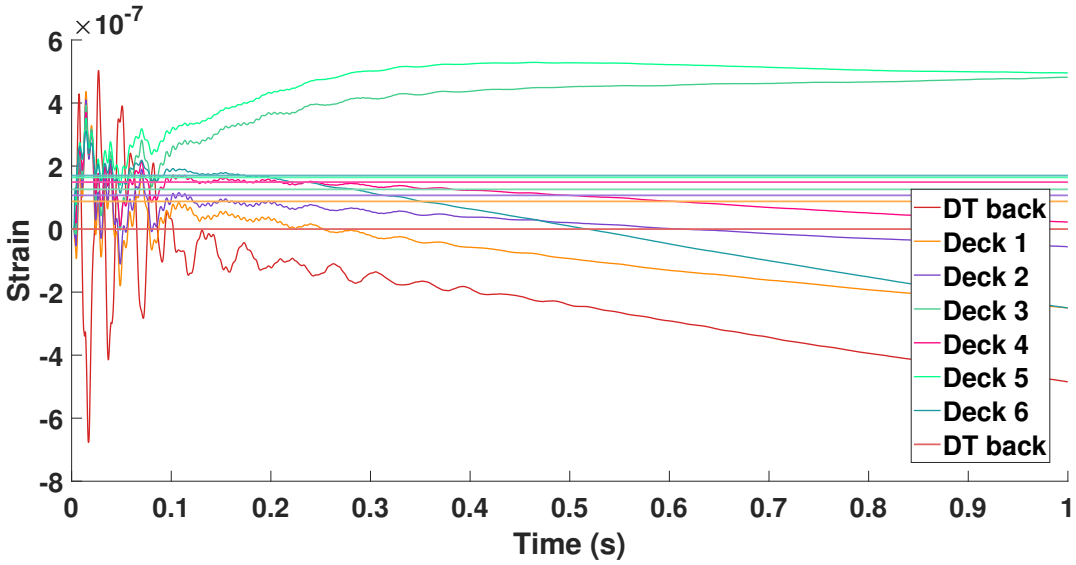


Figure 6.13: A comparison of the strain output under static assumptions (the flat lines) and dynamic responses for the superimposed, uncorrected basis impulses. It is clear that there is significant drift in the model, as for a constant load one would expect the strain output to approach the static values.

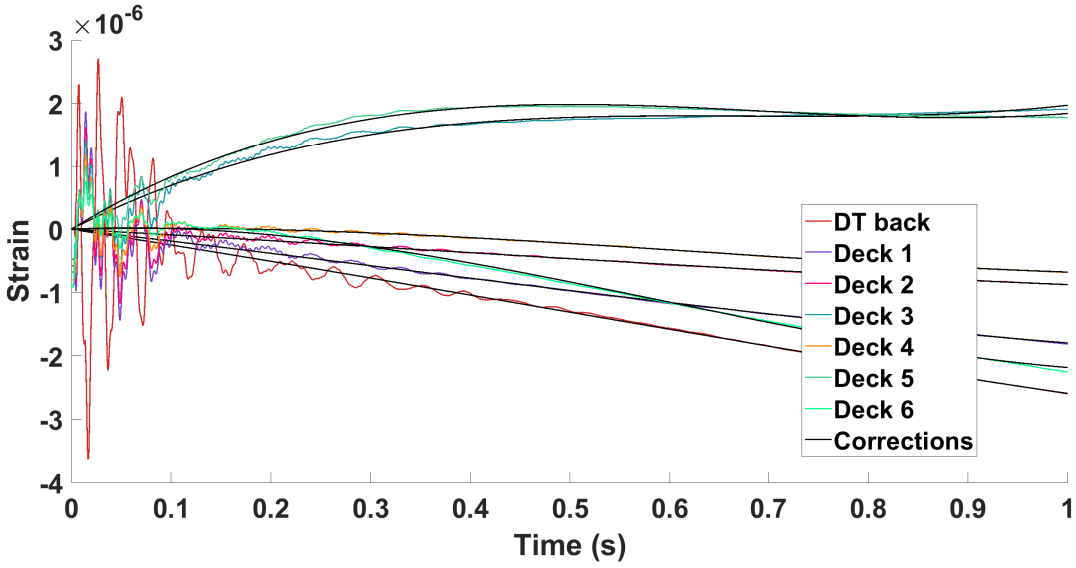


Figure 6.14: The coloured lines show the dynamic strain from superimposed basis impulses with the calculated strain from the static model removed from this. The black lines show the cubic thermal drift corrections. The strain response in this graph is from basis impulses applied at the location of $\boldsymbol{f_6}$.

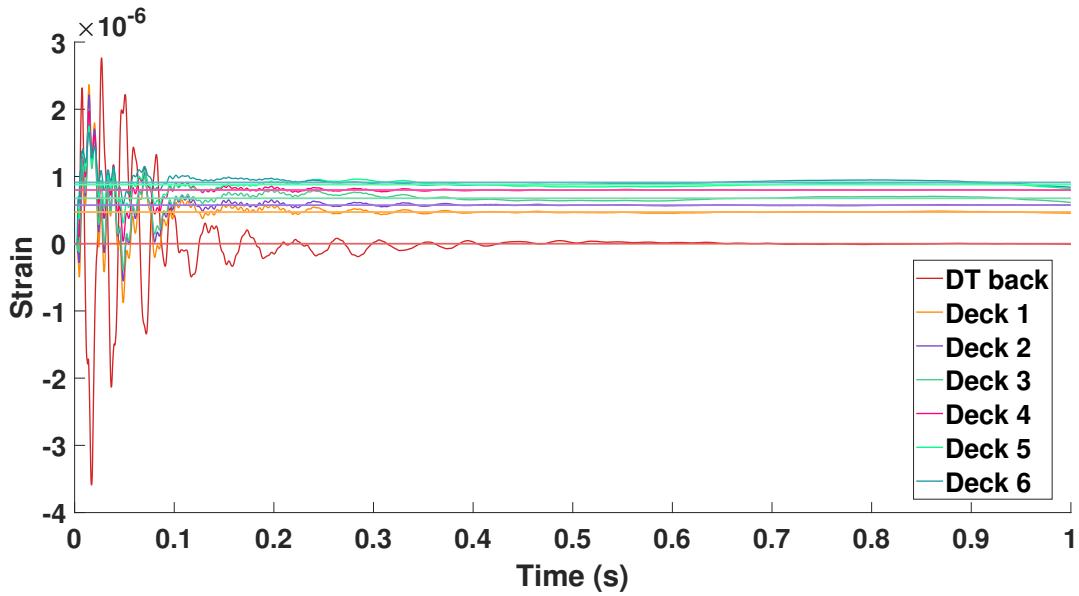


Figure 6.15: The corrected dynamic strain response compared with the calculated static strains caused by the loading applied in figure 6.13. The strain response in this graph is from loads applied at the location of f_6. As can be seen, the cubic fitting allows the dynamic respones to tend towards the static response for larger timescales.

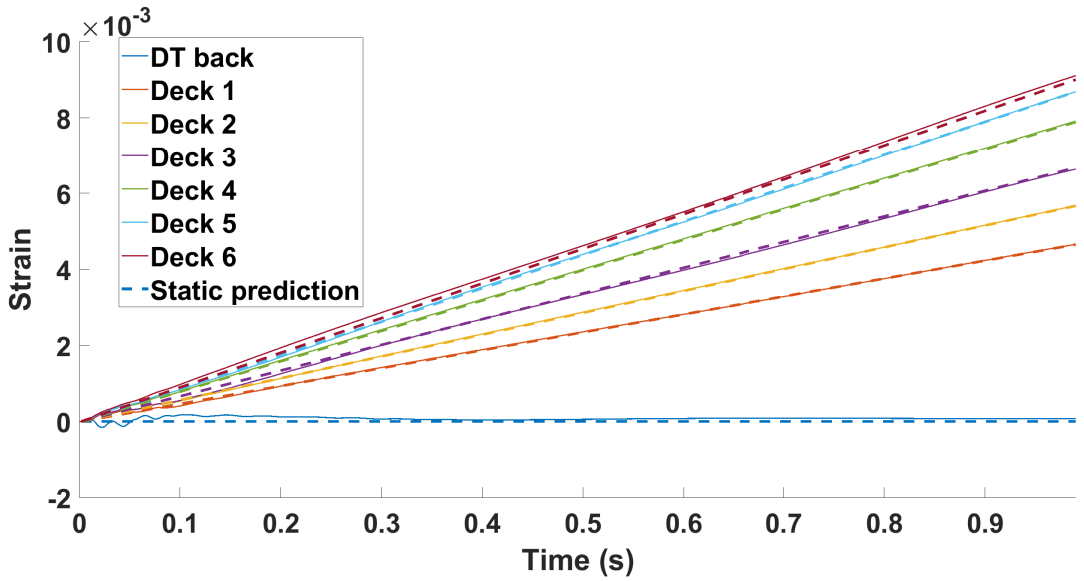


Figure 6.16: This figure shows the strain response from a linearly increasing load applied at the location of f_6. The reason for doing this is to see how much of the noise is likely due to effects that can be corrected with a cubic function. If, for example, a significant proportion of the drift were due to normally distributed noise, one would not expect the function that corrects for a constant load would correct well for a linearly increasing load.

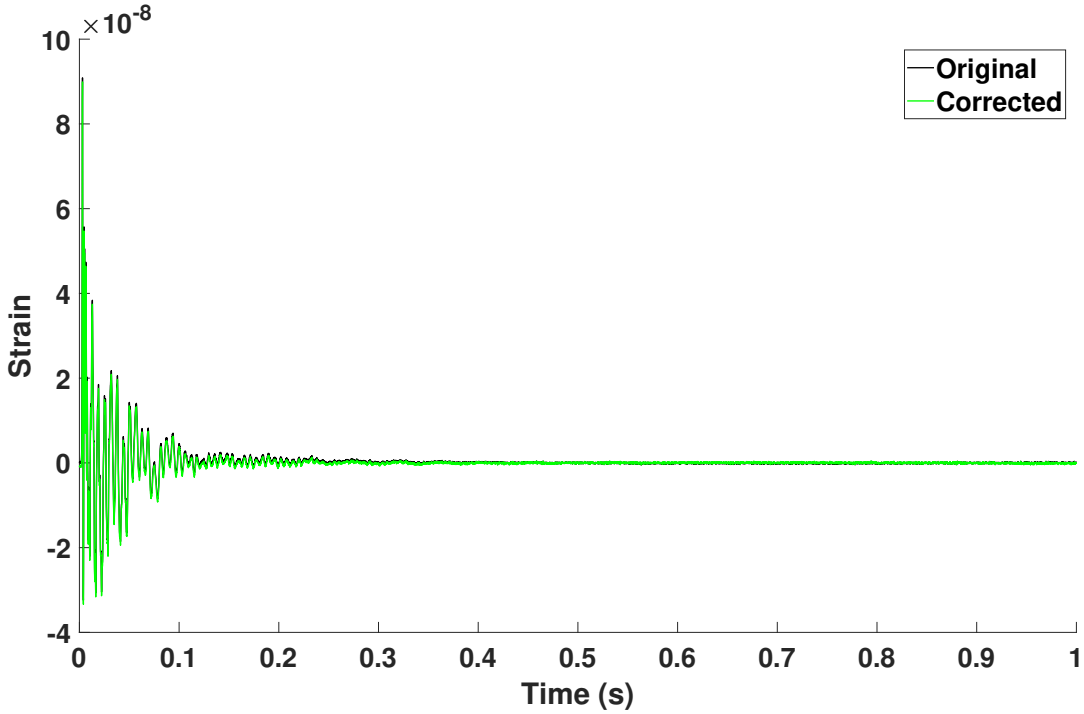


Figure 6.17: A comparison of the original and corrected impulse (strain) response at deck strain gauge 5 from a single applied basis impulse at $\boldsymbol{f_6}$. The change is small for a single impulse.

6.4 Adjusting the shape of the basis impulses

The basis impulses that resulted from the hammer were very narrow (relative to data from scooter stunts). Reconstructing the loads applied to a stunt scooter using a wider basis impulse is more efficient. A wider basis impulse is less susceptible to over-fitting and is computationally cheaper to solve. It was also desirable to have basis impulses in the shape of a triangle, as it would allow the reconstructed impulse to have the shape of a series of connected straight lines between each impulse measurement point. To construct wider basis impulses, time-shifted narrow basis impulses of varying relative magnitude were superimposed. The magnitude of basis impulses varied as 1, 17, 33, ... 145, 161, 145, ... 33, 17, 1, i.e. starting at a value of 1 and increasing by 16 each time until reaching a peak value of 161, before decreasing by 16 until the final impulse has a relative magnitude of 1. Each basis impulse in this series was time shifted by 10^{-4} s. This wider basis impulse was then normalised to have a total impulse of 1 mNs. For a comparison of an original basis impulse and a modified (wider) basis impulse, see figure 6.18. The resultant wider basis impulse approximated a triangular impulse of width 2 ms. To test how well this could approximate the shape of a triangular load, a superposition of 20 times the basis impulse + 40 times the basis impulse time shifted by 1 ms + 60 times the basis impulse etc. up to a peak of 100 times the basis impulse, and then back down to 20 times the basis load, with each increment time shifted by 1 ms ..... (to approximate a triangle of peak magnitude 100 N and width 0.01 s) was made. The reason for doing this was to see if superimposing wider basis impulses time shifted by 1 ms could give a force output that had the form of a straight line. If the force output had a straight line, the shape of the force reconstruction should be able to approximate most force outputs well, as long as the force response is not faster than this timescale. Results were positive and can be seen in figure 6.18. Finally, the strain responses were aligned with the basis impulses. Deck impulses ($\boldsymbol{f_{2-5}}$) were time-shifted such that the peak force of the impulse aligned with the time at which the first deck strain gauge to peak reached 10 % of its peak value. In cases where deck strain gauges reached their maximum strain simultaneously, the deck strain gauge with a lower number was chosen. For $\boldsymbol{f_1}$, the peak of the basis impulse was aligned with the time at which the strain reached 10 % of the first down tube strain minima.

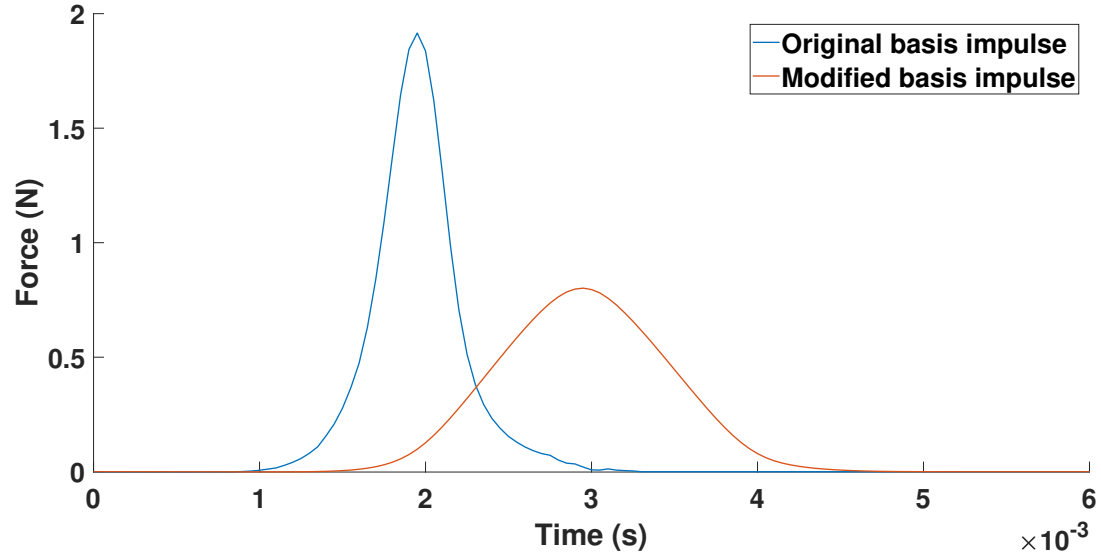


Figure 6.18: A comparison of the original basis impulse, and a modified, wider and more triangular version of the basis load f_4.

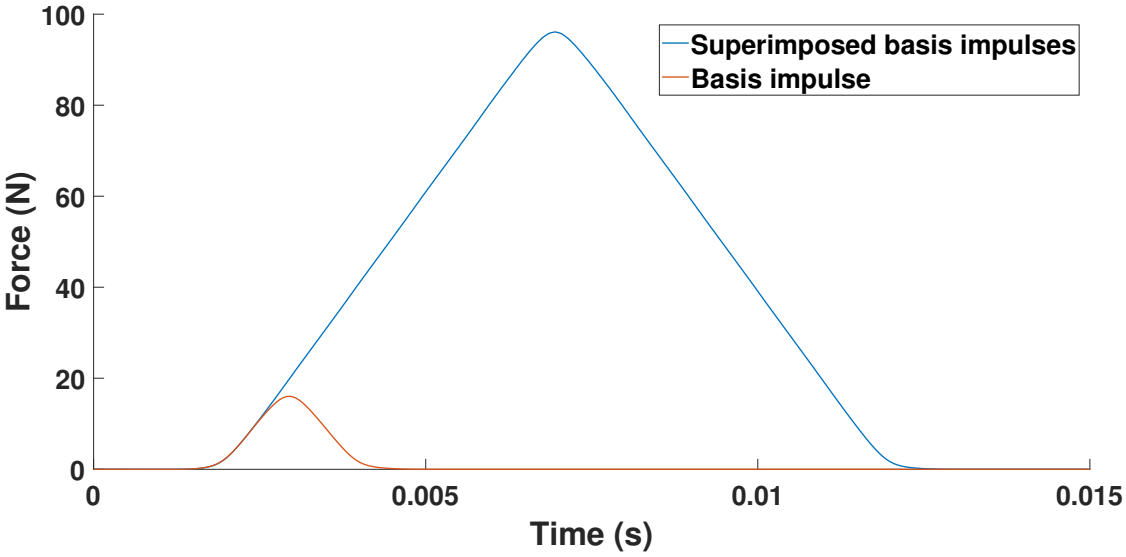


Figure 6.19: The figure shows the widened basis impulse in orange (multiplied by 20), and a series of timeshifted superimposed widened basis impulses that are time shifted by 1 ms. The magnitude of the time shifted impulses varies as: 20, 40, 60, 80 ,100, 80, 60, 40, 20. Given the shape approximates a triangle that is 0.01 s wide, and 0.5 Ns in magnitude, the peak value of force should be approximately 100 N.

6.5 Conclusion

This chapter started by describing the theory behind the dynamic force reconstruction model, and was then followed by a section on the experimental calibration. During the experimental calibration,

the basis impulses were modified in various ways to improve the performance of the model. These modifications included correcting for drift in the basis impulses, and superimposing shifted impulses to fine tune the width and shape of new basis impulses. These new basis impulses are more suitable for the force reconstruction of scooter stunts. The next chapter (7) will add one more modification to the force reconstruction, namely Tikhonov regularisation. This is best discussed in the context of analysing data of scooter stunts, and has therefore been included there. Aside from this, we now have functioning static and dynamic force reconstruction models, as well as a suitable experimental setup for use on stunt scooters. The stage is now set for analysing real-world scooter stunt data.

Chapter 7

Force Reconstructions

7.1 Introduction

The previous chapters have established: the experimental setup (chapter 4), and models that calculate the applied load to the scooter as a function of measured strain (see chapter 5 for a model with static assumptions, and chapter 6 for a model that includes dynamic effects). The stage has been set for an investigation into the loads applied to stunt scooters during use. One final modification to the dynamic model, the inclusion of Tikhonov regularisation (and a justification for suitable regularisation parameters) are included at the start of this chapter, in section 7.2. This chapter then examines the strain and force histories of the scooter during stunt use. The order in which stunts are analysed in this chapter is the following: bunnyhops (figure 7.4), j-hops (figure 7.5), tailwhips (figure 7.11), heelwhips (figure 7.12), barspins (figure 7.13), opposite barspins (figure 7.14), backside 180s (figure 7.15), back side half-cabs, frontside 180s (figure 7.16), frontside half-cabs, backside 360s (figure 7.17) and frontside 360s (figure 7.18). These stunts are the common 'basic' stunts on a scooter. The stunts provide the foundation for many other stunts, which are multiples or combinations of these.

7.2 Tikhonov regularisation

Even with constraints and the widening of basis impulses from the previous chapter, the reconstruction of the forces in the scooter was still ill-posed. Ill-posed solutions are prone to overfitting data. In the context of this project, unregularised data had impulses of rapidly fluctuating magnitude. The fluctuations in magnitude were too high-frequency to be realistic (look at the relative frequency of the loading in figure 7.1a and the measured strain in figure 7.1b). The problem of ill-posedness is common with inversion problems; there is extensive literature on the topic (e.g. [131–134]). Figures 7.1a and 7.2 show the differences between static, unregularised dynamic, and Tikhonov reconstructed force histories (from j-hop data). As can be seen, the unregularised data calculates a rapidly oscillating load history. The oscillations, in large part, (likely) cancel each other out, and the true load history is a somewhat smoothed-out version of this. As the data is being over-fitted in this way (due to noise, or to accuracy limitations of the model), Tikhonov regularisation can smooth out the data. For a system of equations $\mathbf{Ax} = \mathbf{b}$, Tikhonov regularisation functions by adding a penalty term. The penalty term smooths out the function by applying a cost term, which has a more significant impact on large values of the basis impulse coefficients. Mathematically, this is formulated as:

$$\min_{\mathbf{x}} \left\{ \|\mathbf{Ax} - \mathbf{b}\|^2 + \lambda \|\mathbf{Lx}\|^2 \right\} \tag{7.1}$$

Where $\|\mathbf{Ax} - \mathbf{b}\|^2$ is the residual norm. The residual norm represents the discrepancy between the observed data $\mathbf{b}$ and the model $\mathbf{Ax}$. If one can perfectly reconstruct the data, $\|\mathbf{Ax} - \mathbf{b}\|^2$ is zero. $\lambda \|\mathbf{Lx}\|^2$ is the regularisation term, which imposes a penalty on the solution $\mathbf{x}$. λ is the regularisation parameter, which controls the trade-off between the data fidelity and regularisation terms. The higher λ is, the smoother the reconstructed force will be, at the expense of fit to the measured solution. λ is defined to always be positive. $\mathbf{L}$ is the regularisation matrix which controls the relative weighting of different parts of the data. One can, for example, construct $\mathbf{L}$ to weigh the solution more heavily to data points known with greater precision. In our case, there were no apriori grounds to elevate the importance of one basis load over another, so the identity matrix was initially used for the regularisation matrix (see below for more details). As alluded to in chapters 5 and 6, equation

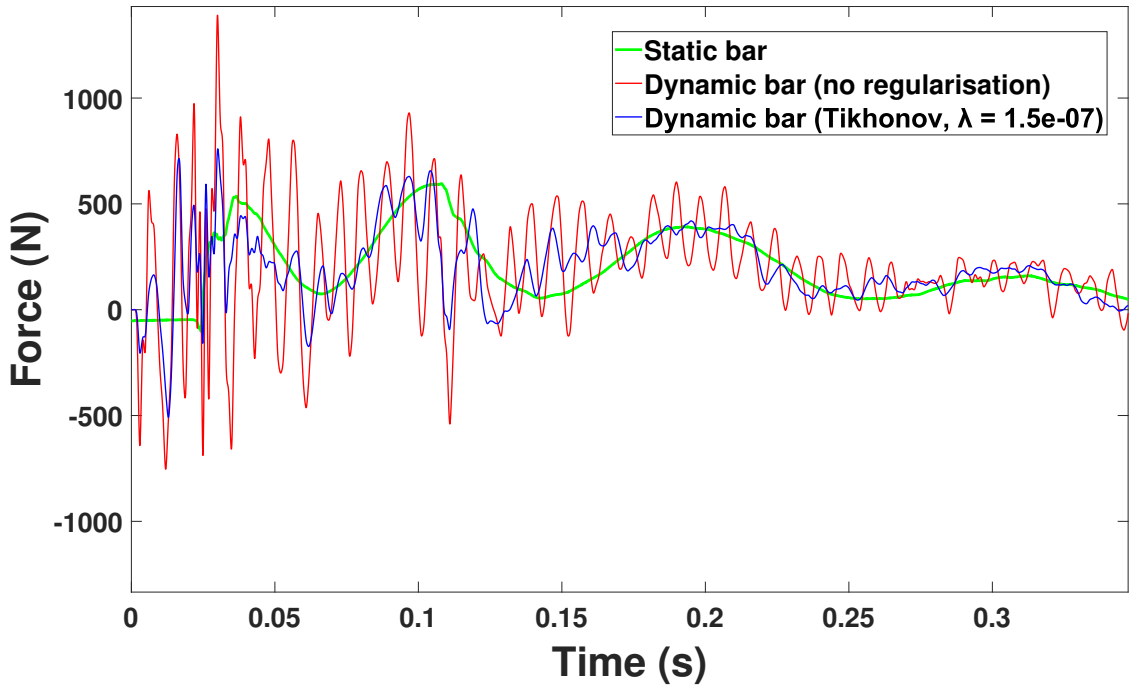
7.1 was also subject to the constraint that the deck impulses must be positive (downwards).

Choosing suitable values for λ

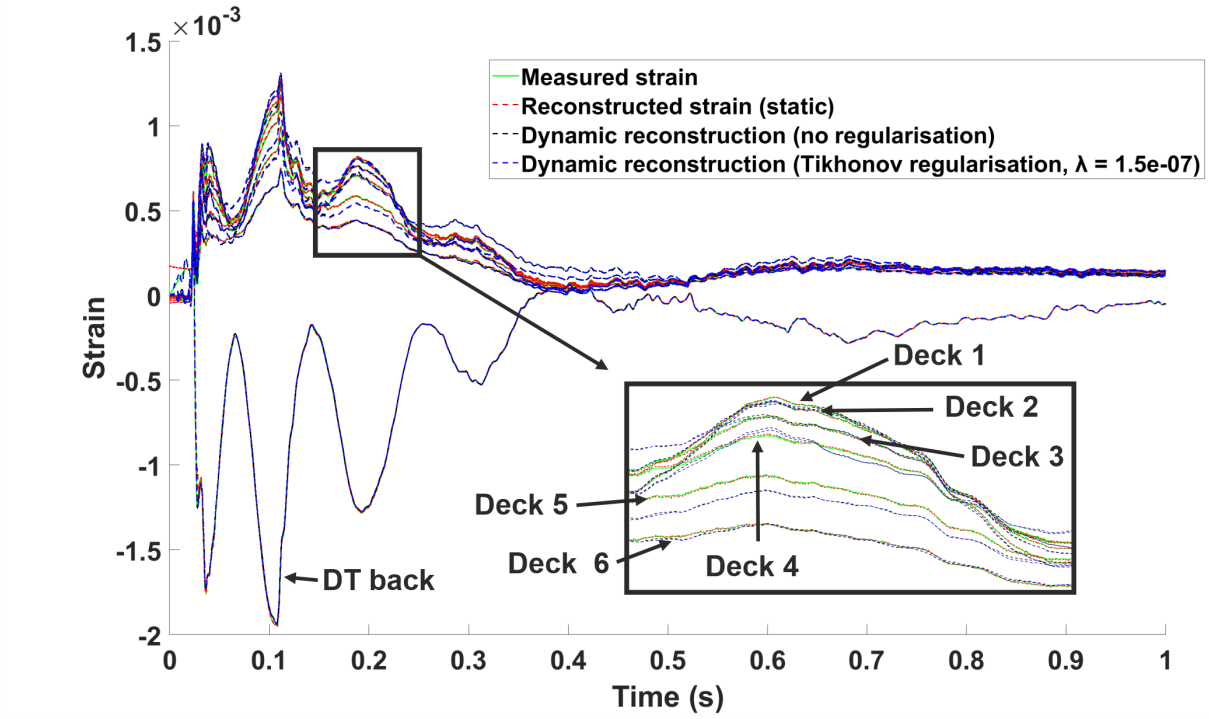
When using Tikhonov regularisation, a key question is which value of λ to use. It is often not possible to calculate a suitable value for λ on apriori grounds. Various solutions have been proposed in the literature to give a suitable criterion for determining λ [131, 132]. A common method for this is the L-curve method [132, 134]. The L-curve method aims to optimise the trade-off between fit to measured data and realistic smoothing of the solution. Generally, if one makes a log-log plot of the 'regularisation norm' term $\|\mathbf{Lx}\|$ against the residual norm $\|\mathbf{Ax} - \mathbf{b}\|^2$ for various values of λ, the curve will form a distinct L shape [132]. An example L-curve from a reconstruction of j-hop data can be seen in figure 7.3a. The value of λ chosen corresponds to the point of highest curvature in the L (i.e. at the corner of the L).

As only a finite number of values of λ can be plotted, an initial test with λ varying between 10^{-10} to 10^{-5} was carried out. Following this, the test was repeated with narrower ranges to more precisely determine the appropriate value for λ. Subsequent tests had the ranges 7×10^{-8} to 4×10^{-7} and 9×10^{-8} to 2.1×10^{-7}. The final calculated optimal value of λ was 1.5×10^{-7}. As previously mentioned, a comparison of the regularised data with the static and unregularised data can be seen in figures 7.1a, and 7.2, with the strain distributions in figure 7.1b.

As shown in figures 7.2 and 7.1a, the static force does not have spurious high-frequency loading when unconstrained. This is unsurprising. The static model assumes that the total strain measured depends only on the strain measured at a single time step, so one would expect the frequency of the reconstructed load to match that of the strain. It was, however, the case that immediately after landing, the deck forces calculated by the static model tended to be almost entirely comprised of $\boldsymbol{f_2}$, even when the rider's feet were not above the location of $\boldsymbol{f_2}$. Consequently, tests to obtain a suitable value of λ for the static model were carried out. For the static model, as each time step is solved individually, it is possible to calculate a value for λ according to the L-curve criteria at each time step. The decision was made to use the criteria at the point of maximum measured down tube strain in a j-hop. This is a suitable point for which to optimize the loading, as it likely causes the



(a) A comparison of unregularised static, regularised dynamic and unregularised dynamic force reconstructions on handlebar loads for the landing of a j-hop (see figure 7.5 for a j-hop). The spurious high frequency oscillations in the unregularised model are clear, and can still be seen to a lesser extent in the model regularised with $\lambda = 1.5 \times 10^{-7}$.



(b) The reconstructed strains according to various force reconstruction models from the landing of a j-hop. For a diagram showing where each strain gauge is on the scooter, see figure 5.9. The labels for the strain gauges are for the measured strain and static force reconstruction. The reconstructed strains according to the dynamic models are in the same descending order (i.e. the highest strain is from deck 1, the lowest in deck 6) except that deck strain gauge 4 has a higher reconstructed strain than deck strain gauge 3. The frequency of oscillation on the measured strain is much lower than that for the calculation of an unregularised dynamic force, indicating that the high frequency oscillations in the applied load are spurious.

Figure 7.1

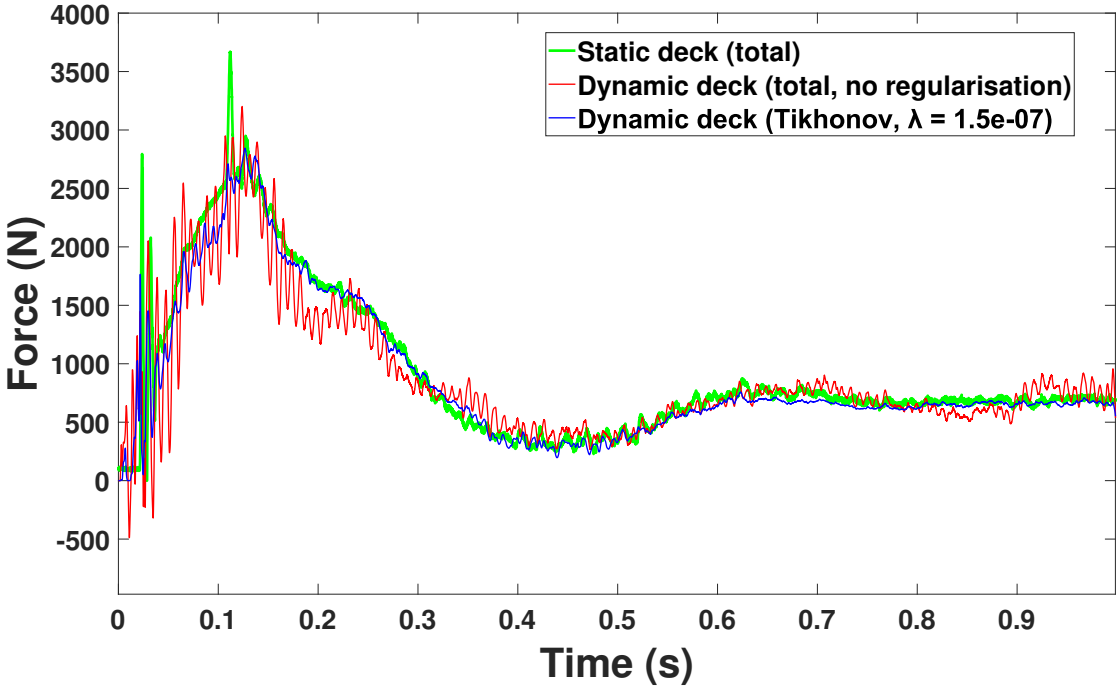
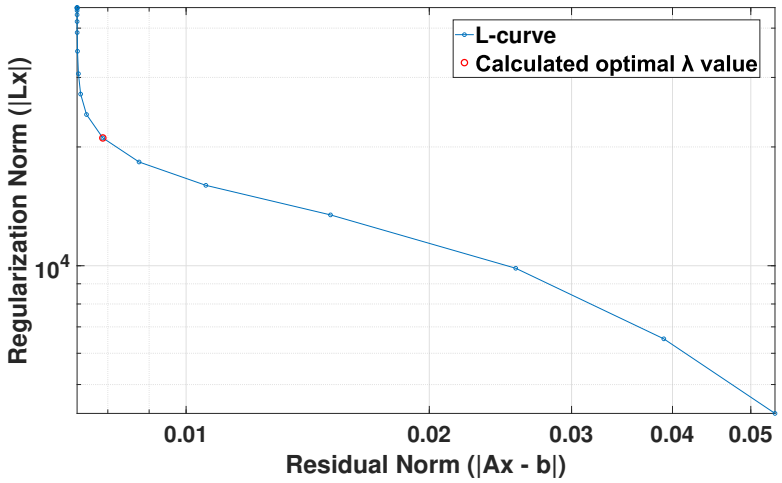


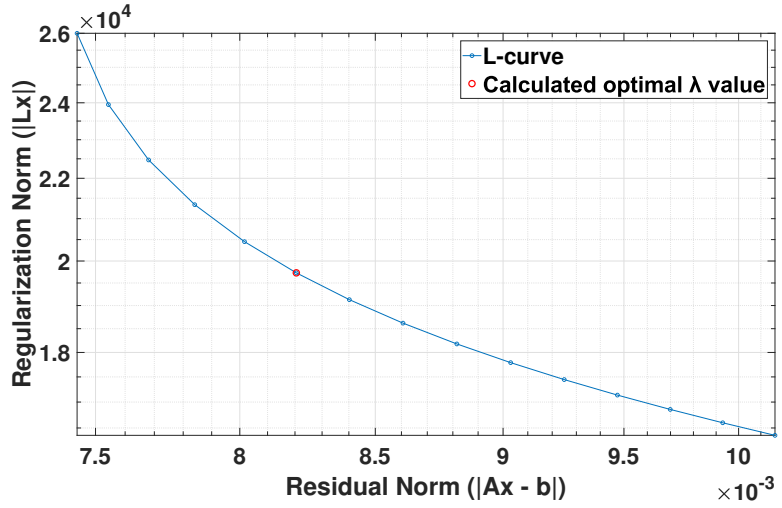
Figure 7.2: A comparison of unregularised static, regularised dynamic and unregularised dynamic force reconstructions on the total deck loads for the landing of a j-hop. The spurrious high frequency oscillations in the unregularised model are clear, and can still be seen to a lesser extent in the model regularised with $\lambda = 1.5 \times 10^{-7}$.

highest stresses in the scooter. The curve formed an approximate L shape, however the point of maximum curvature was at the top of the diagram. The values at this point were so small (less than 10^{-10}) that they made no observable difference to results. In response, a value that looked like it fitted in the corner of the L was chosen. This corresponded to a value of λ of 3×10^{-8}. Even with the regularisation given by the L-curve criteria, there were still some spurious oscillations for the dynamic model, particularly in the handlebar loads of the dynamic model (see figure 7.1a). Because of this, a force reconstruction with a 'heavily regularised' model was also carried out. In this model, the regularisation of deck loads was three times as large, and the regularisation on the handlebars was 12 times that given by the L-curve criteria. A heavily regularised static model was also made, with a value of λ of 1.2×10^{-7}. In total, for the scooter stunts in this chapter, each strain history for the landing of a stunt was solved five times. There were three static models (unregularised, regularised with $\lambda = 3 \times 10^{-8}$ and regularised with $\lambda = 1.2 \times 10^{-7}$) and two dynamic models (regularised with $\lambda = 1.5 \times 10^{-7}$, and regularised with a non-identity matrix

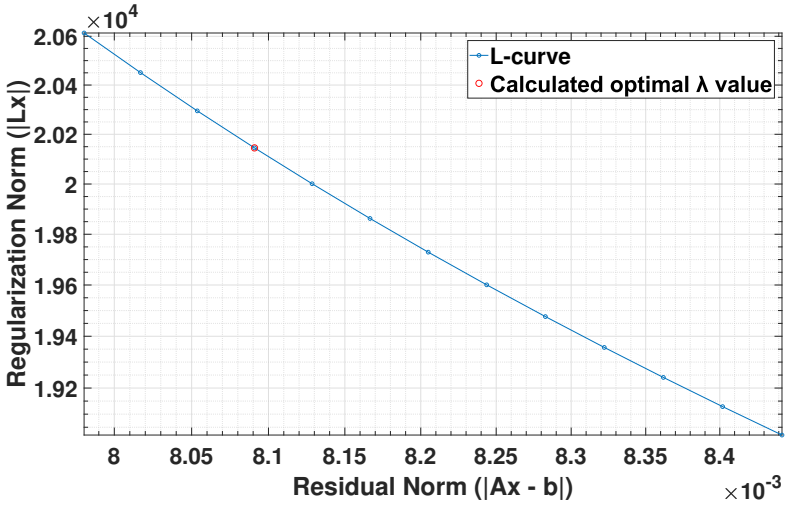
$\mathbf{L}$ such that deck impulses had an equivalent regularisation of $\lambda = 4.5 \times 10^{-7}$, and handlebar impulses had an equivalent regularisation of $\lambda = 1.8 \times 10^{-6}$). In the summary tables of results that follow, only results from the moderately regularised ($\lambda = 3 \times 10^{-8}$) static model and both dynamic models are shown. The reason for this is that the static results were all very similar.



(a)



(b)



(c)

Figure 7.3: Above are successive repititions of the L-curve technique to refine the appropriate value of λ. As only a finite number of points can be evaluated on the L-curve, the calculation is repeated with successive degrees of precision as the approximate location of the L-curve is more closely known.

7.3 General information

Almost all strain data collected was accompanied by video filmed with a Panasonic Lumix G7 camera [135], shooting in 1920×1080 resolution at 50 Hz. Video recording allows for the approximate synchronisation of stunts with their strain histories. Synchronisation made it possible to notice particular features of a specific stunt and to relate these to the strain and force history. It also made it possible to identify cases where the rider fell off the scooter (these results were not used) or landed in an unusual way. Data was essentially processed the same way that the calibration data was processed. One difference was that for some of the data collection, the scooter was being moved at the start (e.g. to show the camera when the data logger was turned on to help with video synchronisation). To ensure that there was still a 'zero-point' to allow for a drift correction, the rider would dismount during riding and stabilise the handlebars with his hands (to stop it from falling over). This point could then be used in conjunction with the end zero-point to obtain a linear drift correction. The same approach was used for 16 of the j-hops and nine of the frontside 360s in cases where one of the deck strain gauge wires snapped before the data had finished being collected.

7.3.1 A note on rider stances

It is worth noting at this point that scooter riders generally have one of two stances. Scooter riders usually have their feet pointing slightly to one side when riding a scooter, either to the right or left. If the feet point to the right, the left foot of the scooter rider is in front of the right foot; this is known as a 'regular' stance. If the feet point to the left, with the right foot forward, this is called a 'goofy' stance (this naming convention originates with surfing). The reason for bringing this up is that certain stunt naming conventions are stance-dependent. For example, a backside rotation is where a rider's back faces the direction of motion (assuming one is not riding backwards) after a $90 - 170^\circ$ spin. For regular riders, backside rotations are clockwise (to the right), whereas for goofy riders, they are to the left. Similarly, the direction of 'whipping' the deck to perform a tailwhip or heelwhip depends on the rider's stance (clockwise for regular riders and anticlockwise for goofy riders).

7.4 Bunnyhops and j-hops

7.4.1 A note on terminology

Despite being the simplest trick/stunt people perform on scooters, there is some variation in the terminology people use when referring to 'hopping' or 'jumping' on a scooter. In this thesis, we will call the type of hop where the rider lifts the front and rear wheels at almost the same time (see figure 7.4) as a bunnyhop, and the type of hop where the rider lifts the front wheel first before levelling out the scooter as a j-hop (see figure 7.5). Bunnyhops are more commonly used by beginners and are also more similar to the type of hop people usually do when performing certain stunts like tailwhips (taking the scooter off being level can make it harder to perform the manoeuvre. J-hops are often done when trying to jump onto obstacles or to jump high). J-hops are often the way experienced scooter riders jump/hop. For the purpose of this section, a description of the strain evolution and summary statistics of each type of hop will be given. More focus will be placed on the j-hop as it is generally used more by experienced scooter riders and results in greater strain and loading in the scooter.

7.4.2 Bunnyhops

A bunnyhop is the simplest scooter stunt. It involves the rider jumping, with the wheels leaving the ground at approximately the same time. The feet should be in contact with the deck. An image of a bunnyhop and its associated strain history can be seen in figure 7.4. You can see the rider preparing to hop in frame 2, getting ready to descend before crouching and pushing down hard on the footplate in frame 3. The rider then starts jumping, starting to leave the ground in frame 4. The rider then reaches peak height in frame 5, and lands in frame 6. The largest strains in the deck and handlebars are immediately upon landing. Summary statistics for the peak strains and loads from 32 bunnyhops can be seen in tables 7.1 and 7.2.

Table 7.1: A Table showing summary statistics of the variation in the maximum magnitude of strain measured in each strain gauge for 32 bunnyhops. Note that the maximum strain in each strain gauge does not necessarily occur simultaneously during the stunt (e.g. often the maximum magnitude of strain the down tube strain gauge is earlier in time than the maximum strains measured in the deck).

All max strains (10^{-3})							
	DT back	Deck 1	Deck 2	Deck 3	Deck 4	Deck 5	Deck 6
Mean	1.35	0.91	0.87	0.80	0.72	0.58	0.43
Std. dev	0.35	0.11	0.10	0.08	0.07	0.05	0.03
Median	1.36	0.91	0.88	0.80	0.73	0.58	0.43
Max	2.22	1.17	1.07	0.95	0.87	0.70	0.52
Min	0.69	0.71	0.68	0.63	0.56	0.49	0.36

Table 7.2: Summary statistics on the variation in peak (maximum magnitude) handlebar and deck loads for 32 bunnyhops.

Max. Loads (N)	Bar forces			Total deck forces		
	stat, reg	dyn, reg	dyn, reg (h)	stat, reg	dyn, reg	dyn, reg (h)
Mean	405	762	237	2814	2397	2403
Std. dev	110	152	88	414	215	177
Median	401	740	216	2615	2338	2362
Max	678	1023	446	3600	2998	2857
Min	212	523	105	2331	2130	2108

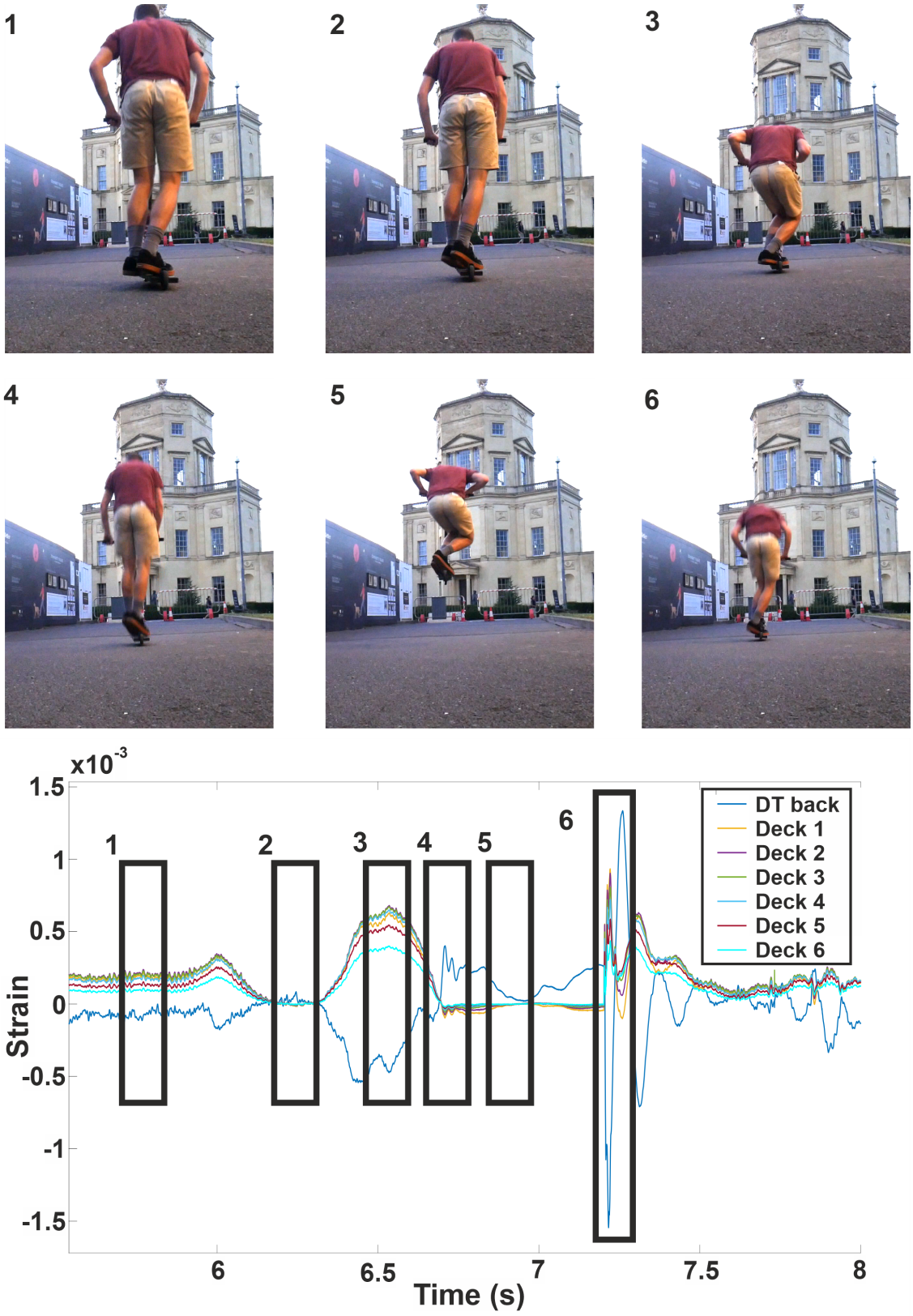


Figure 7.4: The strain evolution of a bunnyhop. The main stages of the stunt are shown with the (approximate) corresponding regions of the strain history. The rider is riding along at 1, before preparing to crouch at 2 and crouching at 3. The rider then starts to leave the ground at 4, reaches the height of the jump at 5 and lands at 6.

7.4.3 J-hops

An example j-hop can be seen in figure 7.5. The rider is getting ready to crouch in frame 1, crouches at 2 and starts jumping at 3. You can clearly see the rider intentionally lifting the front wheel first in frames 3 and 4, before levelling out in frames 5 and 6 as the rider reaches the peak of the jump. The pulling and lifting of the handlebars associated with lifting the front wheel first is presumably what results in the greater strain in the handlebars (the rider commented that he could feel himself pulling back on the handlebars as he performed the initial part of the j-hop). The rider then descends in frame 7 and lands in 8. The major distinction between the initial part of the j-hop and the bunnyhop is a greater pull on the handlebars and, therefore, more strain in the down tube. Additionally, the force in the handlebars tended to be larger upon landing j-hops, likely because the rider tends to lean back more when performing a j-hop than for a bunnyhop. The peak strains in the deck and down tube were quite similar in magnitude when the rider was crouching before leaving the ground compared to landing the j-hop. Below are some detailed plots showing the various force reconstructions and strain reconstructions of a j-hop. Some general features of these results (e.g. the general relation between maximum static and dynamic loads in the scooter) are representative of other scooter stunts. Similar plots have not been included for other stunts for the sake of conciseness.

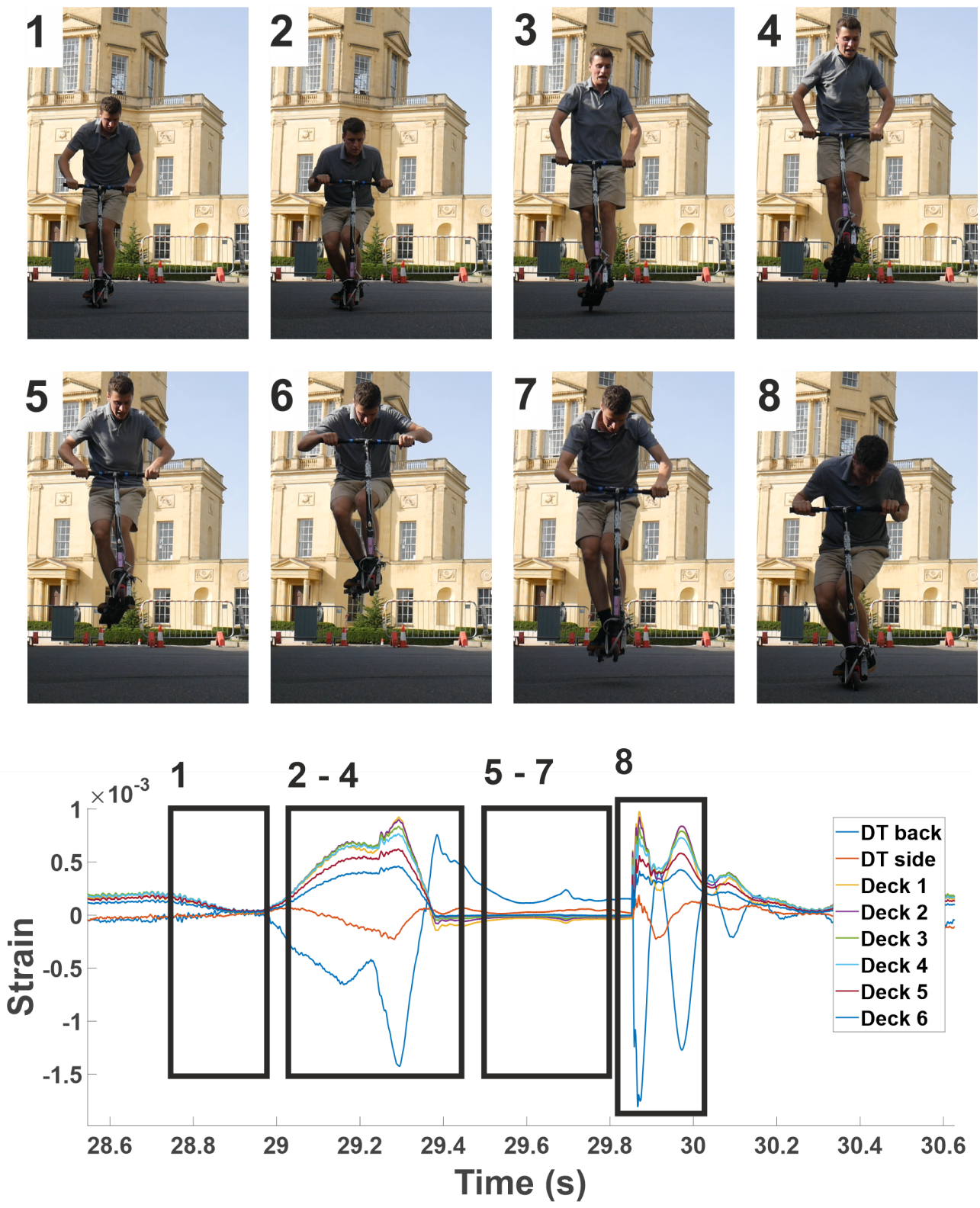


Figure 7.5: The strain evolution of a j-hop (note DT stands for down tube). The main stages of the stunt are shown with the corresponding regions of the strain history. After preparing to jump at stages 1-2, the rider begins the jump across stages 3-4, raising the front wheel first (more so than for a bunny hop) before bringing the scooter with him, levelling the scooter out and reaching peak height at 6. The rider then descends at 7 and lands at 8.

Static force reconstruction with strain

Figure 7.6 shows the force reconstruction of the landing of a j-hop. As can be seen, the peak strain in the down tube occurs much earlier than in the deck (around 0.05 s rather than around 0.17 s). Figure 7.7 shows a j-hop where the landing is 'front heavy', i.e. that the rider lands leaning forwards. Such landings are often (probably) associated with a large downwards force through the crossbar (it at least feels that way), with riders often commenting that they cause pain in the wrists. The figure is included to show that the precise nature of the strain history (and loading) can vary significantly. Note that the peak magnitude handlebar load in this case is negative.

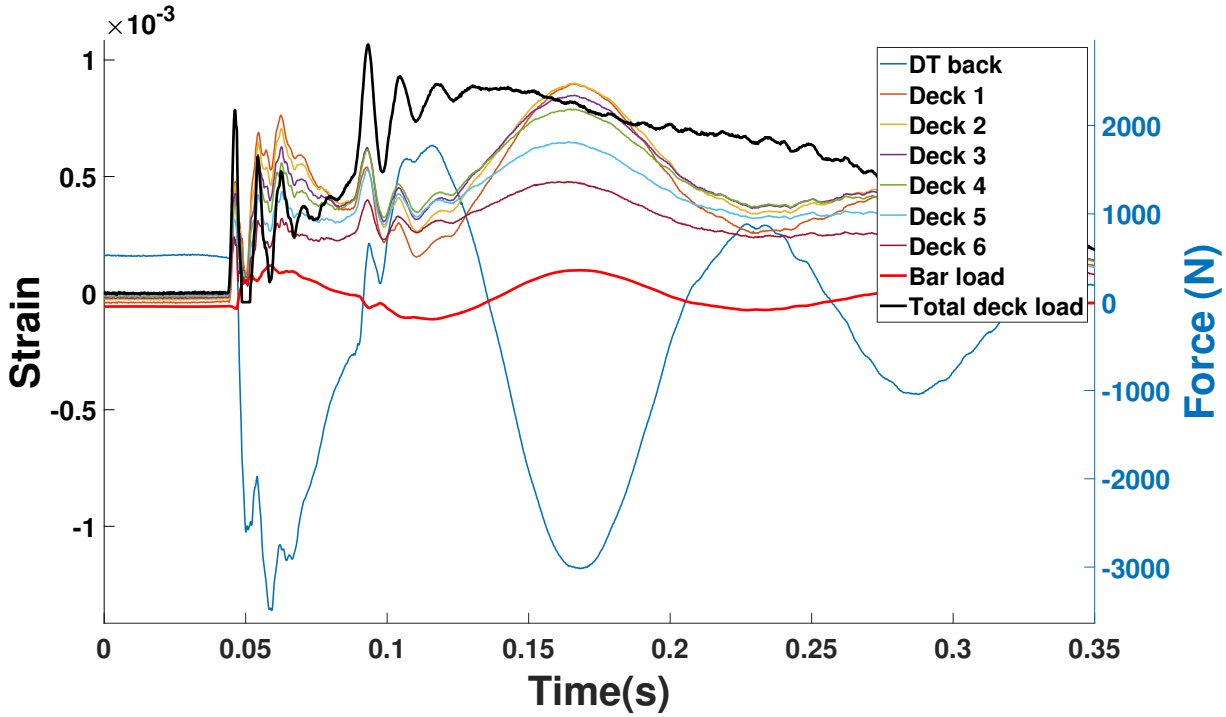


Figure 7.6: The measured strain and static force reconstruction of a j-hop.

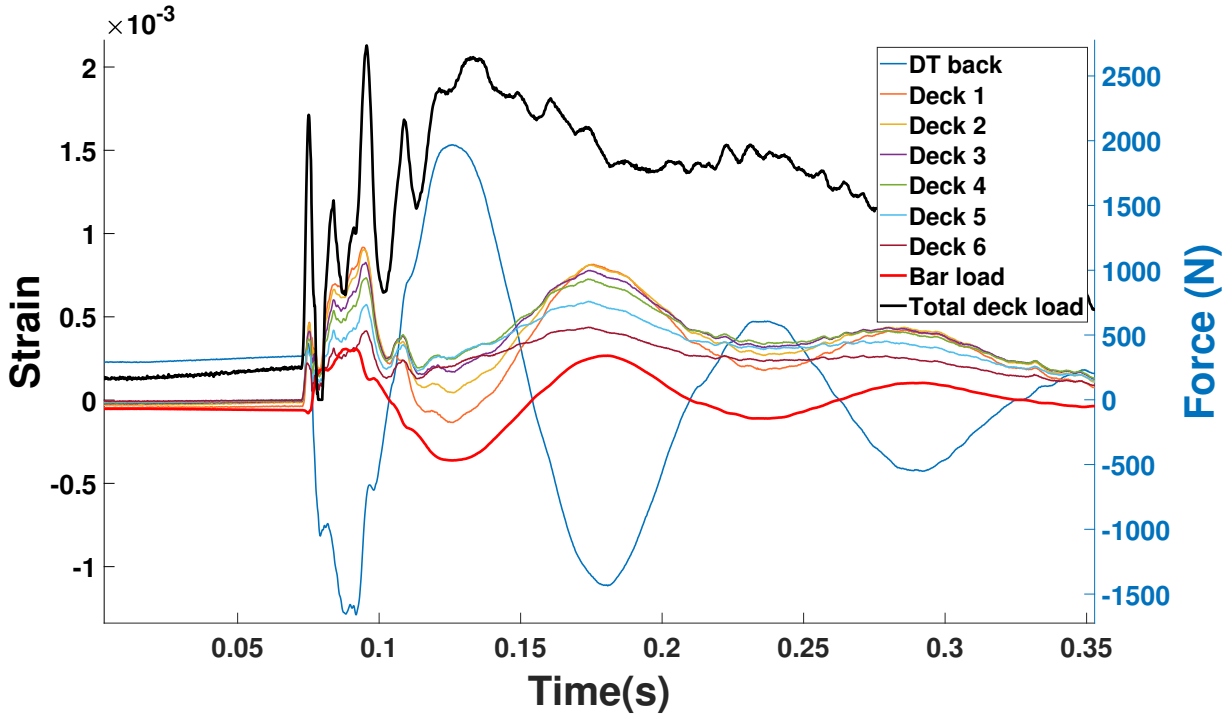
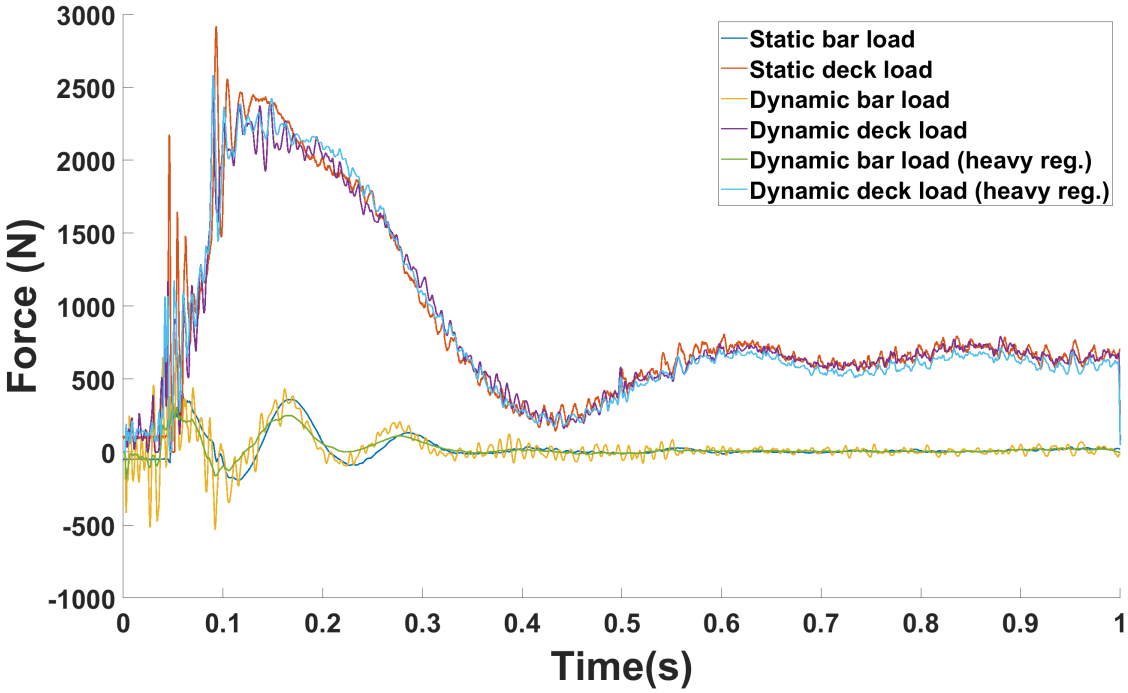


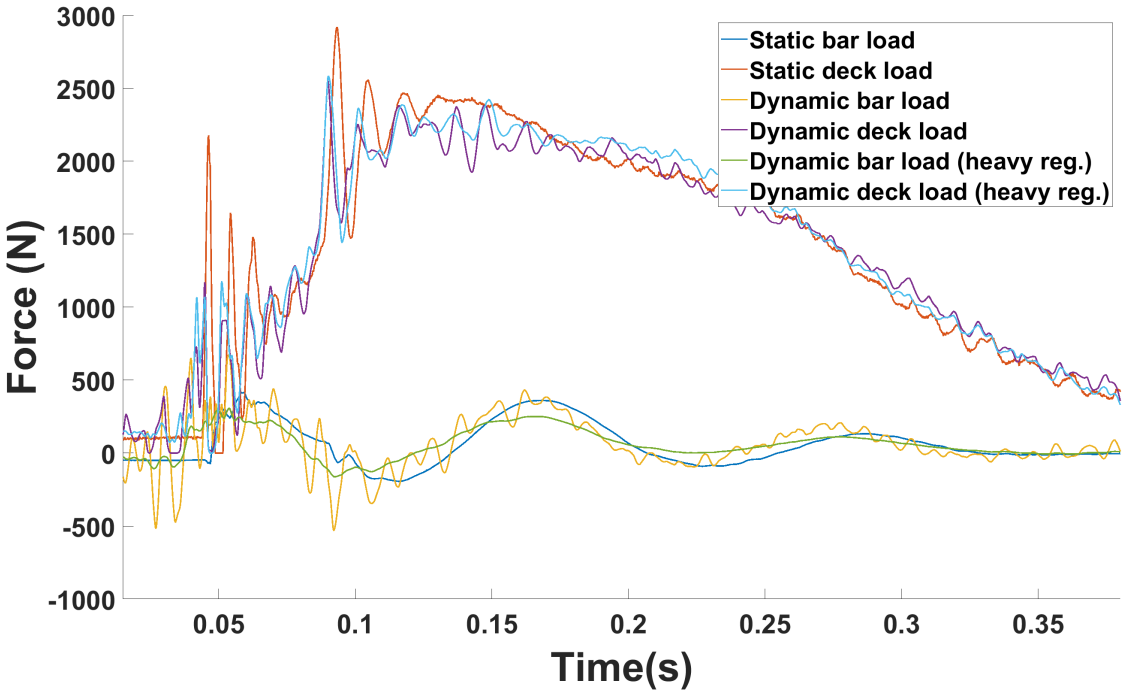
Figure 7.7: The measured strain and static force reconstruction of a j-hop where the landing is more 'front heavy'. Notice that here the largest strain at the back of the down tube (DT back) is tensile, not compressive.

Force reconstruction comparison

The dynamic force reconstruction that is regularised according to the value given by the L-curve criteria can be seen in figure 7.8. It differs from the static force reconstruction in several key respects. One is that there is overfitting on the handlebars, meaning there are high-frequency oscillations in the calculated bar load. Because of these high-frequency oscillations, the maximum magnitude of the handlebar load calculated by this model is significantly higher than the total handlebar load, even though the total impulse over the the entire force reconstruction is very similar. These oscillations are not present for the heavily regularised model. The dynamic force reconstructions also tend to have a lower maximum load value for the total deck load. One possible reason for this is that a constant dynamic load will initially overshoot the steady-state value, so to match a transient strain peak, a lower load magnitude may suffice. This may also explain why the maximum load magnitude of the heavily regularised Tikhonov bar load is lower than that of the static bar load. The features of this graph appear to be representative of the j-hops collected, as table 7.4 shows. The force histories are in close agreement at larger times. A factor that makes this more likely is that the long-term behaviour of a constant dynamic load has been modified to match that of the static case.



(a)



(b)

Figure 7.8: A comparison of the static force reconstruction (with $\lambda = 3 \times 10^{-8}$) and both dynamic force reconstruction models on a j-hop. It is clear (especially for the handlebar loads) that the heavily regularised dynamic model has fewer spurious oscillations, and therefore is much more similar to the static force reconstruction.

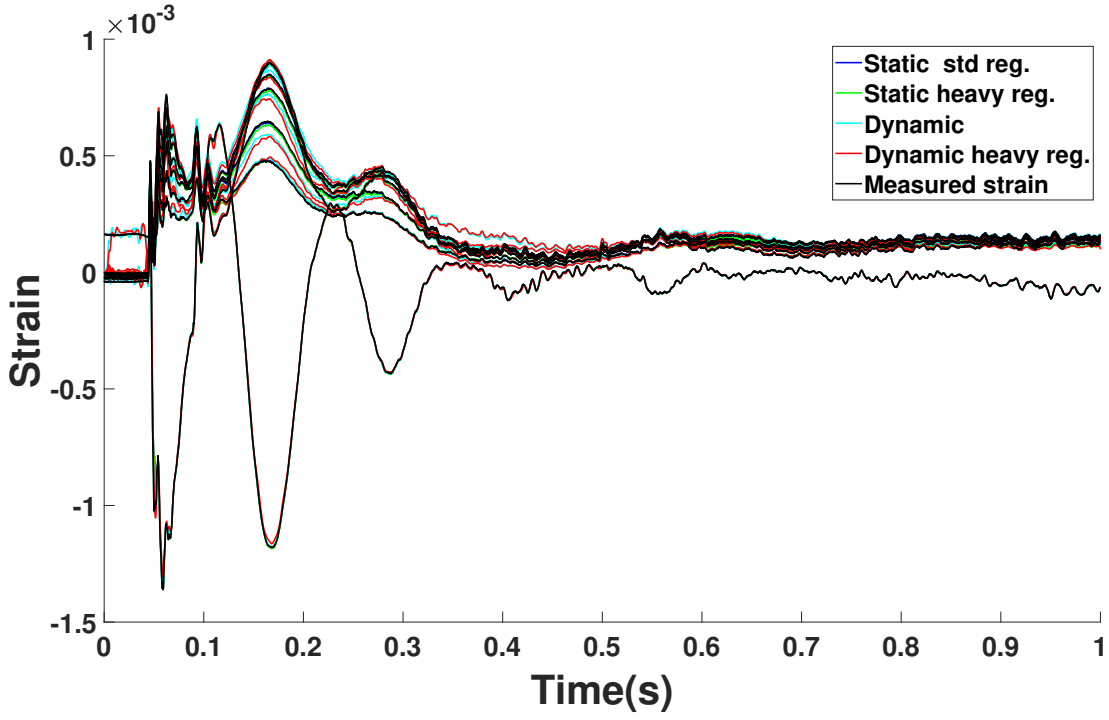
Strain reconstruction

A comparison of the reconstructed strains according to the various models with the measured strain can be seen in figure 7.9. Generally, the reconstructed strains are in good agreement with the measured strain. The static reconstruction tends to reconstruct the strain more closely than the dynamic strain. This is of particular note around the region of the peak strains measured in the deck, which can be seen in figure 7.9. For the dynamic reconstructed deck strains, the values in strains for some of the strain gauges are either above or below the measured value (although the peak measured deck strain is still quite similar). Perhaps unsurprisingly, the dynamic model struggles with strain matching most in deck strain gauges 3 - 5 (see figure 7.9b and the figure caption). Whereas the measured strain has either deck strain gauge 1 or 2 having the peak strain value, and then has peak strains descending with strain gauge number, the dynamic model often has deck strain gauge 4 giving a higher peak strain than deck strain gauge 3. This is probably the region where the complexities of loading from the rider's feet most impact the measured strain. Outside of this region, the strains on the deck are very similar. Thankfully, the peak strains measured in the deck are usually very similar as they are in deck strain gauges 1 and 2. The one region where the dynamic force reconstruction is consistently more accurate is shortly after the landing of a stunt, as can be seen in figure 7.10.

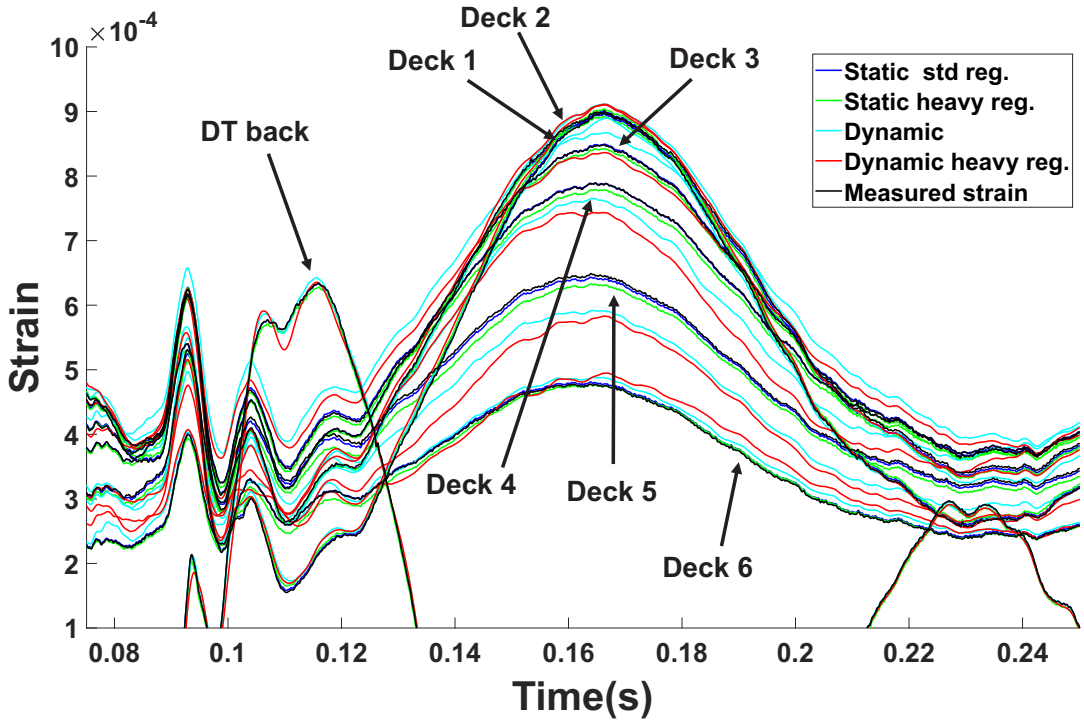
Below are some tables summarising some of the data of the 36 j-hops analysed:

Table 7.3: A table showing summary statistics from 36 j-hops for the variation in the maximum magnitude of strain measured in each strain gauge.

All max strains (10^{-3})							
	DT back	Deck 1	Deck 2	Deck 3	Deck 4	Deck 5	Deck 6
Mean	1.72	1.02	1.00	0.94	0.88	0.74	0.56
Std. dev	0.30	0.15	0.15	0.16	0.15	0.13	0.10
Median	1.65	0.98	0.96	0.91	0.85	0.70	0.53
Max	2.61	1.42	1.32	1.27	1.20	1.01	0.76
Min	1.17	0.78	0.76	0.68	0.65	0.57	0.43



(a)



(b)

Figure 7.9: A graph showing the reconstructed strains of a j-hop for various force reconstruction models. The reconstructed strain is in descending order on the deck (except that deck 1 and 2 have almost identical peak strains). The dynamic model is the same, except that deck 4 has a higher peak strain than deck 3. The static force reconstruction is generally more accurate than the dynamic one near the peak deck strain values.

Table 7.4: Summary statistics on the variation in peak (maximum magnitude) handlebar and deck loads for 36 j-hops.

Max. Loads (N)	Bar forces			Total deck forces		
	stat, reg	dyn, reg	dyn, reg (h)	stat, reg	dyn, reg	dyn, reg (h)
Mean	526	767	378	3320	2751	2849
Std. dev	90	123	79	567	372	409
Median	505	751	352	3422	2736	2857
Max	797	1053	528	4519	3714	3790
Min	358	547	201	2118	2162	2005

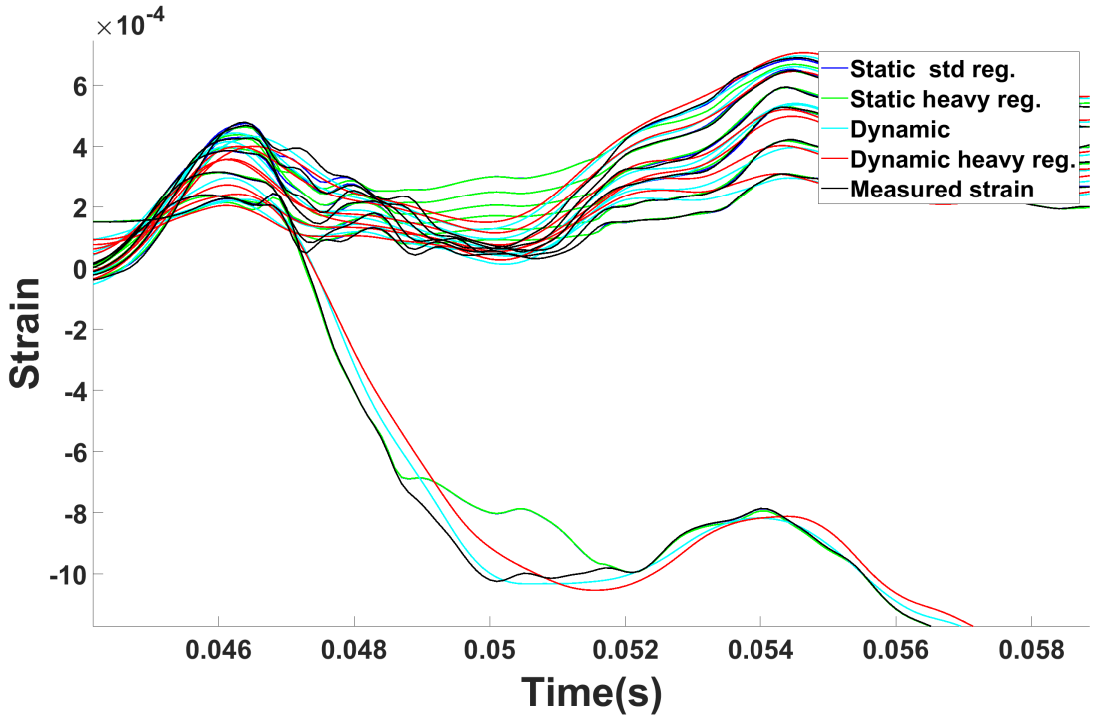


Figure 7.10: The one region of the hop where the dynamic force reconstruction is consistently more accurate than the static model. This is just after landing a stunt upon the first trough in the strain data.

7.5 Tailwhips and heelwhips

Tailwhips and heelwhips are both stunts where the deck rotates 360° about the axis of the handlebars/fork, whilst the rider does not. Most riders naturally find tailwhips easier to execute. As figures in the following subsections will make clear, a rider will usually kick the deck with the toes/ball of their foot during a tailwhip. During a heelwhip, riders will usually kick the deck with their heels.

7.5.1 Tailwhips

Figure 7.11 shows the strain history of a tailwhip. The rider is crouched at 1, before starting the hop at 2. The rider whips the deck of the scooter around clockwise (looking down) from 3 to 6. The rider reaches the peak of the jump around 6 - 7, and is also in the processes of 'catching' the deck. If a rider 'catches' a stunt, it means that the rider completes the motion of the stunt before landing. Catching the tailwhip allows the rider to position themselves to land smoothly upon completing a stunt. Riders (especially beginners) do not always manage to catch the deck before landing. After catching the deck, the rider descends in 8 - 9 and lands at 10. Summary statistics for the peak strains and loads from 40 tailwhips can be seen in tables 7.5 and 7.6.

Table 7.5: A table showing summary statistics of the variation in the maximum magnitude of strain measured in each strain gauge for 40 tailwhips.

All max strains (10^{-3})	DT back	Deck 1	Deck 2	Deck 3	Deck 4	Deck 5	Deck 6
Mean	1.42	0.88	0.86	0.81	0.75	0.63	0.48
Std. dev	0.38	0.10	0.10	0.08	0.07	0.07	0.06
Median	1.48	0.89	0.87	0.82	0.76	0.62	0.48
Max	1.94	1.05	1.07	1.04	1.02	0.89	0.68
Min	0.63	0.60	0.61	0.59	0.57	0.50	0.38

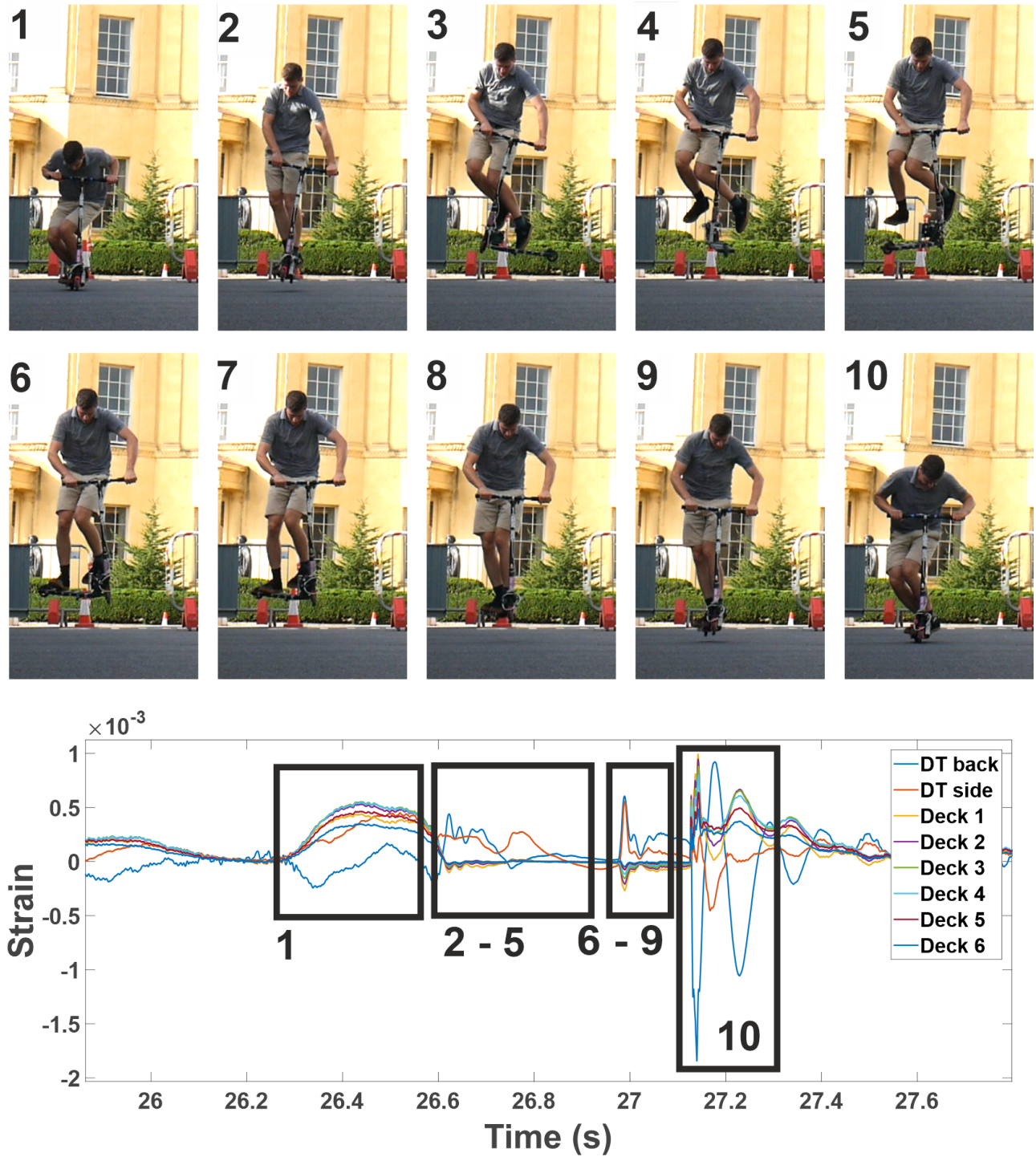


Figure 7.11: Showing the main stages of a tailwhip (with an associated strain history), including the pre-hop crouch (1), the jumping and whipping of the deck (2 - 5), the catching of the deck and descent (6 - 9), and the landing (10).

Table 7.6: Summary statistics on the variation in peak (maximum magnitude) handlebar and deck loads for 40 tailwhips.

Max. Loads (N)	Bar forces			Total deck forces		
	stat, reg	dyn, reg	dyn, reg (h)	stat, reg	dyn, reg	dyn, reg (h)
Mean	427	789	270	2981	2598	2544
Std. dev	120	163	75	469	256	255
Median	452	726	268	2857	2576	2537
Max	591	1235	391	4342	3165	3307
Min	192	566	116	2506	1970	2001

7.5.2 Heelwhips

Figure 7.12 gives the strain history of a heelwhip. Unlike for the other figures where the strain corresponds to the exact hop that the images are taken from, this strain data is from an a different heelwhip. The reason for taking this data was that it included strain data from the crossbar, which helps highlight an interesting feature of the strain history. In 1 the rider is lowering himself before crouching. At 2 the rider has crouched and is exerting a lot of force on the deck to gain amplitude. at 3 the rider starts jumping, leaving the ground at 4.

From 5 - 11 one can see the rotation of the deck for a heelwhip. It is interesting to note, that for the second half of the heelwhip rotation (around 7 - 11) the left and right sides of the crossbar go into tension and compression respectively. This is likely because the 'whipping' motion of the deck involves trying to angle the deck such that the wheel is pointing downwards between 1/2 and 3/4 way through the rotation, so that it will spin faster (as the rider is regular, the heelwhip makes the deck spin anti-clockwise). Summary statistics for the peak strains and loads from 40 heelwhips can be seen in tables 7.7 and 7.8.

Table 7.7: A table showing summary statistics of the variation in the maximum magnitude of strain measured in each strain gauge for 40 heelwhips.

All max strains (10^{-3})							
	DT back	Deck 1	Deck 2	Deck 3	Deck 4	Deck 5	Deck 6
Mean	1.52	0.96	0.97	0.94	0.89	0.75	0.57
Std. dev	0.25	0.12	0.13	0.12	0.12	0.11	0.09
Median	1.53	0.95	0.95	0.93	0.87	0.73	0.55
Max	2.04	1.26	1.28	1.20	1.15	0.98	0.77
Min	0.67	0.75	0.73	0.74	0.69	0.58	0.44

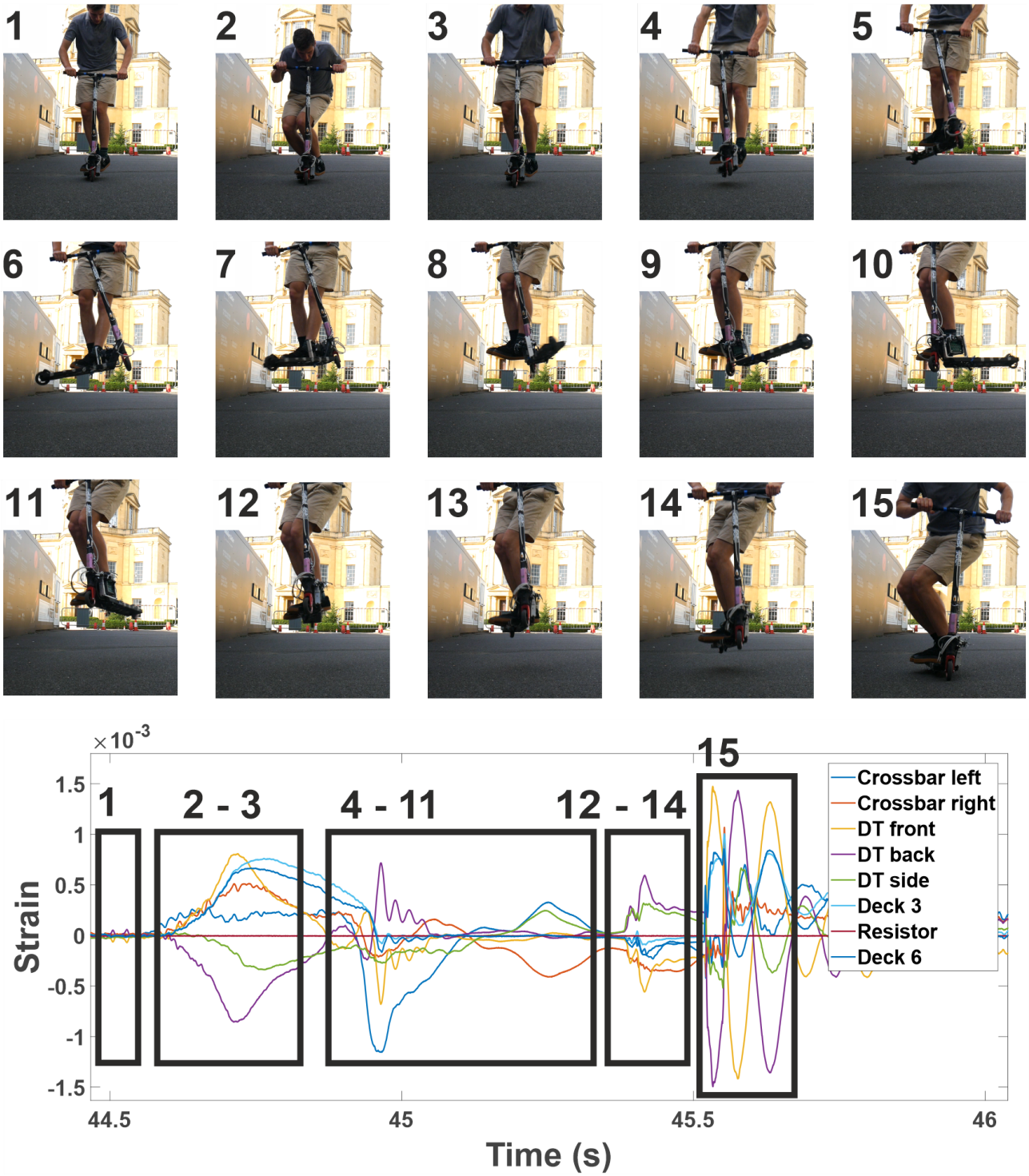


Figure 7.12: The main stages of heelwhip with an associated strain history. The rider prepares to crouch at 1 and crouches at 2, ready to hop. At 3 the rider is about to leave the ground. from 4 - 12 the rider leaves the ground and performs the heelwhip. before catching at 12, descending from 13 - 14 and landing at 15.

Table 7.8: Summary statistics on the variation in peak (maximum magnitude) handlebar and deck loads for 40 heelwhips.

Max. Loads (N)	Bar forces			Total deck forces		
	stat, reg	dyn, reg	dyn, reg (h)	stat, reg	dyn, reg	dyn, reg (h)
Mean	462	784	308	3811	3277	3208
Std. dev	78	179	56	478	314	299
Median	466	752	312	3787	3266	3173
Max	622	1276	495	4928	4563	4161
Min	204	532	177	2986	2704	2790

7.6 Barspins and opposite barspins

A barspin is a stunt whereby the rider jumps into the air with the scooter and rotates the handlebars 360°. The rider can rotate the handlebars clockwise or anti-clockwise. A rider will generally have a natural preference for one direction. If a rider does a barspin against the preferred direction, the stunt is known as an opposite barspin. The rider from whom data was collected barspins clockwise. An illustration of the rider performing a barspin can be seen in figure 7.13. It is worth noting here that when performing a regular barspin, the rider completely lets go of the handlebars. This is somewhat unusual and is colloquially known as a 'throw bar'. When performing an opposite barspin, the rider does, however, tend to hold on to the bars for at least the vast majority of the stunt, which is more common. The summary data is from 39 barspins and opposite barspins performed on flat ground.

7.6.1 Barspins

Figure 7.13 shows the link between the strain history and the various features of a barspin. After lowering himself and crouching at 1 - 2, the rider begins to leave the ground at 3. The rider then starts doing the barspin at 4, and completely lets go of the handlebars at 5. The rotation of the handlebars is 3/4 done by 6. The rider catches the bars at 7 and lands at 8. A small perturbation in the down tube strain can be seen as the rider catches the handlebars in the air before landing. In this stunt, the rider did not start the barspin until after having reached a significant height. Riders do not always do this. Riders (especially beginners) often start the barspin almost as soon as they have left the ground to try and execute the rotation of the handlebars as fast as possible. If jumping

over obstacles more experienced riders will often delay starting the barspin, aiming first to jump as high as possible to get over the obstacle, before exectuing the barspin with the time left in the air. Summary data for the maximum magnitude strains and forces from 39 barspins can be seen in tables 7.9 and 7.10.

Table 7.9: A table showing summary statistics of the variation in the maximum magnitude of strain measured in each strain gauge for 39 barspins.

All max strains (10^{-3})	DT back	Deck 1	Deck 2	Deck 3	Deck 4	Deck 5	Deck 6
Mean	1.89	1.11	1.05	0.96	0.87	0.70	0.53
Std. dev	0.33	0.13	0.12	0.11	0.10	0.07	0.05
Median	1.97	1.11	1.04	0.96	0.88	0.71	0.53
Max	2.34	1.36	1.29	1.20	1.08	0.90	0.68
Min	0.67	0.61	0.60	0.60	0.59	0.53	0.41

Table 7.10: Summary statistics on the variation in peak (maximum magnitude) handlebar and deck loads for 39 regular barspins

Max. Loads (N)	Bar forces			Total deck forces		
	stat, reg	dyn, reg	dyn, reg (h)	stat, reg	dyn, reg	dyn, reg (h)
Mean	573	918	387	3076	2683	2658
Std. dev	101	156	73	433	210	241
Median	600	894	398	2955	2659	2617
Max	713	1399	512	4281	3283	3327
Min	204	629	225	2544	2273	2284

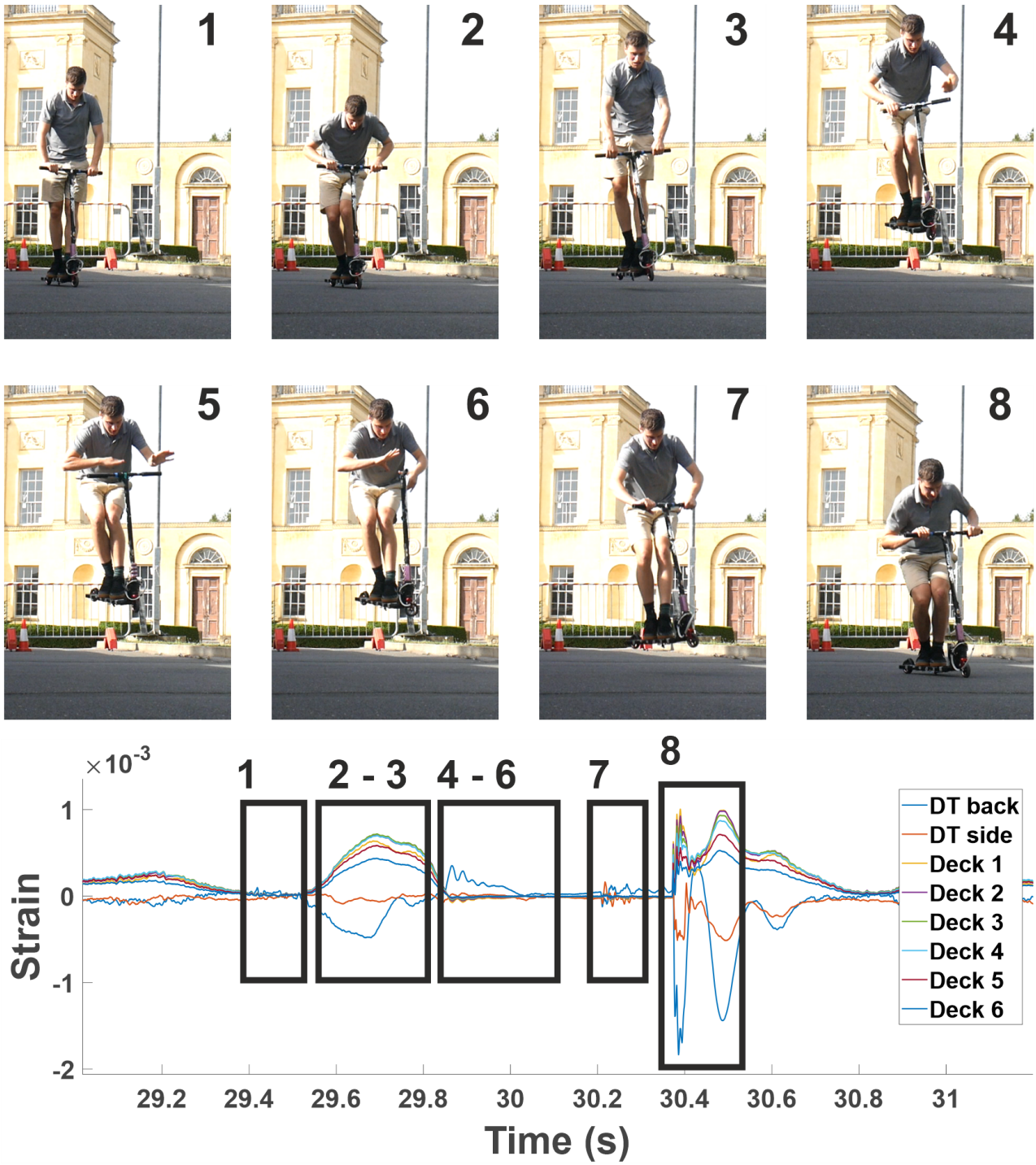


Figure 7.13: The main stages of a barspin and their associated strain history. The rider is prepares to crouch at 1, crouches at 2, is jumping at 3 and is throwing the barspin at 4. At 5 the bars have rotated approximately 180°, and at 6 approximately 270°. The rider catches the bars at 7 and lands at 8.

7.6.2 Opposite barspins

Figure 7.14 shows the strain history of an opposite barspin. The rider prepares to crouch at 1, before crouching at 2, and jumping at 3. By 4, the rider has already started rotating the bars, having done over half the rotation by 5. At 6 the rider is passing the bars from one hand to the other. The rider's left hand cannot still hold onto the handlebars after (approximately) three-quarters of the rotation, however by this point the right hand has already caught the handlebars. At 7 both hands are just about holding on to the crossbar, and the rider lands at 8. Compared to the standard barspin in the previous section, the strain upon catching the barspin is larger. The peak strain at the start of the jump as the rider leaves the ground is also larger. This may be because the rider is pushing the handlebars around as opposed to throwing them. Comparing the summary table of results for barspins and opposite barspins, the maximum strain tends to be larger in regular barspins. The reason for this is not entirely clear. It may be that the rider jumps higher when performing regular barspins. Summary data for 39 opposite barspins can be found in tables 7.11 and 7.12.

Table 7.11: A table showing summary statistics of the variation in the maximum magnitude of strain measured in each strain gauge for 39 opposite barspins.

All max strains (10^{-3})	DT back	Deck 1	Deck 2	Deck 3	Deck 4	Deck 5	Deck 6
Mean	1.59	0.91	0.89	0.87	0.82	0.69	0.52
Std. dev	0.26	0.13	0.13	0.11	0.10	0.09	0.07
Median	1.67	0.92	0.91	0.85	0.81	0.68	0.51
Max	1.97	1.22	1.18	1.10	1.06	0.91	0.70
Min	0.79	0.56	0.54	0.56	0.56	0.51	0.40

Table 7.12: Summary statistics on the variation in peak (maximum magnitude) handlebar and deck loads for 39 opposite barspins.

Max. Loads (N)	Bar forces			Total deck forces		
	stat, reg	dyn, reg	dyn, reg (h)	stat, reg	dyn, reg	dyn, reg (h)
Mean	482	804	330	3039	2636	2685
Std. dev	81	101	64	631	335	416
Median	511	797	339	2780	2587	2560
Max	599	1150	454	4682	3536	3827
Min	240	607	177	2285	2189	2246

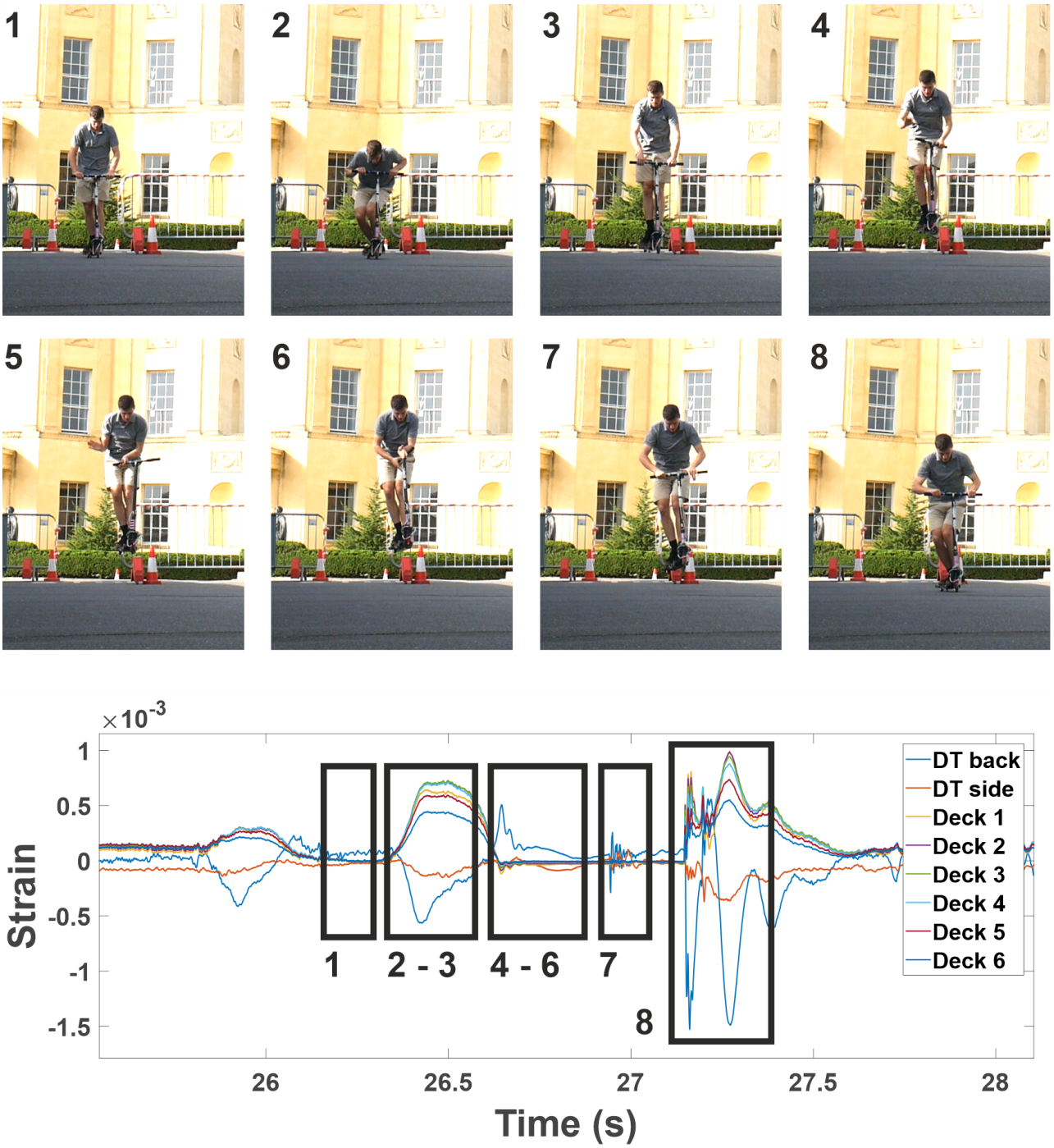


Figure 7.14: The main stages of an opposite barspin and their associated strain history. The rider is prepares to crouch at 1, crouches at 2, is jumping at 3 and is throwing the barspin at 4. At 5 the rider is pushing the bars around (they have rotated approximately 135° at this point). By 6 the bars have have rotated approximately 270° and the rider is letting go of the bars with the left hand and catching them with the right. At 7 the rider is almost finished with catching the handlebars and the rider lands at 8.

7.7 Backside 180s (and backside half-caballerial)

A 180 is a stunt where the rider hops and spins 180° in the air. As mentioned previously, backside means that if riding in the forward direction and jumping, the rider's back will face the direction of motion after a 90° - 180° turn. In the case of a regular rider, backside spins are clockwise/to the right. If a rider lands a 180 and is still rolling, they will be riding backwards. Riding backwards is known as riding 'fakie'. There are different ways to get out of fakie. The way done in the following section is by executing a half-caballerial (almost always called a half-cab). A half-cab simply involves doing another hop 180 from fakie so that one is riding in the forwards direction again. In this section, backside 180s were all followed by backside half-cabs. In the results that follow, the amount of time spent in fakie varies. In addition, the amount of spin in the air performed during a half-cab varies. As one generally turns the handlebars to start rotating before executing a half-cab, one can rotate as much as 90° before leaving the ground. Riders often carve a little before 180s (although this happens much more for stunts such as 360s and 540s). This means that the rider will often turn in the direction of spin before jumping to make the rotation easier to perform in the air. Figure 7.15 shows the strain sequence for a backside 180 followed by a backside half-cab. At 1 and 2 the rider is carving, having also crouched at 2 ready to jump. By 3 the rider has rotated 90° and landed fakie at 4. In 5 the the rider is riding fakie, before carving slightly then crouching a little in 6. By 7 the rider is approximately halfway through the half-cab, and has landed by 8.

Data was analysed from from 30 backside 180s and 30 half-cabs. Summary peak strains and forces for backside 180s are in tables 7.13 and 7.14 respectively. Similar data for backside half-cabs are in tables 7.15 and 7.16. It is sometimes the case that when riding in fakie riders will jump in order to reposition the scooter to maintain balance. Such hops are known as 'fakie hops' or 'correction hops'. This happened very ocassionally with data collected from the rider, however the strains associated with these were relativley small.

Table 7.13: A table showing summary statistics of the variation in the maximum magnitude of strain measured in each strain gauge for 30 backside 180s.

All max strains (10^{-3})	DT back	Deck 1	Deck 2	Deck 3	Deck 4	Deck 5	Deck 6
Mean	1.02	0.78	0.78	0.72	0.67	0.57	0.44
Std. dev	0.31	0.15	0.13	0.11	0.09	0.06	0.04
Median	1.03	0.78	0.78	0.72	0.67	0.57	0.42
Max	1.63	1.11	1.09	1.00	0.91	0.72	0.53
Min	0.48	0.53	0.60	0.55	0.54	0.49	0.38

Table 7.14: Summary statistics on the variation in peak (maximum magnitude) handlebar and deck loads for 30 backside 180s

Max. Loads (N)	Bar forces			Total deck forces		
	stat, reg	dyn, reg	dyn, reg (h)	stat, reg	dyn, reg	dyn, reg (h)
Mean	310	672	191	2817	2516	2481
Std. dev	94	113	47	318	252	235
Median	314	654	178	2766	2469	2435
Max	498	997	308	3646	3049	2976
Min	145	508	126	2407	2071	2065

Table 7.15: A table showing summary statistics of the variation in the maximum magnitude of strain measured in each strain gauge for 30 backside half-cabs.

All max strains (10^{-3})	DT back	Deck 1	Deck 2	Deck 3	Deck 4	Deck 5	Deck 6
Mean	1.13	0.73	0.72	0.67	0.63	0.53	0.41
Std. dev	0.31	0.18	0.15	0.13	0.12	0.09	0.07
Median	1.13	0.72	0.71	0.67	0.62	0.52	0.41
Max	1.69	1.18	1.14	1.05	0.98	0.78	0.58
Min	0.44	0.27	0.35	0.35	0.33	0.29	0.22

Table 7.16: Summary statistics on the variation in peak (maximum magnitude) handlebar and deck loads for 30 half-cab 180s.

Max. Loads (N)	Bar forces			Total deck forces		
	stat, reg	dyn, reg	dyn, reg (h)	stat, reg	dyn, reg	dyn, reg (h)
Mean	343	644	229	2643	2290	2299
Std. dev	96	158	69	535	309	316
Median	343	629	215	2588	2261	2288
Max	517	1035	400	4228	3107	3289
Min	135	389	106	1620	1540	1575

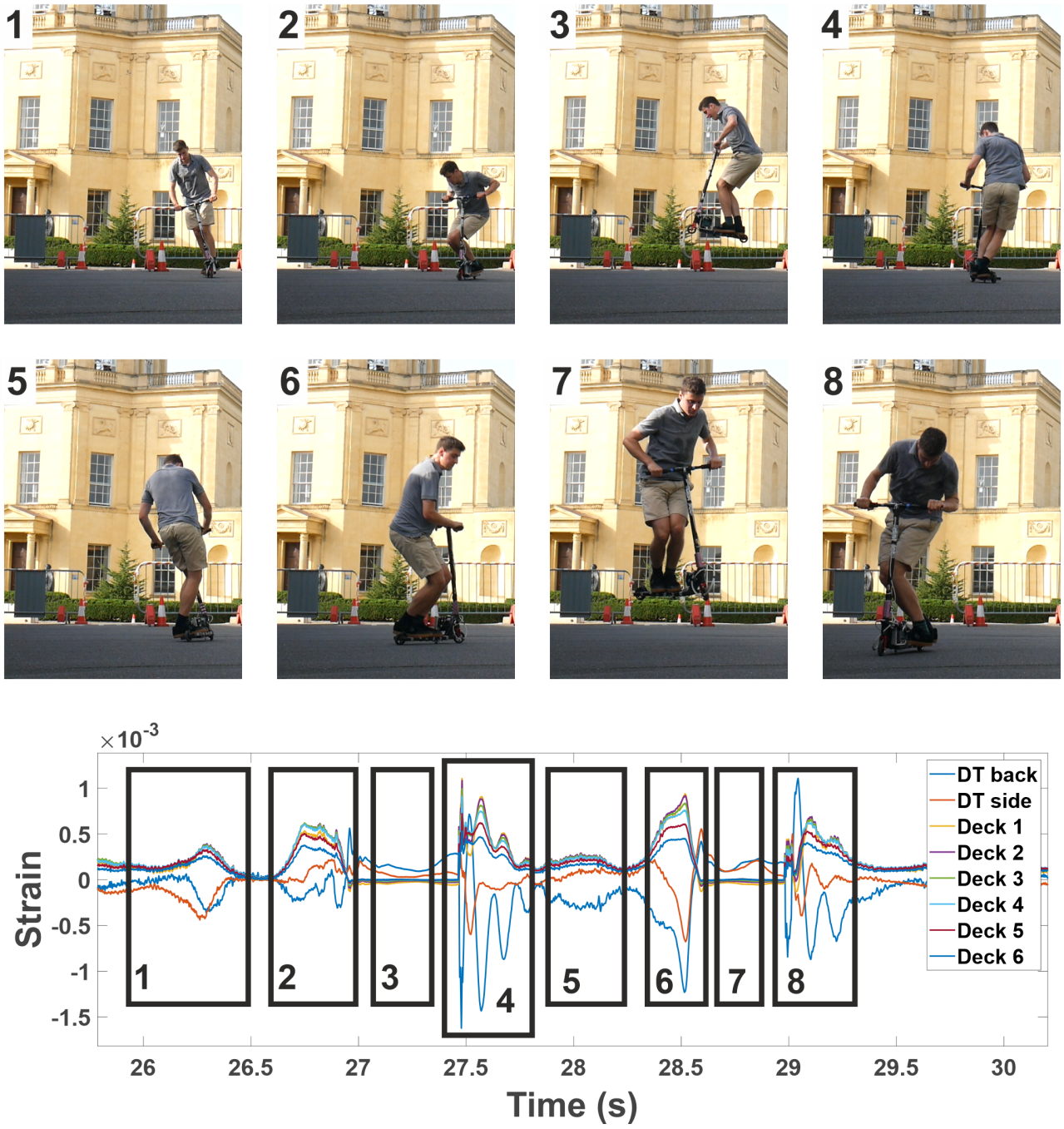


Figure 7.15: The strain history backside 180 and backside half-cab with associated images. The rider is slightly carving at 1, crouching at 2 before jumping into the air. At 3 the rider has rotated approximately 90° and landed in fakie at 4. at 5 the rider is riding fakie. The rider carves a little, crouches and is about to jump at 6. At 7 the rider has rotated approximately 90° and has landed riding forwards again at 8.

7.8 Frontside 180s (and frontside half-caballerial)

Frontside 180s are similar to backside 180s, except that the rider rotates the other way. In this section the rider performs frontside 180s to fakie, then proceeds to do a frontside half-cab. In the particular hop analysed, the fakie for the frontside 180 is longer than that of the backside 180. Figure 7.16 shows a frontside 180 followed by a frontside half-cab. For frontside spins, the rider genearlly carved less than for backside spins. The rider reported that he naturally spins backside, and feels more balanced carving a significant amount for backside spins. The rider is riding at 1 before carving slightly and crouching at 2, jumping at 3, and landing in fakie at 4. in 5 and 6 the rider is riding fakie before crouching at 7. The rider jumps and has rotated approximately 90° by 8, and finally lands riding normally again at 9. Data was analysed for 27 frontside 180s and frontside half-cabs. Summary data for peak strain magnitudes can be seen in tables 7.17 and 7.19 for frontside 180s and halfcabs. Similarly, summary data for peak force magnitudes can be seen in tables 7.17 and 7.20. The 180s and halfcabs generally had a lower mean maximum strain than for all the other hops. This was statistically significant (assuming a normally distributed data) when comparing the difference in maximum mean strain between the DT back strain for all of the 180s/half-cabs and regular barspins. This was also the case for some of the deck strain gauges for some of the 180/half-cab types.

Table 7.17: A table showing summary statistics of the variation in the maximum magnitude of strain measured in each strain gauge for 27 frontside 180s.

All max strains (10^{-3})							
	DT back	Deck 1	Deck 2	Deck 3	Deck 4	Deck 5	Deck 6
Mean	0.99	0.72	0.71	0.67	0.63	0.53	0.41
Std. dev	0.31	0.11	0.09	0.08	0.07	0.05	0.04
Median	1.07	0.75	0.74	0.68	0.65	0.53	0.41
Max	1.60	0.87	0.84	0.77	0.76	0.69	0.55
Min	0.29	0.46	0.51	0.50	0.50	0.42	0.31

Table 7.18: Summary statistics on the variation in peak (maximum magnitude) handlebar and deck loads for 27 frontside 180s.

Max. Loads (N)	Bar forces			Total deck forces		
	stat, reg	dyn, reg	dyn, reg (h)	stat, reg	dyn, reg	dyn, reg (h)
Mean	301	688	197	2871	2525	2503
Std. dev	95	101	42	504	272	269
Median	327	698	189	2744	2441	2446
Max	490	852	316	4042	3400	3400
Min	89	459	123	2286	2177	2185

Table 7.19: A table showing summary statistics of the variation in the maximum magnitude of strain measured in each strain gauge for 27 frontside half-cabs.

All max strains (10^{-3})							
	DT back	Deck 1	Deck 2	Deck 3	Deck 4	Deck 5	Deck 6
Mean	1.18	0.69	0.69	0.66	0.63	0.54	0.41
Std. dev	0.27	0.13	0.10	0.08	0.06	0.05	0.03
Median	1.17	0.68	0.70	0.67	0.63	0.55	0.42
Max	1.63	0.94	0.92	0.82	0.76	0.62	0.46
Min	0.48	0.42	0.48	0.47	0.47	0.40	0.32

Table 7.20: Summary statistics on the variation in peak (maximum magnitude) handlebar and deck loads for 27 frontside half-cabs.

Max. Loads (N)	Bar forces			Total deck forces		
	stat, reg	dyn, reg	dyn, reg (h)	stat, reg	dyn, reg	dyn, reg (h)
Mean	357	700	251	2740	2368	2376
Std. dev	84	129	41	377	158	156
Median	359	702	245	2682	2368	2384
Max	498	1038	331	3764	2753	2749
Min	145	524	195	2228	1996	2111

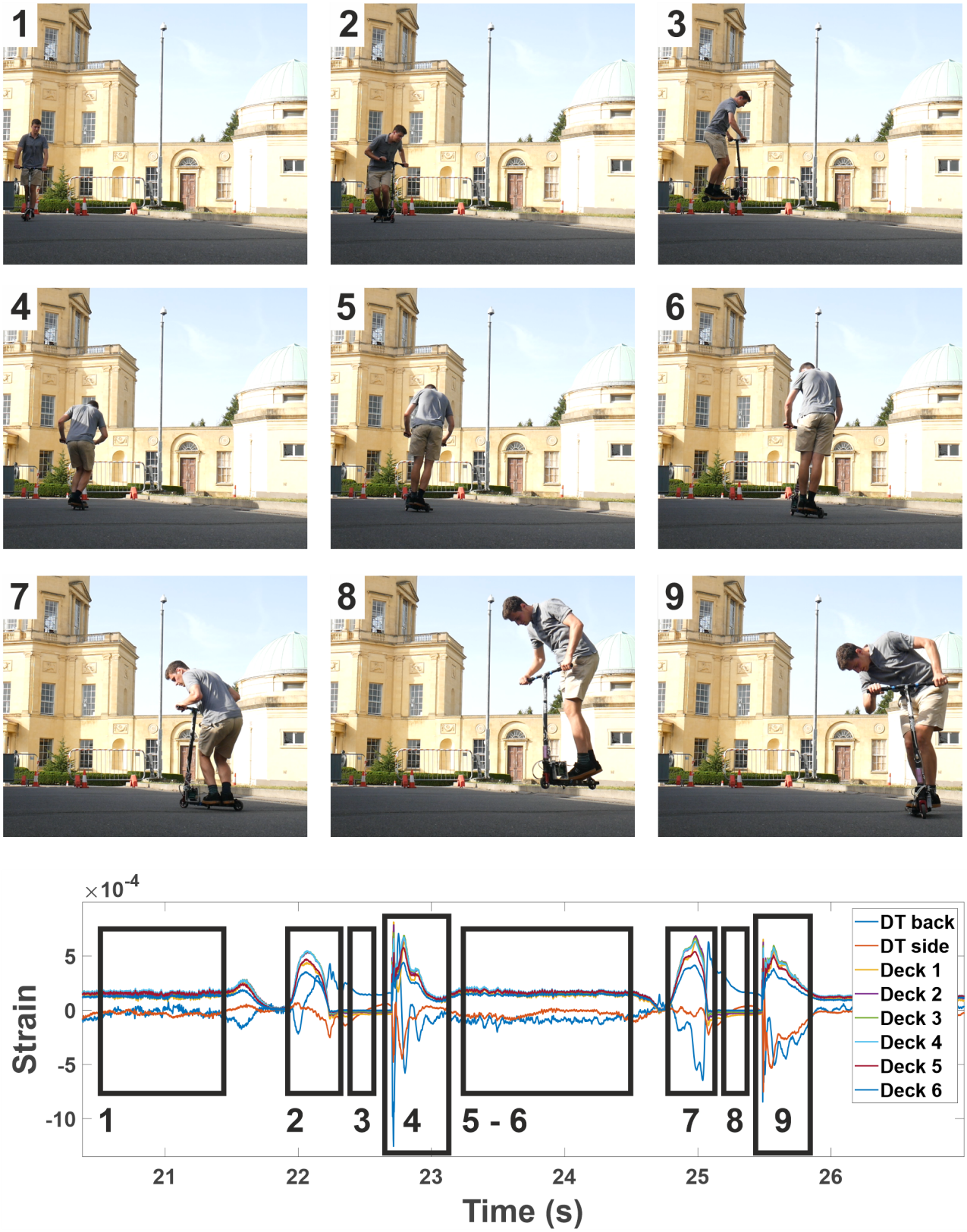


Figure 7.16: The strain history frontside 180 and backside half-cab with associated images. The rider is riding along at 1, before slightly carving at 2, and jumping, having rotated approximately 90° by 3. At 4 the rider has lands in fakie and is riding in fakie in 5 and 6. The rider crouches in 7, before jumping, having rotated approximately 90° at 8. The rider finally lands and rolls away riding forwards in 9.

7.9 Backside 360s

Having discussed 180s, we now come to 360° spins. The stunt involves the rider jumping into the air, rotating 360°, and then landing. As can be seen in figure 7.17, it is common for the rider to carve significantly before jumping. The rider starts carving in the direction of rotation before jumping to leave the ground so it is easier to spin. If the rider has a lot of speed, carving can occur for quite some distance before they start leaving the ground. The general strain features of the hops are similar to those of a bunnyhop. The rider prepares for the 360, riding along in 1, and starting to carve in 2. By 3 the rider has crouched, about to jump. By 4 the rider has just left the ground and almost rotated 90°. The rider continues to rotate in the air, having rotated approximately 180° by 5, 270° by 6 and 360° by 7. By 7 the rider's back wheel has also just touched the floor. The rider has fully landed by 8.

Data was analysed for 40 backside 360s; summary results are in tables 7.21 and 7.22.

Table 7.21: A table showing summary statistics of the variation in the maximum magnitude of strain measured in each strain gauge for 40 backside 360s.

All max strains (10^{-3})	DT back	Deck 1	Deck 2	Deck 3	Deck 4	Deck 5	Deck 6
Mean	1.30	0.84	0.84	0.77	0.71	0.60	0.46
Std. dev	0.31	0.12	0.10	0.09	0.08	0.06	0.04
Median	1.29	0.85	0.84	0.77	0.71	0.59	0.45
Max	1.86	1.10	1.06	0.94	0.85	0.72	0.54
Min	0.44	0.59	0.62	0.56	0.51	0.44	0.34

Table 7.22: Summary statistics on the variation in peak (maximum magnitude) handlebar and deck loads for 40 backside 360s

Max. Loads (N)	Bar forces			Total deck forces		
	stat, reg	dyn, reg	dyn, reg (h)	stat, reg	dyn, reg	dyn, reg (h)
Mean	395	720	272	2932	2586	2551
Std. dev	97	132	58	417	266	291
Median	395	698	267	2891	2577	2477
Max	568	1030	410	4037	3319	3403
Min	135	533	149	2294	2006	2036

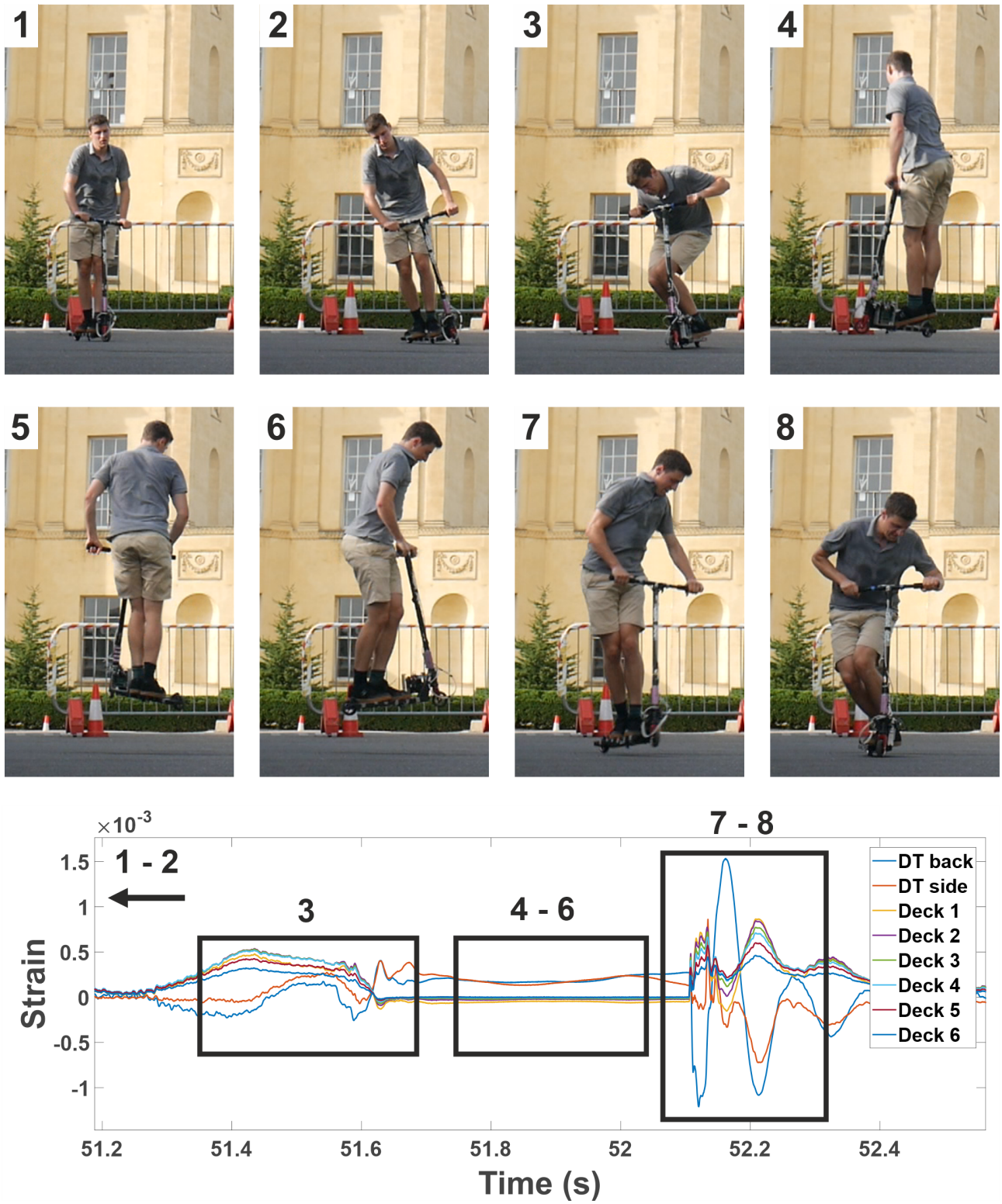


Figure 7.17: The strain history with snapshots of video footage for a backside 360. The rider is riding at moderate speed in 1, carves in 2 and crouches ready to jump in 3. The rider has left the ground and started rotating in 4, and continues to rotate in 5 and 6. By 7 the rider has rotated almost the full 360° and his back wheel has touched the ground. The rider fully lands at 8 before rolling away.

7.10 Frontside 360s

Figure 7.18 shows the main stages in a frontside 360. They are very similar to those of a backside 360. The rider prepares for the jump, riding along and slightly carving. At 2 the rider has crouches. At 3 the rider has just left the ground and started rotating. the rotation continues throuch stages 4 - 7, Before the rider finally lands at 8.

Data from 49 Frontside 360s was analysed. Tables 7.23 and 7.24 show summary statistics.

When comparing frontside with backside 360s, the mean maximum strain is higher for all the strain gauges in frontside 360s. The mean maximum loads (bar and total deck) are also higher for all of the models in frontside 360s. One possible reason for higher peak loads and strains in frontside 360s is that the rider naturally does backside 360s. This higher level of comfort with the stunt may mean he is able to land more smoothly, reducing the size of the maximum applied load.

Table 7.23: A table showing summary statistics of the variation in the maximum magnitude of strain measured in each strain gauge for 49 frontside 360s.

All max strains (10^{-3})	DT back	Deck 1	Deck 2	Deck 3	Deck 4	Deck 5	Deck 6
Mean	1.60	0.88	0.87	0.82	0.77	0.65	0.50
Std. dev	0.29	0.09	0.09	0.08	0.08	0.06	0.05
Median	1.57	0.87	0.87	0.81	0.77	0.64	0.49
Max	2.24	1.08	1.09	1.01	0.95	0.81	0.62
Min	0.95	0.69	0.72	0.67	0.62	0.54	0.42

Table 7.24: Summary statistics on the variation in peak (maximum magnitude) handlebar and deck loads for 49 frontside 360s.

Max. Loads (N)	Bar forces			Total deck forces		
	stat, reg	dyn, reg	dyn, reg (h)	stat, reg	dyn, reg	dyn, reg (h)
Mean	487	981	394	3312	2928	2891
Std. dev	88	105	51	555	422	447
Median	479	995	388	3393	2952	2823
Max	685	1218	513	4496	3973	4098
Min	281	744	280	2255	2083	2125

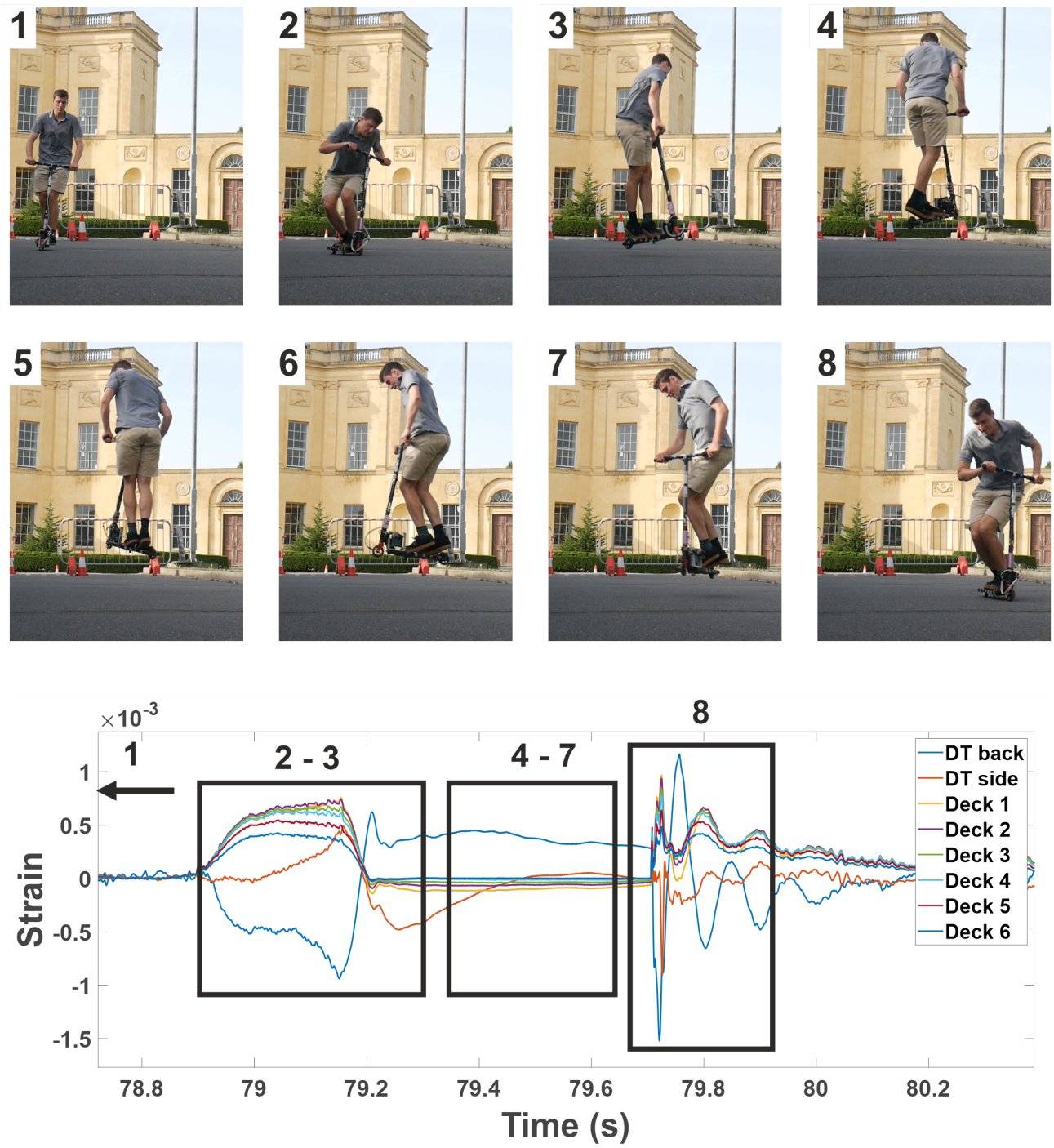


Figure 7.18: Snapshots of a frontside 360 and its associated strain history. The rider approaches at 1, getting ready to do a frontside 360. At 2 the rider is carving, before jumping. At 3 the rider has just left the ground, spinning. The rider carries on spinning from 4 - 7 before landing at 8.

7.11 Discussion

7.11.1 Testing for the normality of the data

Tests were performed to assess the normality of the peak strain magnitudes at each strain gauge. Shapiro-Wilk tests are especially suitable for assessing the normality of smaller sample sizes (n $<$ 50) [136]. All data sets were smaller than 50. When using the Shapiro-Wilk test, the null hypothesis is that the data is normally distributed. If the p-value is below 0.05, the null hypothesis is rejected. There was a surprising variety in the results, which can be seen in table 7.25. The green cells are those for which the p-value is above 0.05, and the red cells where the value is below it. The maximum p-value ($p = 0.978$) was for the deck 6 strain gauge on bunnyhops. The minimum was for the down tube strain gauge for opposite barspins ($p = 2.45 \times 10^{-4}$). The table shows how peak strains from stunts involving only hops or spins (i.e. not whips or barspins) appear more normally distributed. Bunny hops and all spin variations had p-values above 0.05 for all strain gauges, with only three exceptions. The exceptions were deck strain gauge 4 for frontside 360s, deck strain gauge 5 for backside 180s and deck strain gauge 6 for frontside 180s (and in all of these cases, the p-value was 0.035 – 0.049). An exception to the larger trend was j-hops, for which five of the strain gauges had a p-value less than 0.05, and all of the p-values were below 0.1. The reason for this is not entirely clear.

Stunts where the handlebars and deck rotate with respect to each other had some interesting features. They all had very low p-values for the down tube strain gauge, all below 0.009. Regular barspins also tended to have lower p-values near the front of the deck, and the whip tricks tended to have lower p-values near the rear of the deck. Tailwhips were of particular note, with the p-values for deck strain gauges 4 - 6 all below 0.0035. It may have something to do with the way the rider catches the deck with his feet and lands that gives rise to this result. Conversely, there may be some similar type of effect caused by the way the rider catches the bars when doing regular barspins. Regular barspins had far lower p-values in deck strain gauges 1 and 2 than opposite barspins, and this difference may be due to the way the barspin is 'thrown' rather than 'passed' (as was the case with opposite barspins). Histograms and QQ plots for four different stunts are given in figures 7.19,

	DT	Deck 1	Deck 2	Deck 3	Deck 4	Deck 5	Deck 6
B hops	0.84	0.66	0.87	0.56	0.93	0.87	0.98
BS 180s	0.68	0.62	0.20	0.20	0.09	0.04	0.11
BS half-cabs	0.74	0.25	0.43	0.58	0.23	0.21	0.14
BS 360s	0.06	0.52	0.82	0.90	0.72	0.93	0.78
FS 360s	0.09	0.55	0.44	0.10	0.04	0.20	0.18
Tailwhips	0.01	0.06	0.17	0.11	0.00	0.00	0.00
Heelwhips	0.00	0.25	0.29	0.19	0.02	0.00	0.08
Normal bars	0.00	0.00	0.00	0.07	0.22	0.74	0.47
Oppo bars	0.00	0.08	0.16	0.15	0.49	0.64	0.10
J-hops	0.09	0.04	0.03	0.05	0.04	0.02	0.01
FS 180s	0.11	0.06	0.11	0.13	0.35	0.33	0.05
FS half-cabs	0.73	0.93	0.97	0.88	0.84	0.12	0.24

Table 7.25: A table showing the p-value of results from Shapiro-Wilk tests applied to the maximum strain magnitudes on each strain gauge. There is a large disparity in the calcualted p-values. Boxes marked green have a p-value higher than 0.05, and those in red have a value below 0.05.

7.20 and 7.21. Subfigures a) - d) for all three figures show: a very high p-value, a lower p-value that is still significantly above the $p = 0.05$ threshold, a p-value slightly below the threshold, and a p-value significantly below the threshold respectively. The QQ plot shows that there appears to be significant skew towards the edges of the distributions, especially for the lower p-values. It is difficult to conclude what is generally the case from this data, and further research should be carried out to see how these findings change with more data and if the distribution changes with different riders. In a (normal) QQ plot the quantiles given by the data are plotted against the quantiles given by the normal distribution. Quantiles are the spacings between which there are an equal number of data points for the data. All of the plots appear to experience at least some skew at the edges, indicating that a normal distribution may not be appropriate for scooter stunts. A QQ plot of the data (normalised) with a uniform distribution is given in figure 7.21. The data does not appear to match a uniform distribution well either.

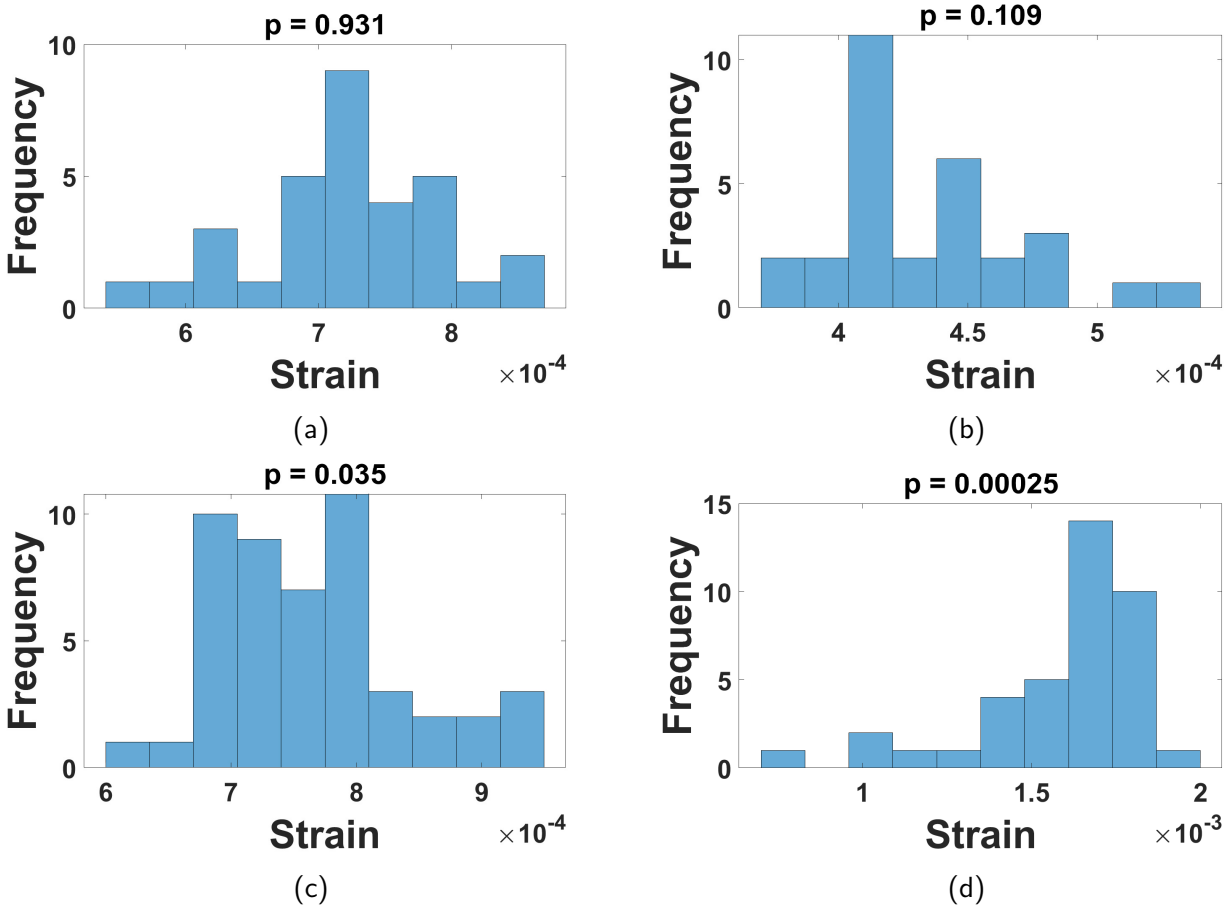


Figure 7.19: Histograms for the distribution of peak strains in various strain gauges with varying p-values. a) is from bunny hop data on deck strain gauge 4, b) is from backside 180 data on deck strain gauge 6, c) is from frontside 360 data on deck strain gauge 4 and d) is from opposite barspin data on the down tube strain gauge. All of the histograms are divided into 10 bins.

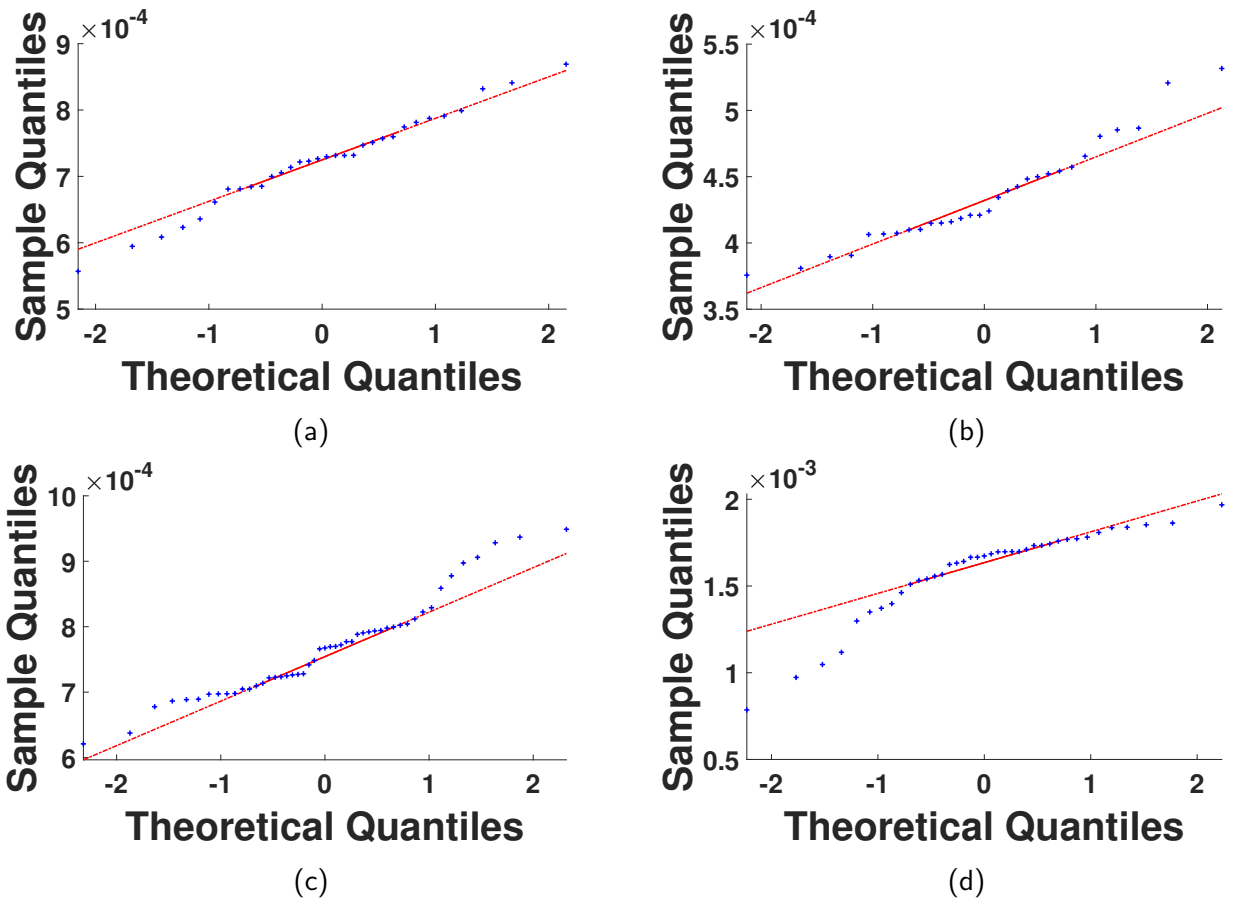


Figure 7.20: Normal QQ plots for the data used to make histograms in figure 7.19.

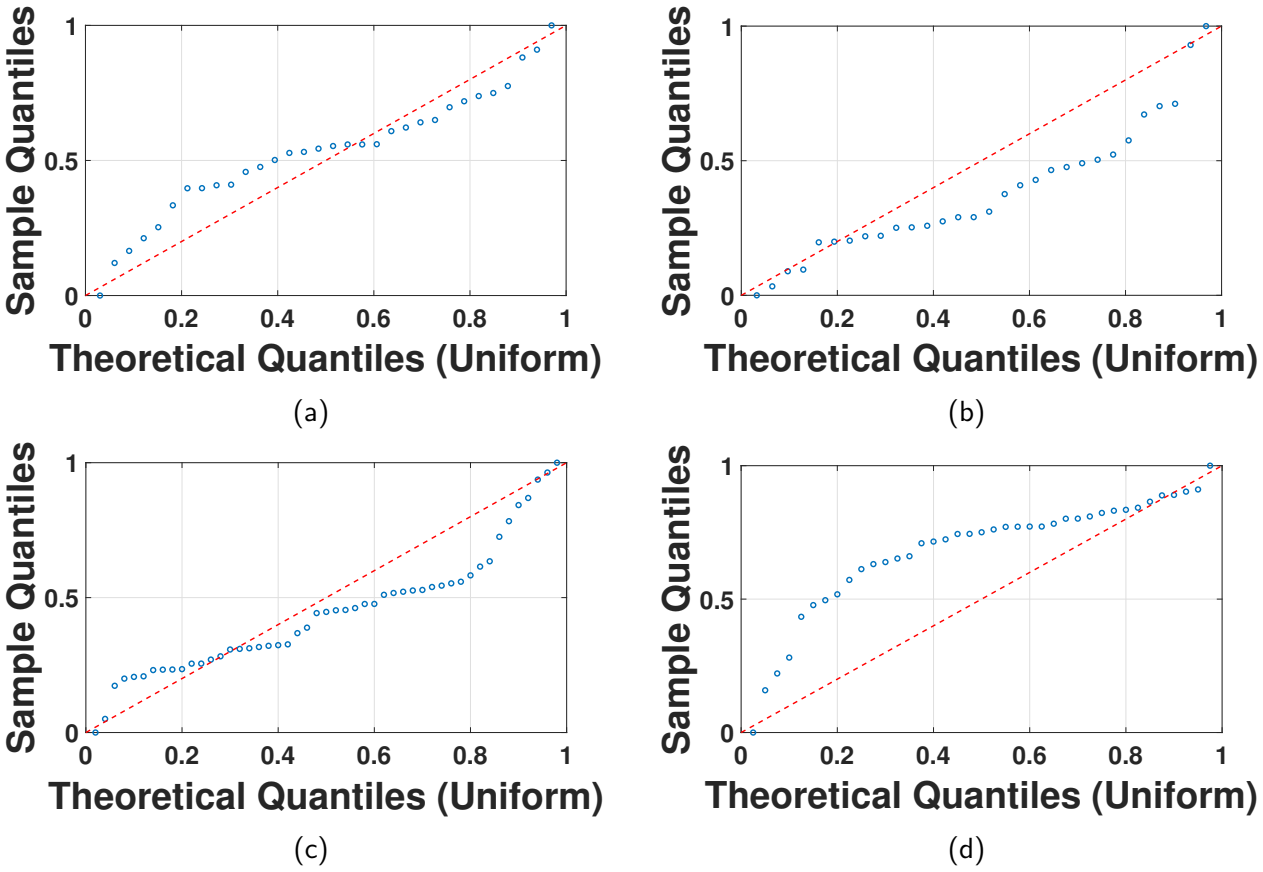


Figure 7.21: Uniform QQ plots for the data used to make histograms in figure 7.19. The data has been normalised against the highest peak strain in its data set.

7.11.2 Other considerations

Comparing the results, there are a few interesting points. The first is that there is a significant standard deviation in peak strain (at every strain gauge) for all the stunts. There is no stunt that has a mean peak strain (in any strain gauge) that is more than one standard deviation above the equivalent mean peak strains of all the other stunts.

The mean peak strains in the down tube and deck strain gauges 1 - 3 were the largest from the regular barspin data. This was unexpected, as the motion of the jump is fairly similar to that of a bunny hop. Intuition suggests that stunts such as 360s may involve more leaning or pushing. The largest mean peak strains in deck strain gauges 4 - 6 were from heelwhips, with j-hops close behind (the mean peak strain was only 10^{-5} lower in each strain gauge). Additionally, this data in this chapter is collected from one rider. Individual riders will perform different stunts in different ways, have different preferences for tricks, be different sizes, have different weights, etc. so we should be careful of generalising. Stunts were intentionally performed as 'naturally' as possible, but future studies could involve doing stunts over an obstacle of a fixed height to gauge the difference between stunts.

One unanimous result from all stunts is that the mean peak strains in the deck are greatest for the deck 1 and/or 2 strain gauges and after that decrease as the deck strain gauge number increases. This implies that the stresses near the front of the footplate are expected to be higher than those at the rear. This could have significant implications for scooter design. Deck 1 mean peak strains are more than two standard deviations away from deck 6 strains for all stunts other than backside half-cabs. The mean peak strains in the deck 6 strain gauge (calculated from the distribution of deck 6 peak strains) are more than two standard deviations less than deck strain gauges numbered 4 and below for all stunts.

By evaluating the reconstructed forces according to the various models, some patterns are evident. The (mean) peak load magnitude for the $\boldsymbol{f_1}$ (handlebar) loads were always significantly higher for the dynamic reconstruction with the standard (L-curve) regularisation parameter. Given the spurious oscillations, this is unsurprising. The static value was always higher than the heavily regularised model. One potential reason for this is that the strain of a dynamic load will initially overshoot the

steady-state value. Hence, the static force reconstruction model may be overestimating the value of the peak load. Comparing the mean peak deck loads, the static reconstructed load was always the largest, and both dynamic models gave very similar values (sometimes the L-curve regularised one had a slightly larger peak mean load, and sometimes vice-versa). Again, it is plausible that the static model is giving an overestimation of the peak value because of the overshoot effect described above. The heavily regularised dynamic model is probably significantly more realistic than the standard model using regularisation parameters derived from the L-curve method.

Overall, it is clear that the static model can reconstruct the strain data best. For the peak strains in the down tube, there is very little difference in the reconstructed strains. The area where the dynamic force reconstruction model is significantly less accurate is in reconstructing deck strain gauges 3 – 5. These strain gauges do not give rise to the largest strains in the scooter. The highest strains measured in the footplate (extrusion profile) are further forward, nearer deck strain gauges 1 and 2. The maximum strains in the down tube are significantly greater than strains in any of the deck strain gauges.

A nuanced approach is likely best for using these reconstructed forces as design loads. Dynamic simulations are significantly more costly than static simulations. Because of this, detailed dynamic simulations that investigate areas of stress concentration may not be feasible. Small fillets lead to very small elements, which in turn will lead to a reduction in the minimum stable time increment. The impact on simulation time is therefore much more significant for dynamic simulations. One approach could be to apply the static loads that give rise to the maximum strains in the scooter and compare results to a dynamic simulation with reconstructed dynamic loads. One important factor is whether the ratios of the peak strains and stresses in various regions of a scooter component are similar for the different loading regimes. This comparison should be made in regions away from any sharp corners in the simplified dynamic model (where it will be inaccurate). If the static model gives rise to stresses that are a reasonable approximation of those in the dynamic model, this can then be used for optimisation. Given the iterative nature of techniques such as topology and shape optimisation, they would be especially costly on dynamic simulations. In addition, topology optimisation should have a design domain, and the elements in this domain should be small enough to give a refined

geometry. This makes optimisation with a dynamic model even more computationally costly.
The reconstructed forces in this chapter are suitable for investigating the peak stresses and strains in the deck and down tube. Because none of the models incorporate information about the loads applied in the vertical (x_3) direction, they are unsuitable for investigating the optimisation of the forks or crossbar of the scooter.

7.12 Conclusion

In this chapter, after a discussion on the use of Tikhonov regularisation, force reconstruction data of 12 different scooter stunts have been presented. Force reconstructions were performed for three different static models and two dynamic models (differences within models were the extent to which calculations were Tikhonov regularised). Static results were all similar to one another. A general difference between the static and first dynamic force reconstruction model (with a Tikhonov parameter taken from L-curve results) is that the dynamic model has some high-frequency oscillations, such that its maximum handlebar load exceeds that of the static model. Apart from this, the peak loads in the static model exceed those of both dynamic models. One potential reason for this could be the initial overshoot in strain response from a dynamic load to the steady-state value.
Shapiro-Wilk tests were performed on the mean-peak strains of all of the data. Results tended to show that stunts that only involve the rider jumping (or jumping and rotating) appeared much more normally distributed than for barspin or whip stunts. The variation in strains between stunts was such that no single stunt gave rise to peak (magnitude) strains that were more than one standard deviation away from corresponding peak strains for other stunts (at a given strain gauge). It is difficult to comment on how statistically significant this is, because it is unclear which distribution is best to model all of the scooter data. For all stunts, the mean peak strain decreased as the as the deck strain gauge number increased beyond deck strain gauge 2.

Chapter 8

Simulations and Optimisation

8.1 Introduction

This chapter makes some suggestions for how the data collected in the thesis might be used for the optimisation of scooter components. It starts by detailing a dynamic FE model in section 8.2. This includes checks for various types of convergence, as well as tests for linearity and symmetry. The following section (8.3.4) details a rough estimate of various parameters to approximate the appropriate damping and sources of non-linearity in the scooter, and compares the simulated results with experimental data. This section is also important in determining how significant these sources of non-linearity are likely to be for an accurate FE model.

The main reasons for having a dynamic model are firstly to see if a suitable dynamic model can be made describing the behaviour of the scooter, and perhaps more importantly to see whether optimisation performed on the static model will be relevant to a scooter subject to dynamic loads. A comparison between the results of simulation results on the static and dynamic models is given in section 8.4, before a short topology optimisation study is run on the headtube of the scooter in section 8.5.

8.2 Finite element model (dynamic simulations)

This section outlines the creation of a dynamic FE model of the scooter (a description of the scooter parts and CAD model are given in section 5.2). The model used was dynamic explicit, which is better suited to high loading rates than implicit analyses. The model geometry was the same as that of the static model. The material properties (a Young's modulus of 68.9 GPa and a Poisson's ratio of 0.33) were the same as in the static model, with the addition of a density parameter of 2700 kg m^{-3}. In addition, Rayleigh (material) damping was present in the model (with $\alpha = 100$ s^{-1} and $\beta = 0$ s) for the convergence studies below (a discussion on Rayleigh damping follows in section 8.3.1). The headset bearings were assumed to be made from solid aluminium, and the axles were fixed. Material damping parameters, headset bearing stiffness and the compliance of the axles will all be discussed following the convergence studies in section 8.3.

Dynamic simulations are significantly more costly than static simulations. A series of tests outlined below ensured the model had converged yet was not too computationally costly.

Note that for the simulations in this chapter, as the strain varies in time, it is not possible to make a 2D plot that varies in space, time and location on the scooter. Because of this, single elements are used, usually in locations that are where strain gauges are located, or in locations near them. Figure 8.1 shows the distance convention used for deck and down tube elements.

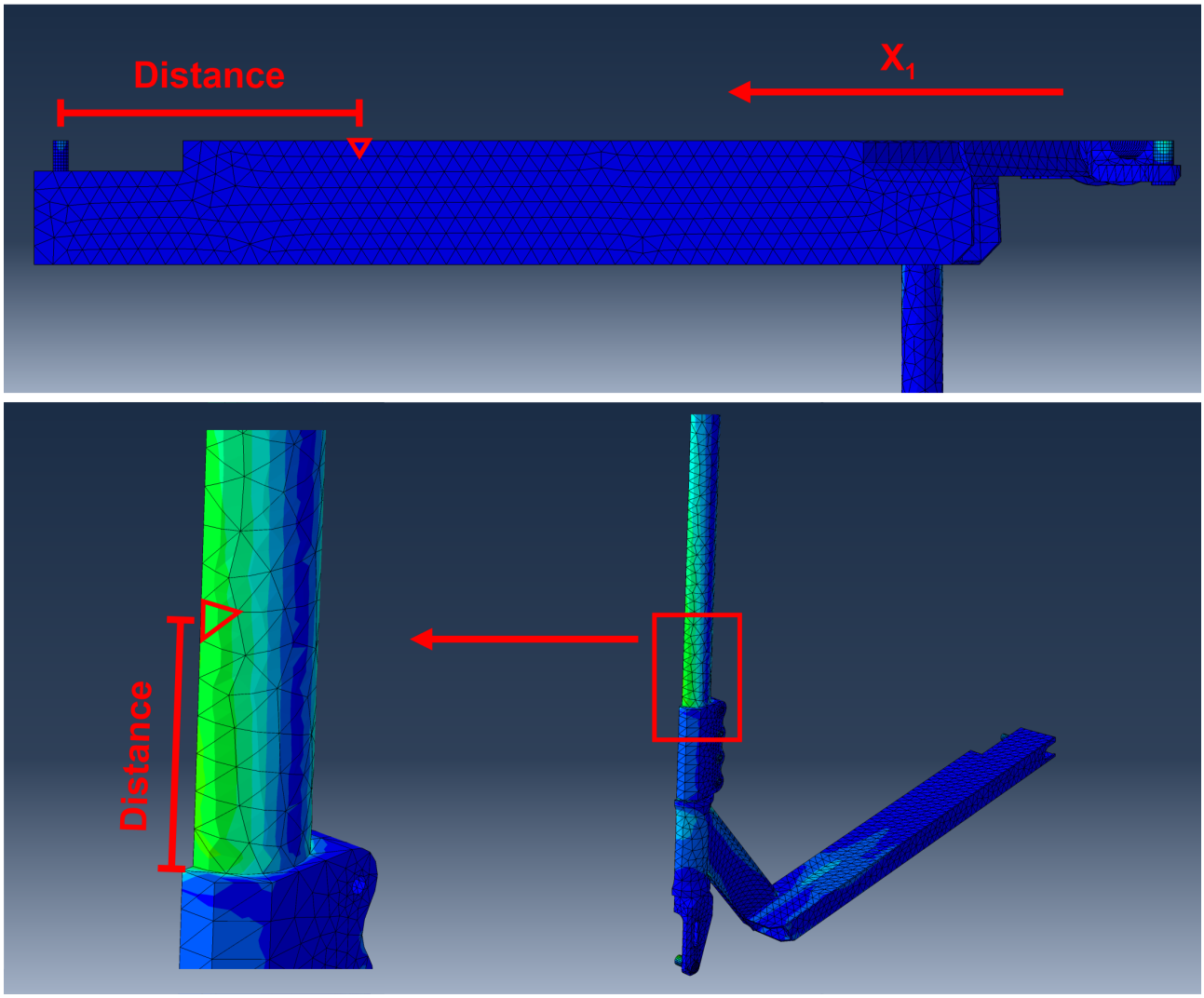


Figure 8.1: Showing the distance conventions used in this chapter describing convergence on elements. Note that the distance along the down tube is not in the x_3 direction, but 7° away from it towards the x_1 direction.

8.2.1 Single vs double output precision

Once the the FE model was configured correctly, the first step was to compare the results of single and double output precision. Double output precision reduces the effect of round-off errors when doing explicit analyses. Results were slightly different for a 10 mm mesh size, as shown in figure 8.2 (with an FFT of the results in figure 8.3). Nodal output precision tests were also conducted. Changing the nodal output precision had no impact on results. For simulations used to analyse the strains in hops, double output precision and single nodal output precision were used.

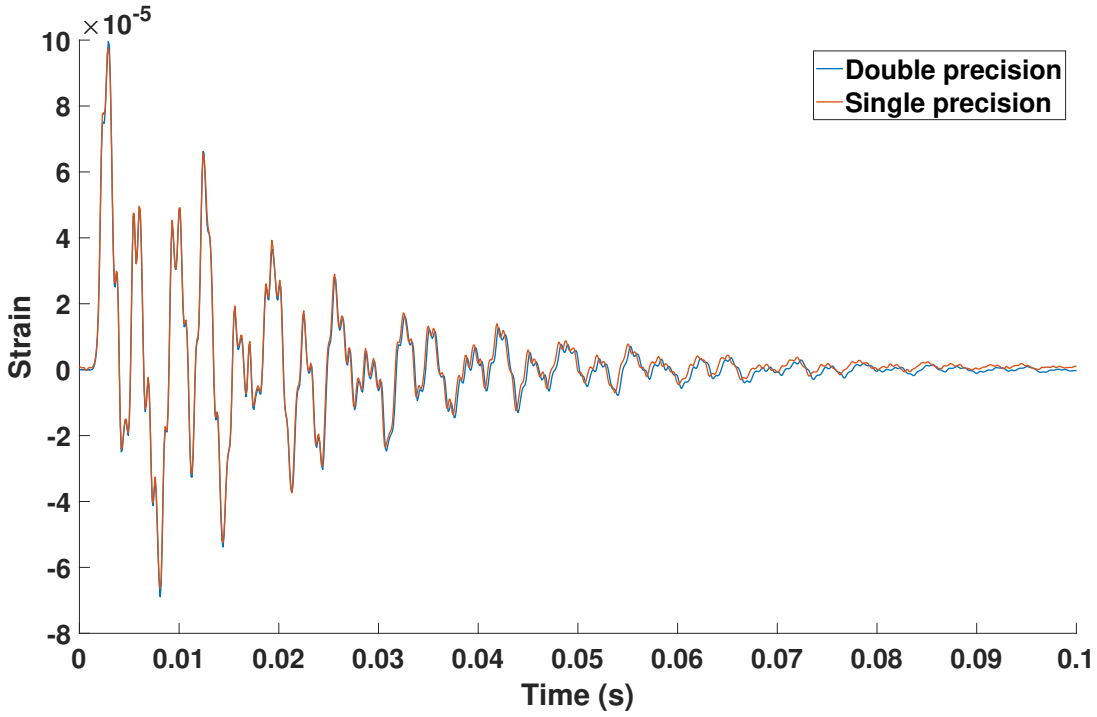


Figure 8.2: A figure showing the difference in strain output when either single or double output precision is used.

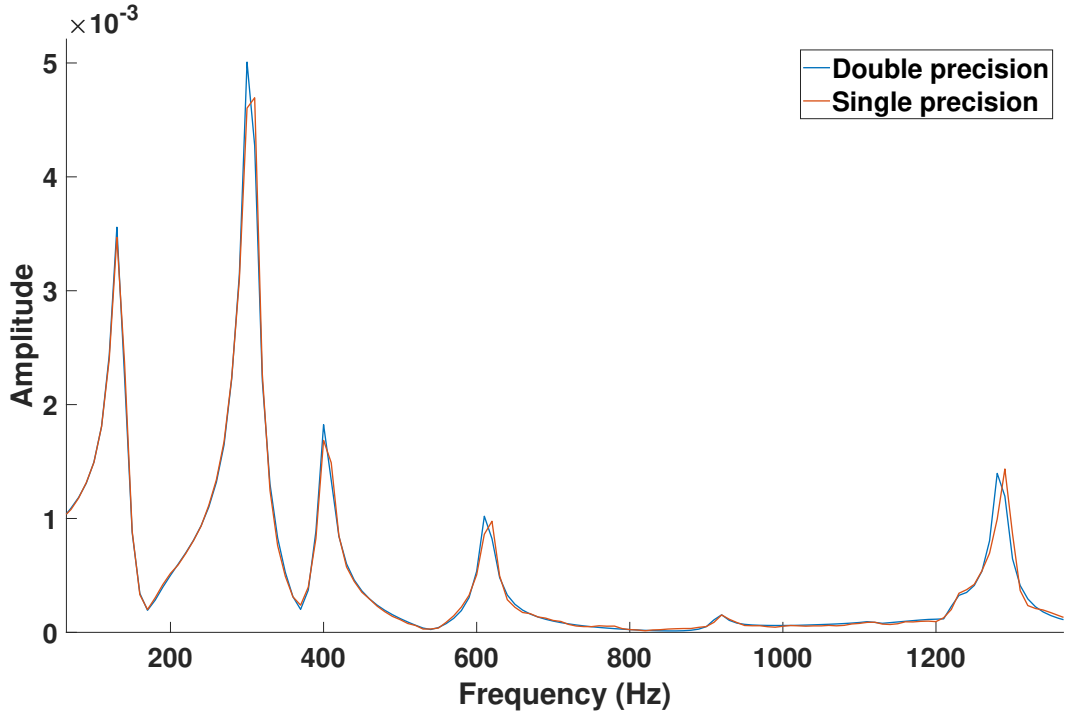


Figure 8.3: This is the FFT of the above figure showing the small difference in results for single and double output precision.

8.2.2 Element type and mesh convergence

Following output precision, the next question concerned which element type to construct the mesh from. For explicit analyses, the main options were linear tetrahedral (C3D4), quadratic tetrahedral (C3D10M) and linear hexahedral (C3D8R) elements. Abaqus explicit does not offer quadratic hexahedral elements. A mesh consisting purely of hexahedral elements was not possible, as the geometry was too complex for the scooter to be able to mesh. The options were, therefore, either a fully tetrahedral mesh or a mesh that had a mix of hexahedral and tetrahedral elements. One advantage of a mesh containing hexahedral elements was the significantly lower computational cost. A test model was constructed with mixed hexahedral and tetrahedral elements by partitioning the model. The bulk of the extrusion profile of the footplate, as well as the portions of the down tube and crossbar that were simple prismatic shapes (i.e. not where they meet), were assigned hexahedral elements. Results were compared to those of a quadratic hexahedral mesh. As linear and hexahedral element shapes are incompatible with tetrahedral elements (their nodes do not coincide at the same points in the whole mesh), Abaqus would create tie constraints between the interfaces where the element type changed. As shown in figure 8.4, the model containing hexahedral elements had a stress distribution that varied very abruptly at the interface between the different element types. Because of this, a fully tetrahedral element model was used.

Quadratic C3D10M and linear C3D4 tetrahedral elements exist within the Abaqus explicit environment. As linear tetrahedral elements have a constant strain throughout, they are generally to be avoided due to poor convergence. A much more refined mesh is required [137, 138], leading to a more computationally expensive model than a quadratic tetrahedral mesh of the same accuracy. A convergence study can be seen in figure 8.5 for C3D10M elements with sizes from 10 mm - 4 mm. A mesh size of 10 mm was used for the comparison simulations in section 8.3.4, as this had sufficient accuracy in the regions of interest. For a comparison with linear elements, the 10 mm quadratic model was compared against 2 mm and 4 mm (element size) linear meshes. The linear elements appear stiffer, with the 4 mm elements having a higher frequency response than the 2 mm elements. In addition, the simulations with linear elements are relatively costly. The 2 mm linear elements took 273 minutes for a .01 second simulation, whilst the equivalent time on the 10 mm quadratic

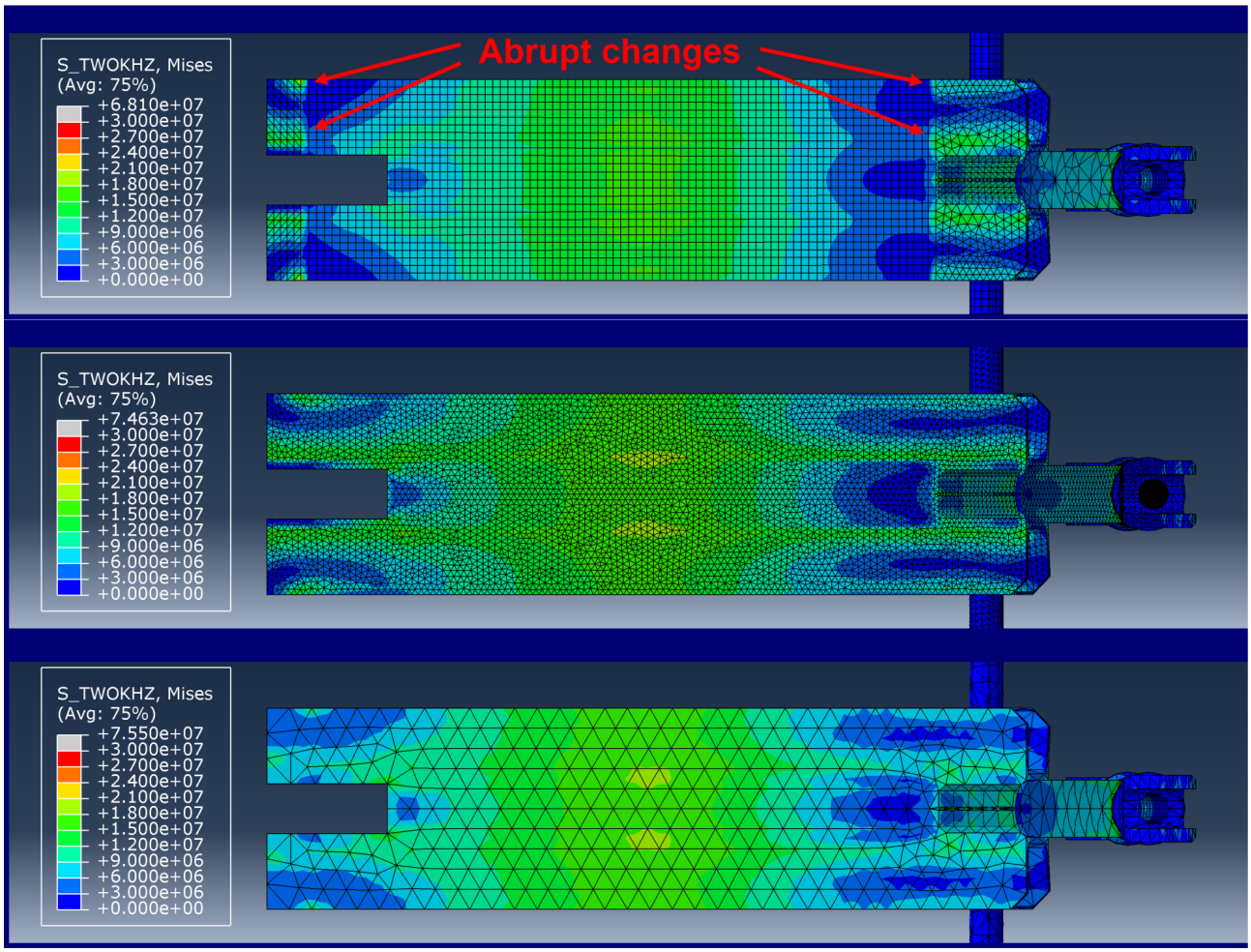


Figure 8.4: A comparison of the Von Mises stress distribution for meshes with: mixed hexahedral and tetrahedral elements (top image), with meshes containing only tetrahedral elements (middle and bottom). As can be clearly seen, there are abrupt changes in the stress at the interfaces between the tetrahedral and hexahedral regions of the mixed mesh which are highlighted with red arrows.

mesh took only 41 minutes on the same computer (see table 8.1). The results can be seen in figure 8.6.

	10 mm quad	4mm linear	2 mm linear
time for 0.01 s of simulation (min)	41	27	273
number of elements	16936	85824	519614
number of nodes	33328	26600	133074

Table 8.1: A comparison of the time taken to perform a simulation with various mesh conditions. Simulaton performed with a 2 kHz second order Butterworth filter and double output precision. Note that simulation times may not be exact upon replication, as the computer used is shared by multiple users who may have been running programmes. The computer used had 64 GB of RAM, and an intel i9-7900x 3.3 GHz CPU (these dynamic explicit calculations could not utilise GPU acceleration).

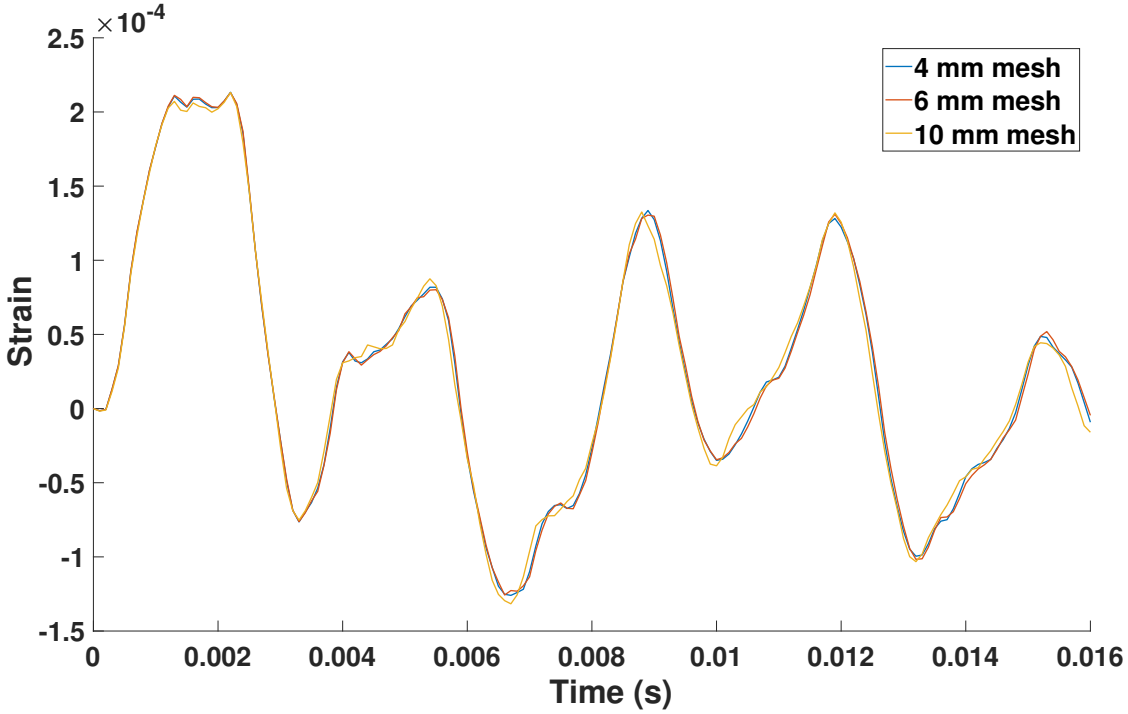


Figure 8.5: A convergence study for 4 mm, 6 mm and 10 mm mesh sizes. The centroids of the elements are 171 - 172 mm from the centre of the back axle. The impulse applied is a step function of height 1 kN and width 2 ms applied at as an area load covering the static area of $\boldsymbol{f_4}$. No result from the 15 mm mesh is shown, as it did not have a centriod in the same region. Results from other regions where the 15 mm mesh coincided with the 4 mm mesh showed quite noticeable differences.

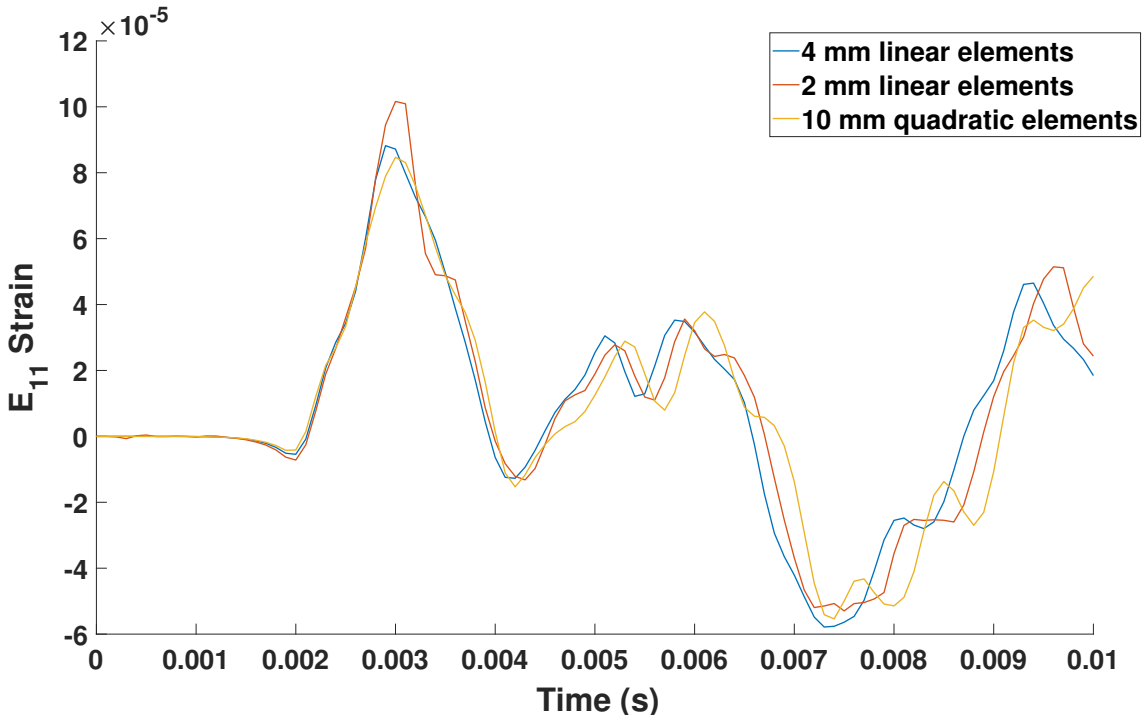


Figure 8.6: A comparison of C3D10M and C3D4 elements. The location of the measured strain is equivalent to that of deck strain gauge 1. A hammer impulse (small area impulse) that peaks at 1 kN was applied at the location of $\boldsymbol{f_4}$

8.2.3 Using symmetry

It was possible to reduce the computational cost by exploiting the symmetry in the x_1 / x_3 plane. This allowed for a model with approximately half the number of elements. Results comparing equivalent loading conditions can be seen in figure 8.7.

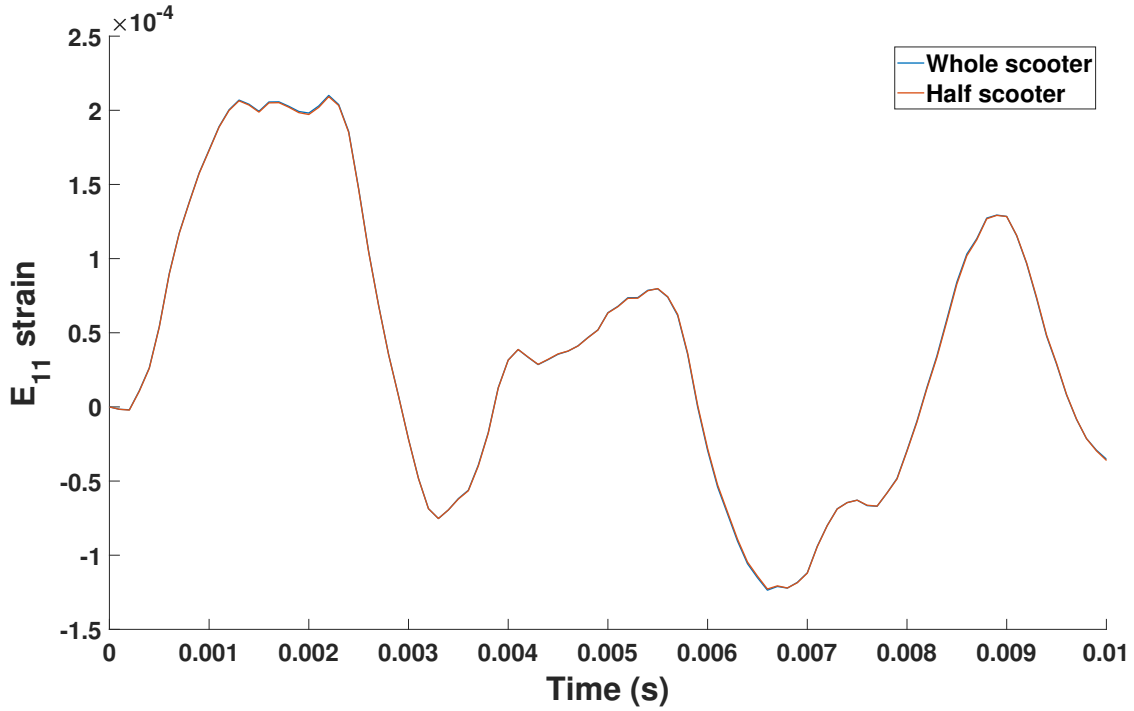


Figure 8.7: A simulation showing that the scooter behaves virtually identically with symmetry applied. The element centroid is 168 mm from the back axle.

8.2.4 Timestep convergence and mass-scaling

It is necessary to have timestep convergence to be able to have confidence in any predictions made. The timestep is generally dictated by the size (including aspect ratio) and density of elements. First, a timestep convergence study with timesteps of 5×10^{-8}s, 2.5×10^{-8}s and 1.25×10^{-8}s was conducted. The simulation with timestep size 5×10^{-8}s aborted. Results with timesteps of size 2.5×10^{-8}s and 1.25×10^{-8}s can be seen in figure 8.8, the results are virtually identical.

An approach often used to increase the possible timestep is mass-scaling. Mass-scaling involves increasing the density of some (or all) elements in the model. Increasing the density of all the elements in the model would change the scooter's frequency response, which is important in this

project. However, because the model has some complexity, there were a small number of elements in non-crucial locations (such as the head tube) with a large aspect ratio. Increasing the density of these elements alone was not expected to change the system's frequency response significantly. Semi-automatic mass-scaling can be implemented in Abaqus, whereby a target timestep can be set. Abaqus will increase the density of the elements that need to be denser for that timestep size to run. Figure 8.9 also shows the results of meshes with target timesteps of 5×10^{-8} s and 1×10^{-7} s. As can be seen, semi-automatic mass-scaling with a timestep of 5×10^{-8} s did not significantly affect the system's response and, therefore, was used for subsequent models.

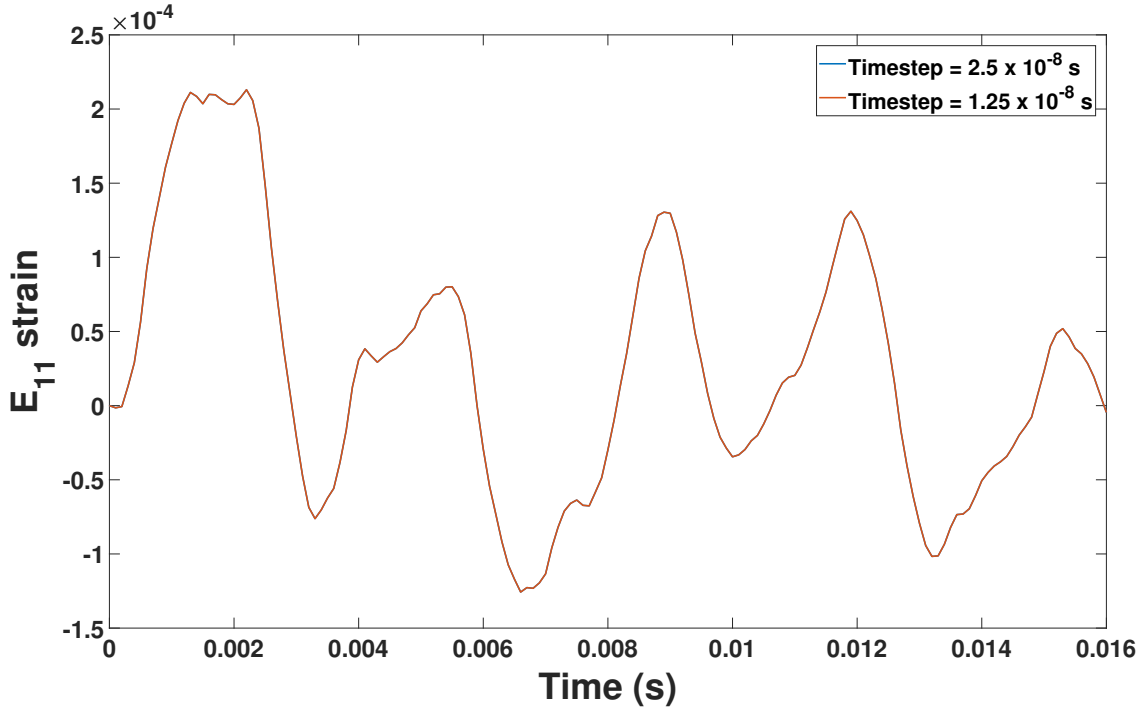


Figure 8.8: A graph showing timestep convergence for the 4 mm mesh. The centroid of the element is 170 mm from the back axle.

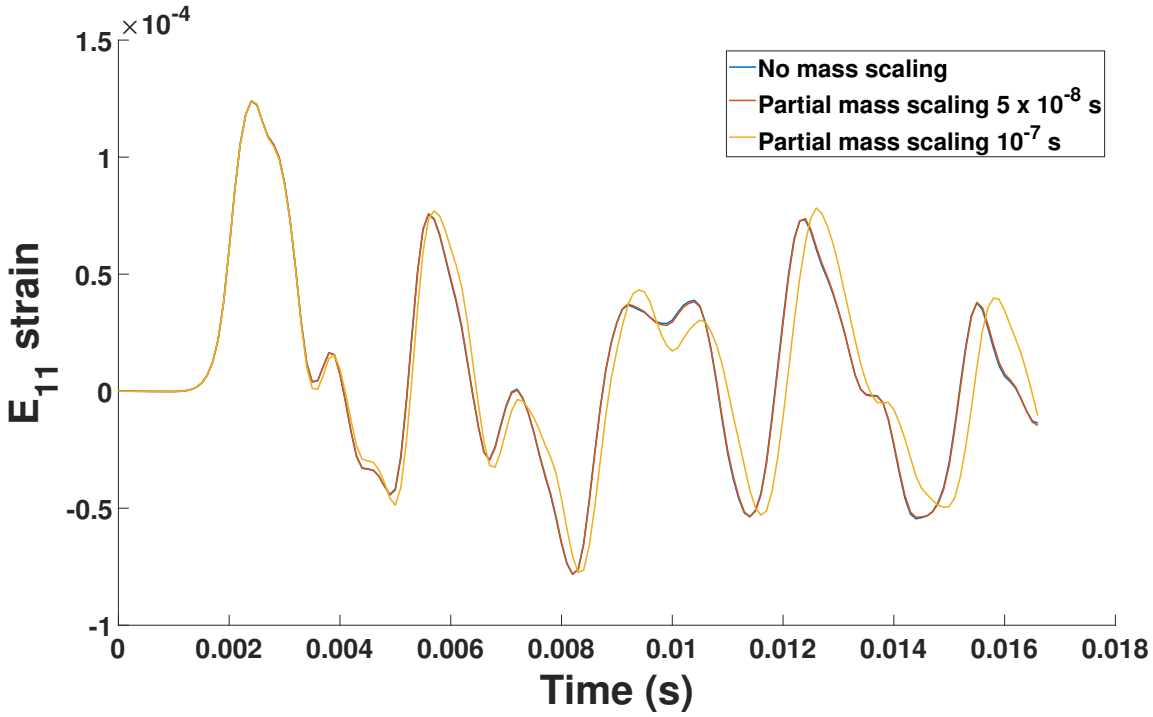


Figure 8.9: A plot showing that partial mass-scaling with target time increment of 5×10^{-8} s does not significantly affect the frequency response of the scooter for 10 mm mesh size. The effect begins to become apparent for a target time increment of 10^{-7} s. A basis impulse was applied at the location of $\boldsymbol{f_4}$ with a peak magnitude of 1 kN

8.2.5 Small area load vs large area load comparison

In section 6.3.1, justification is given as to why impulses were applied over relatively small areas when conducting the dynamic calibration. As the loads the rider subjects to the scooter are over a larger area, the difference in strain response between smaller and larger area loads was compared. A standard basis load (of the size used in the static model, with width 70 mm) was compared with a load spread over a 5 mm $\times$ 5 mm area. First, a static simulation was executed to gauge the difference in the strain distribution between the two models across the whole underside of the footplate. As shown in figure 8.10, the strain distributions on the underside of the deck are very similar, more so than that predicted by Euler-Bernoulli beam theory. This is because the load is transmitted through the walls/spars in the deck, yet there is some strain relief along the centreline of the deck (see figure 8.11). For dynamic simulations, measurements both far away and near the region of the applied load were taken, an example result can be seen in figure 8.12. The strain response along the middle of the deck (where the deck strain gauges are) is very similar.

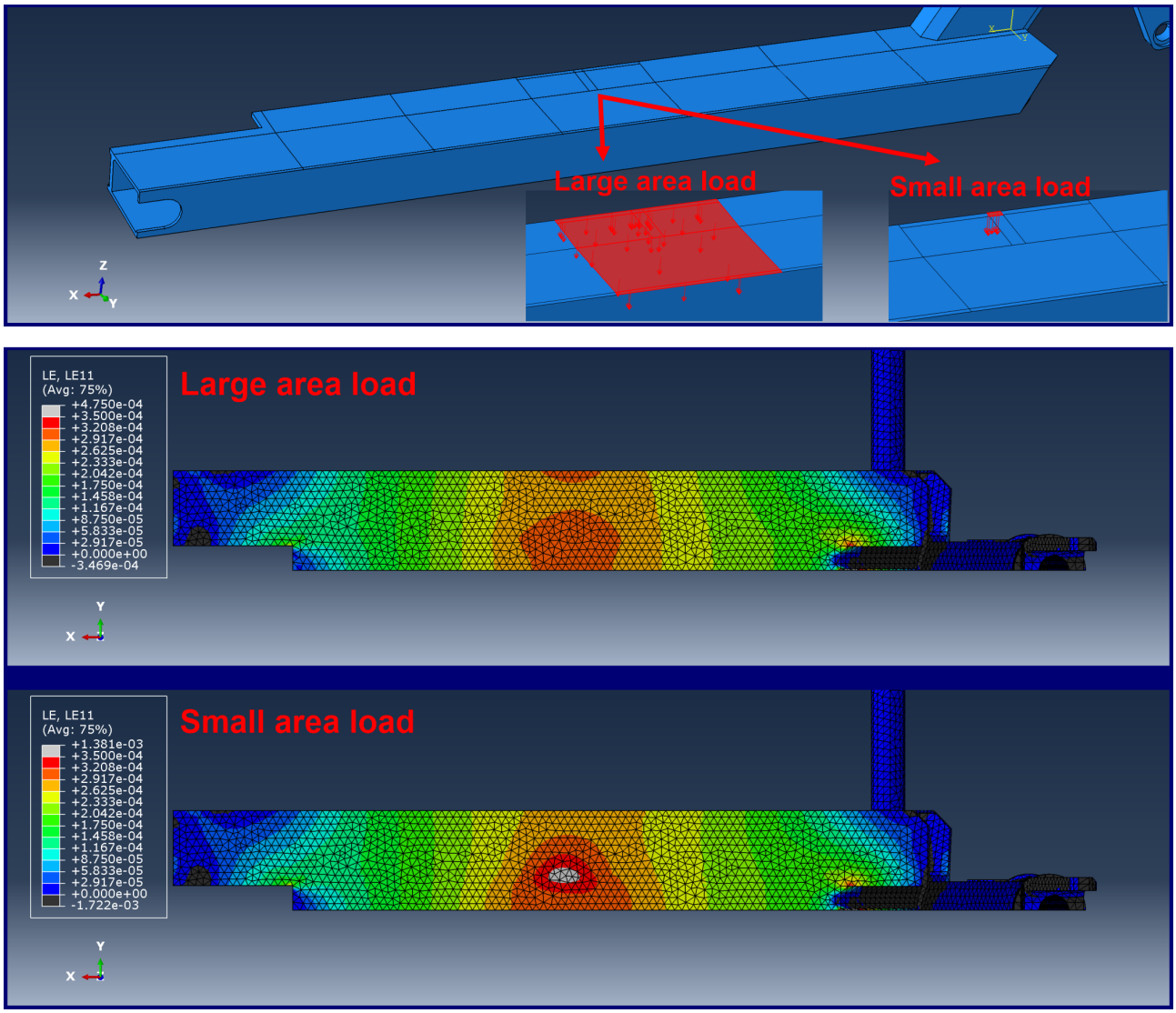


Figure 8.10: The E_{11} strain distribution along the underside of the deck for the larger area and smaller area loads. The larger area load (middle) replicates the loading distribution applied for the static calibration, and the smaller load (bottom) is an approximation of the loading applied for the dynamic calibration.

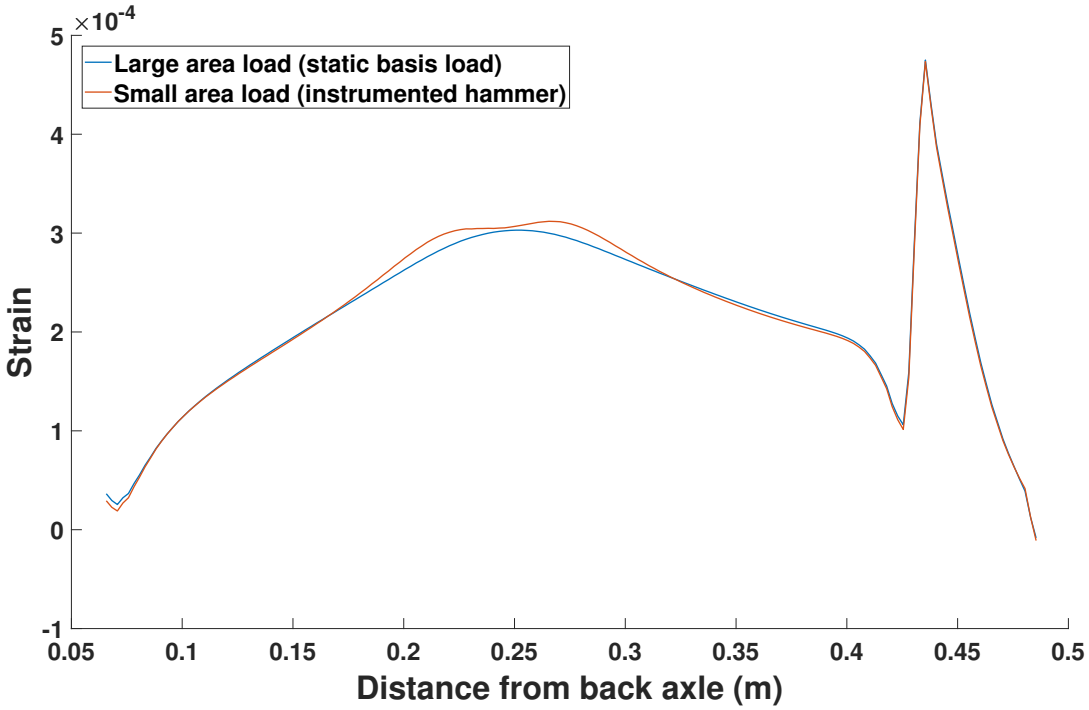


Figure 8.11: Showing the difference in strain distribution along the underside of the deck for small and large area loads. The difference in strain distibution is less than that predicted by Euler-Bernoulli beam theory. Note that this simulation is static, such that data from the centerline of the underside of the deck can fit onto a single 2D plot. The mesh size for this simulation is 5 mm, the elements are C3D10 (static). The load applied is 1 kN, at the location of $\boldsymbol{f_4}$.

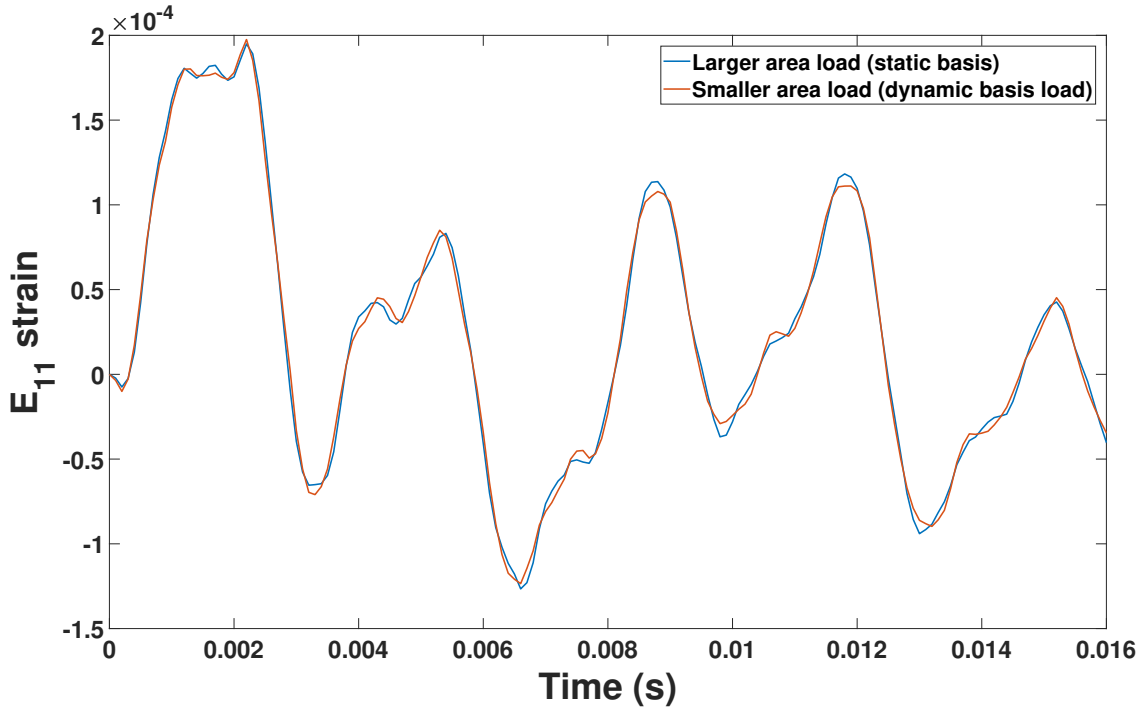


Figure 8.12: Comparing the dynamic strain response from an impulse applied over the larger area load (static calibration) and the smaller area load (dynamic calibration). The element is taken from the centre of the scooter deck, with its centriod 148 mm away from the back axle. The impulse applied is a step impulse of load magnitude 1 kN that endures for 0.02 s. The impulse is applied at the location of $\boldsymbol{f_4}$. The strain distribution is clearly very similar.

8.2.6 Axle boundary condition

Two boundary axle conditions were compared. The first boundary condition was applied across a line element (on the surface of the back dropout [where the rear axle is] and fork) and was compared with a model with steel axles and a frictional contact (see figure 8.13). The axles had a hard normal interaction and a frictional penalty of 1 % for the tangential behaviour. As can be seen in figure 8.14, the results are similar.

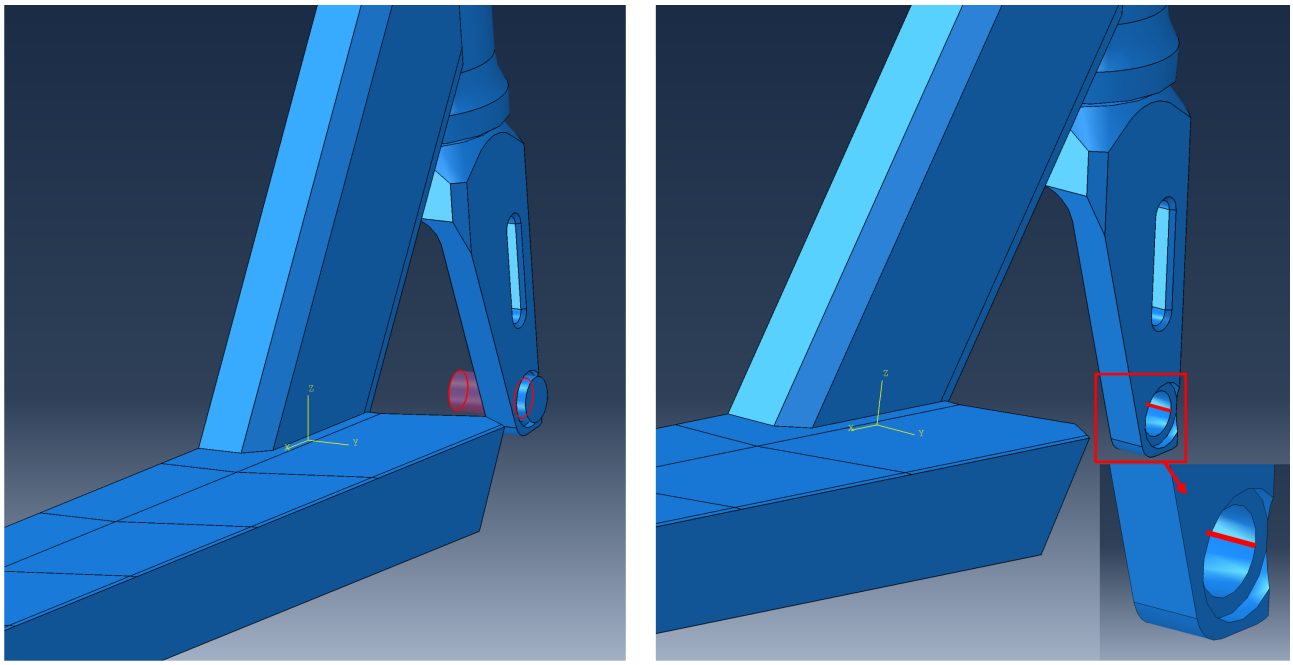


Figure 8.13: Showing the different axle/back droupout boundary conditions tested. The left hand case shows the axle with a 1 % frictional penalty and hard tangential contact definition, and the right side shows a line element on the inner surface of the front fork that is fixed. Figure 8.14 shows that the results are very similar.

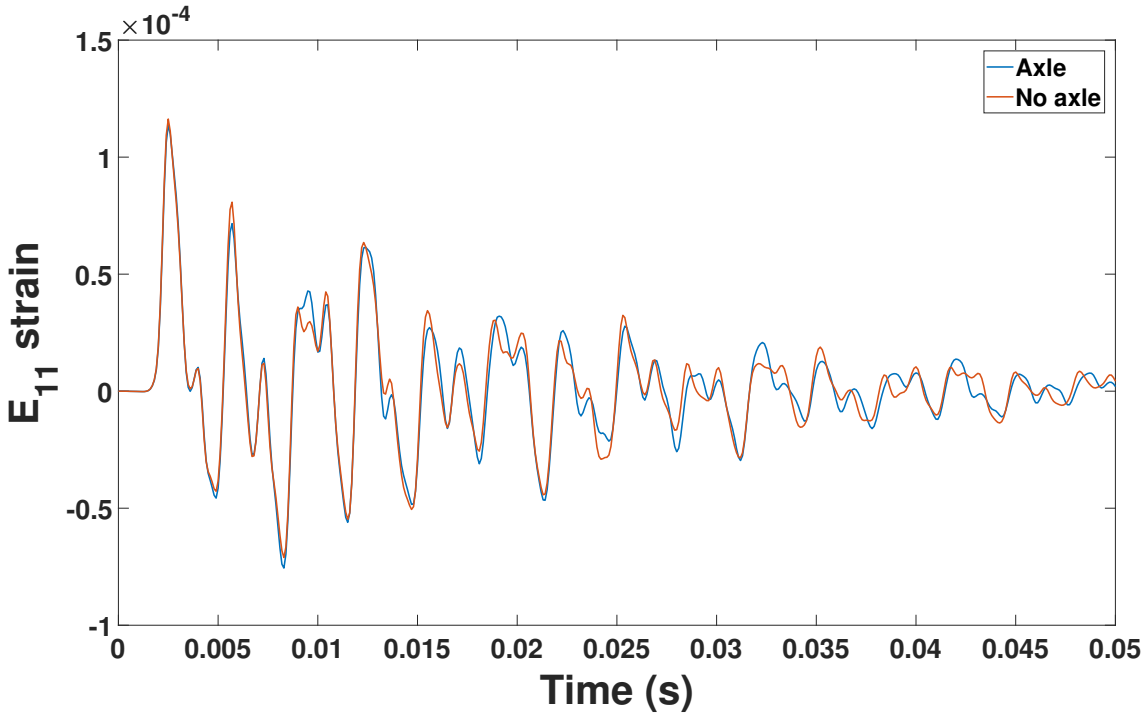


Figure 8.14: The comparison of the strain response with an axle and a simplified boundary condition. The contact between the axle and the scooter has a frictional penalty of 1 %. The mesh size of the simulation is 10 mm mesh hammer, and the load applied is a hammer impulse at the location of $\boldsymbol{f_4}$ with a 1 kN peak force. The strain data is taken from the location of deck strain gauge 5.

8.2.7 Natural frequency tests

Natural frequency tests were conducted to compare the natural frequencies of the FE model with the experimental setup, and to test the convergence of the natural frequencies of the FE model. Convergence was tested with mesh sizes of 4 mm and 10 mm. Frequencies up to 2000 Hz were investigated. The simulations converged to within 2 % for modal frequencies.

Table 8.2: A table showing the convergence of natural frequencies of the model for 10 mm and 5 mm mesh sizes. The modes are all the modes from the first 1000 Hz. Modes denoted (s) are modes that are symmetric in the x_1 / x_3 plane (i.e. modes that are present when the symmetry boundary condition is applied).

mode number	Frequency (Hz) 10 mm mesh	5 mm mesh	Difference (%)
1	27.6	27.2	1.29
2 (s)	28.3	28.2	0.34
3	82.8	82.6	0.32
4	119.4	118.1	1.11
5 (s)	133.9	133.4	0.38
6	218.4	215.8	1.19
7 (s)	263.5	262.0	0.55
8 (s)	293.0	292.2	0.26
9	304.9	300.3	1.54
10 (s)	307.7	303.5	1.38
11 (s)	403.7	401.6	0.51
12	483.2	472.8	2.19
13	593.6	578.9	2.53
14 (s)	617.3	611.7	0.92
15	915.6	909.7	0.64
16 (s)	925.2	915.9	1.02
17	962.9	962.1	0.09

8.2.8 Filtering

Tests were carried out on otherwise identical simulations that either used a second order 2 kHz Butterworth filter, or did not (2 kHz was the cut-off frequency used on collected strain data). For the simulation data, it made almost no distinguishable difference, aside from a small phase shift. Results can be seen in figure 8.15. Some of the graphs in the preceding sections used a filter, but for the final simulations in section 8.3.4 no filter was applied in Abaqus. The reason for this was that it allowed for more freedom in post-processing, and simulations without a filter were faster.

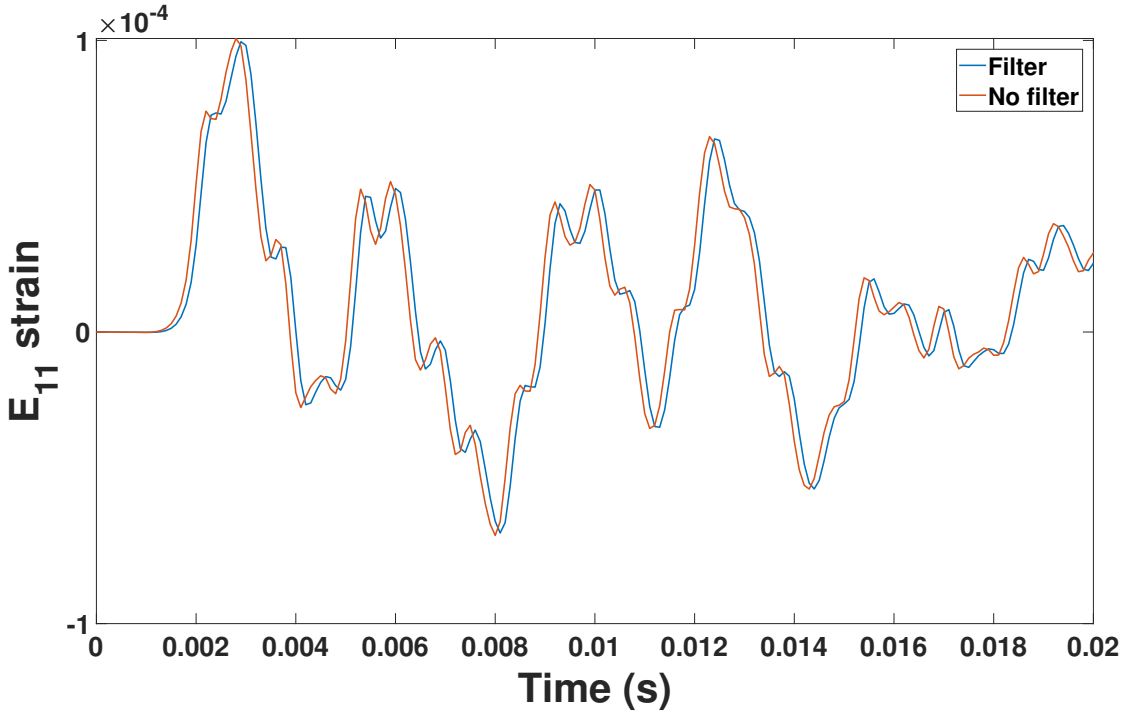
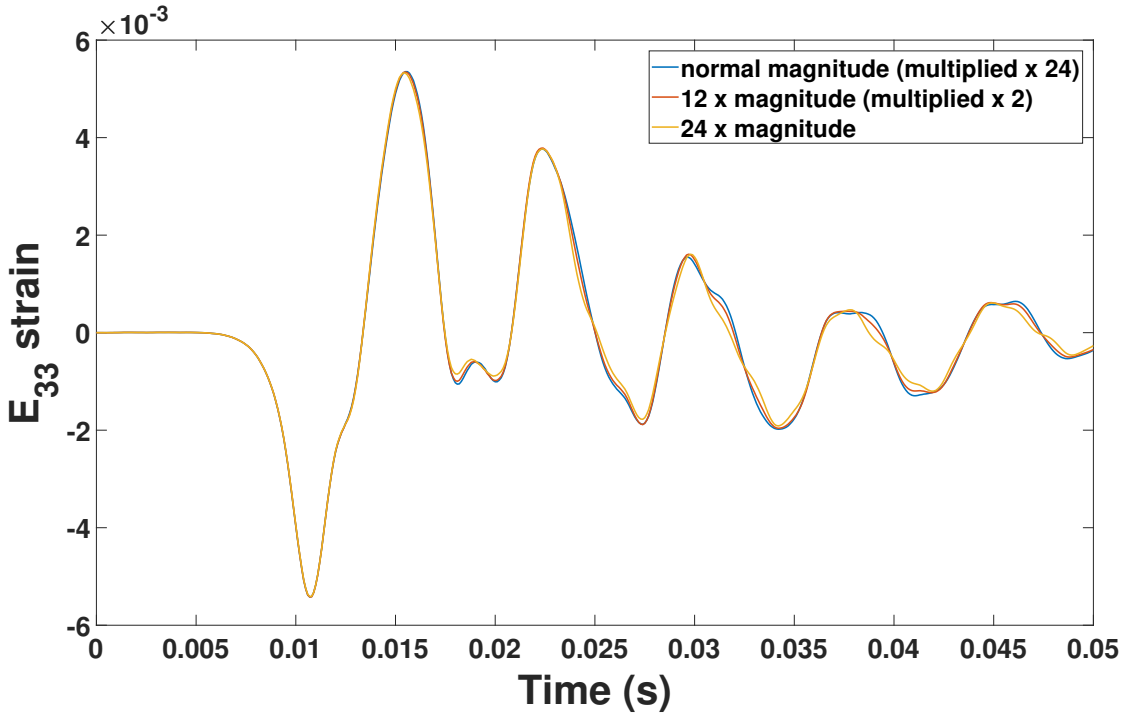


Figure 8.15: A comparison of results on the difference between using a 2 kHz second order Butterworth filter on a 10 mm mesh.

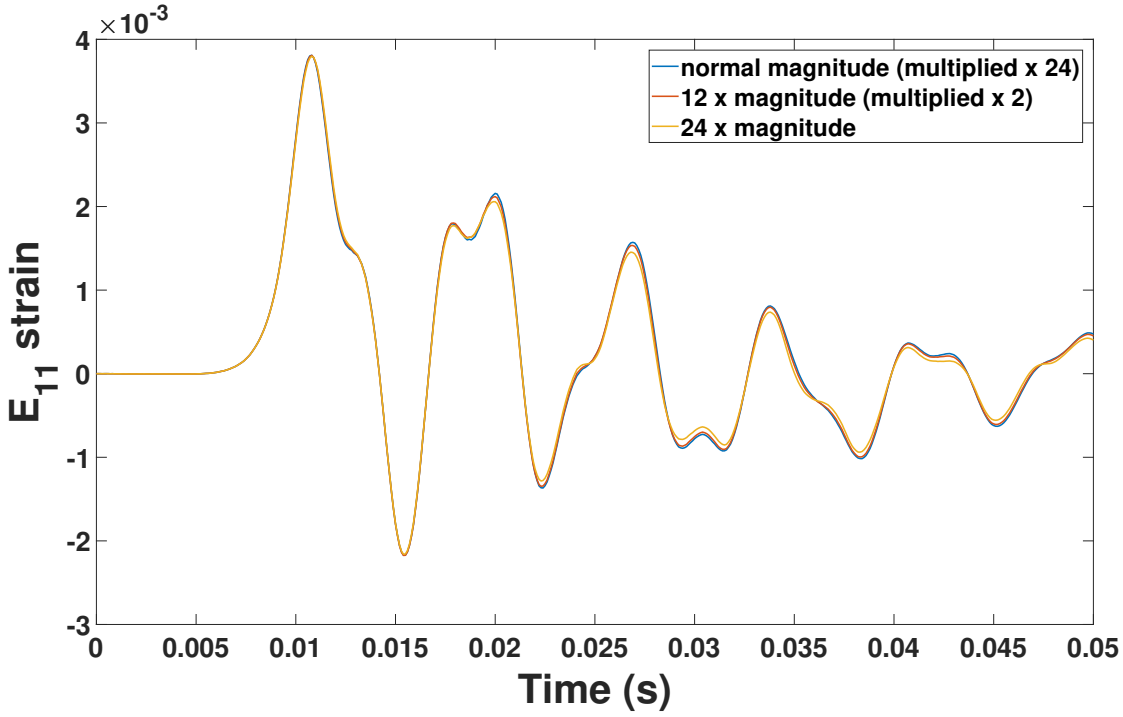
8.2.9 Linearity tests

Further tests were conducted to investigate the linearity of the geometry when the magnitude of the impulse was increased. Even after the point where significant yield would occur in parts of the scooter (a linear elastic model was used), the model still behaved linearly to a very good approximation. Comparisons of smaller-scaled impulses with larger basis impulses are in figures 8.16a and 8.16b. A linear-elastic model was deemed suitable for this analysis as whilst it is possible that some microscopic

yield may occur during use, stunt scooters clearly do not face substantial (visible) yield during normal use, or it would be noticed in the geometry (and components would break very quickly).



(a)



(b)

Figure 8.16: Showing the strain response for various impulses from simulated hammer impulses. The impulses have the form of one of the original basis impulses but widened (stretched) in time by a factor of 5 to help achieve higher peak strains. The plot shows the strain response of an original magnitude hammer hit (original peak load 1 kN, multiplied by 24), an impulse that is 12 times the magnitude of the original (multiplied by two), and an impulse with 24 times the magnitude of the original. Figure a) shows the response on the front of the down tube 35 mm from the clamp, and figure b) shows the strain response at the location of deck strain gauge 1. The impulses are applied at $\boldsymbol{f}_4$.

8.3 Axle boundary conditions, Material damping, and headset bearing stiffness

In the above section, little attention was paid to the material damping, headset bearing stiffness and axle boundary conditions. In reality, the axles are mounted on wheels which have contact with the ground. The wheels will deform somewhat upon landing. The axle is in contact with bearings, which are in contact with a machined, spoked aluminium core, which is bonded to a urethane tread which contacts the ground. The bearing and the urethane tread are likely sources of significant non-linearity. In a static model, this should have no impact on the stresses or strains in the model, however in a dynamic model, this could have a significant effect. The headset bearings are also another non-linear contact. It is worth noting at the start of this section, that to analyse these conditions in detail could be a project in and of itself. The arguments given here are cursory, and parameters chosen are also based on fit with measured data.

8.3.1 Material damping

When the scooter is subject to an excitation, the excitation will dampen out over time. One way to model this loss of energy to the surroundings is through material damping. One of the common ways to do this in Abaqus is through the use of Rayleigh damping [139]. Rayleigh damping is defined by two parameters, α and β. α is for mass proportional damping, and β is for stiffness proportional damping. The damping will be different for each mode of vibration, with the fraction of critical damping (ζ) for mode i being given by:

$$\zeta_i = \frac{\alpha}{2\ \omega_i} + \frac{\beta\ \omega_i}{2} \tag{8.1}$$

As can be seen from this equation, α damps lower frequencies more than it does higher frequencies. Conversely β damps higher frequencies more than it does lower frequencies. Importantly, the stable increment for Abaqus explicit depends on the fraction of critical damping according to the following equation:

$$\Delta t = \frac{2}{\omega_{\mathsf{max}}} \left(\sqrt{1 + \zeta_{\mathsf{max}}^2} - \zeta_{\mathsf{max}} \right) \tag{8.2}$$

where ζ_{max} is the critical damping of the highest frequency mode. In the case for the scooter model used in this project, when using a β value of 10^{-6} s, the time increment was 3.81×10^{-11} s, as opposed to 2.44×10^{-8} s in the case where the value for β was 0 s (in both cases the simulations were done without mass-scaling and with a α value of 100 s^{-1}). This value of β would correspond to approximately 0.3 % damping at 1000 Hz, and would therefore likely be negligible to simulation results. Given that such a simluation would take over 600 times as long, and any further damping would increase the simluation time linearly (this is expected from equation 8.3.1, but a test with a β value of 10^{-5} s was also carried out, giving a time increment was 3.81×10^{-12} s). Because of this, it was clearly untenable to have β damping in the simulation, so only α damping was used.

Some experiments were performed to approximately determine what the value of α should be. In the case where only α damping is present, the relationship between the critical damping factor and α is:

$$\zeta_i = \frac{\alpha}{2\ \omega_i} \tag{8.3}$$

This can be used in conjunction with information on the relationship between the logarithmic decrement (δ) and the critical damping factor to obtain an expermintal value for α. δ is a measure of the decay between successive peaks when there is damping. The equation relating δ and the amplitude of successive peaks is:

$$\delta \ = \ \frac{1}{n} \ln \left(\frac{x(t)}{x(t + nT)} \right)$$

where T is the period of oscillation, n is any natural number, and $x(t)$ is the peak value (subtracting the steady state value if it is not 0) of the function measured in some oscillation. The relationship between δ and ζ is given by:

$$\zeta = \frac{\delta}{\sqrt{\delta^2 + 4\pi^2}}$$

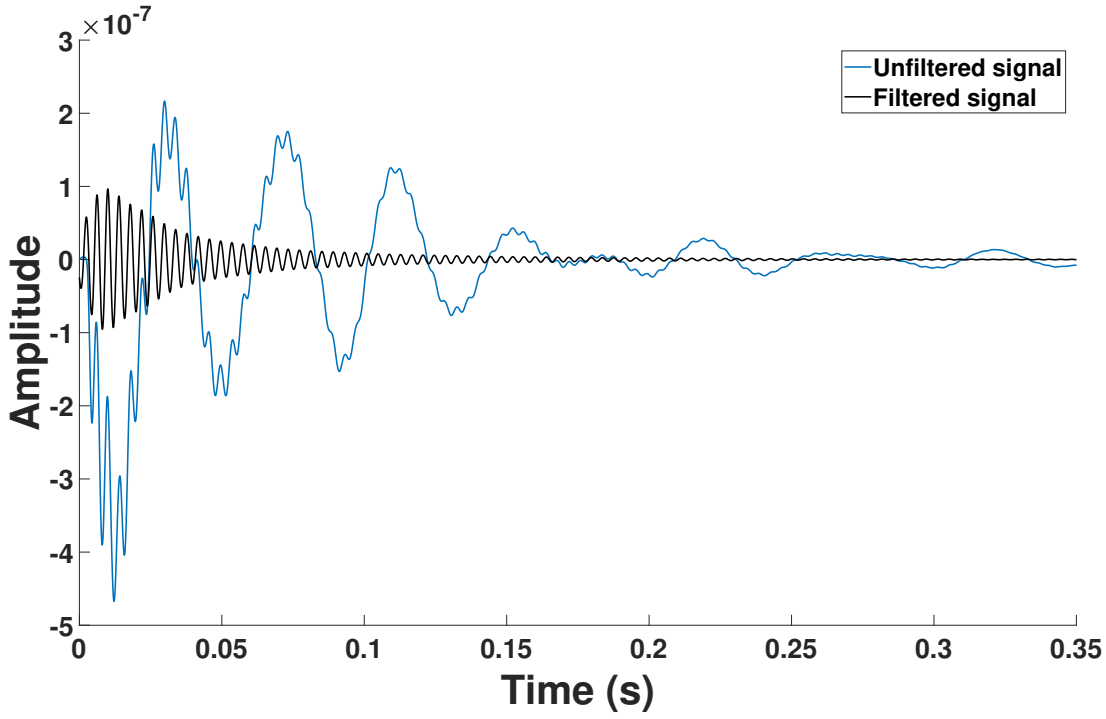
This allows α to then be calculated via equation (8.3). One issue with this was that the data of hammer impulses collected gave rise to a complex strain output containing information from many modes. Moreover, in most cases, the Fourier transform of the modes overlapped, making it difficult to determine the exact rate of decay. In addition, especially because only α damping was considered, different values would be calculated for different different modes. In response to these complexities, values of α were calculated for different frequencies by applying a passband across the frequencies of interest. Responses were taken from the basis impulses observing both the response in the strain gauges and the deck. The mode at 254 Hz from the basis impulse applied at $\boldsymbol{f_1}$ did not overlap significantly with other peaks. The strain output of the isolated frequency and its associated FFT can be seen in figure 8.17. Figure 8.18 shows a similar approach being taken with basis impulse $\boldsymbol{f_5}$. In this case, there are no peaks in the FFT that are not entangled with other peaks. In this case, there is a certain amount of beating. This effect likely increases the calculated value of α. The lowest frequency peak (17 Hz) for this basis load was also isolated in the same manner, however a filter order of four rather than eight was used to avoid numerical instability in the filter. This peak had significant overlap with other peaks. To avoid the other peaks interfering with the signal, the passband was narrow, more so than it would be if the the other peaks were not present. Because of this, the calculated value of α is probably lower than it should be. Results for the calculated values of α can be seen in tables 8.3 and 8.4. It is worth noting that because α damps lower frequencies more, if the damping is uniform, the calculated values of alpha from the higher frequency modes will be an overestimate of the optimal value for α, and those from the lowest modes will be an underestimate. It appears as if the appropriate value of α is likely to lie somewhere in the range of 10 - 70 s^{-1}, with most of the experimental results giving values in the range 45 - 65 s^{-1}.

Table 8.3: Showing the calculated values of α for various strain measurements from basis impulse 1 ($\boldsymbol{f_1}$). The strain measurements are from the down tube strain gauge. The frequency of the mode excited is 254 Hz, and the filter order is an eighth order zero-phase Butterworth filter. The passband is from 230 - 320 Hz.

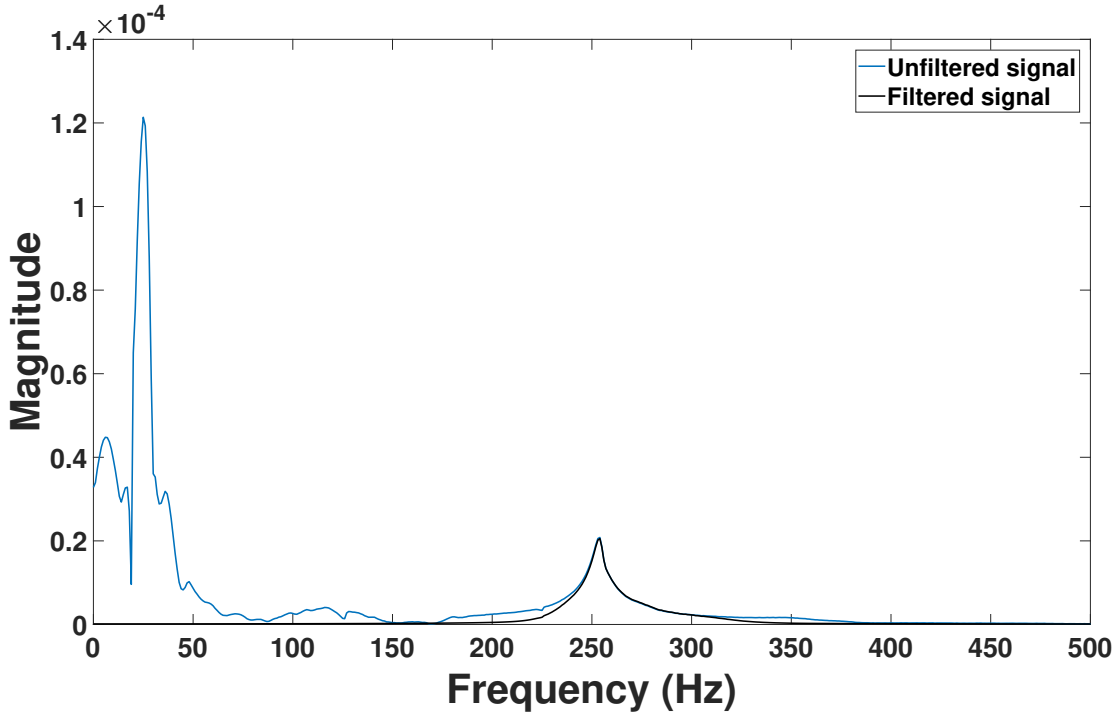
number after initial peak of measurement	log decrement	calculated damping ratio	calculated α value (s^{-1})
1	0.106	0.017	54
2	0.123	0.020	62
3	0.119	0.019	60
4	0.124	0.020	63
5	0.135	0.022	69
6	0.143	0.023	72

Table 8.4: Showing the calculated values of α for various strain measurements from basis impulse 5 ($\boldsymbol{f_5}$). The strain measurements are from deck strain gauge one, except those labelled * which are from deck strain gauge 4. A Butterworth filter (zero-phase) of order four (two for each pass in the zero-phase filter) was used for entries labelled **, and order eight for all others. Entries labelled ** are for a modes of frequency 17 Hz, whereas all the other results are of frequency 158 Hz.

passband used (Hz)	log decrement	calculated damping ratio	calculated α value (s^{-1})
105 - 210	0.160	0.026	51
105 - 210	0.176	0.028	56
105 - 210	0.154	0.025	49
105 - 210	0.150	0.024	48
135 - 210 *	0.148	0.023	47
135 - 210 *	0.140	0.022	44
135 - 210 *	0.144	0.023	45
135 - 210 *	0.150	0.024	47
13 - 22 **	0.266	0.042	9
13 - 22 **	0.544	0.086	18

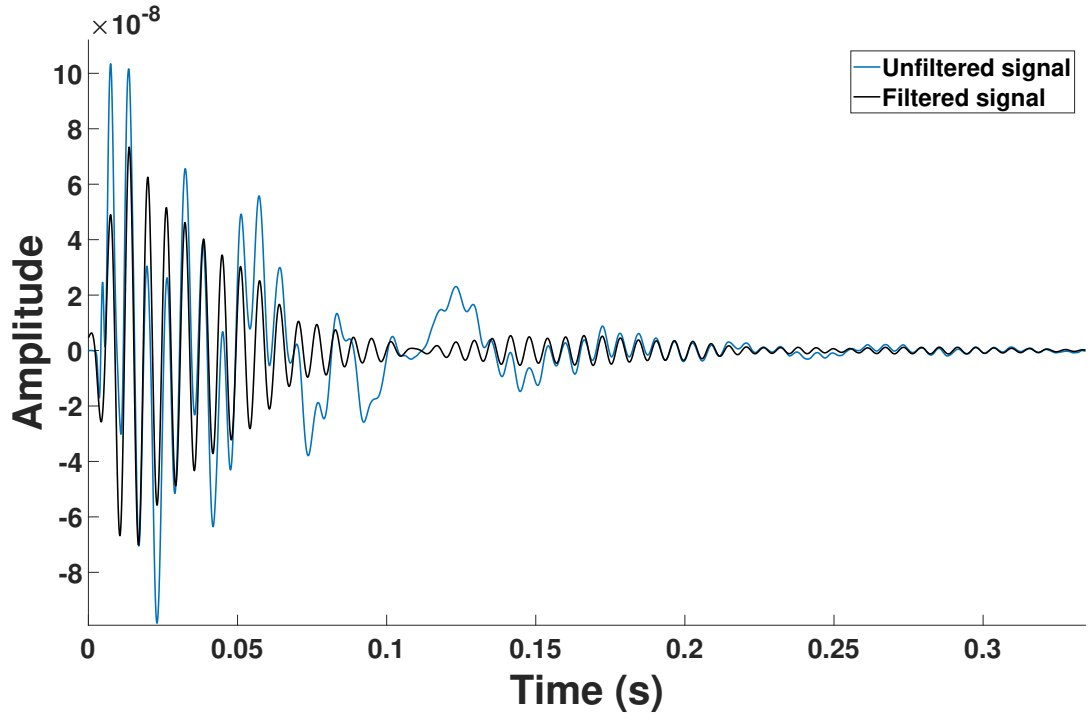


(a)

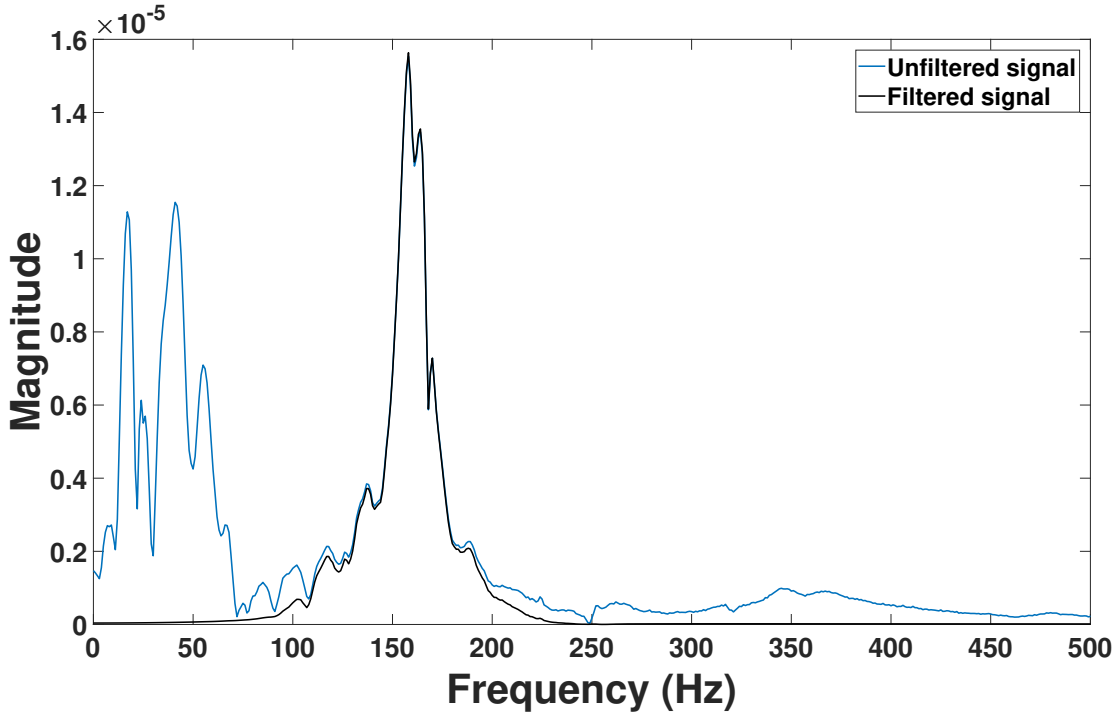


(b)

Figure 8.17: Showing the frequency response of the unfiltered and filtered response of basis impulse $\boldsymbol{f_1}$ in a), and the associated FFTs in b). The passband is 230 - 320 Hz.



(a)



(b)

Figure 8.18: Showing the frequency response of the unfiltered and filtered response of basis impulse f_5 in a), and the associated FFTs in b). The passpand used is 105 - 210 Hz.

8.3.2 Axle boundary conditions

The axle boundary conditions were modelled by assuming that the axles were mounted on a (linear) spring and dashpot. In reality, the details of the stiffness and damping characteristics of a steel axle in contact with bearings, which is in contact with an machined aluminium core bonded to a polyurethane tread, will be more complex than this. Bearings are known for having a stiffness that depends on the loading applied to them [140], and upon how much the bearing is tightened in the direction perpendicular to the applied load. Given that the wheel is spoked, it is also likely that the stiffness of the aluminium core will vary depending on the location of the spokes when the rider lands. Polyurethane is also a highly non-linear material. The polyurethane will have a stiffness that changes with load magnitude, loading rate [141], and temperature [142]. The wheels on the scooter had a diameter of 100 mm with an external tread thickness of approximately 12 mm. The approach to taking these factors into account was a mixture of intuition about what sensible values would be for the maximum displacement of the wheel during riding, as well as a good fit with experimental data. Initial tests simulating j-hop data involved the scooter being mounted on springs for the front and rear axle of stiffness $k = 25\ 000$, 100 000 or 500 000 Nm^{-1} (as only half the model was being simulated, this is the whole scooter would be mounted on a spring with double this stiffness). The front axle was constrained to only be able to move in the vertical (x_3) direction, whilst the rear axle could also move in the (x_1) direction. The maximum displacements in the front axle for the various spring stiffnesses can be seen in figure 8.19. The maximum displacements for the springs were 2.2, 7.7 and 29 mm respectively. 2.2 mm seems likely too small, given the amount of rubber on the wheel, and 29 mm is clearly too much. 7.7 mm is also likely more displacement than is realistic, especially given that the back wheel displaces more, but as will be seen in next section 8.3.4 results from the $k = 100\ 000$ Nm^{-1} fitted surprisingly well with data. Further tests were performed varying k more, along with other parameters such as the material damping and headset stiffness (see section 8.3.4).

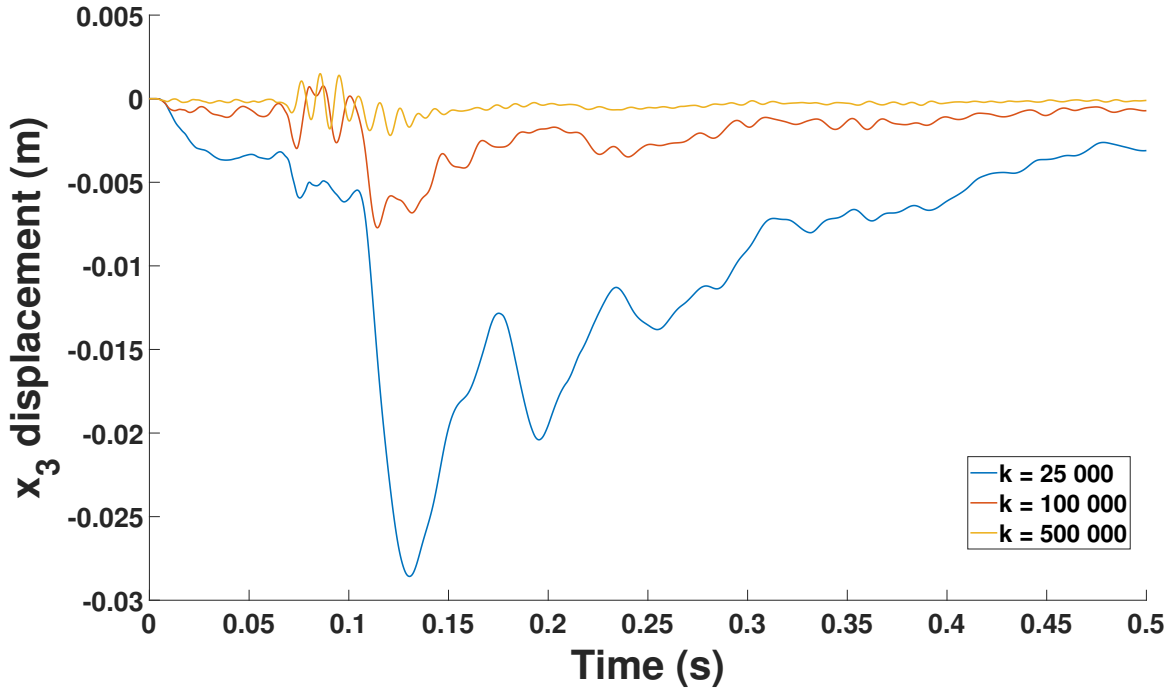


Figure 8.19: Showing how the displacement of the front axle varies with time for the (heavily regularised) dynamic force reconstruction of a barspin.

8.3.3 Headset bearings

The headset bearings were made of steel (exact alloy unknown). As they are bearings however, they will have a reduced relative stiffness compared to a solid block of steel of the same outer dimensions. An exteremely crude approximiation used for the simulations earlier in the chapter was just to assume they were made from solid blocks of aluminium. For the final simulations, however, a few calculations and simulations were made to very approximately determine the stiffness of the bearings. The bearings contain small steel balls, and hence will have a non-linear stiffness. To simplify the simluations, the bearings were assumed to be made from a solid block of material. modelling the ball bearings would give rise to extremely small elements which would slow down dynamic simulations significantly. To give an 'effective stiffness' for the bearings, an intial lower bound was made by approximating the bearing stiffness with a single ball bearing of diameter 3 mm in contact with two infinite half blocks, and a compressive force of 500 N applied. The equation for the displacement of the ball bearing relative to one of these surfaces is: $u = \left(\frac{9F^2}{16E^{*2}r}\right)^{\frac{1}{3}}$, where $E^* = \frac{E}{2(1-v^2)}$. Using a value for E of 200 GPa, v of 0.29, and r of 1.5 mm, The displacement of

the ball was 2×10^{-5} m (a total displacement of 4×10^{-5} m for both surfaces). As bearing races aren't flat (they have a groove), and because there are multiple ball bearings in the headset, the displacement should be significantly lower than this value. To give an upper bound for the stiffness, a simple FE simulation was performed where a model of a half-bearing, where the bearings were fixed to the bearing races, faced a 500 N load. This was simulated alongside a solid block of 6061 aluminium with the same outer dimensions. The displacements of these were 1.3×10^{-7} m for the solid block and approximately 2×10^{-6} m for the bearing race (see figure 8.20). As the simulation was linear and static, the ratio of displacements could be used to get an 'effective Young's modulus' of the bearing. The effective modulus of the simulated bearing was 4.5 GPa, and that of the Hertzian contact was 0.23 GPa. The best linear approximation of the stiffness should be somewhere within this region. The simulation of the bearing should give an overestimate of the stiffness, as the ball bearings are fixed to the bearing races, meaning that ball bearings further away from the applied load are contributing more to the stiffness than they should be.

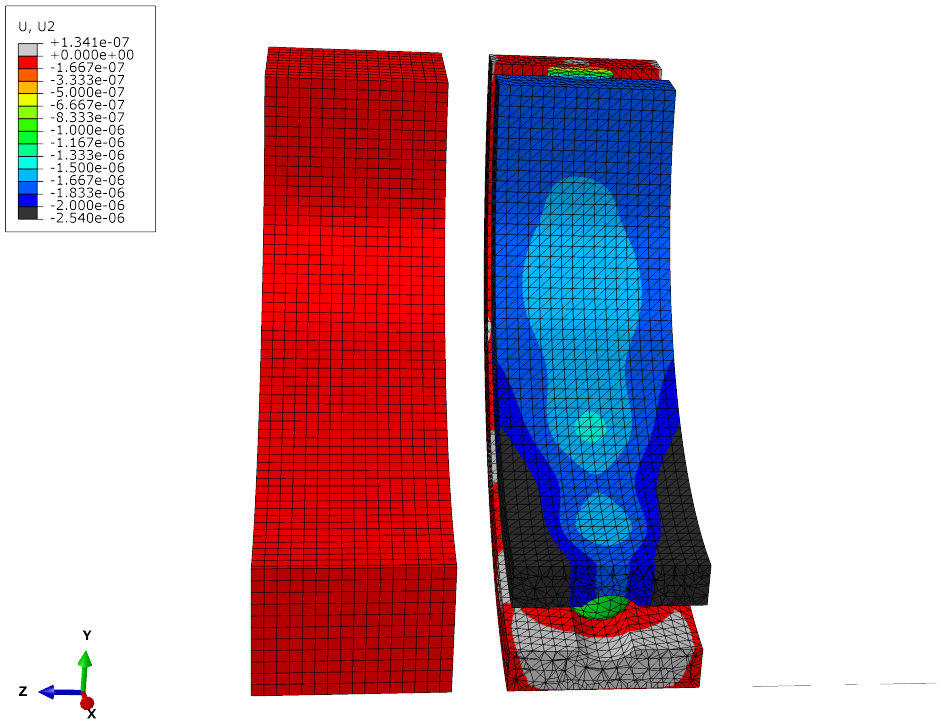


Figure 8.20: A figure showing the displacement on the inner bearing race when a 500 N force is applied in the downwards direction. The solid aluminium block can be seen to the left, however it deforms by less than 10 times as much.

8.3.4 Testing the impact of the various conditions

A series of simulations were carried out with various parameters, given values informed by the above discussion. Simulations (that were otherwise identical) were run with different values for: the spring stiffness (and dashpot) connected to the axles, the Young's modulus given to the headset bearings, and the material damping. Results were compared with experiment. The main criteria were: fit with the peak magnitude of the measured strain, and a reasonable degree of physical plausibility. A table detailing results from the load histories of two regular barspins are given in table 8.5. Plots of the various conditions can be seen in figure 8.21. The various simulated strain responses have not been given individual colours as the plot becomes difficult to interpret. The results in the down tube match the peak magnitude of the measured strain. Higher frequency components do not dampen as quickly in the simulation. This is unsurprising given that β was zero. The positive strain region of the first oscillation is also significantly higher for the simulated strain output than it is for the measured strain. Two different hops were simulated. The first tests were on a randomly chosen barspin hop, and were used to gauge how accurate the fit of the model was with various parameters. The second hop simulated (noted by * in the table), was the barspin that gave rise to the highest down tube strain of all the barspin hops. The conditions denoted by † is the one used for generating the optimised results in sections 8.4 and 8.5. The reason for this decision is that the to use the model with conditions denoted by † was that the axle displacement was plausibly realistic, and the fit with experimental results was reasonable. Whilst the data from one of the models with a spring constant of $k = 100$ kNm^{-1} had a better fit (under 5 % for all measurements), it gave rise to a rear axle displacement of over 11 mm, which seems implausible for a wheel with a radius of 50 mm (for a comparison of axle displacements varying with spring stiffness see figure 8.22).

A final linearity check was done with the updated model with springs, dashpots and the more compliant headset bearing. In this case load magnitudes of 0.5, 1 and 1.5 times the load that gave rise to the maximum downtube strain in the bar were used. the reason for the upper limit is that at this point the load magnitude is approaching yield in a large portion of the down tube, at which point the model would not be appropriate anyway. Results showed that the model was still largely linear (see figure 8.23 for results).

Table 8.5: The table shows the variation in measured peak strain magnitude for 14 different parameter conditions for the dynamic FE model. The worst fit of any model on any strain gauge is 22 % which is for the only model with $\alpha = 25$ s^{-1} , not including that model the largest error was 17 %. The best model had a fit within 5 % for all of the measurements. The results denoted by * are from the barspin that gave rise to the highest down tube strain. The result denoted by † was the simulation used for the comparison in section 8.4.

				Maximum strain magnitude		
k (kNm^{-1})	C (Nsm^{-1})	α (s^{-1})	E (GPa)	DT	Deck 1	Deck 3
100	0	100	1	1.05	0.95	1.01
100	100	100	1	0.9	0.96	1.01
100	1500	100	1	0.93	0.98	1.02
100	500	100	1	0.83	0.97	1.02
100	1500	50	1	1.14	1.08	1.05
100	500	50	1	1.02	1.01	1.04
200	500	25	1	1.22	1.14	1.07
200	500	50	1	1.09	1.03	1.06
350	500	50	1	0.93	0.98	1.03
200	500	50	68.9	1.09	1.02	1.06
200	500	50	5	1.11	1.02	1.06
275	500	50	5	1.15	1.03	1.06
350 *†	500	50	1	.94	.91	.88
200 *	500	50	5	.92	.90	.88

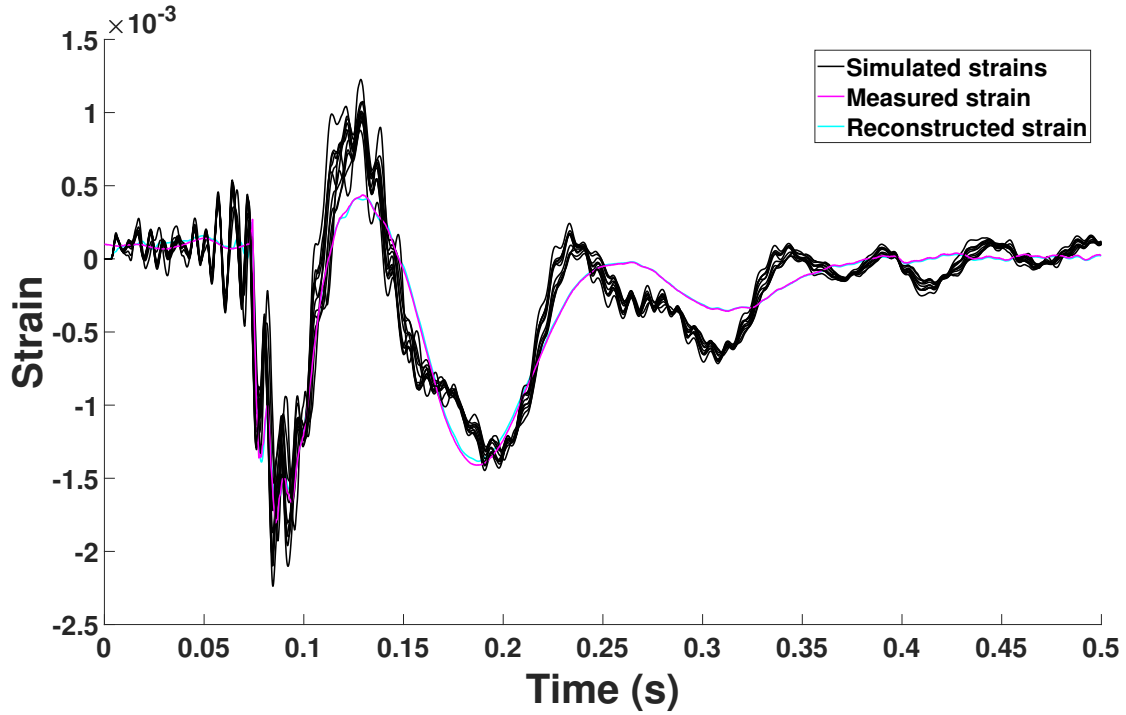


Figure 8.21: Showing the strain output as a function of time for the first 11 entries of table 8.5.

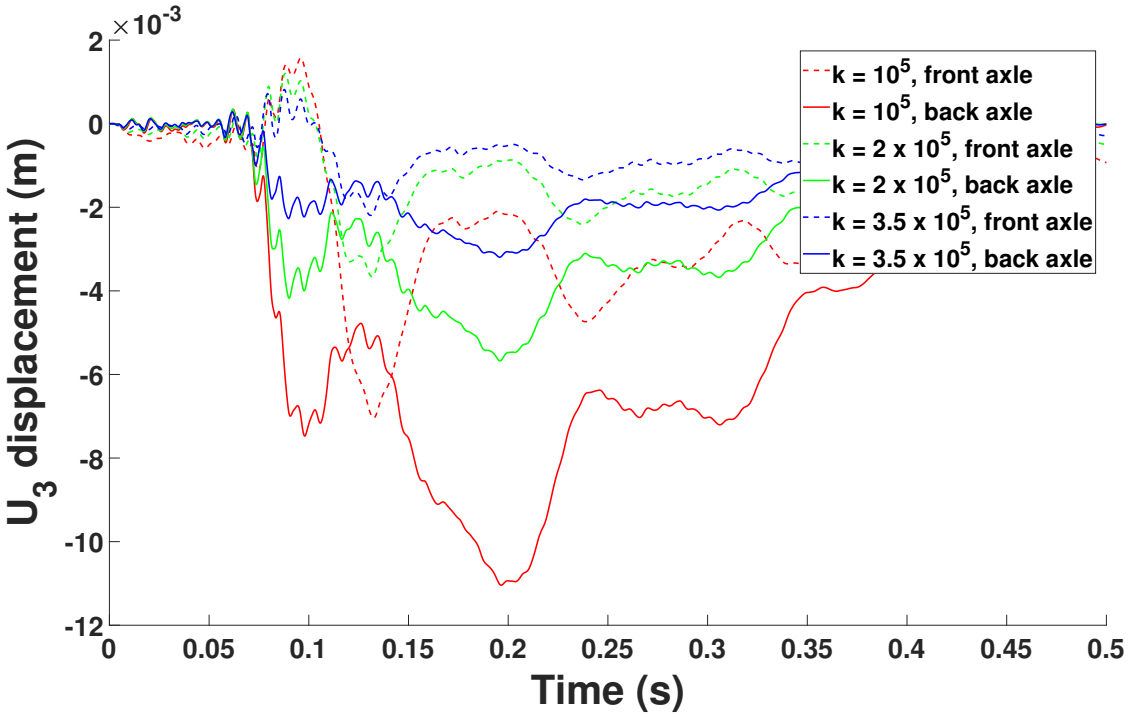


Figure 8.22: Showing the displacement histories of the front and rear axle for various values of a barspin hop. The values of the other parameters are $C = 500$ Nsm^{-1}, $\alpha = 50$ s^{-1} and $E_{\text{headset}} = 1$ GPa)

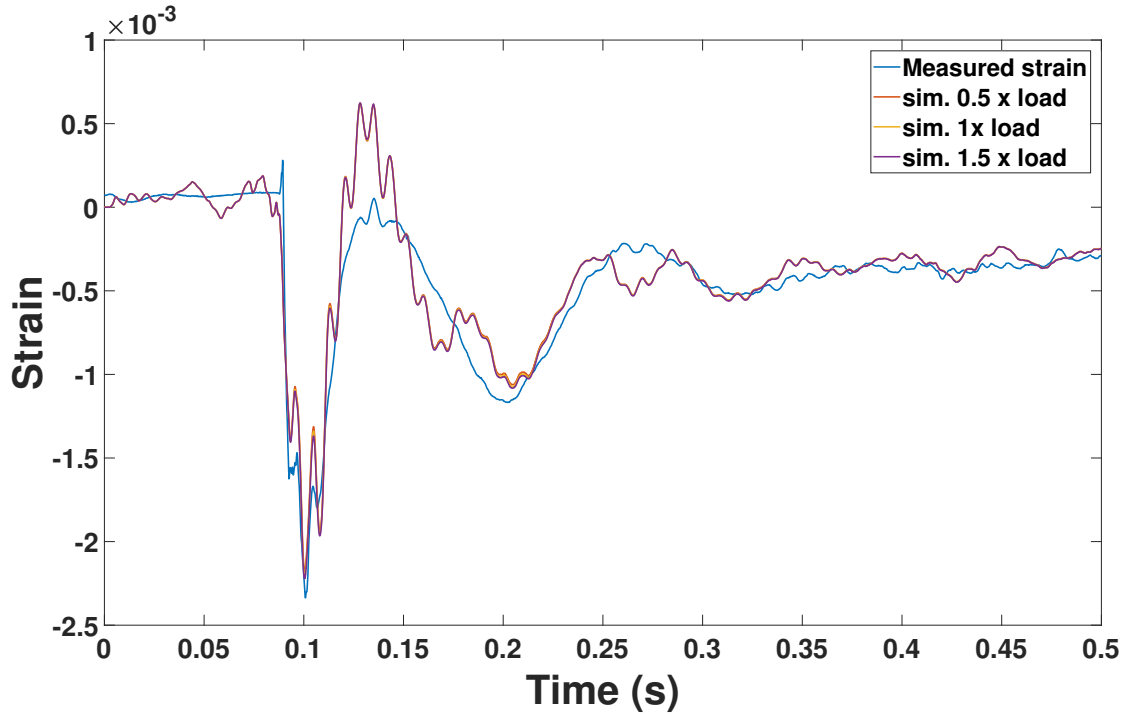


Figure 8.23: A comparison of the variation of strain with time for normalised strain responses of the barspin hop that gave rise to the maximum measured down tube strain in the scooter.

8.4 Comparison between static and dynamic model

For the optimisation in the next section, the simulations were linear, and stress was being minimised rather than constrained to be below a certain value. In such cases, what matters is the ratios of loading/stress distribution, not the total magnitude of the loads. Optimisation should still obviously be performed on the load cases that are most likely to lead to failure. Six measurements of the ratio (henceforth called R) of the down tube to deck 1 strains were taken. R was taken from two static simulations, one where the loading was based on what gave rise to the peak strain in the down tube, and one that gave rise to the peak measured strain in the deck. R was also taken from the measured strains at equivalent points in time, and and also from the equivalent points in a dynamic simulation ($k = 350\ 000$ Nm^{-1}, $C = 500$ Nsm^{-1}, $\alpha = 50$ s^{-1} and $E_{\text{headset}} = 1$ GPa).

The difference in R is much larger between the down tube and deck load cases than it is between the static model, dynamic model and measured strain (see table 8.6. The static model unsurprisingly gives a more similar value for R in both cases than the dynamic model. Results from optimisation studies on the static loading that gives the peak down tube strain and the loading gives the peak deck strain should give some insight into how good an approximation the static optimisation is of the dynamic load case. If the results between the optimisation studies for the two load cases are significantly different, we will have less confidence that the results are similar to what an optimisation study on the dynamic model would give.

Table 8.6: A table showing the ratio (R) of the strain in the down tube strain gauge to that of the deck 1 strain gauge at two points in the strain history. The static simulations are from force reconstructions of the timesteps which give rise to the maximum down tube strain and deck 1 strain respectively. Measured results are simply the R values at the times when the peak down tube strain and deck strain occur. The values for R in the dynamic simulation are also from the times of maximum peak down tube and deck 1 strain.

Static sim. DT	Static sim. deck	Measured DT	Measured deck	Dynamic sim. DT	dynamic sim. deck
2.18	1.30	2.34	1.36	2.68	1.12

8.5 Topology optimisation

When performing topology optimisation, It is important to consider what design domain is being used (i.e. where the material is allowed to be). Initially, a rather large domain (see figure 8.24) was used.

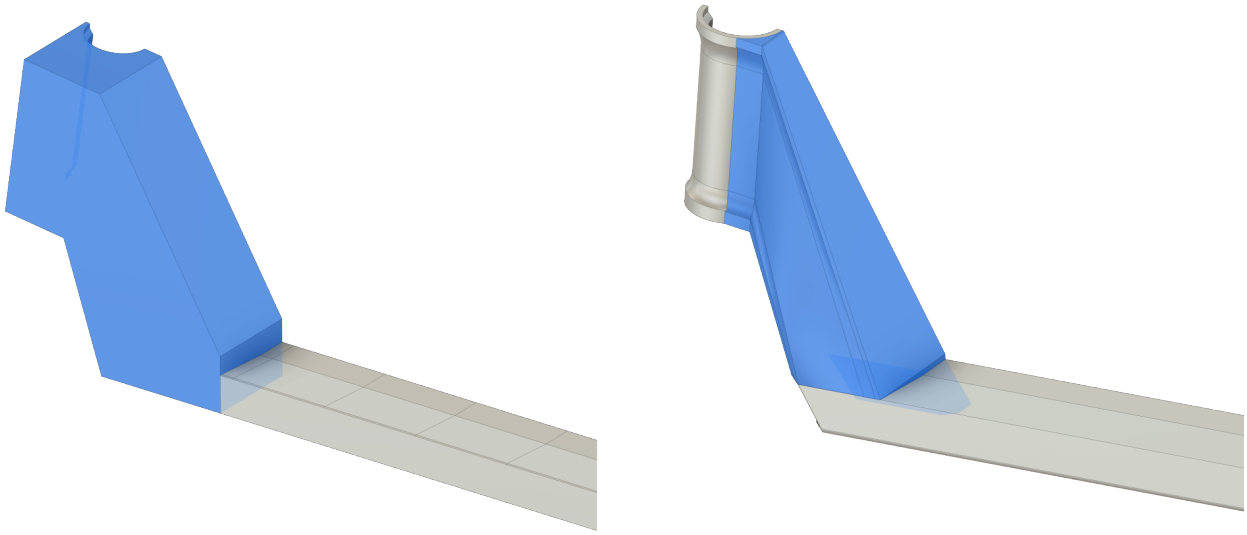


Figure 8.24: The design domain is highlighted in blue. The domain used for the first topology optimisation studies (left), and those used for the final ones (right).

Because there were a high number of low-density elements, the suggested shapes from this domain were unhelpful for the final design. Because of this, a smaller design domain was used. For both domains, it will be noted the domain was not allowed to go further back on the footplate than the original headtube of the Native STEM deck. With a larger domain, it should be possible to generate geometries that have a higher section modulus for the same mass. When riding a scooter, riders do not want the neck of the headtube taking up all of the foot space on the footplate. The trade-off between the strength (or weight) of the headtube and foot space is a subjective design judgment. Hence, the design domain was constrained so that the foot space would not decrease. The loading conditions used for the optimisation were from the barspin hop which gave rise to the largest measured strain in the down tube. Regular barspins gave, on average, the highest measured strains in the deck and down tube. The maximum strain measured in the deck for this hop (1.35×10^{-3}) was within $0.5\ \%$ of the maximum measured strain in the deck from all the barspin data.

All topology optimisation studies were run with 50 cycles.

For the final optimisation study, the static loading at the timestep that gave rise to the highest measured strain in the down tube was used. To test how much the optimised geometry varied with loading, a study was also performed at the timestep which gave rise to the highest measured strain in the deck. The resultant geometries were very similar, and can be seen in figure 8.25. Because of this, it was decided that only one topology optimisation study would be needed.

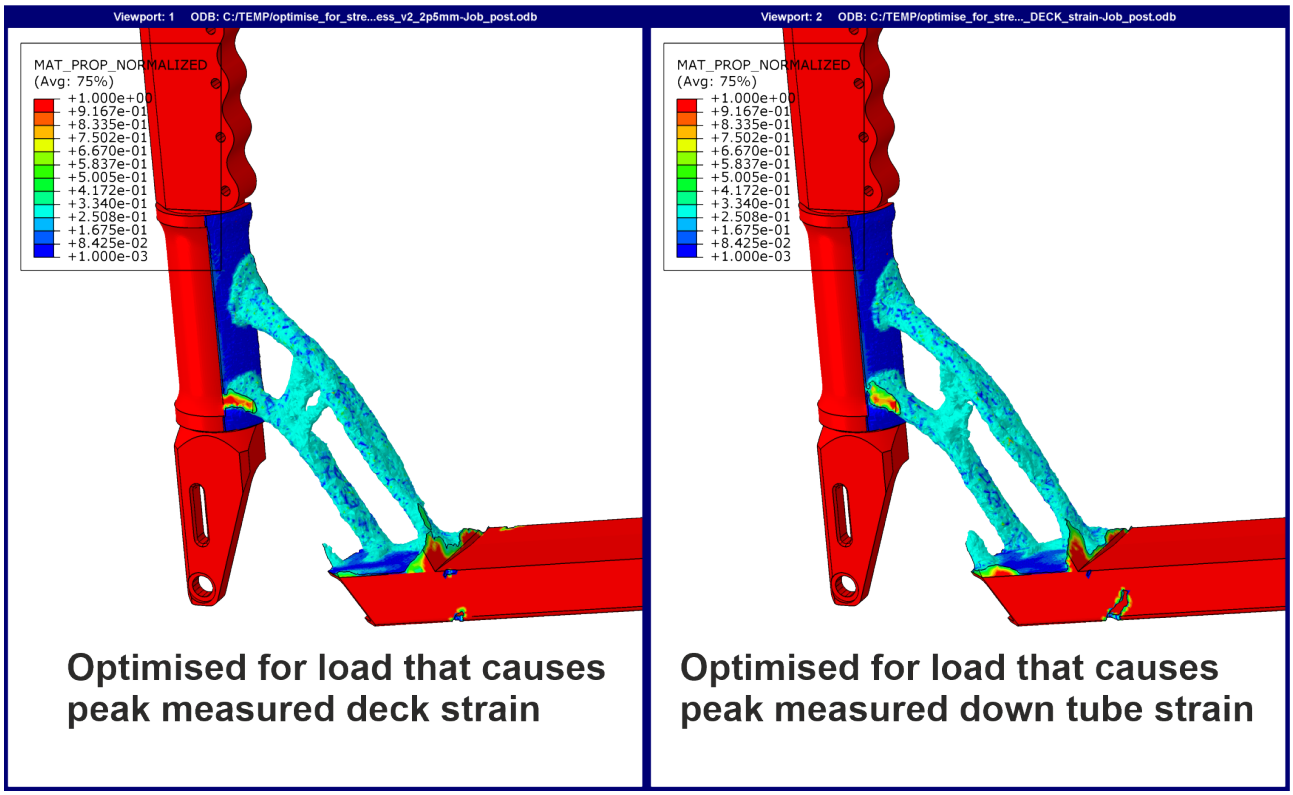


Figure 8.25: The results from topology studies that optimise for the load case that causes the maximum strain in any of the deck strain gauges (left), and that which causes the maximum strain in the down tube strain gauge. As can be seen, the results are very similar. Note that the legend shows the relative density of elements, as topology optimisation allows for intermediate density elements.

A topology study for the maximum down tube strain load case was run with mesh sizes of 5 mm and 2.5 mm. The general shape of the optimised structure looks similar, although the distribution of the density of the elements is significantly different (see figure 8.26). The final optimisation used the condition to minimise the peak stress in the region of the headtube, as this would likely improve the lifetime of the component the most. Scooters are not usually optimised according to stiffness, as it is not the case that riders just want the scooter to be as stiff as possible. A topology optimisation

study that had the stiffness (minimum strain energy) of the deck was carried out. This was to see how much the result would differ, and because optimising for stiffness is much less sensitive to any singularities related to stress concentrations. The result was very similar. A volume fraction constraint was placed on the design domain such that the mass of the result would be the same as the mass of the normal Native STEM deck.

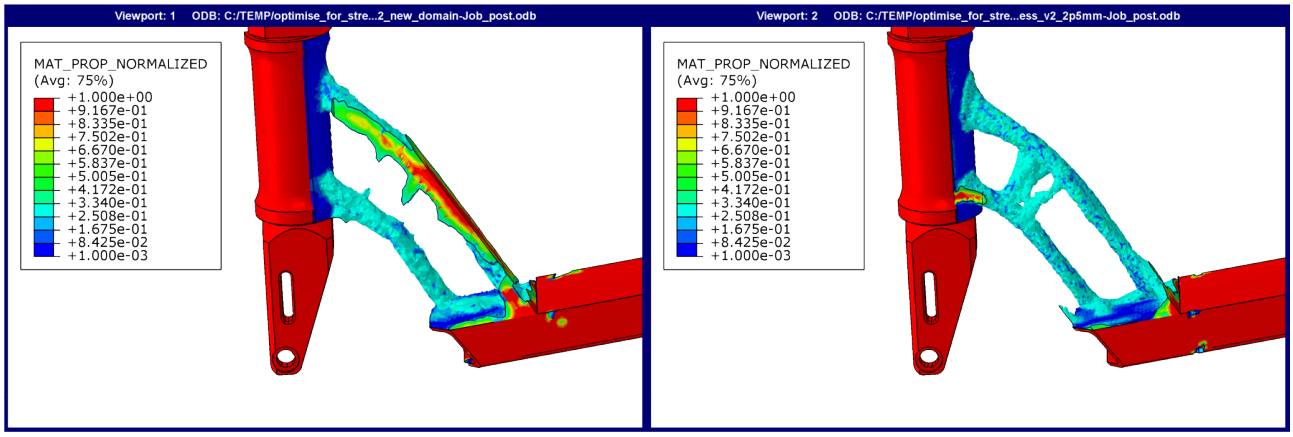


Figure 8.26: Showing the optimised geometry according to a simulation with 5 mm elements (left) and 2.5 mm elements (right). The general shape is similar, although the 2.5 mm mesh has a truss member joining the top and bottom truss members in the neck at 0.3 density.

Another worry was that the optimisation of the design domain according to stress may be influenced by sharp corners at the edge of the design domain (even though the maximum stress was in the middle of the neck, away from any sharp corners). To adress this issue, a modified domain was made that did not have sharp corners that could give rise to unrealistically high stresses in the design domain. Results from this optimisation study meant that the extrusion profile geometry was significantly changed (material was removed from it, so that there could be more material in the neck of the deck to reduce peak stresses). The resultant shape of the neck was essentially the same, just that the truss members of the neck were thicker (see figure 8.27 for the comparison).

Interpreting the topology results to bring about a realistic geometry is not straightforward. The final mesh that was used as a basis for a new design had a large range of intermediate-density elements. Figure 8.28 shows results where only element densities over a certain value are visible. In addition, because the intermediate densities were more compliant, the stresses were higher in regions where the density of the elements was higher. This meant that stresses were higher in the middle of

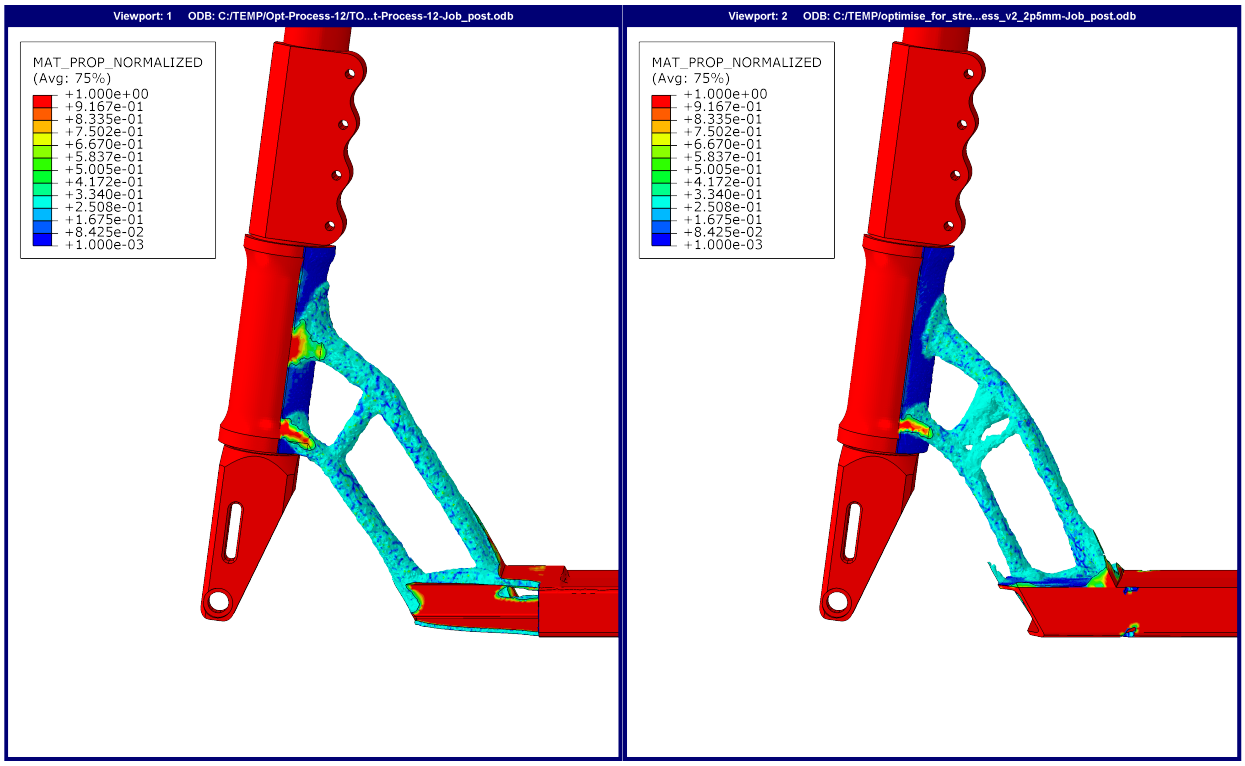


Figure 8.27: A plot of relative density showing the optimsed headtube (left) with a larger design domain that was modified to avoid sharp edges that could cause unrealistically high stress values. As during optimisation this model removes material from the extrusion profile, the truss elements are slightly thicker. The overall geometry of the neck is similar to that of the design domain used for the optimisation study (right).

the trusses. To reduce the number of intermediate-density elements, the penalisation factor was increased (from 3 to 5 and 6). The result was, however, even worse in terms of having elements with higher densities.

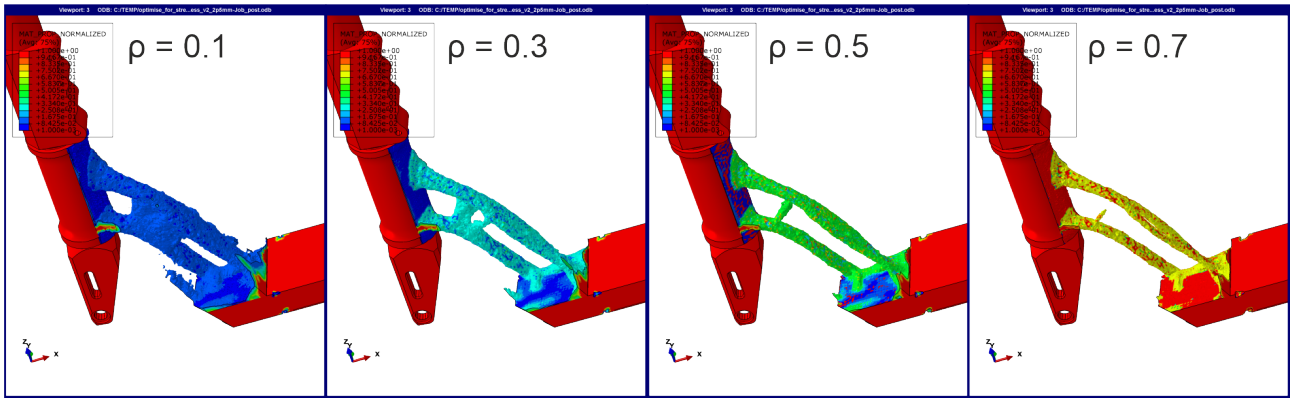


Figure 8.28: Showing the results for the topology optimisation study with only elements above various densities are visible. The cut-off densities displayed are 0.1 (far-left), 0.3 (left), 0.5 (right), 0.7 (far-right).

To get from the topology optimisation result in Abaqus to something that could theoretically be manufactured, a cut-off density of 0.3 was applied to the optimised result. This meant that only elements with a density of 0.3 or higher were included in the output mesh file. The output stl. file was imported into Autodesk Fusion so that a design based on the topology optimisation results could be made. Replicating the shape of the optimised structure required a series of lofts, sweeps and fillets. Fusion has a feature that makes it possible to project a cross-section of the mesh onto a sketch plane, making it possible to reconstruct the optimised result more accurately. An image of the reconstructed headtube with the exported mesh overlayed can be seen in figure 8.29. It is interesting to note that the neck design looks remarkably similar to that used in the ethic pandemonium V2 [143] (see figure 8.30). A video explaining the design process of this deck does mention the use of topology optimisation for the neck/headtube and briefly shows a topology-optimised headtube mesh [144] (the load cases were presumably just estimated). .



Figure 8.29: Showing how the optimised 3D CAD model designed in Autodesk Fusion is similar to that of the mesh surface with a cut-off value of 0.3. The mass of this neck is similar to that of the original Native STEM deck. The mesh is darker grey, and the solid designed part is in lighter grey. The mesh is overlayed (so they are on top of each other), to show how closely they match.

The same load conditions were applied to the model of the topology-optimised headtube, and the results were compared to the original headtube design. As can be seen in figure 8.31, the stresses in the topology-optimised headtube were higher than in the original design. The same figure also shows that the stress distribution looks significantly different from the topology result before post-

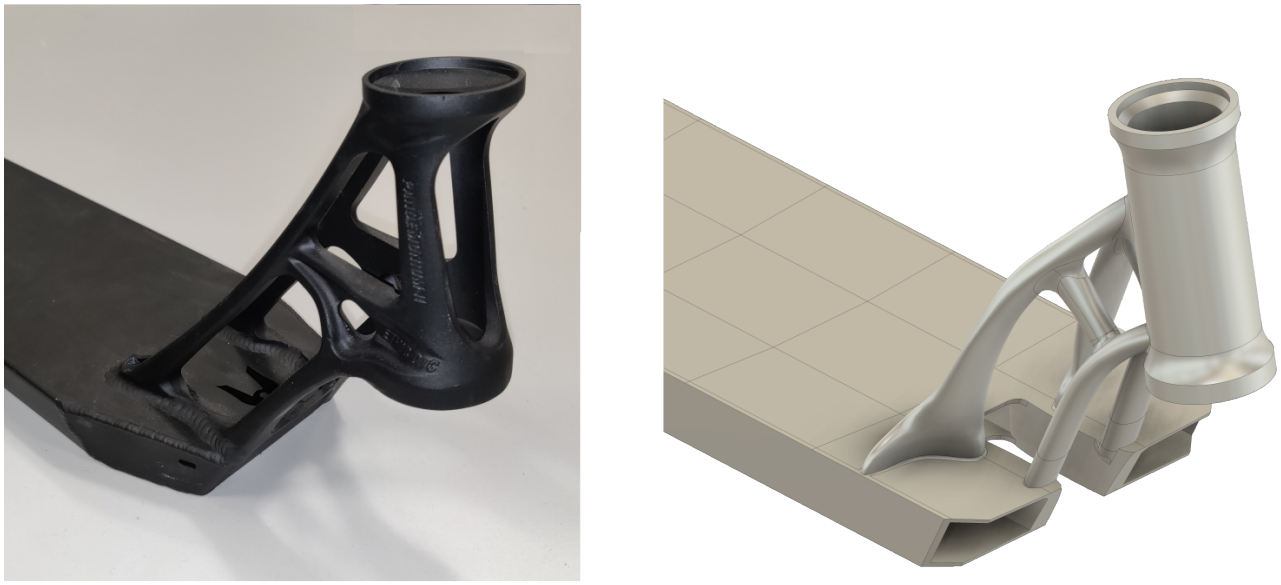


Figure 8.30: Showing that the optimised headtube (right) is similar to the existing design of a scooter neck (left), namely that of the Ethic DTC Pandemonium V2.

processing. The difference is likely due to the existence of intermediate-density elements. The reason the 'optimised' mesh has worse results than the original native STEM neck (near the middle of the neck) is probably because it has a truss structure rather than a closed-form structure. Truss-latice structures are generally 2 - 3 times less stiff than closed form lattice structures [145]. The result highlights the importance of using knowledge of engineering principles and simulation rather than blindly using popular computational methods.

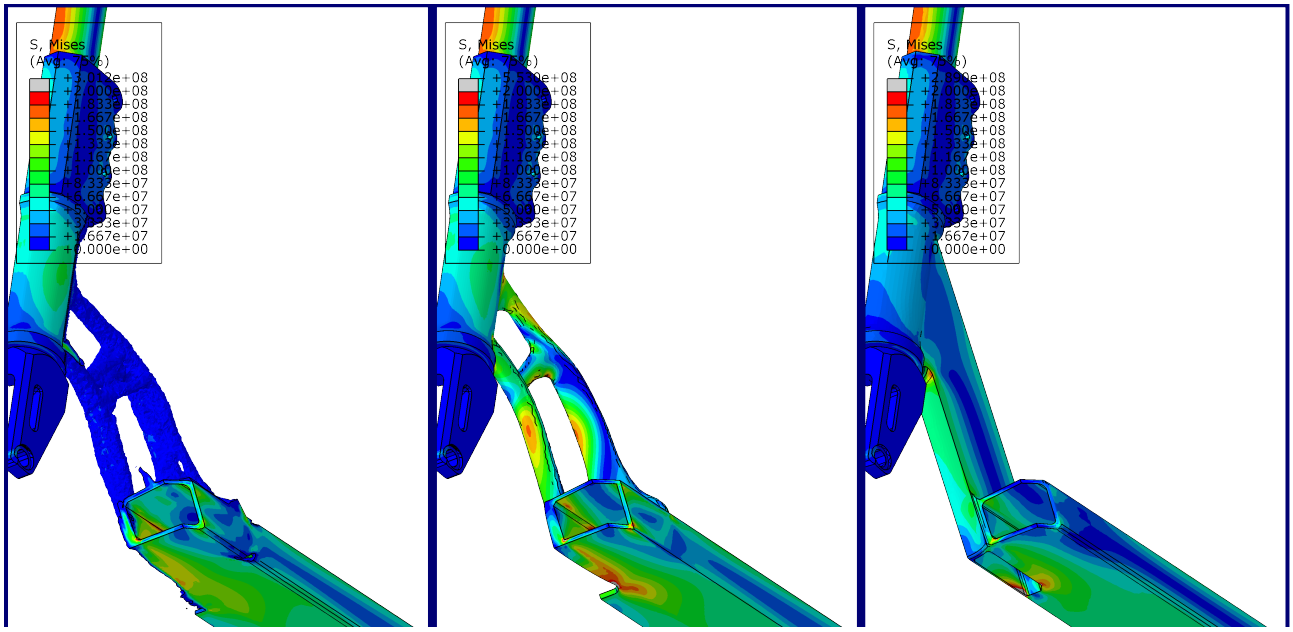


Figure 8.31: Showing the Von Mises stress distribution for the topology optimisation study result (left), the design based off the study result (middle), and the original Native STEM deck (right).

Chapter 9

Conclusion

This work has provided two models that reconstruct the forces applied to stunt scooters in real-world use. The construction of a novel data logging system was necessary as none of the systems commercially available or in the literature were fit for use. Literature for data collection on bicycles was investigated, as there was no suitable literature on kick scooters. The data logging system measured data from strain gauges and utilised quarter-Wheatstone bridges and instrumentation amplifiers. To help shockproof the data logging system, it was mounted on springs that acted as suspension. The data logging system could measure up to eight channels of strain data at a rate of up to 62.5 kHz. The system could withstand the shock loading of stunt scooter use. A force reconstruction model was devised that calculated the loading applied to the scooter from the measured strain under static assumptions. The model assumed that the loads applied by the rider were uniformly distributed loads applied to the handlebars or the deck. The force was calculated to best match the measured strain according to an ordinary least-squares criterion. Constraints ensured that forces applied by the rider's feet to the deck must be positive. Having more strain measurement points than basis loads (overdetermining the problem) also helped reduce overfitting. Experimental calibration for this model was carried out using an Instron 5582 Universal Testing Machine. Strains reconstructed from the force reconstruction model were all less than 3.5 % in magnitude. The error for the reconstructed force magnitude was less than 16 % for all reconstructed forces. The error in the magnitude of the reconstructed forces was much larger for forces applied near the rear end of

the scooter, where the average strain per unit force in the strain gauges was lowest.

The static force reconstruction model was followed by another force reconstruction model, which took dynamic effects into account. In the dynamic model, basis impulses were used rather than basis forces. Experimental calibration was performed with a DJB IH-05 instrumented impact hammer. The basis impulses from the hammer required two main modifications. The first was a drift correction to account for thermal drift and noise. Multiple hammer impulses were applied and averaged to account for noise. To account for thermal drift, the long-term behaviour of the superimposed basis impulses (replicating a constant applied load) were matched to the static strain response. The second modification was the widening of the basis impulses. The widening was performed by superimposing time-shifted versions of the original basis impulses of varying magnitude before normalising the new wider basis impulse to have a magnitude of 1 mNs. The modified basis impulse was approximately triangular in shape. This was desirable as it allowed the reconstructed force to approximate the shape of any continuous force so long as the frequency was not too high. This second modification was primarily performed to reduce overfitting of the the data, although it also had the benefit of reducing the computational cost of the model. Even with the constraint that deck forces could not be negative and with wider impulses, the dynamic model was still prone to over-fitting data. Tikhonov regularisation was used to further improve the fitting. As there were no apriori grounds for a value of the regularisation parameter, the L-curve method was used to find one. The regularisation parameter given by the L-curve method still gave rise to reconstructed forces with spurious oscillations (the frequency of the reconstructed force was significantly higher than that of the measured strain). Because of this, two dynamic models were used for the final force reconstruction, one with the regularisation parameter given by the L-curve criterion and one more heavily regularised model.

Force reconstruction was performed on at least 25 of the following 12 scooter stunts: bunnyhops, j-hops, tailwhips, heelwhips, barspins, opposite barspins, backside 180s, backside half-cabs, frontside 180s, frontside half-cabs, backside 360s and frontside 360s. The maximum measured strain on any of the strain gauges was 2.61×10^{-3} in the down tube, which happened upon landing a j-hop. On average, regular barspins led to the greatest measured strains in both the handlebars and deck. The

maximum measured strain in the down tube was larger than that measured in the deck for all of the stunts. Whilst peak strains in many of the strain gauges for most of the scooter stunts gave rise to results that appeared to be approximately normally distributed, there were many exceptions. 19/84 peak strains failed the Shapiro-Wilk test for normality, and 16/19 of the cases that failed the test came from whip, barspin or j-hop data.

The final major chapter of the thesis sketches out an approach for how the information collected could be used to optimise scooter components. A series of convergence studies and other tests are performed on a dynamic finite element model to ensure that it is suitable for comparison with experimental data. These tests are followed by further tests that try to account for material damping and non-linearities in the scooter geometry associated with the wheels/axles and headset bearings. The load history for the barspin that gave rise to the highest peak strain measured in the down tube is then simulated. Final simulation results of peak measured strains are within 12 % or less of measured data. The ratio of peak measured strains in the down tube and deck help inform whether results from a static topology optimisation study will likely approximate results from a dynamic study.

A static topology optimisation study is performed to generate a new neck geometry of the scooter deck. The topology optimisation study was insensitive to the ratio of peak handlebar and deck strain, indicating that results from a static model may well be similar to those of a dynamic model. This new neck has a truss/lattice structure rather than the closed form structure of the original neck on the deck. The topology optimised neck receives higher peak stresses than the original neck for equivalent loading, highlighting the need for more work to be done in this area.

Chapter 10

Future Work

This project has laid the groundwork for future research into the loading scooters face in use and their optimisation. As this is the first published literature on the loading and optimisation of scooters, there are many ways to branch out from this research.

Data collection: Data was collected for 12 of the basic stunts on a scooter on flat ground. Future work could involve doing more advanced scooter stunts and, perhaps more importantly, analysing the forces applied to scooters on other types of terrain. For example, scooter riders often ride on ramps in skateparks. On these ramps, scooter riders get more air time and therefore the scooter likely experiences higher peak loads upon landing. Loading is probably especially high when scooter riders are riding 'flyout', i.e. doing a stunt out of a ramp but landing on a flat surface. Flyout riding should result in faster decelerations (and therefore loading) than when landing on a ramp. Doing stunts over obstacles of set height or doing stunts off obstacles of varying heights would also be interesting. One could seek to establish a relationship between the loading history and the height of the obstacle jumped from. This would help assess the peak loads associated with 'street' scooter riding.

Another avenue for data collection would be to collect data from different scooter riders. This would allow for an investigation of how much the loading applied to scooters varies between riders. One could look at whether the variation in loading is determined primarily by the rider's height and weight or whether riders of similar stature apply significantly different loads due to their riding styles.

Another avenue for exploration would be to see whether the loading applied to the scooter varies significantly with scooter geometry. For example, if the handlebars were taller, one would expect the strain in the downtube (and deck) to be larger, as the moment applied from the top of the handlebars would be larger for a given load. It may well be the case, however, that the applied loading changes because of changes in the rider's posture. The other main geometry that could be investigated would be the length (and possibly width) of the deck. Changes in geometry would be slightly more labour-intensive to research, as calibration would need to be performed for each new geometry, as well as any modifications needed to mount the data logging system to the scooter. Wheel size could be another avenue of exploration, analysing the impact of wheel size on the applied loading. Do larger wheels have a significant 'suspension' effect compared to the 100 mm wheels used in this study?

One could also explore how the in the applied loading changes with component material. Such an investigation would primarily be for changes in handlebars. Stunt scooter decks are almost exclusively made from aluminium, whereas handlebars are commonly made from steel, aluminium or titanium (and in the future possibly carbon fibre). Forks are made from steel or aluminium. The difference in the frequency response of these materials may significantly affect the applied loading and even the lifetime of other scooter components.

A rather obvious way to extend this research would be to research beyond stunt scooters. Electric scooters have grown hugely in popularity over recent years, and are expected to continue to grow. Commuting scooters are also commonly used for inner-city transport, sometimes preferred to bikes if part of the journey involves public transport. As standard riding cases should not lead to failure, crash cases or the loading associated with riding off a kerb could be analysed.

Data logging system: A more advanced data logging system could allow for more advanced reconstruction models. More channels of strain data could allow for an investigation into the loading component applied to the crossbar in the vertically downward direction. For stunts such as barspins, the location of the rider's hands move. It may be necessary to have multiple strain gauges on each side of the crossbar to determine both the location of the rider's hands and the magnitude of the applied load. Note that if one were not interested in the strength of the crossbar or the forks, this

information would not be as important, as the bending moment applied at the downtube would be something of more significance. An investigation into the loads applied at the crossbar may also allow for force reconstruction that measures the angle of the crossbar over time (in a similar way to that suggested in section 5.6.1). Rosette strain gauges could be used to investigate the torsional loading applied to the deck. This would, however, be expected to be relatively small given that the footplate is rarely wider than 150 mm, and so is not a top priority. Other measurements could also be incorporated into the force reconstruction model. Accelerometers would likely be the easiest to implement. Comparisons could be made between force reconstruction models using strain data, acceleration data and a combination of the two.

Other force reconstruction models: Other force reconstruction models could be used and compared to those used in this thesis. Models could be derived from the properties of the materials, including much more thorough investigations into the properties of the axle and bearing contacts than in chapter 8. I think reliance on experimental data rather than a physical model may be more promising, especially if the computational cost of the force reconstruction depends on the model size. The scooter has a significantly more complicated geometry than any geometries in section 2.2 of the literature review. An experimental approach that utilises a Kalman filter or a machine learning approach could be promising. A Kalman filter should be able to be used to combine predictions based on dynamic calibration with actual measurements to reconstruct the applied forces. It is also worth noting that the dynamic model from this thesis may become unwieldy if the number of strain measurement channels and the complexity of the force reconstruction model increase. Increases in strain measurement channels and the number of basis impulses have a multiplicative effect on the matrix size used to solve the dynamic force reconstruction. It would be interesting to see comparisons between different dynamic force reconstruction models.

Working on obtaining more realistic boundary conditions for the axles may also be important. Because of the short duration of the applied basis impulses, the axles may even have 'bounced' slightly in use, which is likely not the case when a rider lands a stunt. It may also be possible to perform dynamic calibration with something other than a hammer. Tekscan pressure sensors, whilst probably impractical to mount on the scooter for data collection in situ, may be helpful for dynamic calibra-

tion. They were, unfortunately, far beyond the budget of this project. Tekscan pressure sensors may be especially effective in combination with a machine learning based force reconstruction approach, as one could apply a variety of complex loading scenarios to the deck to train the model.

Further optimisation work: The optimisation work in this thesis only scratched the surface of what is possible. It may be that bespoke topology optimisation code, or other software should be used instead of Abaqus, due to the surprising number of intermediate density elements from the results in section 8.5. More advanced topology optimisation (and shape optimisation) could take into account manufacturing constraints and use weighted objective functions from large sets of data (including data from multiple riders).

Topology (and shape) optimisation on fatigue life could also be invaluable to improving scooter components. More detailed dynamic simulations on high-performance computers (and even topology optimisation based on dynamic loading conditions) could also give more confidence in the veracity of optimised designs. A rigorous investigation into the optimisation of scooter parts must, however, consider how manufacturing techniques affect material properties. The effect of welding is of particular importance. Scooter components frequently break at the welds or in the heat-affected zone of a weld. Investigations into the difference in material properties (especially fatigue life) at or near the weld could shed light on how to design welded components effectively. Optimised geometries could be manufactured and tested against existing component designs to benchmark the improvement.

Appendix A

Additonal Calibration Data and Errors

The following are the potential sources of noise in the measured strain for calibration data:

- Gauge factor error (magnitude: Gauge factor error is $0.3\ \%$ according to the manufacturers description (on the packaging). For force measurement this error would be discounted as an error when collecting data would be cancelled by the error during calibration.)
- Strain drift (magnitude: maximum $3\ \times\ 10^{-6}$)
- Noise (magnitude: maximum $2\ \times\ 10^{-6}$. Note that for static calibration this error is negligible as data is averaged over hundreds or thousands of measurements.)
- Descretization error (magnitude: maximum $1.5\ \times\ 10^{-6}$)
- Amplification error in instrumentation amplifier, due to gain variation (magnitude: negligible)
- Normalisation error (magnitude: neglibible)

  These errors are uncorrelated and are therefore added in quadrature. For a strain of $5\ \times\ 10^{-4}$ this is an error of $0.8\ \%$. For a strain of $1.5\ \times\ 10^{-3}$ this is an error of $0.4\ \%$.

Bibliography

[1] Ian Polmear, Dr. David St. John, and Vilupanur Ravi. *Light Alloys: From Traditional Alloys to Nanocrystals, 4th edition, pg. 126.* Elsevier Science & Technology, Oxford, UNITED KINGDOM, 2005.

[2] ASM material data sheet. 6061 aluminium - `http://asm.matweb.com/search/SpecificMaterial.asp?bassnum=MA6061T6` - last accessed 12/10/24.

[3] Ian Polmear, Dr. David St. John, and Vilupanur Ravi. *Light Alloys: From Traditional Alloys to Nanocrystals, 4th edition, pg. 127.* Elsevier Science & Technology, Oxford, UNITED KINGDOM, 2005.

[4] *ASM Handbook, Volume 1: Properties and Selection: Irons, Steels, and High-Performance Alloys, Chapter: Hardenable Carbon and Low-Alloy Steels - January 1990 -* `ht tp s: // wa te rm ar k. si lv er ch ai r. co m/ a0 00 10 28 .p df ?t ok en =A QE CA Hi 20 8B E4 90 oa n9 kk hW _E rc y7 Dm 3Z L_ 9C f3 qf KA c4 85 ys gA AA y8 wg gM rB gk qh ki G9 w0 BB wa gg gM cM II DG AI BA DC CA xE GC Sq GS Ib 3D QE HA TA eB g l gh kg BZ QM EA S4 wE QQ MF NY Wa sJ LF pS jR 7I 4A gE Qg II C4 qZ es sf YE rD PA lG TM nm Us mj CM nE ct JS A_ AP Gm Sv tc Sj jZ PS mv et 3h yz lB 9j 3V De Bl -uf rL __ SZ CV Ee 8b Dh -ZK 4i l -iY h-D2 kN 8g Rb Et kW Uo my Sv EJ Dr 6B L0 tk QE dw 5p sn ti 0N iS Vj O7 DT E6 8_ z2 0W pJ Mo ZF AC - he Az 31 Bk 7i YC o8 rl U9 kf Ls eR 8A Dg eX 6G Ec dD Zw _V _w dI h_ t1 _E b-Lz 7J Tw Hp QZ kE CQ k2 iN Cj BD Q0 dq LA lr 5Z 99 bH nu fw dR Ng Nr 50 ic Fu aW R4 1M oK OM uH Ab zJ be sm 6T 5Z x9 jp 1s fd kY In aP wV YK _8 DX C2 Aj T1 Nu TB 50 vk YE Bt XE 0n T1 9Z Kt x0 J1 Cw 6T KD Ve Us rb GT Wv 7I Pc _J IP wq mb ru Wu MM YN y0 QY g_ sG kD bO fP Pa Sq 2n hh -`

71 w7 Ls Q-5f ea ok kU 4C UU B7 KE 1D sg uu gK x2 Nj ay nD ca fQ K6 1U xs kZ _s -hD KC bI UL R0 od _T tH iY kt fN z6 4z lS Z-_q KJ qq wN JW FR ni UG ay Qj 9_ kO Gu 7C Ub by SA qn 9D WD XX 2y el QD JS U0 -do Z2 Ny Qe Co 4O uq _8 ke gr Xf 73 DA XL 0T J1 Gv kT MD FE XR tE G2 YI NX 7C c6 Tz MT 0E SS JX 1Q Sc _J Bu Xj xe 67 vg gX _P hR vl -nA Yb Zz Lv 2s P-15 jn 39 Tq yo kS Qy 36 oS Qv I1 km Zn vd o4 qm oh mJ 2W FL iY p3 7J GR rV 0T Y3 4O 5o GN qB Kt Ly 9d Xx yT 05 jN YI 7f OH SH Kr Hw pi 37 m7 GN Cf d1 NZ pd a_ Vx B0 v3 k0 xn Hx ng Ya qs BL Eb n7 EG VH 8-0Y 2Y h8 wh BI xm uj j2 Be xu np xi wK Ci ro 9Q FU 7b Lw xg 7L z0 fq yb hf aG 60 xa jL pE 4h c9 0A te Uv pi Ce tk zI WY 9X 9X 8r b8 kb pp JA zG _s lC Nz 8Z yx _y zb h-d6 tW fi Lx uC D8 A3 uu Ck uU n6 Fd TS 0r 8m 6o aD YL 0e sD fe f8 sy bB Jv P0 0V Fm pb Ms fp 8g v6 Mt cn _j 8t FC QT C0 4r FG DK H1 s_ Ji Nv Sb x8 EA - last acessed 08/02/25. Elsevier Science & Technology, Oxford, UNITED KINGDOM.

[5] MatWeb - AISI 4130H Steel, normalized at 870°C - `https://www.matweb.com/search/datasheet.aspx?matguid=a083c5452ce848d0b45ffe9b052330ce` - last acessed 08/02/25.

[6] Razor United Kingdom - Corporate History - http://www.razor.com/about-razor/corporate-history/ - last accessed 12/10/24.

[7] B. Kilbury. Colchester Footage (https://www.youtube.com/watch?v=H0n6GhMUqy4&ab_channel=brandonkilbury - last accessed 12/10/24).

[8] B. Boston. How to lock a folding mech (https://www.youtube.com/watch?v=b2X7lJaZ2-o&ab_channel=BrianBoston - last accessed 22/07/24).

[9] How to hot glue scooter wheels. thescootertutorials and coltonjr2 - YouTube - last accessed 12/10/24, https://www.youtube.com/watch?v=rj7-toqwh5u.

[10] A. Broussard. PROTO Scooters - Standard Compression System - https://www.youtube.com/watch?v=2GVMTSQ3qZg&ab_channel=protoscooters - last accessed 12/10/24.

[11] BikeBiz. 'Kick scooters are going to be very strong this year' - https://bikebiz.com/kick-scooters-are-going-to-be-very-strong-this-year/ - last accessed 12/10/24, July 2011.

[12] Blunt and Envy Scooters UK - `https://www.bluntandenvy.co.uk/` - last acessed 08/02/25.

[13] Research and Markets ltd. Global electric kick scooter market by battery type - forecast 2024-2030 https://www.researchandmarkets.com/reports/5715488/global-electric-kick-scooter-market-by-battery - last accessed 12/10/24.

[14] T. Reed. micromobility potential in the us, uk and germany - available at https://www2.inrix.com/micromobility-study-2019 - last accessed 12/10/24.

[15] UK becomes first major economy to pass net zero emissions law - https://www.gov.uk/government/news/uk-becomes-first-major-economy-to-pass-net-zero-emissions-law - last accessed 12/10/24.

[16] Cal Stone and Maury Hull. Rider/Bicycle Interaction Loads during Standing Treadmill Cycling. *Journal of Applied Biomechanics*, 9:202–218, August 1993.

[17] Cal Stone and Maury Hull. The effect of rider weight on rider-induced loads during common cycling situations. *Journal of biomechanics*, 28:365–75, May 1995.

[18] Y. Champoux et. al. Measuring the Dynamic Structural Load of an Off-Road Bicycle Frame. *Experimental Techniques*, 28(3):33–36, 2004.

[19] Y. Champoux and S. Richard. Bicycle Structural Dynamics. *Sound and Vibration*, page 7, 2007.

[20] R. Oberheim A. Belli B. Stapelfeldt, G. Mornieux and A. Gollhofer. Development and evaluation of a new bicycle instrument for measurements of pedal forces and power output in cycling. *International Journal of Sports Medicine*, 28(4):326–332, April 2007.

[21] M. L. Hull and R. R. Davis. Measurment of pedal loading in bicycling: I. Instrumentation. *Journal of Biomechanics*, 14(12):843–855, January 1981.

[22] R. R. Davis and M. L. Hull. Measurement of pedal loading in bicycling: II. Analysis and results. *Journal of Biomechanics*, 14(12):857–872, January 1981.

[23] R. F. Reiser, M. L. Peterson, and J. P. Broker. Instrumented bicycle pedals for dynamic measurement of propulsive cycling loads. *Sports Engineering*, 6(1):41–48, March 2003.

[24] A. Girarda A. Betika W. Bertucci, F. Grappea and J. D. Rouillonc. Effects on the crank torque profile when changing pedalling cadence in level ground and uphill road cycling. *Journal of Biomechanics*, 38(5):1003–1010, May 2005.

[25] P. D. Soden and B. A. Adeyefa. Forces applied to a bicycle during normal cycling. *Journal of Biomechanics*, 12(7):527–541, January 1979.

[26] Guillaume Mornieux, Karim Zameziati, Elodie Mutter, Régis Bonnefoy, and Alain Belli. A cycle ergometer mounted on a standard force platform for three-dimensional pedal forces measurement during cycling. *Journal of Biomechanics*, 39(7):1296–1303, January 2006.

[27] M. J. A. J. M. Hoes, R. A. Binkhorst, A. E. M. C. Smeekes-Kuyl, and A. C. A. Vissers. Measurement of forces exerted on pedal and crank during work on a bicycle ergometer at different loads. *Internationale Zeitschrift für angewandte Physiologie einschließlich Arbeitsphysiologie*, 26(1):33–42, March 1968.

[28] Jean-Marc Drouet, Yvan Champoux, Sylvain Dorel, and Margaret. Estivalet. Development of Multi-platform Instrumented Force Pedals for Track Cycling (P49). In *The Engineering of Sport 7*, pages 263–271. May 2008.

[29] R. Giannetti, F. Chichi, and P. Erzegovesi. Low-cost lightweight strain measurement system for bicycle application. *IEEE Transactions on Instrumentation and Measurement*, 47(4):893–899, August 1998.

[30] D Lorenzo and Maury Hull. A Hub Dynamometer for Measurement of Wheel Forces in Off-Road Bicycling. *Journal of biomechanical engineering*, 121:132–7, February 1999.

[31] D. S. De Lorenzo and M. L. Hull. Quantification of structural loading during off-road cycling. *Journal of Biomechanical Engineering*, 121(4):399–405, August 1999.

[32] Christin Hölzel, Franz Hoechtl, and Veit Senner. Operational loads on sport bicycles for possible misuse. *Procedia Engineering*, 13:75–80, January 2011.

[33] Miha Pirnat, Zdenko Savšek, and Miha Boltežar. Measuring Dynamic Loads on a Foldable City Bicycle. *Journal of Mechanical Engineering*, 57(1):21–26, January 2011.

[34] Anton Koellner, Christopher J. Cameron, and Mark A. Battley. Measurement and Analysis System for Bicycle Field Test Studies. *Procedia Engineering*, 72:350–355, January 2014.

[35] Anton Koellner, Christopher J. Cameron, and Mark A. Battley. Structural Responses on a BMX Racing Bicycle. *Procedia Engineering*, 72:618–623, January 2014.

[36] M. J. A. J. M. Hoes, R. A. Binkhorst, A. E. M. C. Smeekes-Kuyl, and A. C. A. Vissers. Measurement of forces exerted on pedal and crank during work on a bicycle ergometer at different loads. *Internationale Zeitschrift für Angewandte Physiologie Einschließlich Arbeitsphysiologie*, 26(1):33–42, 1968.

[37] R. Davis and M. L. Hull. Design of Aluminum Bicycle Frames. *Journal of Mechanical Design*, 103(4):901–907, October 1981.

[38] Farhad Bolourchi and Maury Hull. Measurement of Rider Induced Loads during Simulated Bicycling. *International Journal of Sport Biomechanics*, 1:308–329, November 1985.

[39] Kyowa Measuring Equipment General Catalog 2022 - pages (1 - 3) - (1-4), and (9 - 7) - (9 - 8) (the page numbering system is chapter then page in that chapter). https://kyowa-ei.meclib.jp/e2022/book/#target/page_no=441 - last accessed 12/10/24.

[40] F. F. Hines. in Proc. Western Regional Strain Gauge Committee, 1960, pp. 39–44. 1960.

[41] I. Bernabucci M. Schmid D. Bibbo, S. Conforto and T. D'Alessio. A wireless integrated system to evaluate efficiency indexes in real time during cycling. In *4th European Conference of the International Federation for Medical and Biological Engineering*, IFMBE Proceedings, pages 89–92, Berlin, Heidelberg, 2009. Springer.

[42] Bluesense AD pdf catalogs (https://pdf.medicalexpo.com/pdf/corscience/bluesense-ad/68115-78785.html - last accessed 29/8/21) - after returning to the page since then unable to find the relevant catalogue.

[43] Tekscan pressure mapping, force measurement tactile sensors - https://www.tekscan.com/ - last accessed 12/10/24.

[44] D. M. Trujillo. Application of dynamic programming to the general inverse problem. *International Journal for Numerical Methods in Engineering*, 12(4):613–624, 1978.

[45] Henry R. Busby and David M. Trujillo. Solution of an inverse dynamics problem using an eigenvalue reduction technique. *Computers & Structures*, 25(1):109–117, January 1987.

[46] P. E. Hollandsworth and H. R. Busby. Impact force identification using the general inverse technique. *International Journal of Impact Engineering*, 8(4):315–322, January 1989.

[47] M. T. Martin and J. F. Doyle. Impact force identification from wave propagation responses. *International Journal of Impact Engineering*, 18(1):65–77, January 1996.

[48] L. Dong-Chering C. Ma, T. Pan-CHIO and L. Chao-Shih. A study of an inverse method for the estimation of impulsive loads. *International Journal of Systems Science*, 29(6):663–672, June 1998.

[49] Robert Adams and James F. Doyle. Multiple force identification for complex structures. *Experimental Mechanics*, 42(1):25–36, March 2002.

[50] J. Sanchez and H. Benaroya. Review of force reconstruction techniques. *Journal of Sound and Vibration*, 333(14):2999–3018, July 2014.

[51] E. Jacquelin and P. Hamelin. Force recovered from three recorded strains. *International Journal of Solids and Structures*, 40(1):73–88, January 2003.

[52] S. S. Law, T. H. T. Chan, and Q. H. Zeng. Moving force identification: a time domain method. *Journal of Sound and Vibration*, 201(1):1–22, March 1997.

[53] N. S. Vyas and A. L. Wicks. Reconstruction of turbine blade forces from response data. *Mechanism and Machine Theory*, 36(2):177–188, February 2001.

[54] M. C. Djamaa, N. Ouelaa, C. Pezerat, and J. L. Guyader. Reconstruction of a distributed force applied on a thin cylindrical shell by an inverse method and spatial filtering. *Journal of Sound and Vibration*, 301(3):560–575, April 2007.

[55] Yi Liu and W. Steve Shepard. An improved method for the reconstruction of a distributed force acting on a vibrating structure. *Journal of Sound and Vibration*, 291(1):369–387, March 2006.

[56] S. Granger and L. Perotin. An inverse method for the identification of a distributed random excitation acting on a vibrating structure part 1: Theory. *Mechanical Systems and Signal Processing*, 13(1):53–65, January 1999.

[57] Masaaki Tanio, Yoshito Hirata, and Hideyuki Suzuki. Reconstruction of driving forces through recurrence plots. *Physics Letters A*, 373(23):2031–2040, May 2009.

[58] E. Zhang, J. Antoni, and P. Feissel. Bayesian force reconstruction with an uncertain model. *Journal of Sound and Vibration*, 331(4):798–814, February 2012.

[59] C. K. Ma, J. M. Chang, and D. C. Lin. Input forces estimation of beam structures by an inverse method. *Journal of Sound and Vibration*, 259(2):387–407, January 2003.

[60] Shaowen Xu, Xiaomin Deng, Vikrant Tiwari, Michael A. Sutton, William L. Fourney, and Damien Bretall. An inverse approach for pressure load identification. *International Journal of Impact Engineering*, 37(7):865–877, July 2010.

[61] E. Lourens, E. Reynders, G. De Roeck, G. Degrande, and G. Lombaert. An augmented Kalman filter for force identification in structural dynamics. *Mechanical Systems and Signal Processing*, 27:446–460, February 2012.

[62] K. Maes, A. W. Smyth, G. De Roeck, and G. Lombaert. Joint input-state estimation in structural dynamics. *Mechanical Systems and Signal Processing*, 70-71:445–466, March 2016.

[63] Qiaofeng Li and Qiuhai Lu. Force localization and reconstruction using a two-step iterative approach. *Journal of Vibration and Control*, 24(17):3830–3841, September 2018. Publisher: SAGE Publications Ltd STM.

[64] Dynamic force reconstruction techniques from incomplete measurements - V. Jayalakshmi, K. Lakshmi, A. Rama Mohan Rao, 2018.

[65] A novel method for force identification based on filter and FEM - Zhanpeng Zheng, Chengjun Wu, Donghong Wang, 2019.

[66] M. Aucejo and O. De Smet. An iterated multiplicative regularization for force reconstruction problems. *Journal of Sound and Vibration*, 437:16–28, December 2018.

[67] Gang Yan and Hao Sun. A non-negative Bayesian learning method for impact force reconstruction. *Journal of Sound and Vibration*, 457:354–367, September 2019.

[68] Mike McLeod. Fearless design - https://www.design-engineering.com/features/fearless-design/ - last accessed 12/10/24.

[69] L. Peterson Londry, K. 1986. Finite-Element Structural Analysis: A New Tool for Bicycle Frame Design: The Strain Energy Design Method. Bike Tech: Bicycling Magazine's Newsletter for the Technical Enthusiast, 1986.

[70] E. Elton M. Milne R. Morris D. Covill, S. Begg and T. Katz. Parametric Finite Element Analysis of Bicycle Frame Geometries. *Procedia Engineering*, 72:441–446, January 2014.

[71] J. Drouet D. Covill, P. Allard and N. Emerson. An Assessment of Bicycle Frame Behaviour under Various Load Conditions Using Numerical Simulations. *Procedia Engineering*, 147:665–670, January 2016.

[72] J. A. Nemes L. B. Lessard and Patrick L. Lizotte. Utilization of FEA in the design of composite bicycle frames. *Composites*, 26(1):72–74, January 1995.

[73] F. Höchtl, M. Hein, S. Klug, and V. Sennera. On the effect of chain stay impact on the structural safety of CFRP structures in mountain biking. *Procedia Engineering*, 34:664–669, January 2012.

[74] S. Klug F. Hšchtl, M. Hein and V. Sennera. A method for quantifying impact loads from stone impact in mountain biking. *Procedia Engineering*, 34:415–420, January 2012.

[75] Jean-Richard Cormier and Gabriel LaPlante. Study of the effects of low-velocity impact on a composite bicycle down tube. *Composite Structures*, 198:144–155, August 2018.

[76] AFNOR EN 14781. Bicyclettes de course – Exigences de sécurité et méthodes d'essai; 2006.

[77] Thomas Jin-Chee Liu and Huang-Chieh Wu. Fiber direction and stacking sequence design for bicycle frame made of carbon/epoxy composite laminate. *Materials & Design*, 31(4):1971–1980, April 2010.

[78] S. N. Zahari N. A. Z. Abdullah M. S. M. Sani, N. A. Nazri and G. Priyandoko. Dynamic Study of Bicycle Frame Structure. *IOP Conference Series: Materials Science and Engineering*, 160:012009, November 2016.

[79] G. Mehta J. Gandhi J. Shah, S. Shah and M. Gor. Vertical stiffness of bicycle frame and its influence on rider comfort. *SN Applied Sciences*, 2(10), 2020.

[80] M. Loccufier J. Vanwalleghem, I. Baere and W. V. P. Sensor design for outdoor racing bicycle field testing for human vibration comfort evaluation. *Measurement Science and Technology*, 24(9):095002, July 2013.

[81] Julien Lépine, Yvan Champoux, and Jean-Marc Drouet. The relative contribution of road bicycle components on vibration induced to the cyclist. *Sports Engineering*, 18(2):79–91, December 2014.

[82] Niels Aage, Erik Andreassen, Boyan S. Lazarov, and Ole Sigmund. Giga-voxel computational morphogenesis for structural design. *Nature*, 550(7674):84–86, October 2017.

[83] Ji-Hong Zhu, Wei-Hong Zhang, and Liang Xia. Topology Optimization in Aircraft and Aerospace Structures Design. *Archives of Computational Methods in Engineering*, 23(4):595–622, December 2016.

[84] Antonio Viviani, Luigi Iuspa, and Andrea Aprovitola. Multi-objective optimization for re-entry spacecraft conceptual design using a free-form shape generator. *Aerospace Science and Technology*, 71, September 2017.

[85] Henrik Polk Mads Baandrup, Ole Sigmund and Niels Aage. Closing the gap towards super-long suspension bridges using computational morphogenesis. *Nature Communications*, 11(1):2735, June 2020.

[86] Boyan Lazarov, Fengwen Wang, and Ole Sigmund. Length scale and manufacturability in density-based topology optimization. *Archive of Applied Mechanics*, 86:1–30, January 2016.

[87] Linfeng Mei and Qian Wang. Structural Optimization in Civil Engineering: A Literature Review. *Buildings*, 11(2):66, February 2021.

[88] Marco Cavazzuti, Andrea Baldini, Enrico Bertocchi, Dario Costi, Enrico Torricelli, and Patrizio Moruzzi. High performance automotive chassis design: a topology optimization based approach. *Structural and Multidisciplinary Optimization*, 44(1):45–56, July 2011.

[89] L. Maestrelli and A. Falsini. Bicycle frame optimization by means of an advanced gradient method algorithm, 2008.

[90] Iain McEwen, David E. Cooper, Jay Warnett, Nadia Kourra, Mark A. Williams, and Gregory J. Gibbons. Design & Manufacture of a High-Performance Bicycle Crank by Additive Manufacturing. *Applied Sciences*, 8(8):1360, August 2018.

[91] Ahmad Yusuf Ismail, Gangta Na, and Bonyong Koo. Topology and Response Surface Optimization of a Bicycle Crank Arm with Multiple Load Cases. *Applied Sciences*, 10(6):2201, January 2020.

[92] S. Pearson. Stress Analysis for the Optimisation of Freestyle Scooter Components (Master's Thesis). *2020*.

[93] Suchandrima Das, Felix Hofmann, and Edmund Tarleton. Consistent determination of geometrically necessary dislocation density from simulations and experiments. *International Journal of Plasticity*, 109:18–42, October 2018.

[94] Kaisa Miettinen. *Nonlinear Multiobjective Optimization*, volume 12 of *International Series in Operations Research & Management Science*. Springer US, Boston, MA, 1998.

[95] Yongxin Li, Quanwei Yang, Tao Chang, Tao Qin, and Fenghe Wu. Multi-load cases topological optimization by weighted sum method based on load case severity degree and ideality. *Advances in Mechanical Engineering*, 12(8):1687814020947510, August 2020.

[96] G. I. N. Rozvany. A critical review of established methods of structural topology optimization. *Structural and Multidisciplinary Optimization*, 37(3):217–237, January 2009.

[97] M. P. Bendsøe and O. Sigmund. Material interpolation schemes in topology optimization. *Archive of Applied Mechanics*, 69(9):635–654, November 1999.

[98] Ole Sigmund and Kurt Maute. Topology optimization approaches. *Structural and Multidisciplinary Optimization*, 48(6):1031–1055, December 2013.

[99] G.I.N. Rozvany. Aims, scope, methods, history and unified terminology of computer-aided topology optimization in structural mechanics. *Structural and Multidisciplinary Optimization*, 21(2):90–108, April 2001.

[100] Erik Andreassen, Anders Clausen, Mattias Schevenels, Boyan S. Lazarov, and Ole Sigmund. Efficient topology optimization in MATLAB using 88 lines of code. *Structural and Multidisciplinary Optimization*, 43(1):1–16, January 2011.

[101] M. Zhou, Y.K. Shyy, and H.L. Thomas. Checkerboard and minimum member size control in topology optimization. *Structural and Multidisciplinary Optimization*, 21(2):152–158, April 2001.

[102] Ole Sigmund and J. Petersson. Numerical instabilities in topology optimization: A survey on procedures dealing with checkerboards, mesh-dependencies and local minima. *Structural Optimization*, 16:68–75, August 1998.

[103] About Us - https://razor.com/about-us/ - last acessed 12/10/24. Publication Title: Razor.

[104] Jean-Marc Drouet and Yvan Champoux. Development of a three-load component instrumented stem for road cycling. *Procedia Engineering*, 34:502–507, January 2012.

[105] Jean-Marc Drouet, Yvan Champoux, Sylvain Dorel, and Margaret. Estivalet. Development of Multi-platform Instrumented Force Pedals for Track Cycling (P49). pages 263–271, May 2009.

[106] OpenLogger - Digilent Reference - https://digilent.com/reference/test-and-measurement/openlogger/start?srsltid=AfmBOoq0IBj4RP1f1Xf5ds--hOhQ895l9NWH3QHt5V3r06ltZu63vd05 - last acessed 12/10/24.

[107] Texas Instruments - TLV767-Q1 low dropout voltage regulator - https://www.ti.com/product/TLV767-Q1 - last acessed 08/02/25.

[108] Texas Instruments - INA828 low-power, precision instrumentation amplifier - https://www.ti.com/product/INA828 - last acessed 08/02/25.

[109] Omega Engineering linear strain gauges - https://www.omega.co.uk/pptst/SGD_LINEAR1-AXIS.html - last accessed 12/10/24.

[110] Urgenex 1000 mAh 7.4 V Li-Po battery - https://www.amazon.co.uk/URGENEX-Battery-Batteries-1100mah-WLtoys/dp/B08Y8ZJ94K/ref=asc_df_B08Y8ZJ94K?mcid=5fa13bfa0c1c3cc1b333b02b897ce0e4&tag=googshopuk-21&linkCode=df0&hvadid=697272933764&hvpos=&hvnetw=g&hvrand=11245472415367497851&hvpone=&hvptwo=&hvqmt=&hvdev=c&hvdvcmdl=&hvlocint=&hvlocphy=9198084&hvtargid=pla-1370723037025&psc=1&gad_source=1 - last acessed 08/02/25.

[111] Autodesk Fusion | 3D CAD, CAM, CAE & PCB Cloud-Based Software | Autodesk.

[112] Native STEMstunt scooter deck - https://www.skatepro.uk/243-35728.htm?stockcode=NTSTEMDECK/KAI-520&gad_source=1&gclid=Cj0KCQjw3bm3BhDJARIsAKnHoVVfLrXsivYKl4e9eJYIFk5s-rJmGTGBc-EjmG0-3ejsqd3e75aHPF0aAptbEALw_wcB - last accessed 21/09/24.

[113] District S-Series AL115 Bar | Parts | Alpha Pro Scooters - https://www.alphaproscooters.com/en-gb/products/district-s-series-al115-bar?variant=40059035811901 - last accessed 21/09/24.

[114] Micro MX 180 fork – Micro Scooters Australia - https://www.microscooters.com.au/collections/micro-mx-180-scooter-spare-parts/products/mx1101-fork-180-black - last accessed 12/10/24.

[115] Blazer Pro Scooter SCS Compression Kit 6061 Alloy - https://rollbackworld.com/scooters/blazer-pro-scooter-scs-compression-kit-6061-alloy/.

[116] Ethic Mogway 100mm Wheel | Parts | Alpha Pro Scooters - https://www.alphaproscooters.com/en-gb/products/ethic-mogway-110mm-wheel?srsltid=AfmBOop00WZnFbA343sNELGF-yTjG5mEXbDD8PLAiifrsb8GW3og_VZ0 - last accessed 21/09/24.

[117] Tilt Metra Stunt Scooter Grips | SkatePro - https://www.skatepro.uk/246-35284.htm - last acessed 21/09/24.

[118] Abaqus - https://www.3ds.com/products/simulia/abaqus, July.

[119] Ian Polmear, Dr. David St. John, and Vilupanur Ravi. *Light Alloys: From Traditional Alloys to Nanocrystals, 4th edition, pg. 153*. Elsevier Science & Technology, Oxford, UNITED KINGDOM, 2005.

[120] Matweb, aluminum 6061-T6; 6061-T651.

[121] MATLAB documentation - lsqlin function - https://www.mathworks.com/help/optim/ug/lsqlin.html - last acessed 08/02/25.

[122] S. Pearson. Stress Analysis for the Optimisation of Freestyle Scooter Components (Master's Thesis). *2020*.

[123] Ethic Pandemonium Deck - Black | Alpha Pro Scooters - Parts - https://www.alphaproscooters.com/en-gb/products/ethic-pandemonium-deck-black - last acessed 12/10/24.

[124] Prescale - Pressure measurement film | Fujifilm [United Kingdom] - https://www.fujifilm.com/uk/en/business/inspection/measurement-film/prescale - last accessed 12/10/24.

[125] Yusuke Sakai, Shinya Yamada, Toshiki Sato, Ryota Hayakawa, Ryota Higurashi, and Nao Kominato. Richardson–Lucy Deconvolution with a Spatially Variant Point-spread Function of Chandra: Supernova Remnant Cassiopeia A as an Example. *The Astrophysical Journal*, 951(1):59, July 2023. Publisher: The American Astronomical Society.

[126] Tod R. Lauer. Deconvolution With a Spatially-Variant PSF. page 167, December 2002. arXiv:astro-ph/0208247.

[127] DJB Instruments-Instrumented Impact Hammer IH-05 - `https://www.djbinstruments.com/products/instrumentation/impact-hammers/view/ih-05` - last accessed on 12/10/24.

[128] National Instruments, Labview- https://www.ni.com/en/shop/labview.html - last accessed 12/10/24.

[129] National Instruments PXIe-4492 - https://www.ni.com/en-gb/shop/model/pxie-4492.html.

[130] National Instruments PXIe-1082 - https://www.ni.com/en-gb/support/model.pxie-1082.html.

[131] V. A. Morozov. Criteria for Selection of Regularization Parameter. In V. A. Morozov, editor, *Methods for Solving Incorrectly Posed Problems*, pages 32–64. Springer, New York, NY, 1984.

[132] Per Christian Hansen. Analysis of Discrete Ill-Posed Problems by Means of the L-Curve. *SIAM Review*, 34(4):561–580, 1992. Publisher: Society for Industrial and Applied Mathematics.

[133] H. W. Engl. Discrepancy principles for Tikhonov regularization of ill-posed problems leading to optimal convergence rates. *Journal of Optimization Theory and Applications*, 52(2):209–215, February 1987.

[134] Per Christian Hansen and Dianne P. O'Leary. The Use of the L-Curve in the Regularization of Discrete Ill-Posed Problems | SIAM Journal on Scientific Computing, 1993.

[135] Panasonic Lumix DMC-G7K compact DSLR mirrorless camera - `https://www.panasonic.com/uk/consumer/cameras-camcorders/lumix-mirrorless-cameras/lumix-g-cameras/dmc-g7keb.html` - last acessed 08/02/25.

[136] Prabhaker Mishra, Chandra M. Pandey, Uttam Singh, Anshul Gupta, Chinmoy Sahu, and Amit Keshri. Descriptive Statistics and Normality Tests for Statistical Data. *Annals of Cardiac Anaesthesia*, 22(1):67, March 2019.

[137] C. kadpa. novel quadratic bézier triangular and tetrahedral elements using existing mesh generators: Applications to linear nearly incompressible elastostatics and implicit and explicit elastodynamics - Kadapa - 2019 - International Journal for Numerical Methods in Engineering.

[138] C. Kadpa. Linear tetrahedral elements for solid mechanics. don't do it! (online blog), 2019. - https://ckadapa.wordpress.com/2019/11/16/linear-tetrahedral-elements-for-solid-mechanics-dont-do-it/ - last accessed 12/10/24, November 2019.

[139] ABAQUS Analysis User's Manual (v6.6) - `https://classes.engineering.wustl.edu/2009/spring/mase5513/abaqus/docs/v6.6/books/usb/default.htm?startat=pt05ch20s01abm43.html` - last accessed 12/10/24.

[140] Pascal Guay and Ahmed Frikha. Ball Bearing Stiffnesses - A New Approach Offering Analytical Expressions ESA special publication. 737:49, September 2015.

[141] H. M. C. C. Somarathna, S. N. Raman, D. Mohotti, A. A. Mutalib, and K. H. Badri. Rate dependent tensile behavior of polyurethane under varying strain rates. *Construction and Building Materials*, 254:119203, September 2020.

[142] Zisheng Liao, Xiaohu Yao, Longhui Zhang, Mokarram Hossain, Jiong Wang, and Shuguang Zang. Temperature and strain rate dependent large tensile deformation and tensile failure behavior of transparent polyurethane at intermediate strain rates. *International Journal of Impact Engineering*, 129:152–167, July 2019.

[143] Ethic Pandemonium V2 Pro Scooter Deck | SkatePro - https://www.skatepro.uk/243-50650.htm - last accessed 12/10/24.

[144] K. Demay. Pandemonium V2 Ethic: behind the scene - https://www.youtube.com/watch?v=876zedyl44s&t=242s - last accessed 12/10/24.

[145] Perfect designs for imperfect AM - O. Sigmund - CDFAM 24 Berlin - `https://www.youtube.com/watch?v=w0lb_F4tdsE` - last accessed at 12/10/24.